AD-A171 038 'TOWARD 84/86' FIELD EXPERIMENT: INVESTIGATION OF PHYSICS OF SYNTHETIC AP (U) JET PROPULSION LAB PASADENA CA O H SHEMDIN MAY 86 1/3

UNCLASSIFIED F/G 17/9 NL

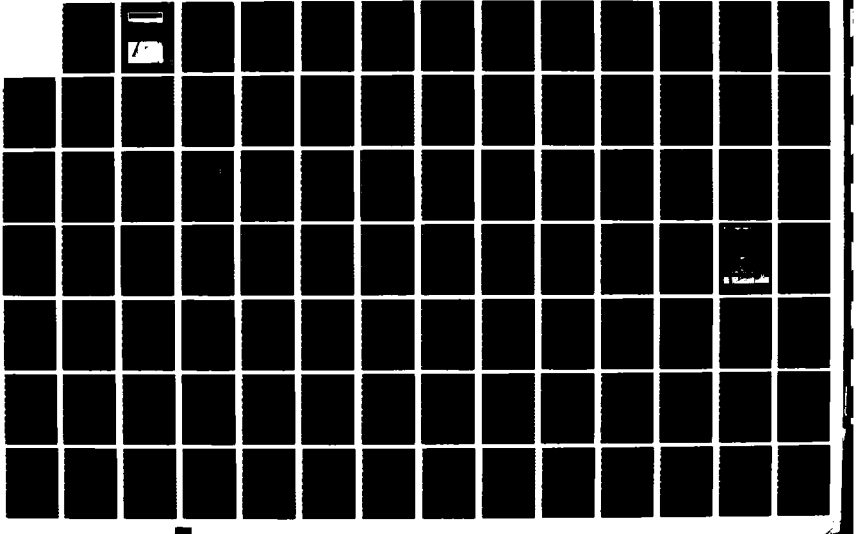

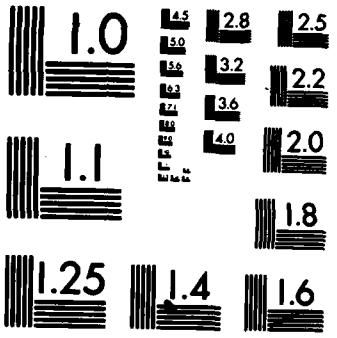

INVESTIGATION OF PHYSICS OF SYNTHETIC APERTURE RADAR IN OCEAN REMOTE SENSING

TOWARD 84/86 FIELD EXPERIMENT

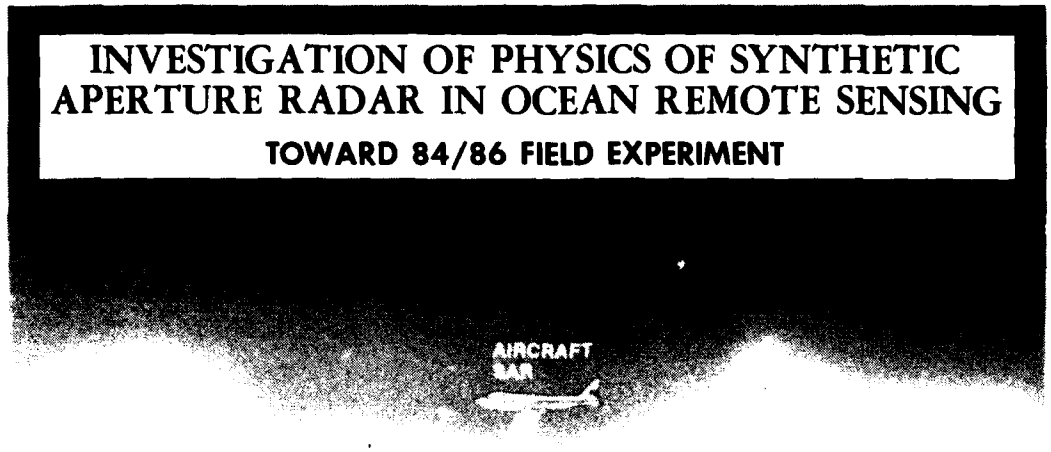

INTERIM REPORT
VOLUME II:
CONTRIBUTIONS OF INDIVIDUAL INVESTIGATORS
MAY 1986

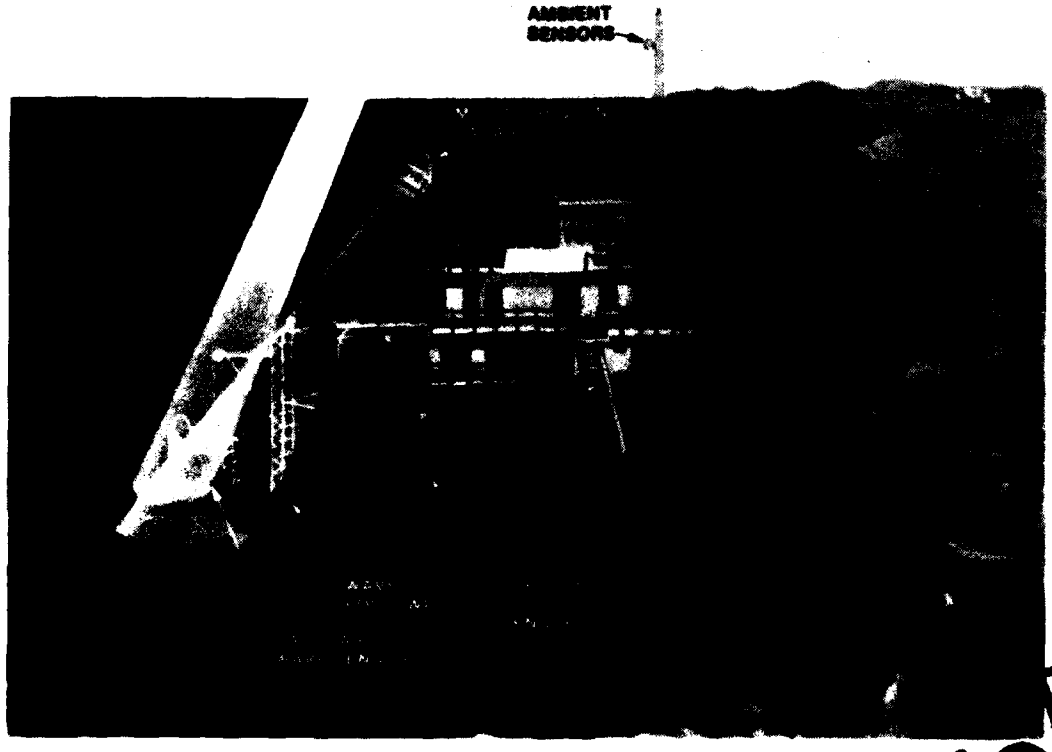

Approved for Public Release; Distribution Unlimited.

"TOWARD 84/86"* FIELD EXPERIMENT
INVESTIGATION OF PHYSICS OF SYNTHETIC APERTURE RADAR IN OCEAN REMOTE SENSING

INTERIM REPORT

VOLUME II: CONTRIBUTIONS OF INDIVIDUAL INVESTIGATORS

OMAR H. SHEMDIN,

PRINCIPAL INVESTIGATOR

LIST OF PARTICIPANTS:

ERIM:	D. Lyzenga	NRL:	W. Garrett
			W. Keller
JPL:	W. Brown		W. Plant
	D. Held		
	D. Hoff	ORE:	P. Hwang
	T. W. Thompson		E. Tajirian
			D. Thomas
NPGS:	K. Davidson		
	G. Geernaert	SIO:	R. Guza
NOSC:	P. Hanson	UKa:	H. Chaudry
	J. Wright		R. Moore
		UMd:	R. Harger

FOR

OCEAN SCIENCES DIVISION
OFFICE OF THE CHIEF OF NAVAL RESEARCH
ARLINGTON, VIRGINIA

(Technical Monitor: Hans Dolezalek)

MAY 1986

(TOWER OCEAN WAVE AND RADAR DEPENDENCE)

TABLE OF CONTENTS

APPENDIX I

Surface Gravity Wave Measurements

R. T. Guza
Scripps Instiution of Oceanography
Center for Coastal Studies
Code A009
La Jolla, CA 92093

The characteristics of surface gravity waves within the California Bight are profoundly influenced by the topographic setting. The Channel Islands and the orientation of the coastline shelter the coast from many wave directions (Figure 1). Pawka [1982, 1983] and Pawka et al [1984] discuss extensive measurements of the directional wave climate at Torrey Pines Beach, approximately 10 km north of the NOSC tower (Figure 1). The waves at these two sites are similar, so the work at Torrey Pines is relevant to the TOWARD experiments. At Torrey Pines, only a narrow directional sector (282°-290°) is directly open to the north Pacific swell which is an important source of coastal wave energy (Figure 1). However, the presence of shallow shoals and banks in the island vicinity (notably Cortez and Tanner Banks in Figure 2) theoretically provide a refractive energy source. Relatively high angle north swell is refracted by the banks towards Torrey Pines (Figure 2). Thus, unimodal, deep ocean north swell theoretically results in a bimodal directional spectrum at Torrey Pines; the open window at about 290° and a refractive peak around 255°. Extensive measurements by Pawka and collegues at Torrey Pines have firmly established the existence of the southern refractive peak (Figure 3). These data were collected in March, 1977 with a 400 m long multi-element linear pressure sensor array and analyzed with high resolution data

adaptive estimators.

Similar high resolution measurements have not been attempted at the TOWARD site. However, theoretical refraction calculations for the Mission Bay entrance Channel (i.e. the NOSC tower) suggest a comparable bimodal response to north swell (Figure 4). Note that the angular location of coastal directional peaks is somewhat insensitive to the deep ocean direction. North swell energy can only reach coastal waters through the open window or via banks refraction.

The NOSC tower site is not locally sheltered from southern swell. Thus, although perhaps less energetic than northern swell outside the Channel Islands, southern swell can be an important component inside the Channel Islands. The characteristics of southern swell, in the northern hemisphere, are not well known. In a classic series of papers, Munk and co-workers established the source as high latitude storms in the south Pacific and Indian Oceans. The superposition of a typical southern swell directional peak (230°) with the bimodal north swell response results in a complex trimodal directional spectrum at Mission Bay (Figure 5). These peaks are separated from each other by about 30° in local deep water (i.e. a few km offshore). Refraction reduces the angular separation at the tower. A long linear array would be required to resolve the directional peaks (Figure 5).

Cost constraints, and the relatively low priority given to directional long wave measurements in this experiment, did not permit the installation of a long linear array in the TOWARD experiment. Four pressure sensors were installed on the tower

legs, about 7 below the surface. These sensors were used to estimate two orthogonal components of sea surface slope, similar to a pitch and roll buoy. This type of directional measurement has relatively low resolution, less than the 150 m long linear array shown in Figure 4. The resolution of pitch and roll type systems, and a variety of analysis techniques are discussed by Hasslemann et al [1980], Lawson and Long [1983] and Oltman-Shay and Guza [1984]. Figure 6 shows that bimodal spectra, with peaks separated by 90°, can be resolved by the estimators discussed by Oltman-Shay and Guza [1984]. For angular separations less than about 60° the peaks are not resolved and the angle estimated to have the maximum power is near the weighted average of the unresolved peaks (Figure 7). The estimator of Hasselmann et al [1980] also resolves widely spaced peaks. Neither estimator can resolve three peaks. It appears that present methods are incapable of resolving the trimodal directional spectra anticipated at the experiment site (Figure 7). The Oltman-Shay and Guza [1984] estimator is used below.

The present analysis is focused on four overflight days of phase 1 (17 Oct, 31 Oct, 4 Nov, 7 Nov 1984) and 8 overflight days of phase 2 (13, 18, 19, 20, 24, 25, 26, 27 March 1985). The time periods analyzed, significant wave heights (obtained from depth corrected pressure sensors about 7 m below the surface), mean currents and wind speed and directions (NOSC sensors) are shown in Tables 1 and 2. Sea Surface elevation spectra are shown in Figure 8. Most of the spectra are peaked around .07 hz (31 Oct is an exception with a peak around .11 hz). The majority of the

spectra are rather broad, with significant energy spanning the .1-.3 hz frequency band. Days with a relatively narrow spectral peak are 4, 7 November and 18, 24 March.

Directional spectral have been estimated for each frequency band in Figure 8. For example, Figure 9 shows estimates for four frequency bands (width .0039 hz) on 31 October. The three lowest bands correspond to peaks in the energy spectrum (vertical arrows on 31 October panel in Figure 8). It is reemphasized that these directional spectra are smoothed (actually convolved) versions of the true spectra. Nevertheless, the directional spreads probably provide at least a relative measure of the spreading in each frequency band.

It is not practical to present the hundreds of directional spectra which have been estimated. The angles with maximum power, and the angular spread at half maximum power are shown in Figure 10. In general the low frequencies show the smallest directional spread reflecting both refractive narrowing (which is stronger for long waves) and the well known tendency for long waves to have narrower beam even in deep water. The lowest frequencies ($f<.07$) frequently show a southerly approach direction. This may indicate the presence of southern hemisphere swell but is also consistent with the increasing importance of the banks refractive peak with decreasing frequency. Note that the measured wave directions at the tower must be modified by refraction prior to comparison with SAR image collected in deeper water.

For convenience, the values plotted in Figures 8 and 10 for 6 days (17, 31 October, 4, 7 Nov, 19, 27 March) with Convair 990 overflights are listed in Table 3. 'FREQ' is the wave frequency in hz. The column labeled "ANG MAXPWR" is the angle (relative to 270°) with the maximum energy. The angles listed are relative to 270°, i.e. 10° = 280°, and -10° = 260°. The column labeled "+- deg to Halfpwr" gives degrees from the peak angle to the half power points. The estimated spectra are usually quite symetric. The "FWHM" is the full width at half maximum power in degrees (the sum of the +- degrees column). The "power" listed is the energy in each frequency band and is not related to directional quantities.

References

Hasselmann, D. E., M. Dunckel, J. A. Ewing, 1980, "Directional wave spectra observed during JONSWAP 1973," J. Phys. Oceanog., v. 10, p. 1264-1280.

Lawson, L. M. and R. B. Long, 1983, "Multimodal properties of the surface-wave field observed with pitch-roll buoys during GATE," J. Phys. Oceanog., v. 13, p. 474-486.

Oltman-Shay, Joan and R. T. Guza, 1984, "A data-adaptive ocean wave directional-spectrum estimator for pitch and roll type measurements," J. Phys. Oceanog., v. 14, n. 11, p. 1800-1810.

Pawka, S. S., 1982, "Wave directional characteristics on a partially sheltered coast," Ph.D. dissertion, Scripps Institution of Oceanography, University of California, San Diego, 246 pp.

Pawka, S. S., 1983, "Island shadows in wave directional spectra," J. Geophys. Res., v. 88, p. 2579-2591.

Pawka, S. S. and R. T. Guza, 1983, "Coast of California waves study - site selection," SIO Ref. Series No. 83-12., 51 pp.

Pawka, S. S., D. L. Inman and R. T. Guza, 1984, "Island sheltering of surface gravity waves: model and experiment Continental Shelf Res., v. 3, n. 1, p. 35-53.

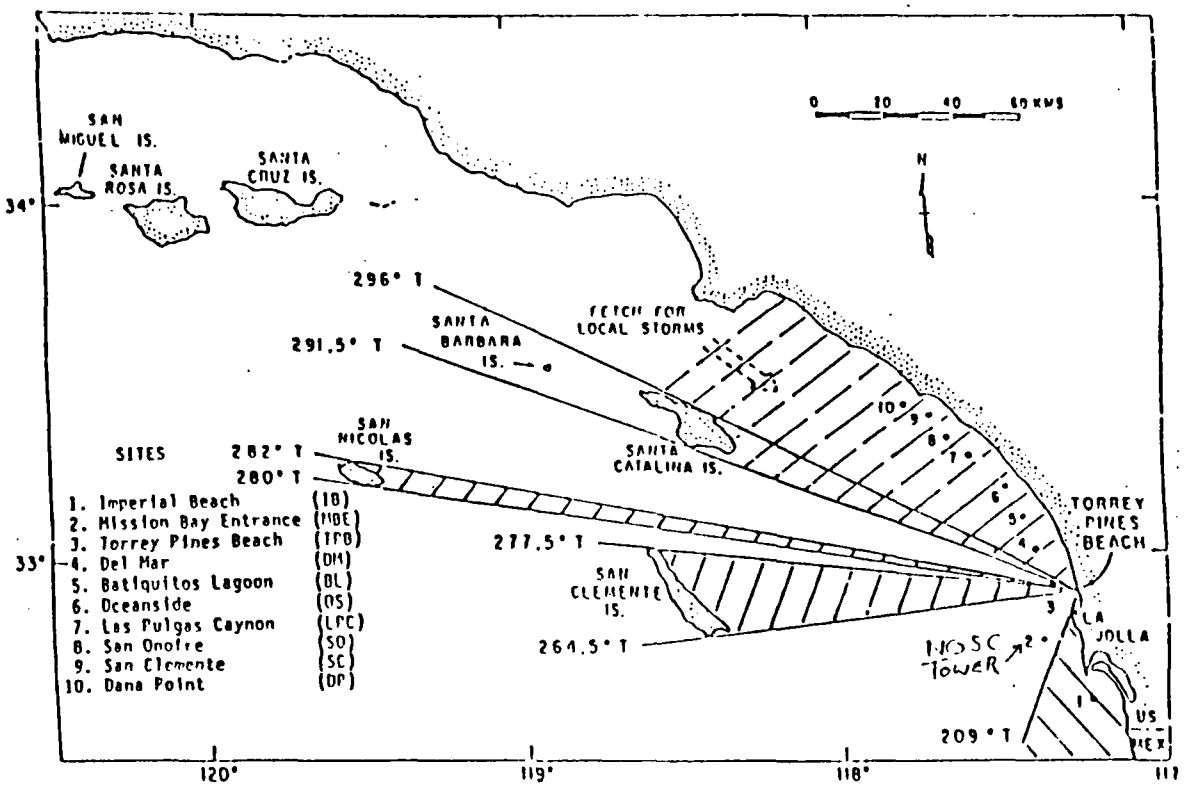

Figure 1. Schematic of the wave shadows at Torrey Pines Beach. The coastal sites included in the waves study of Pawka and Guza [1983] are numbered; the NOSC tower is site number 2.

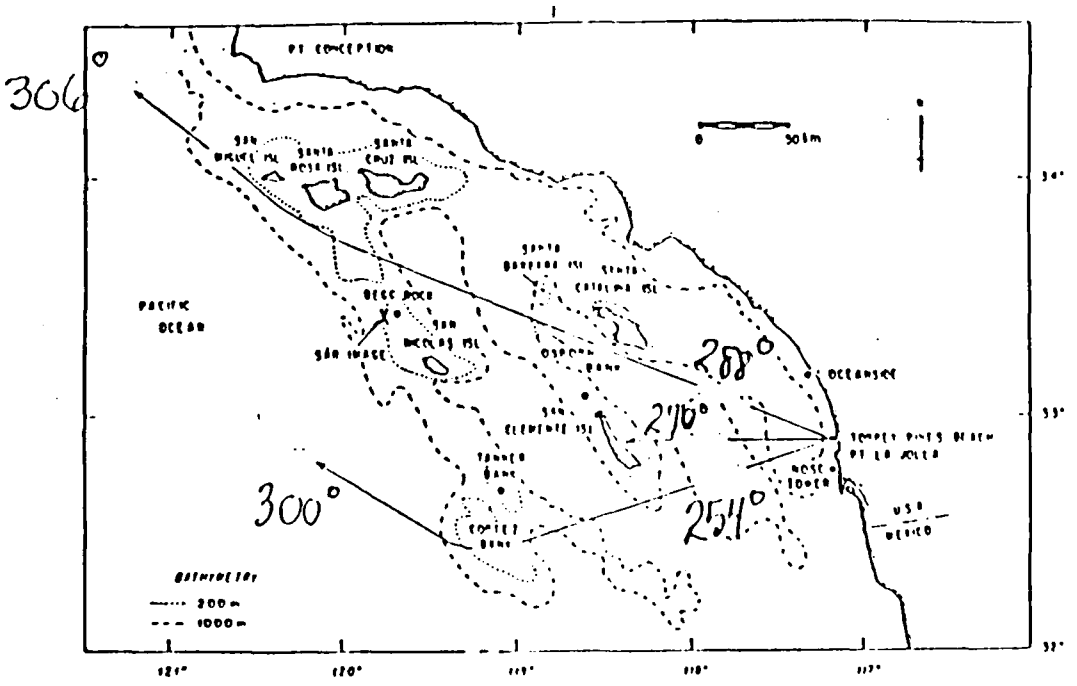

Figure 2. Schematic offshore bathymetry and the path of several wave rays with frequency .059 hz [Pawka et al, 1984].

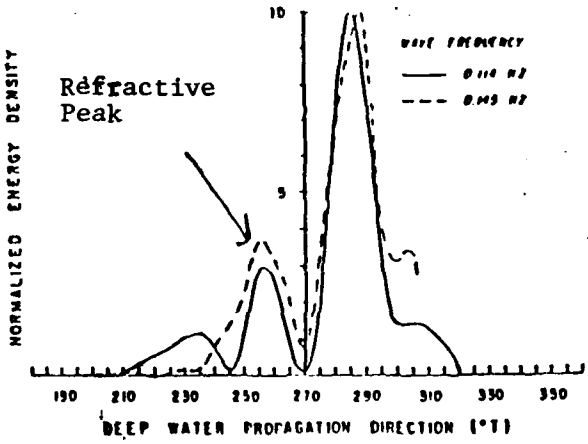

FREQUENCY
0.114 Hz
0.145 Hz

Figure 3. Measured directional spectra at Torrey Pines Beach (refracted into local deep water) for 10 sample days in March 1977. The data runs have a cumulative length of roughly 64 hours [Pawka, 1983].

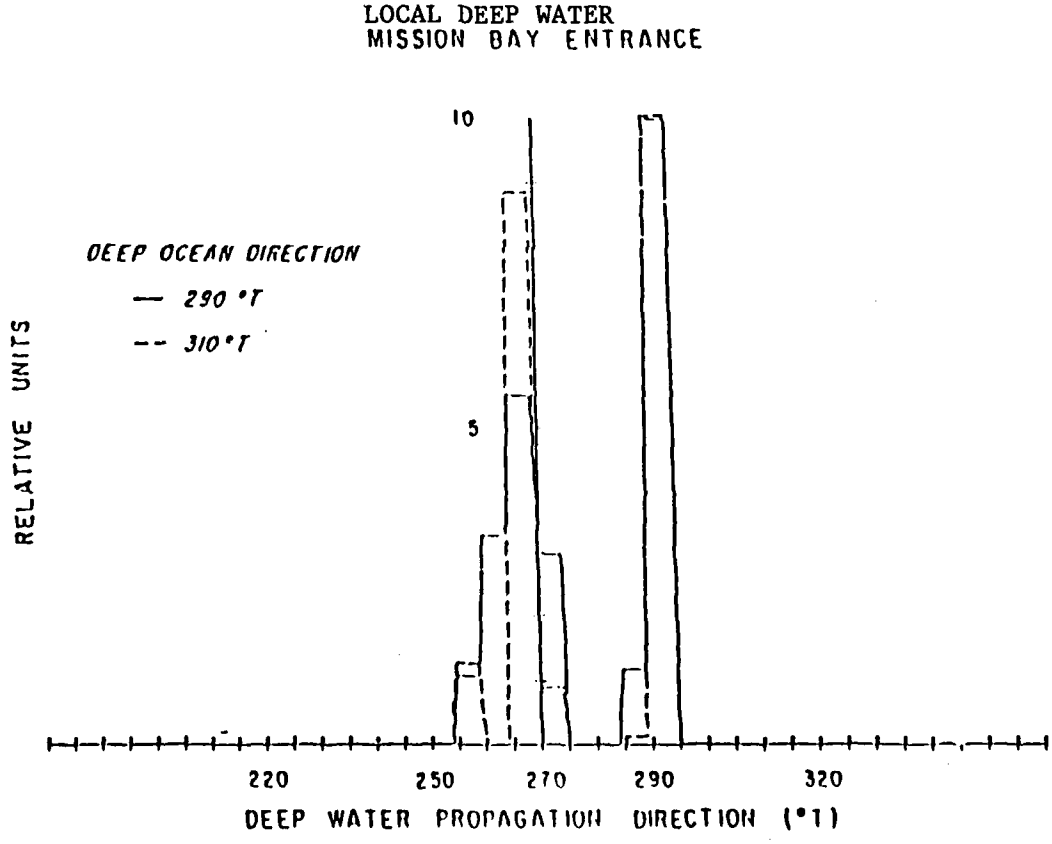

Figure 4. The theoretical deepwater responses at Mission Bay Entrance to two north swell events. The directional distributions of the deep ocean events (not shown) have widths of 20° (full width at half maximum) and are smooth (cos power) functions. The responses have been block averaged into 5° increments [Pawka and Guza, 1983].

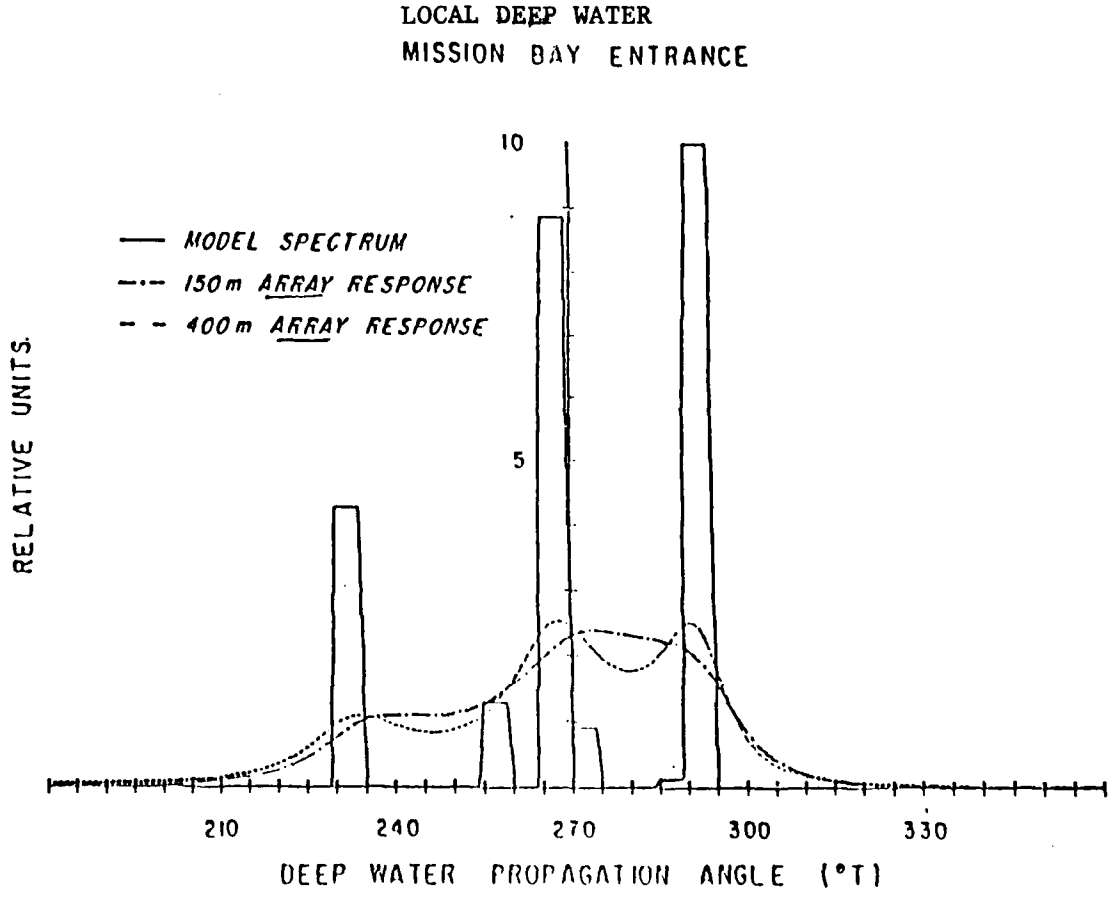

Figure 5. The theoretical response at Mission Bay Entrance ('model spectrum') to a deep ocean mixed north swell (310° T) and south swell (230° T) condition. The model spectrum (coastal response) has been blocked averaged into 5° increments. Analysis is for a wave period of 15.0 seconds. The smearing of the model spectrum by finite length linear arrays is indicated.

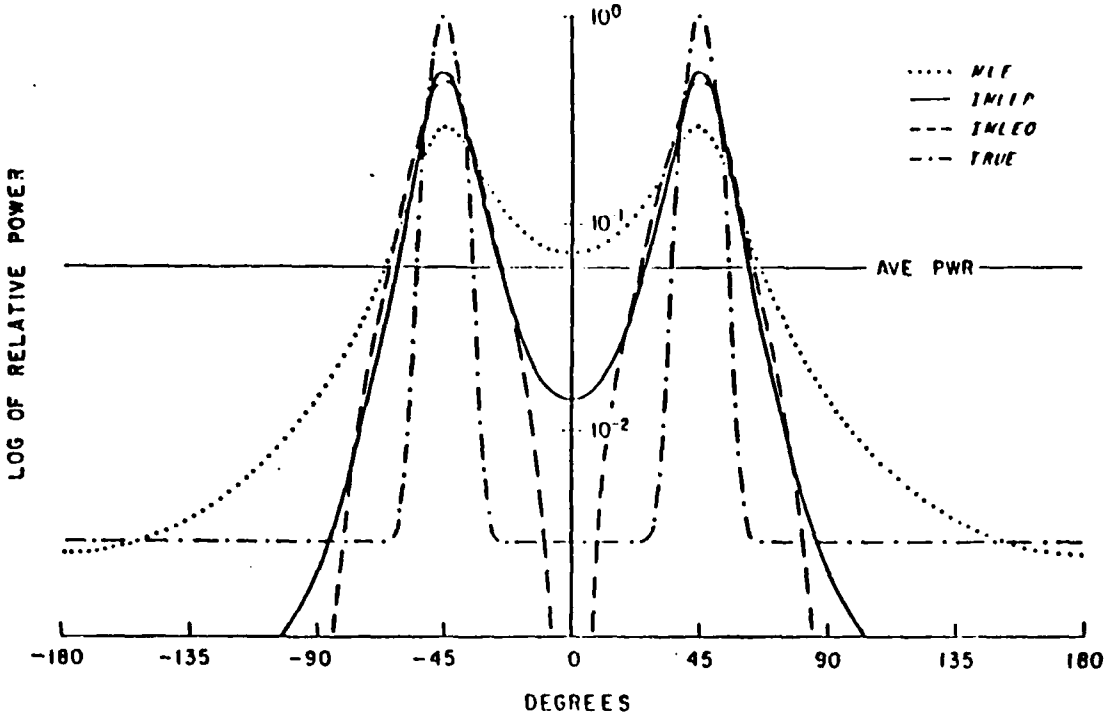

Figure 6. Various maximum likelihood estimates (MLE, IMLEP, IMLEO) of a true bimodal spectrum [Oltman-Shay and Guza, 1984].

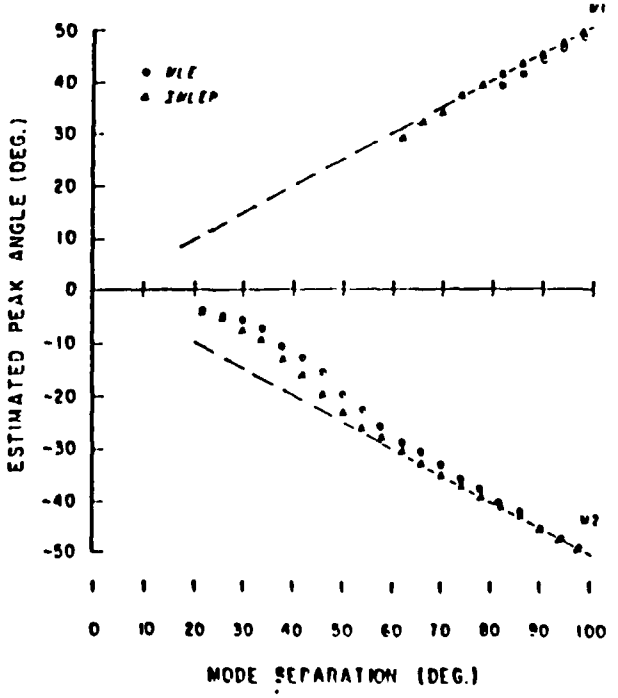

Figure 7. Estimated peak angles of bimodal test spectra with varying angular separation of the modes. One mode (M1) has half the energy of the other (M2). Both modes are 10 degrees full width at half-maximum power [Oltman-Shay and Guza, 1984].

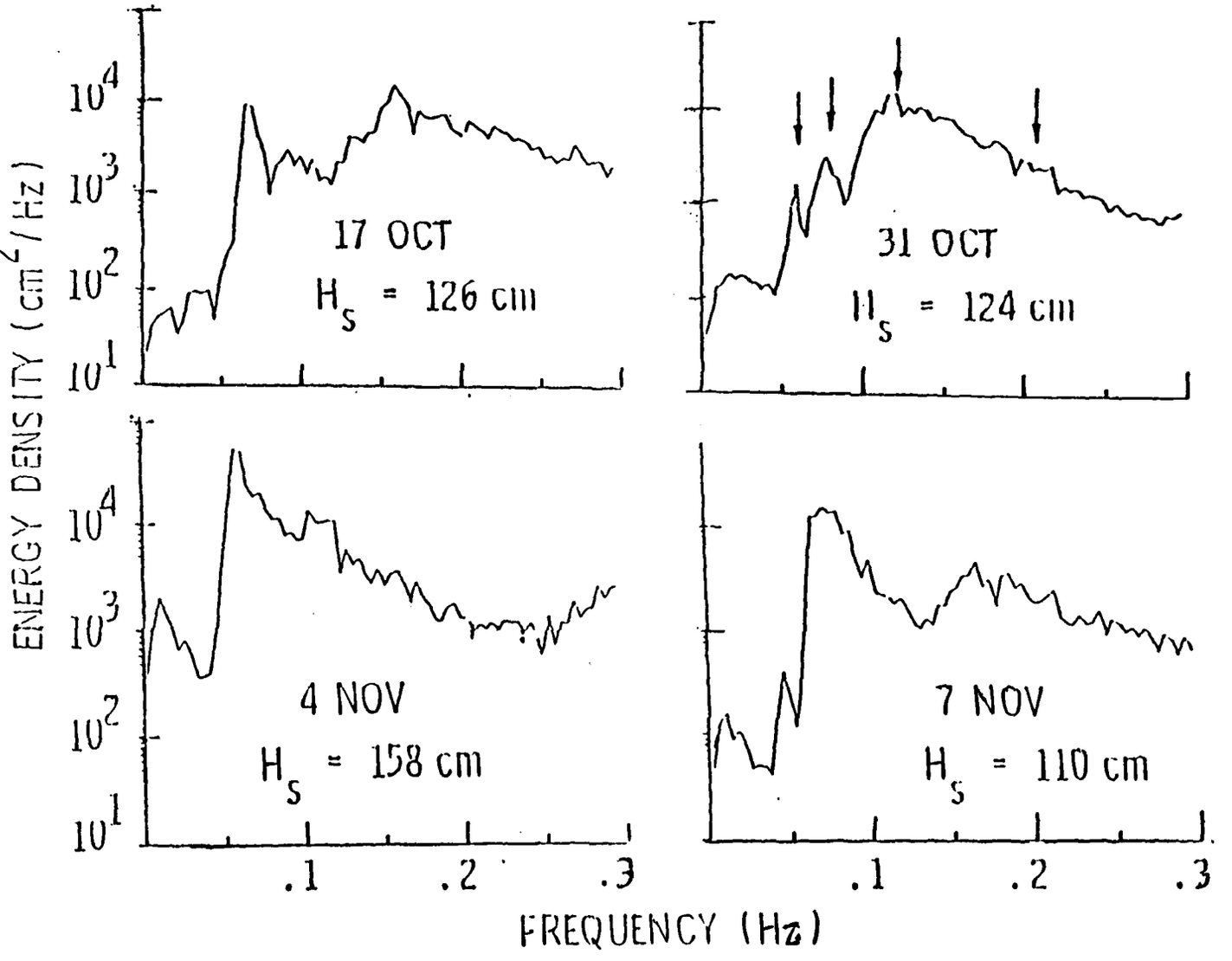

Figure 15. Wave Height Spectra for Four Overflight Days in Phase-1.

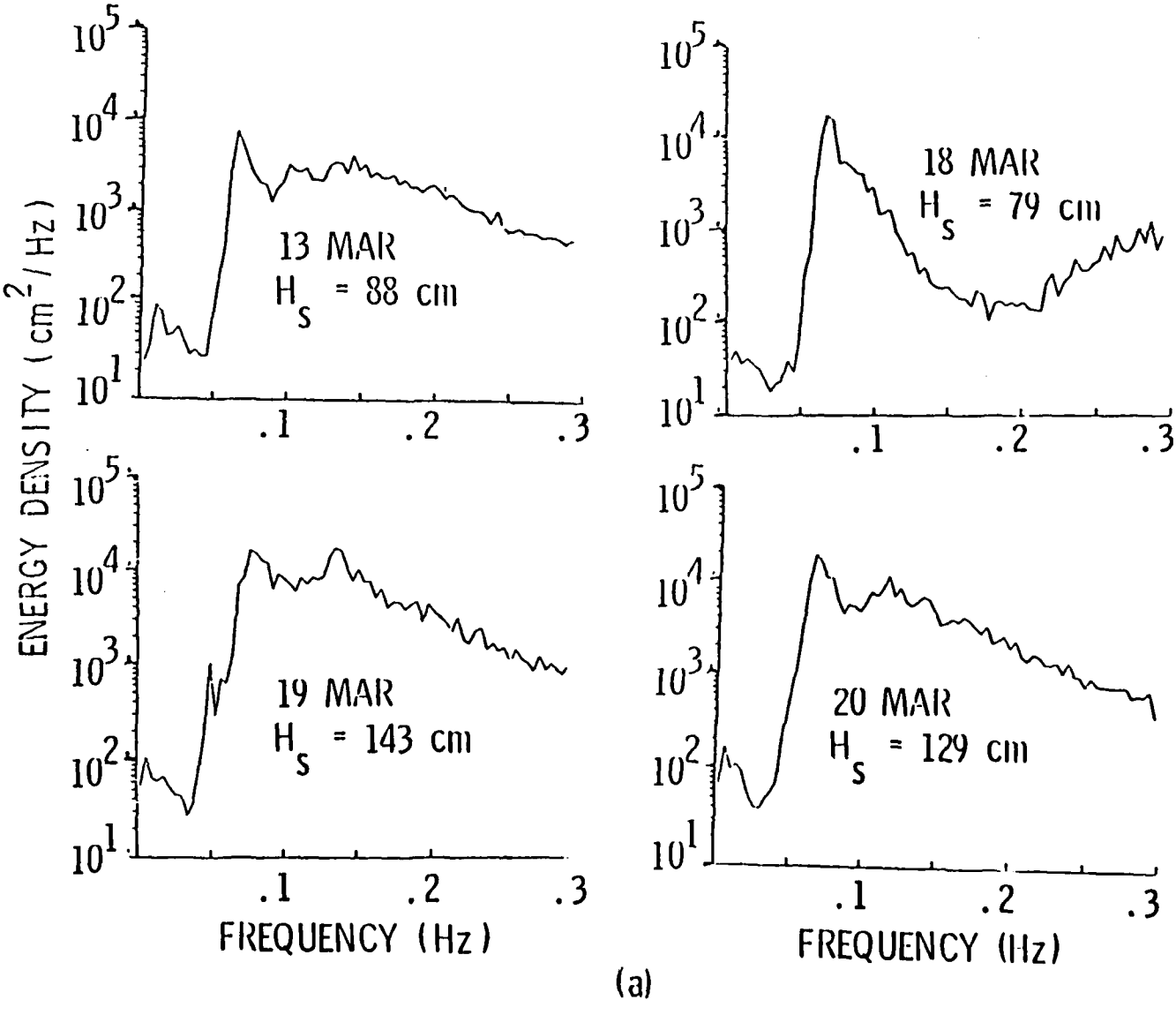

Figure 8b. Wave Height Spectra for Eight Overflight Days in Phase-II.

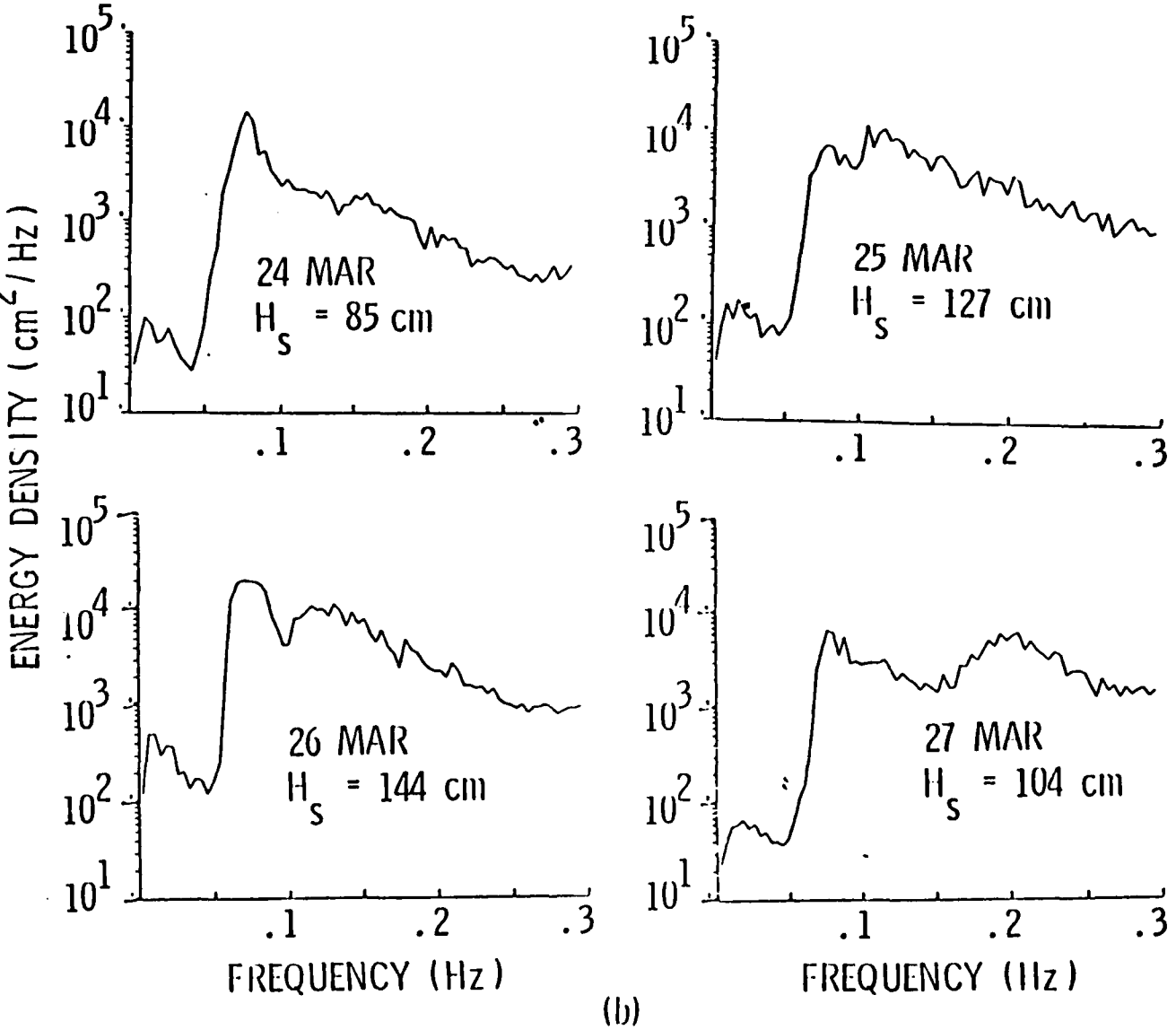

Figure 8c. Wave Height Spectra for Eight Overflight Days in Phase-II. (Continued)

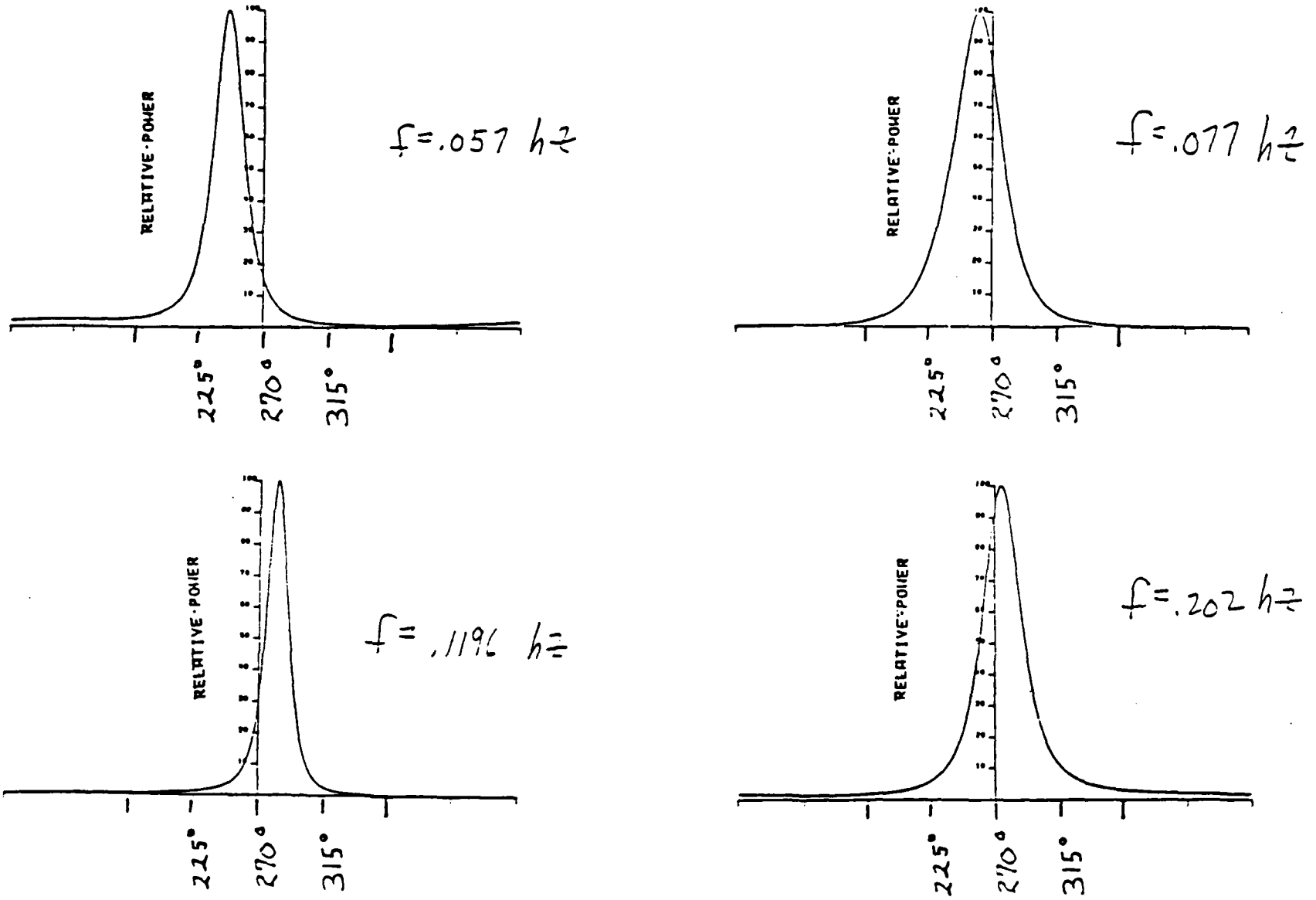

Figure 9. Low resolution directional spectra for 31 October. The vertical scale is linear in arbitrary units.

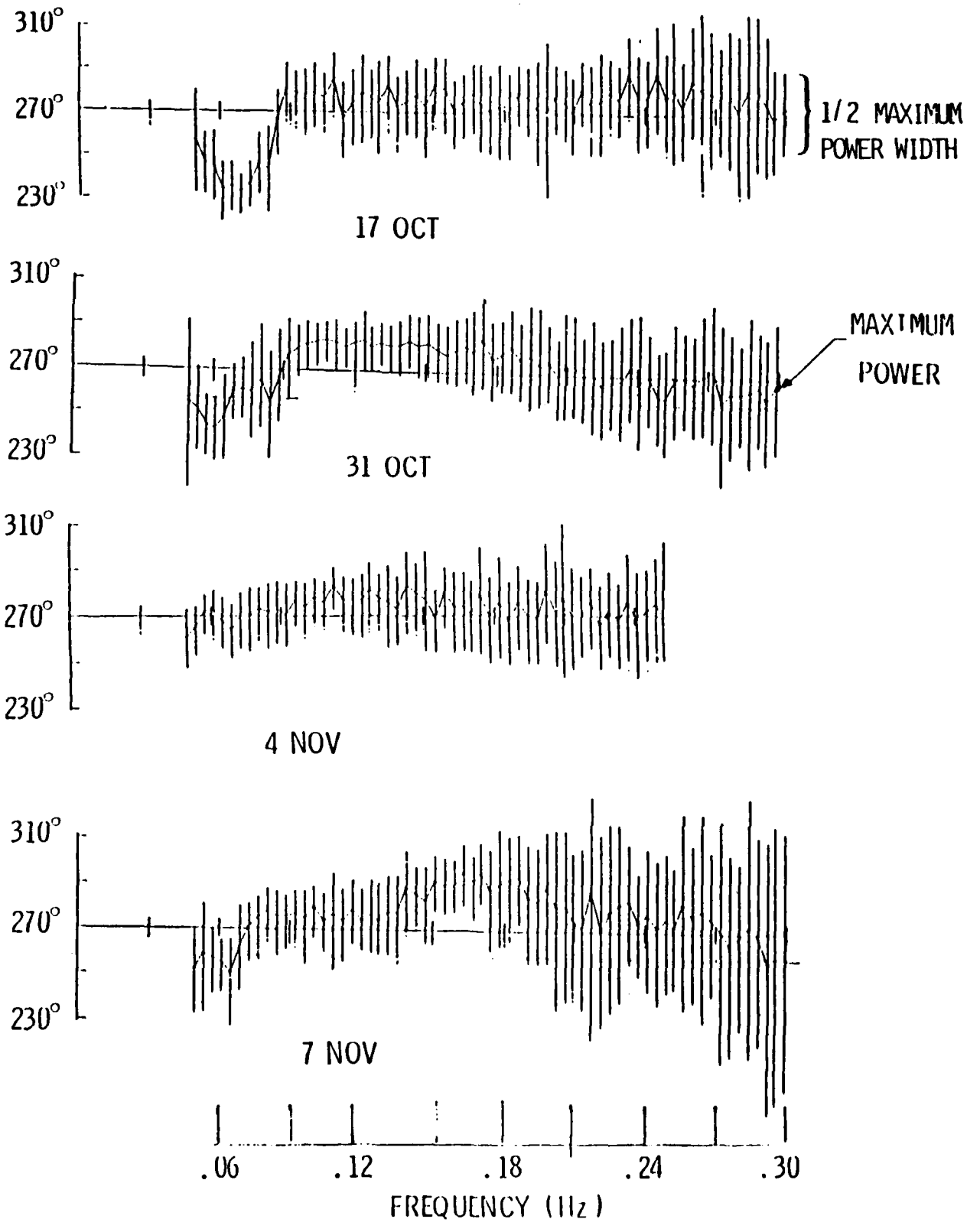

Figure 10a. Wave Direction (at Maximum Power) and Angular Spread (at Half Maximum Power) vs. Frequency, Phase-1.

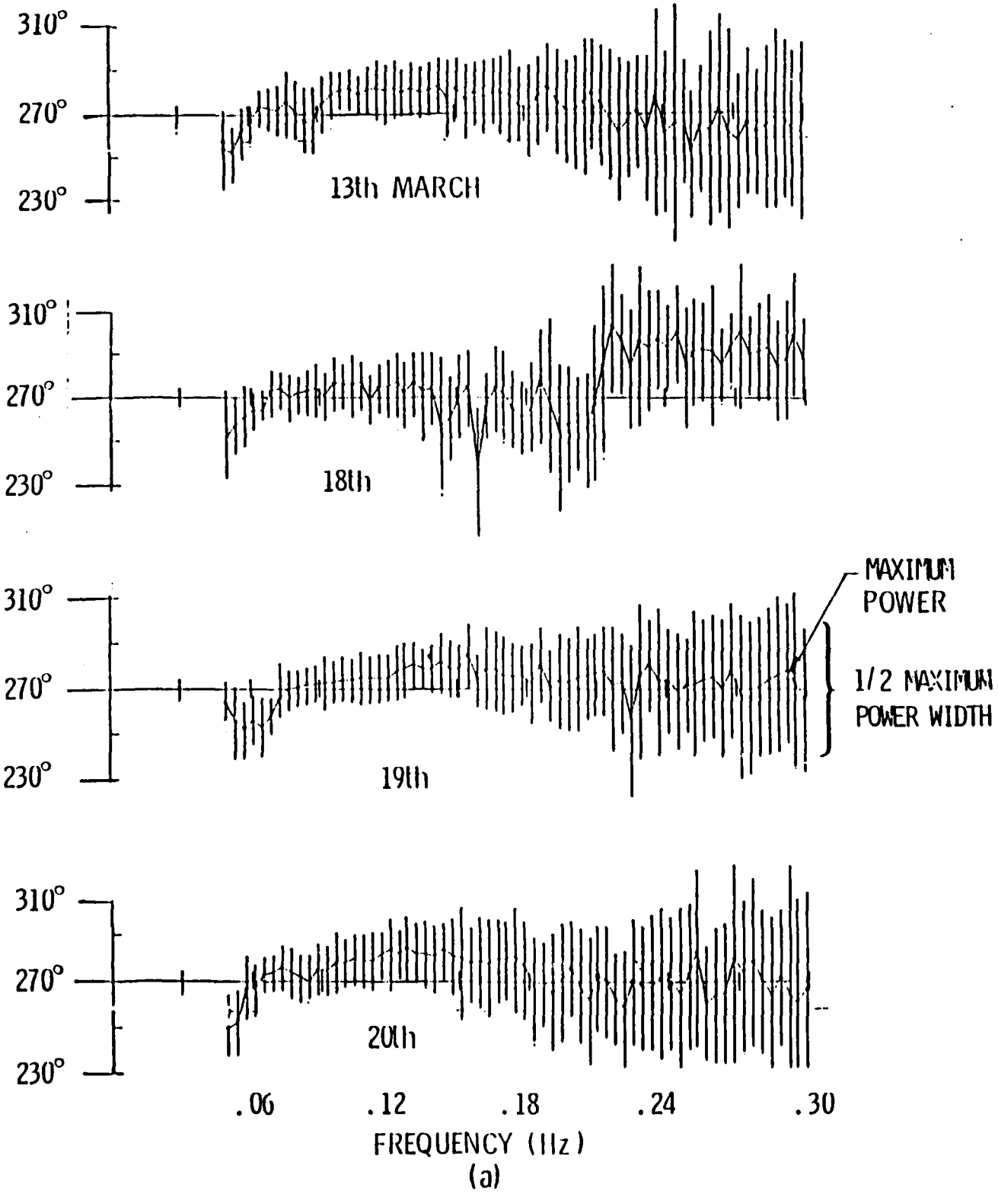

Figure 10b. Wave Direction (at Maximum Power) and Angular Spread (at Half Maximum Power Vs. Frequency), in Phase-II.

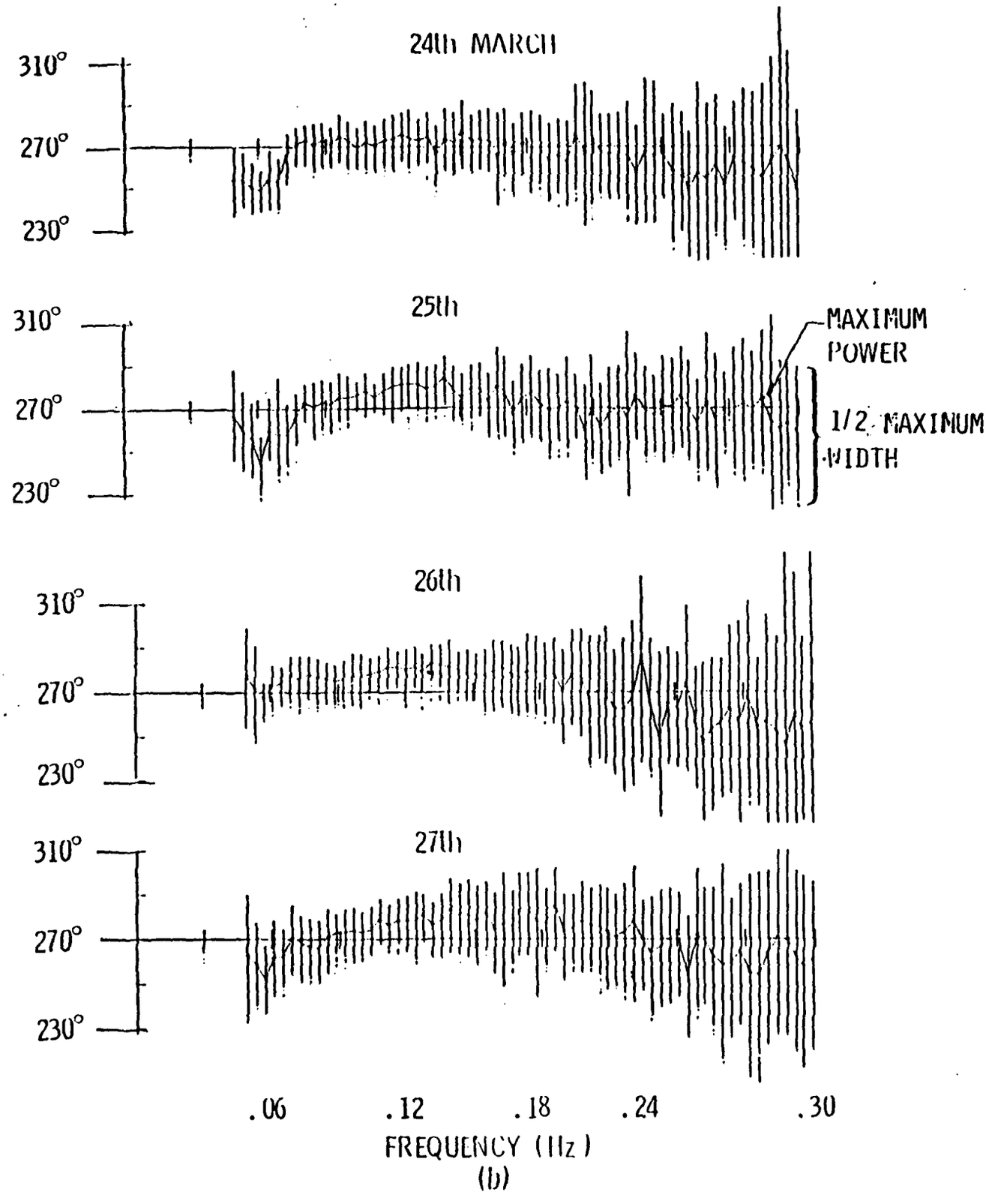

Figure 10c. Wave Direction (at Maximum Power) and Angular Spread (at Half Maximum Power Vs. Frequency). (Continued)

Table 1. Environmental Conditions During Flights in October-November, 1984: Phase-I. Noted Times are in Pacific Daylight Time and Pacific Standard Time Before and After 28 October 1984, Respectively.

Date	17 Oct 1984	31 Oct 1984	4 Nov 1984	7 Nov 1984
Time Analyzed	1250 - 1413	1300 - 1600	1512 - 1625	1412 - 1625
Wind Speed (knots)	15	6-8	5-7	10
Wind Direction (deg)	~275	~280	~300	~250
Mean Current (cm/sec) (5 m below surface)	<5	<5	<5	~10
Significant Wave Height (cm)	126	124	158	110
Air T (°C)	17.2	17.5	18.5	17.5

Table 2. Environmental Conditions During Flights in March, 1985: Phase - II. Noted Times are in Pacific Standard Time.

Day in March 1985	13	18	19	20	24	25	26	27
Overfit + Analyzed Time	1320-1630	1230-1420	1300-1530	1300-1600	1310-1500	1300-1450	1240-1520	1320-1600
Wind Speed (knots)	7-4(2)	5-10(1)	8	8	4-6	8	7	8
Wind Direction	180-290°	300-310°	265-(3) 280°	300-310°	280-(3) 300°	240°	240-(3) 260°	230-(3) 260°
Mean Current (cm/sec) (5 m Below Surface)	<3	4-8	<3	<5	<3	<3	1-7	3-6
Significant Height (cm)	88	79	143	129	85	127	144	104
Air T (°C)	11-14(1)	11.5-13(1)	13.7	13.6	13.5	13.4	13.7	13.3

(1) Increasing (2) Decreasing (3) Veering

Table 3a. 17 October 1984, 1250-1413, 40 degrees of freedom.

FREQ	ANG MAXPWR	+(-)DEG TO HALFPWR		FWHM	POWER
0.493E-01	-13.00	23	24	46.00	0.13E+03
0.532E-01	-23.00	13	15	27.00	0.21E+03
0.571E-01	-25.00	16	16	31.00	0.30E+03
0.610E-01	-36.00	13	14	26.00	0.15E+04
0.649E-01	-34.00	11	12	22.00	0.87E+04
0.688E-01	-37.00	8	10	17.00	0.85E+04
0.728E-01	-33.00	10	11	20.00	0.38E+04
0.767E-01	-24.00	14	14	27.00	0.25E+04
0.806E-01	-26.00	19	20	38.00	0.94E+03
0.845E-01	-3.00	13	14	26.00	0.18E+04
0.884E-01	11.00	12	13	24.00	0.21E+04
0.923E-01	9.00	10	11	20.00	0.28E+04
0.962E-01	8.00	12	14	25.00	0.19E+04
0.100E+00	9.00	14	15	28.00	0.23E+04
0.104E+00	7.00	11	12	22.00	0.15E+04
0.108E+00	15.00	13	14	26.00	0.21E+04
0.112E+00	-3.00	17	18	34.00	0.13E+04
0.116E+00	4.00	16	18	33.00	0.14E+04
0.120E+00	9.00	18	20	37.00	0.12E+04
0.124E+00	7.00	13	16	28.00	0.21E+04
0.127E+00	4.00	20	23	42.00	0.20E+04
0.131E+00	13.00	14	16	29.00	0.39E+04
0.135E+00	3.00	14	16	29.00	0.37E+04
0.139E+00	5.00	15	15	29.00	0.34E+04
0.143E+00	8.00	17	18	34.00	0.44E+04
0.147E+00	3.00	18	19	36.00	0.44E+04
0.151E+00	13.00	13	14	26.00	0.84E+04
0.155E+00	11.00	15	17	31.00	0.97E+04
0.159E+00	1.00	14	14	27.00	0.15E+05
0.163E+00	5.00	13	15	27.00	0.11E+05
0.167E+00	9.00	14	15	28.00	0.92E+04
0.170E+00	4.00	19	21	39.00	0.43E+04
0.174E+00	1.00	17	18	34.00	0.79E+04
0.178E+00	3.00	20	22	41.00	0.68E+04
0.182E+00	1.00	18	19	36.00	0.67E+04
0.186E+00	10.00	13	14	26.00	0.70E+04
0.190E+00	8.00	14	15	28.00	0.72E+04
0.194E+00	2.00	23	25	47.00	0.51E+04
0.198E+00	1.00	33	38	71.00	0.45E+04
0.202E+00	8.00	15	15	29.00	0.41E+04
0.206E+00	5.00	16	17	32.00	0.63E+04
0.209E+00	0.00	17	18	34.00	0.52E+04
0.213E+00	11.00	14	15	28.00	0.47E+04
0.217E+00	4.00	19	21	39.00	0.39E+04
0.221E+00	6.00	23	24	46.00	0.54E+04
0.225E+00	10.00	16	16	31.00	0.47E+04
0.229E+00	7.00	16	17	32.00	0.45E+04
0.233E+00	19.00	18	19	36.00	0.37E+04
0.237E+00	8.00	20	22	41.00	0.39E+04
0.241E+00	8.00	18	19	36.00	0.36E+04
0.245E+00	19.00	23	25	47.00	0.30E+04
0.249E+00	7.00	22	23	44.00	0.32E+04
0.252E+00	12.00	32	33	64.00	0.24E+04
0.256E+00	3.00	22	23	44.00	0.26E+04
0.260E+00	16.00	26	26	51.00	0.21E+04
0.264E+00	11.00	39	44	82.00	0.25E+04
0.268E+00	10.00	30	30	59.00	0.23E+04
0.272E+00	9.00	23	25	47.00	0.34E+04
0.276E+00	9.00	31	32	62.00	0.25E+04
0.280E+00	2.00	36	38	73.00	0.21E+04
0.284E+00	12.00	45	47	93.00	0.22E+04
0.288E+00	12.00	35	37	71.00	0.23E+04
0.292E+00	5.00	33	33	65.00	0.15E+04
0.295E+00	-2.00	24	24	47.00	0.20E+04
0.299E+00	3.00	18	20	37.00	0.12E+04

Table 3b. 31 October 1984, 1300-1600, 88 degrees of freedom.

FREQ	ANG MAXPWR	+(-)DEG TO HALFPWR		FWHM	POWER
0.493E-01	-15.00	37	39	75.00	0.16E+03
0.532E-01	-18.00	19	19	37.00	0.41E+03
0.571E-01	-25.00	13	14	26.00	0.16E+04
0.610E-01	-27.00	14	15	28.00	0.55E+03
0.649E-01	-22.00	19	19	37.00	0.43E+03
0.688E-01	-10.00	12	13	24.00	0.11E+04
0.728E-01	-9.00	14	14	27.00	0.19E+04
0.767E-01	-10.00	22	21	42.00	0.30E+04
0.806E-01	-5.00	25	22	46.00	0.20E+04
0.845E-01	-15.00	23	25	47.00	0.17E+04
0.884E-01	-3.00	21	20	40.00	0.93E+03
0.923E-01	7.00	16	17	32.00	0.13E+04
0.962E-01	10.00	10	11	20.00	0.30E+04
0.100E+00	12.00	10	11	20.00	0.48E+04
0.104E+00	13.00	8	9	16.00	0.68E+04
0.108E+00	14.00	8	9	16.00	0.10E+05
0.112E+00	13.00	10	12	21.00	0.94E+04
0.116E+00	11.00	8	9	16.00	0..15E+05
0.120E+00	13.00	9	11	19.00	0.16E+05
0.124E+00	14.00	13	14	26.00	0.86E+04
0.127E+00	11.00	9	10	18.00	0.12E+05
0.131E+00	13.00	9	10	18.00	0.96E+04
0.135E+00	12.00	9	11	19.00	0.12E+05
0.139E+00	12.00	11	12	22.00	0.10E+05
0.143E+00	14.00	12	12	23.00	0.78E+04
0.147E+00	12.00	13	14	26.00	0.88E+04
0.151E+00	13.00	13	14	26.00	0.86E+04
0.155E+00	10.00	12	14	25.00	0.83E+04
0.159E+00	8.00	13	13	25.00	0.65E+04
0.163E+00	10.00	14	16	29.00	0.56E+04
0.167E+00	12.00	13	15	27.00	0.53E+04
0.170E+00	9.00	19	19	37.00	0.44E+04
0.174E+00	15.00	19	21	39.00	0.40E+04
0.178E+00	6.00	17	18	34.00	0.42E+04
0.182E+00	9.00	15	17	31.00	0.50E+04
0.186E+00	12.00	17	19	35.00	0.41E+04
0.190E+00	6.00	17	18	34.00	0.33E+04
0.194E+00	8.00	23	24	46.00	0.21E+04
0.198E+00	4.00	26	27	52.00	0.31E+04
0.202E+00	5.00	17	18	34.00	0.29E+04
0.206E+00	-1.00	17	19	35.00	0.24E+04
0.209E+00	4.00	24	24	47.00	0.25E+04
0.213E+00	4.00	23	24	46.00	0.23E+04
0.217E+00	-1.00	18	20	37.00	0.26E+04
0.221E+00	0.00	25	26	50.00	0.14E+04
0.225E+00	-5.00	21	23	43.00	0.16E+04
0.229E+00	-3.00	20	21	40.00	0.14E+04
0.233E+00	-2.00	25	26	50.00	0.15E+04
0.237E+00	4.00	23	24	46.00	0.13E+04
0.241E+00	-2.00	30	30	59.00	0.13E+04
0.245E+00	-1.00	20	21	40.00	0.13E+04
0.249E+00	-9.00	20	21	40.00	0.11E+04
0.252E+00	-10.00	22	25	46.00	0.88E+03
0.256E+00	-1.00	25	26	50.00	0.11E+04
0.260E+00	-1.00	21	22	42.00	0.86E+03
0.264E+00	-3.00	22	24	45.00	0.81E+03
0.268E+00	1.00	27	27	53.00	0.89E+03
0.272E+00	3.00	30	32	61.00	0.77E+03
0.276E+00	-11.00	35	38	72.00	0.78E+03
0.280E+00	-7.00	27	29	55.00	0.70E+03
0.284E+00	-7.00	22	23	44.00	0.65E+03
0.288E+00	-6.00	34	34	67.00	0.82E+03
0.292E+00	-4.00	25	26	50.00	0.77E+03
0.295E+00	-10.00	28	29	56.00	0.83E+03
0.299E+00	-3.00	28	30	57.00	0.52E+03

Table 3c. 4 Novemeber 1984, 1512-1625, 40 degrees of freedom.

FREQ	ANG MAXPWR	+(-)DEG TO HALFPWR		FWHM	POWER
0.493E-01	-9.00	12	13	24.00	0.42E+04
0.532E-01	-5.00	9	10	18.00	0.15E+05
0.571E-01	2.00	7	8	14.00	0.54E+05
0.610E-01	3.00	8	10	17.00	0.51E+05
0.649E-01	-2.00	10	11	20.00	0.23E+05
0.688E-01	-6.00	11	12	22.00	0.19E+05
0.728E-01	0.00	10	12	21.00	0.21E+05
0.767E-01	0.00	12	13	24.00	0.14E+05
0.806E-01	3.00	9	11	19.00	0.11E+05
0.845E-01	2.00	12	12	23.00	0.12E+05
0.884E-01	3.00	12	12	23.00	0.80E+04
0.923E-01	1.00	13	13	25.00	0.86E+04
0.962E-01	7.00	8	10	17.00	0.73E+04
0.100E+00	4.00	10	11	20.00	0.75E+04
0.104E+00	8.00	8	10	17.00	0.14E+05
0.108E+00	6.00	9	10	18.00	0.11E+05
0.112E+00	13.00	8	10	17.00	0.11E+05
0.116E+00	7.00	10	10	19.00	0.11E+05
0.120E+00	7.00	9	11	19.00	0.11E+05
0.124E+00	7.00	11	12	22.00	0.36E+04
0.127E+00	11.00	12	12	23.00	0.60E+04
0.131E+00	8.00	10	11	20.00	0.42E+04
0.135E+00	6.00	16	16	31.00	0.50E+04
0.139E+00	3.00	14	14	27.00	0.34E+04
0.143E+00	13.00	15	15	29.00	0.28E+04
0.147E+00	10.00	13	14	26.00	0.38E+04
0.151E+00	7.00	21	22	42.00	0.27E+04
0.155E+00	-1.00	12	14	25.00	0.34E+04
0.159E+00	10.00	11	12	22.00	0.37E+04
0.163E+00	4.00	15	16	30.00	0.29E+04
0.167E+00	4.00	15	17	31.00	0.19E+04
0.170E+00	1.00	14	14	27.00	0.29E+04
0.174E+00	9.00	21	23	43.00	0.21E+04
0.178E+00	0.00	17	18	34.00	0.18E+04
0.182E+00	6.00	20	21	40.00	0.13E+04
0.186E+00	-2.00	17	18	34.00	0.13E+04
0.190E+00	6.00	16	17	32.00	0.17E+04
0.194E+00	0.00	16	17	32.00	0.19E+04
0.198E+00	-1.00	16	17	32.00	0.14E+04
0.202E+00	11.00	21	21	41.00	0.14E+04
0.206E+00	1.00	23	23	45.00	0.99E+03
0.209E+00	8.00	33	34	66.00	0.12E+04
0.213E+00	0.00	21	22	42.00	0.11E+04
0.217E+00	0.00	17	18	34.00	0.12E+04
0.221E+00	6.00	15	17	31.00	0.11E+04
0.225E+00	-4.00	17	19	35.00	0.13E+04
0.229E+00	2.00	17	18	34.00	0.13E+04
0.233E+00	-2.00	16	17	32.00	0.13E+04
0.237E+00	6.00	21	23	43.00	0.10E+04
0.241E+00	-2.00	21	23	43.00	0.13E+04
0.245E+00	2.00	18	20	37.00	0.93E+03
0.249E+00	5.00	20	21	40.00	0.62E+03
0.252E+00	-1.00	16	17	32.00	0.14E+04
0.256E+00				******	0.76E+03
0.260E+00	0.00	17	19	35.00	0.13E+04
0.264E+00	3.00	21	21	41.00	0.12E+04
0.268E+00	4.00	17	19	35.00	0.19E+04
0.272E+00				******	0.14E+04
0.276E+00				******	0.17E+04
0.280E+00				******	0.17E+04
0.284E+00				******	0.28E+04
0.288E+00				******	0.21E+04
0.292E+00				******	0.26E+04
0.295E+00	1.00	13	14	26.00	0.28E+04
0.299E+00				******	0.30E+04

Table 3d. 7 November 1984, 1412-1625, 40 degrees of freedom.

FREQ	ANG	MAXPWR	+(-)DEG TO HALFPWR		FWHM	POWER
0.493E-01	-18.00		17	16	32.00	0.21E+03
0.532E-01	-11.00		22	22	43.00	0.12E+03
0.571E-01	-13.00		13	13	25.00	0.51E+03
0.610E-01	-15.00		10	11	20.00	0.29E+04
0.649E-01	-20.00		15	19	33.00	0.12E+05
0.688E-01	-8.00		18	17	34.00	0.13E+05
0.728E-01	1.00		10	12	21.00	0.16E+05
0.767E-01	5.00		9	12	20.00	0.14E+05
0.806E-01	8.00		10	11	20.00	0.14E+05
0.845E-01	6.00		11	13	23.00	0.86E+04
0.884E-01	6.00		9	10	18.00	0.94E+04
0.923E-01	7.00		10	10	19.00	0.46E+04
0.962E-01	5.00		12	14	25.00	0.32E+04
0.100E+00	10.00		9	11	19.00	0.49E+04
0.104E+00	4.00		12	13	24.00	0.23E+04
0.108E+00	7.00		18	25	42.00	0.22E+04
0.112E+00	4.00		14	16	29.00	0.21E+04
0.116E+00	9.00		13	14	26.00	0.18E+04
0.120E+00	4.00		14	14	27.00	0.21E+04
0.124E+00	7.00		15	17	31.00	0.16E+04
0.127E+00	4.00		17	22	38.00	0.12E+04
0.131E+00	8.00		16	18	33.00	0.11E+04
0.135E+00	8.00		16	17	32.00	0.14E+04
0.139E+00	19.00		16	19	34.00	0.12E+04
0.143E+00	16.00		12	14	25.00	0.18E+04
0.147E+00	13.00		15	17	31.00	0.18E+04
0.151E+00	22.00		11	12	22.00	0.24E+04
0.155E+00	20.00		12	14	25.00	0.26E+04
0.159E+00	20.00		11	12	22.00	0.34E+04
0.163E+00	26.00		12	12	23.00	0.34E+04
0.167E+00	22.00		11	13	23.00	0.47E+04
0.170E+00	26.00		13	14	26.00	0.27E+04
0.174E+00	18.00		18	22	39.00	0.32E+04
0.178E+00	21.00		24	26	49.00	0.18E+04
0.182E+00	23.00		19	23	41.00	0.33E+04
0.186E+00	24.00		19	21	39.00	0.37E+04
0.190E+00	15.00		23	26	48.00	0.26E+04
0.194E+00	13.00		24	27	50.00	0.30E+04
0.198E+00	19.00		25	28	53.00	0.21E+04
0.202E+00	11.00		34	44	77.00	0.19E+04
0.206E+00	11.00		34	40	73.00	0.20E+04
0.209E+00	5.00		30	30	59.00	0.22E+04
0.213E+00	2.00		35	36	70.00	0.25E+04
0.217E+00	18.00		42	67	108.00	0.14E+04
0.221E+00	0.00		43	38	81.00	0.13E+04
0.225E+00	9.00		39	42	80.00	0.12E+04
0.229E+00	12.00		36	40	75.00	0.15E+04
0.233E+00	14.00		25	25	49.00	0.13E+04
0.237E+00	4.00		22	22	43.00	0.13E+04
0.241E+00	8.00		29	31	59.00	0.16E+04
0.245E+00	2.00		30	31	60.00	0.98E+03
0.249E+00	6.00		29	31	59.00	0.14E+04
0.252E+00	2.00		27	27	53.00	0.13E+04
0.256E+00	13.00		40	42	81.00	0.10E+04
0.260E+00	7.00		32	33	64.00	0.12E+04
0.264E+00	10.00		43	45	87.00	0.95E+03
0.268E+00	6.00		30	31	60.00	0.11E+04
0.272E+00	1.00		49	56	104.00	0.93E+03
0.276E+00	-6.00		41	45	85.00	0.68E+03
0.280E+00	-2.00		33	33	65.00	0.10E+04
0.284E+00	3.00		57	54	110.00	0.89E+03
0.288E+00	-2.00		45	47	91.00	0.64E+03
0.292E+00	-14.00		55	65	119.00	0.56E+03
0.295E+00	-11.00		59	61	119.00	0.71E+03
0.299E+00	-11.00		56	57	112.00	0.68E+03

Table 3e. 19 March 1985, 1300-1530, 72 degrees of freedom.

FREQ	ANG MAXPWR	+(-)DEG TO HALFPWR		FWHM	POWER
0.493E-01	-6.00	7	7	17.00	0.10E+04
0.532E-01	-14.00	15	17	31.00	0.29E+03
0.571E-01	-18.00	12	13	24.00	0.71E+03
0.610E-01	-14.00	11	11	21.00	0.62E+03
0.649E-01	-17.00	13	14	26.00	0.13E+04
0.688E-01	-12.00	8	8	15.00	0.69E+04
0.728E-01	-4.00	15	14	28.00	0.84E+04
0.767E-01	0.00	8	10	17.00	0.16E+05
0.806E-01	1.00	7	9	15.00	0.15E+05
0.845E-01	2.00	7	9	15.00	0.13E+05
0.884E-01	2.00	8	8	15.00	0.12E+05
0.923E-01	3.00	11	13	23.00	0.62E+04
0.962E-01	3.00	9	10	18.00	0.71E+04
0.100E+00	4.00	10	10	19.00	0.82E+04
0.104E+00	4.00	7	11	19.00	0.71E+04
0.108E+00	5.00	11	13	23.00	0.59E+04
0.112E+00	5.00	9	11	19.00	0.82E+04
0.116E+00	5.00	10	11	20.00	0.71E+04
0.120E+00	5.00	10	12	21.00	0.85E+04
0.124E+00	8.00	11	13	23.00	0.78E+04
0.127E+00	9.00	11	13	23.00	0.87E+04
0.131E+00	11.00	9	10	18.00	0.14E+05
0.135E+00	9.00	8	9	16.00	0.18E+05
0.139E+00	9.00	10	11	20.00	0.16E+05
0.143E+00	12.00	12	13	24.00	0.11E+05
0.147E+00	9.00	12	13	24.00	0.77E+04
0.151E+00	9.00	10	13	22.00	0.10E+05
0.155E+00	15.00	13	15	27.00	0.75E+04
0.159E+00	4.00	11	12	22.00	0.76E+04
0.163E+00	9.00	18	18	35.00	0.51E+04
0.167E+00	9.00	16	18	33.00	0.64E+04
0.170E+00	6.00	17	18	34.00	0.40E+04
0.174E+00	6.00	14	16	29.00	0.46E+04
0.178E+00	6.00	13	14	26.00	0.45E+04
0.182E+00	3.00	17	18	34.00	0.38E+04
0.186E+00	11.00	16	17	32.00	0.43E+04
0.190E+00	1.00	16	16	31.00	0.47E+04
0.194E+00	4.00	20	22	41.00	0.29E+04
0.198E+00	3.00	19	22	40.00	0.44E+04
0.202E+00	5.00	22	24	45.00	0.35E+04
0.206E+00	6.00	16	19	34.00	0.32E+04
0.209E+00	7.00	17	19	35.00	0.28E+04
0.213E+00	8.00	19	20	38.00	0.23E+04
0.217E+00	2.00	25	27	53.00	0.31E+04
0.221E+00	3.00	21	22	42.00	0.18E+04
0.225E+00	-13.00	32	35	66.00	0.17E+04
0.229E+00	6.00	31	36	66.00	0.23E+04
0.233E+00	11.00	19	21	39.00	0.24E+04
0.237E+00	4.00	31	33	63.00	0.14E+04
0.241E+00	4.00	22	24	45.00	0.17E+04
0.245E+00	-1.00	25	26	50.00	0.14E+04
0.249E+00	2.00	20	22	41.00	0.15E+04
0.252E+00	2.00	32	32	63.00	0.10E+04
0.256E+00	4.00	26	27	52.00	0.15E+04
0.260E+00	5.00	27	27	53.00	0.12E+04
0.264E+00	0.00	30	31	60.00	0.11E+04
0.268E+00	8.00	27	30	58.00	0.87E+03
0.272E+00	-3.00	35	37	71.00	0.12E+04
0.276E+00	-4.00	33	34	66.00	0.88E+03
0.280E+00	1.00	30	31	60.00	0.10E+04
0.284E+00	4.00	31	33	63.00	0.88E+03
0.288E+00	6.00	34	34	67.00	0.80E+03
0.292E+00	8.00	27	31	59.00	0.11E+04
0.295E+00	3.00	37	37	75.00	0.73E+03
0.299E+00	-5.00	31	32	62.00	0.58E+03

Table 3f. 27 March 1985, 1320-1600, 80 degrees of freedom.

FREQ	ANG MAXPWR	+(-)DEG TO HALFPWR		FWHM	POWER
0.493E-01	-7.00	27	27	53.00	0.43E+02
0.532E-01	-11.00	18	18	35.00	0.64E+02
0.571E-01	-18.00	15	15	29.00	0.11E+03
0.610E-01	-8.00	16	17	32.00	0.16E+03
0.649E-01	-8.00	12	13	24.00	0.51E+03
0.688E-01	1.00	14	15	28.00	0.24E+04
0.728E-01	-2.00	12	14	25.00	0.41E+04
0.767E-01	-3.00	12	12	23.00	0.65E+04
0.806E-01	-4.00	12	13	24.00	0.62E+04
0.845E-01	1.00	12	13	24.00	0.35E+04
0.884E-01	3.00	8	9	16.00	0.55E+04
0.923E-01	3.00	10	10	19.00	0.27E+04
0.962E-01	4.00	10	12	21.00	0.31E+04
0.100E+00	3.00	9	10	18.00	0.27E+04
0.104E+00	4.00	10	10	19.00	0.30E+04
0.108E+00	9.00	9	11	19.00	0.30E+04
0.112E+00	6.00	9	10	18.00	0.30E+04
0.116E+00	8.00	10	10	19.00	0.32E+04
0.120E+00	8.00	11	11	21.00	0.25E+04
0.124E+00	8.00	13	15	27.00	0.19E+04
0.127E+00	11.00	9	10	18.00	0.23E+04
0.131E+00	6.00	10	11	20.00	0.20E+04
0.135E+00	8.00	12	13	24.00	0.18E+04
0.139E+00	13.00	14	15	28.00	0.15E+04
0.143E+00	11.00	14	16	29.00	0.18E+04
0.147E+00	11.00	16	17	32.00	0.16E+04
0.151E+00	8.00	16	18	33.00	0.14E+04
0.155E+00	12.00	14	17	30.00	0.22E+04
0.159E+00	4.00	17	18	34.00	0.16E+04
0.163E+00	7.00	23	28	50.00	0.16E+04
0.167E+00	6.00	16	17	32.00	0.28E+04
0.170E+00	13.00	17	19	35.00	0.27E+04
0.174E+00	13.00	17	20	36.00	0.36E+04
0.178E+00	8.00	24	32	55.00	0.31E+04
0.182E+00	7.00	16	16	31.00	0.40E+04
0.186E+00	15.00	17	18	34.00	0.51E+04
0.190E+00	3.00	17	19	35.00	0.44E+04
0.194E+00	5.00	15	16	30.00	0.60E+04
0.198E+00	8.00	18	21	38.00	0.50E+04
0.202E+00	6.00	17	18	34.00	0.57E+04
0.206E+00	5.00	19	21	39.00	0.61E+04
0.209E+00	3.00	20	22	41.00	0.40E+04
0.213E+00	1.00	19	19	37.00	0.50E+04
0.217E+00	3.00	22	24	45.00	0.40E+04
0.221E+00	8.00	25	30	54.00	0.36E+04
0.225E+00	-1.00	18	20	37.00	0.31E+04
0.229E+00	-6.00	25	26	50.00	0.38E+04
0.233E+00	-3.00	25	25	49.00	0.35E+04
0.237E+00	0.00	23	24	46.00	0.21E+04
0.241E+00	-1.00	22	23	44.00	0.23E+04
0.245E+00	-16.00	26	27	52.00	0.24E+04
0.249E+00	2.00	30	32	61.00	0.23E+04
0.252E+00	-1.00	24	26	49.00	0.16E+04
0.256E+00	-7.00	30	31	60.00	0.12E+04
0.260E+00	-11.00	45	43	87.00	0.19E+04
0.264E+00	-11.00	29	31	59.00	0.14E+04
0.268E+00	-5.00	30	32	61.00	0.17E+04
0.272E+00	-15.00	44	48	91.00	0.12E+04
0.276E+00	-16.00	46	47	94.00	0.16E+04
0.280E+00	-6.00	37	38	74.00	0.13E+04
0.284E+00	1.00	39	41	79.00	0.15E+04
0.288E+00	-1.00	41	40	80.00	0.16E+04
0.292E+00	-8.00	39	41	79.00	0.13E+04
0.295E+00	-12.00	41	46	86.00	0.15E+04
0.299E+00	-9.00	35	36	70.00	0.11E+04

APPENDIX II

Development and Utilization of a Surface Energy Measurement System in TOWARD

William D. Garrett
Naval Research Laboratory
Washington, D. C. 20375

BACKGROUND:

Polar organic molecules absorb at the air-sea interface where they may form continuous films which modify numerous small-scale interfacial processes. When the surface concentration of the surface-active material attains a level where the molecules of the surface film come into contact (about 1 mg per sq. meter), the surface becomes relatively incompressible, a thin layer of water at the air-water interface is immobilized, and capillary and short gravity waves are attenuated. Consequently, backscattered microwave radar signals are affected by these film-induced modifications of the sea surface, a condition which occurs when the surface tension has been reduced by as little as 1-2 mN per meter.

The effects of organic films on small-scale dynamics of the air-sea interface are influenced by the film compressibility and film flow across a surface tension gradient (Marangoni effect). Surface tension is inherent in both of these parameters, and is itself an indicator of the existence of a coherent organic film capable of modifying interfacial processes. For these reasons, it was considered important to include the measurement and monitoring of surface tension in the Tower Ocean Wave and Radar Dependence (TOWARD) Experiment.

SURFACE ENERGY MEASUREMENT SYSTEM

A computer-operated system for the semi-continuous measurement of the surface tension of seawater was developed, constructed, mounted on the NOSC Tower, and operated during the two phases of the TOWARD Experiment. The instrumentation included (1) a cetrifugal pump mounted aboard a tethered raft (fig. 1), (2) a tower-mounted surface tension (fig. 2), and (3) a microcomputer. The sensor as well as the sampling pump were interfaced to the microcomputer. At

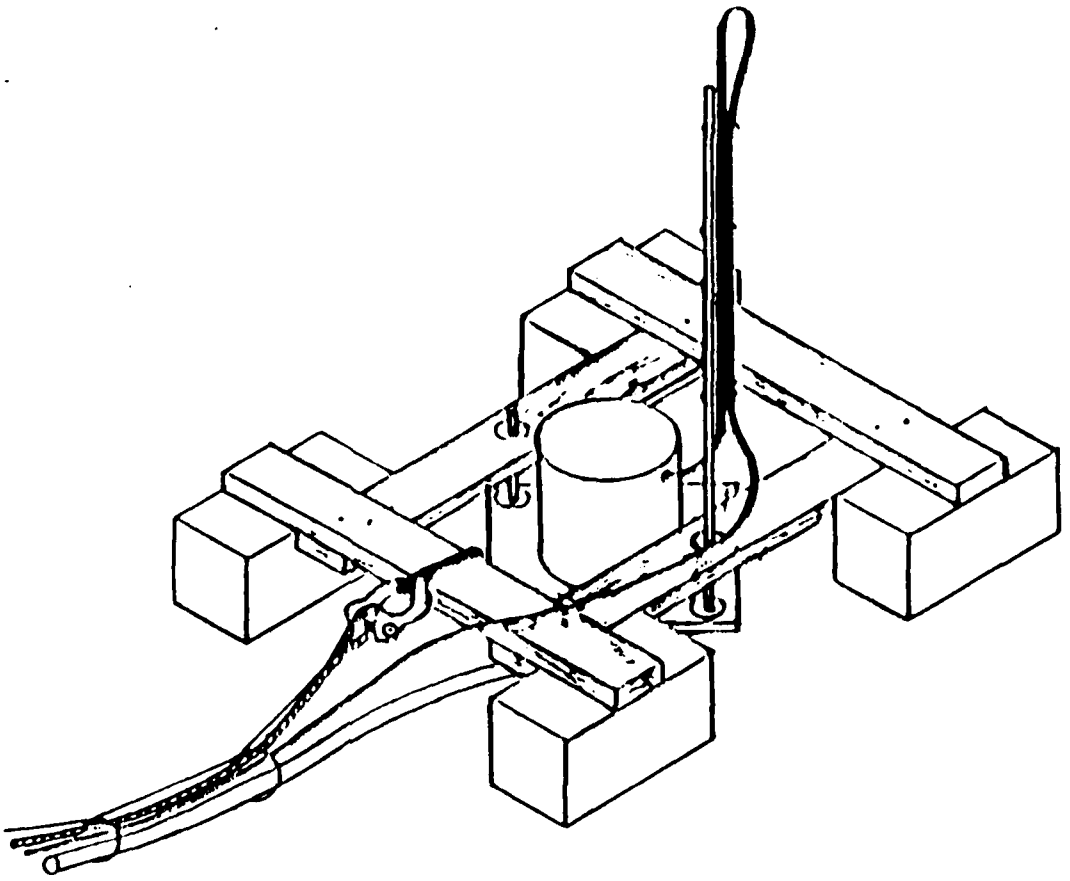

Figure 1. Surface Water Sampling Pump.

predetermined intervals seawater was pumped from the upper 2 cm of the ocean to the measurement chamber. Surface tension was measured automatically by a computer-controlled strain-gauge sensor attached to a hydrophilic plate in contact with the water in the measurement chamber. A graph of the surface tension vs. time was displayed on the computer's video screen and updated every three minutes to present a real-time record of the relative concentration of surface-active organic material in the surface water passing the tower. At the end of each hour, a printer produced a hard copy of the graph of surface tension vs. time during the previous one-hour period.

Microcomputer and Interfaces: An Apple II-E microcomputer with 64 k of RAM and one disk drive was used to control the sampling pump and to take data from the strain gauge. A computer-switchable 5-volt signal was obtained from the game controller IC socket of the computer to operate an optically isolated relay which controlled the AC power to the pump. Two analog-to-digital converter cards were used in the microcomputer, one to read the strain gauge signals, and the other contained a clock to determine the actual time of sampling. A 10.2-volt signal was taken from the A/D strain gauge card to energize the Wheatstone bridge circuit of the strain gauge.

Measurement Strategy: Figure 3 illustrates the typical sequence of events during a 3-minute measurement cycle. The upper part of the figure depicts the voltage reading on the sensor; the lower portion shows the corresponding water level in the measurement chamber. Beginning with a nearly empty sample chamber to which the pump has just begun to send water, a constant voltage reading is observed due to the plate hanging in air. The water rises until it contacts the plate, at which time the plate is pulled downward by the surface tension of the seawater causing a rapid increase in voltage output. The water continues to rise in the chamber to the level of the overflow port. This results in a reduction of the voltage output of the sensor because of buoyancy of the plate in the seawater. As the water flushes through the chamber and overflows, a noisy, constant voltage signal results. When the pump is switched off by the computer, the water drains slowly from the chamber, and the buoyancy effect decreases as less of the plate is submerged. Once the bottom of the sensor plate is

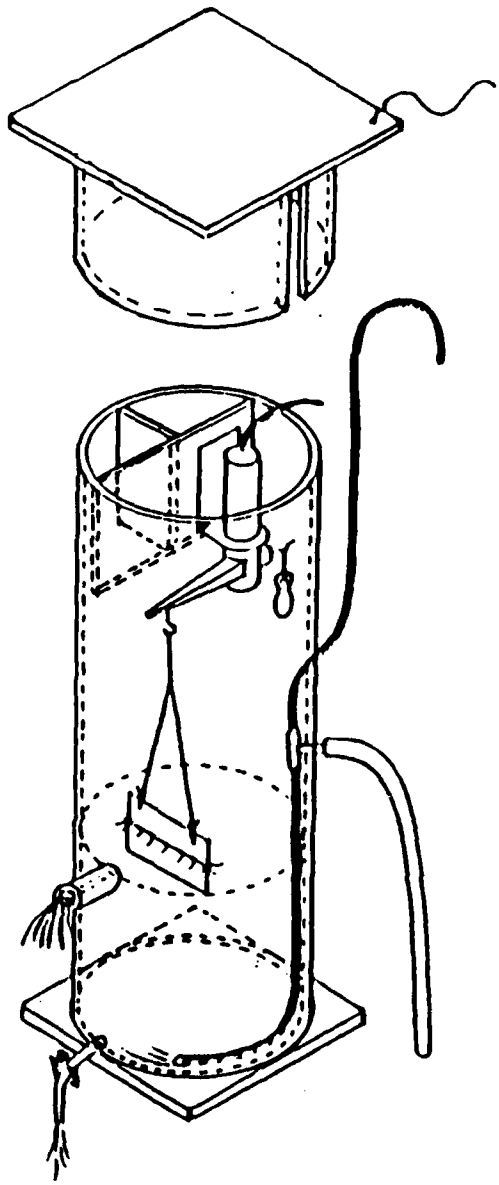

Figure 2. Surface Tension Measurement Cell.

predetermined intervals seawater was pumped from the upper 2 cm of the ocean to the measurement chamber. Surface tension was measured automatically by a computer-controlled strain-gauge sensor attached to a hydrophilic plate in contact with the water in the measurement chamber. A graph of the surface tension vs. time was displayed on the computer's video screen and updated every three minutes to present a real-time record of the relative concentration of surface-active organic material in the surface water passing the tower. At the end of each hour, a printer produced a hard copy of the graph of surface tension vs. time during the previous one-hour period.

Microcomputer and Interfaces: An Apple II-E microcomputer with 64 k of RAM and one disk drive was used to control the sampling pump and to take data from the strain gauge. A computer-switchable 5-volt signal was obtained from the game controller IC socket of the computer to operate an optically isolated relay which controlled the AC power to the pump. Two analog-to-digital converter cards were used in the microcomputer, one to read the strain gauge signals, and the other contained a clock to determine the actual time of sampling. A 10.2-volt signal was taken from the A/D strain gauge card to energize the Wheatstone bridge circuit of the strain gauge.

Measurement Strategy: Figure 3 illustrates the typical sequence of events during a 3-minute measurement cycle. The upper part of the figure depicts the voltage reading on the sensor; the lower portion shows the corresponding water level in the measurement chamber. Beginning with a nearly empty sample chamber to which the pump has just begun to send water, a constant voltage reading is observed due to the plate hanging in air. The water rises until it contacts the plate, at which time the plate is pulled downward by the surface tension of the seawater causing a rapid increase in voltage output. The water continues to rise in the chamber to the level of the overflow port. This results in a reduction of the voltage output of the sensor because of buoyancy of the plate in the seawater. As the water flushes through the chamber and overflows, a noisy, constant voltage signal results. When the pump is switched off by the computer, the water drains slowly from the chamber, and the buoyancy effect decreases as less of the plate is submerged. Once the bottom of the sensor plate is

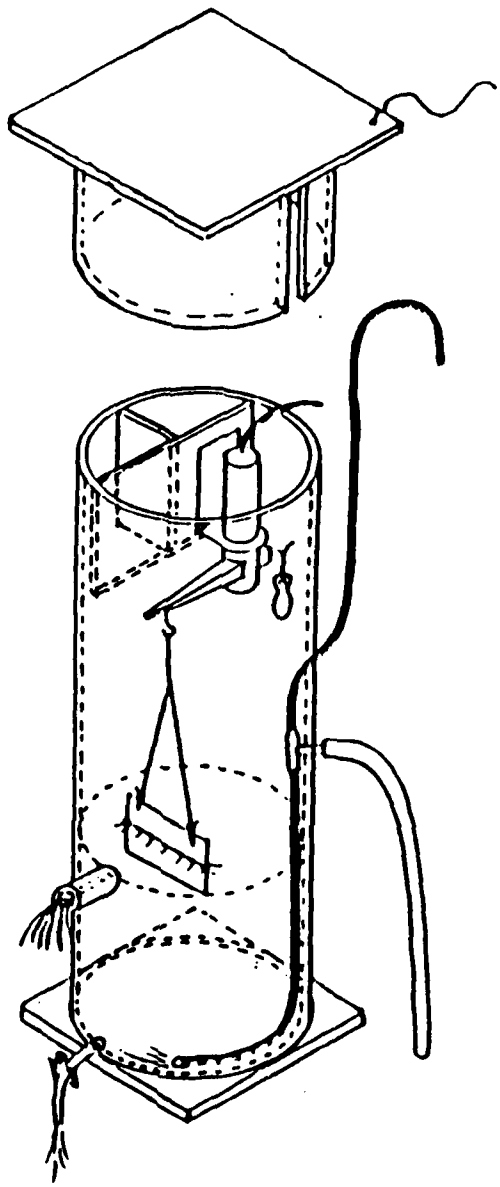

Figure 2. Surface Tension Measurement Cell.

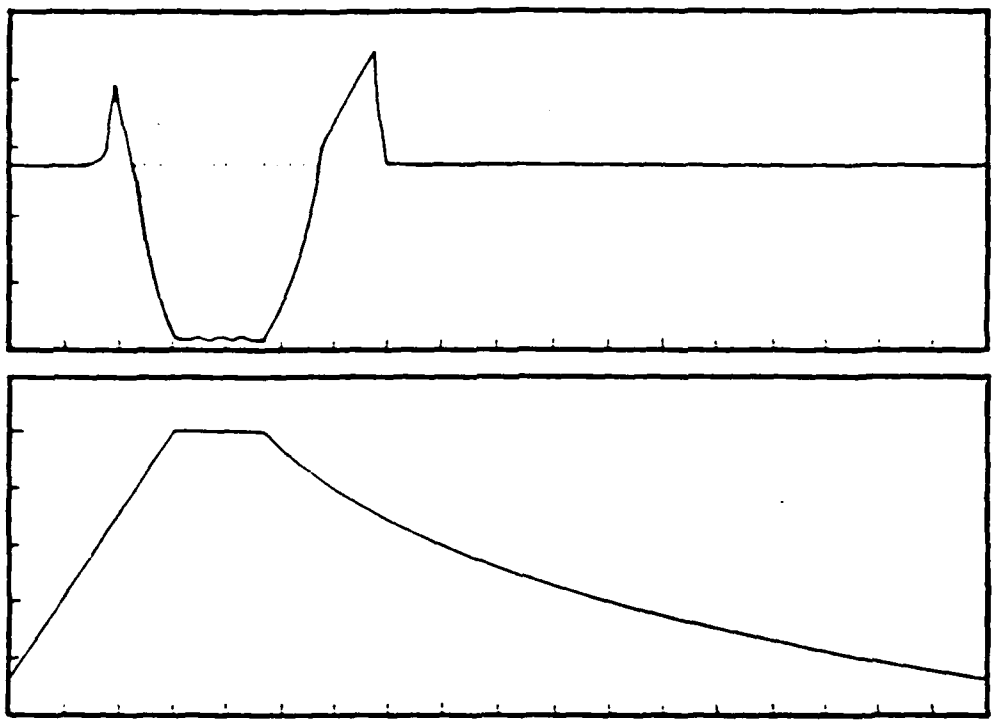

Figure 3. Force on Hydrophilic Plate.

level with the water surface, only the surface tension force is operative. As the water level continues to fall, the plate is detached from the water surface, and the maximum force is recorded. Subsequently, a steady voltage due to the weight of the plate in air results and is recorded. The difference in voltage between that due to the maximum pull on the plate and that due to the weight of the plate in air is directly proportional to the surface tension of the water in the chamber. Appendix I is a flow chart of the computer program which controls the Surface Energy Measurement System.

IN SITU SURFACE TENSION MEASUREMENT AND INSTRUMENT CALIBRATION

A series of laboratory calibrated spreading oils were used periodically to determine the seawater surface tension in situ for comparison with the Surface Energy Measurement System (SEMS). Special events such as natural slicks associated with kelp or internal waves were given particular attention. In addition, a du Nouy, ring-type, interfacial tensiometer was employed to measure the surface tension of collected, film-free surface seawater at constant temperature (T) and known salinity (S), as a test of the empirical expression,

Surface Tension = 75.64 - 0.144T + 0.02215S,

where T is in degrees C and S is in ppt. This expression was found to be accurate to within +/- 0.1 mN per m, the accuracy of the tensiometer. Thus, data on sea surface T and S can be used to fine tune the surface tension data determined by the other methodologies employed in this experiment.

The SEMS was calibrated and its efficacy verified by spreading know monomolecular films upwind of the floating sea surface sampling pump, so that they would drift across the unit and be collected and sent to the measurement chamber. Figures 4 and 5 are computer-generated plots of surface tension vs. time for periods during which the calibration slicks were deployed. Surface tension reductions recorded agreed well with the known values for the monolayers applied to the sea surface. In the case of the strongly surface-active material, isostearyl alcohol (20E), the

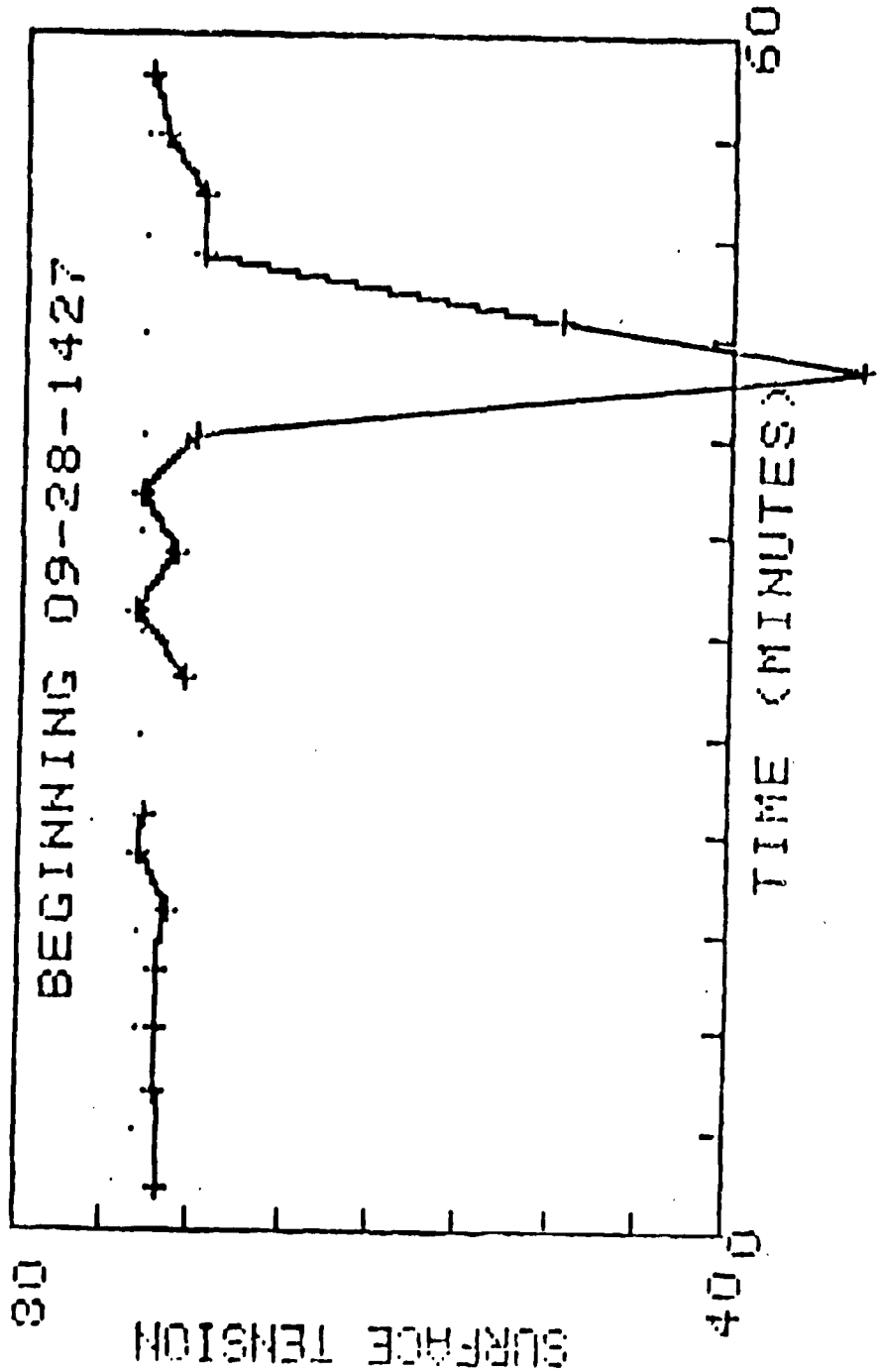

Figure 4. Calibration Monolayer, Isostearyl Alcohol (20E), Surface Tension Reduction.

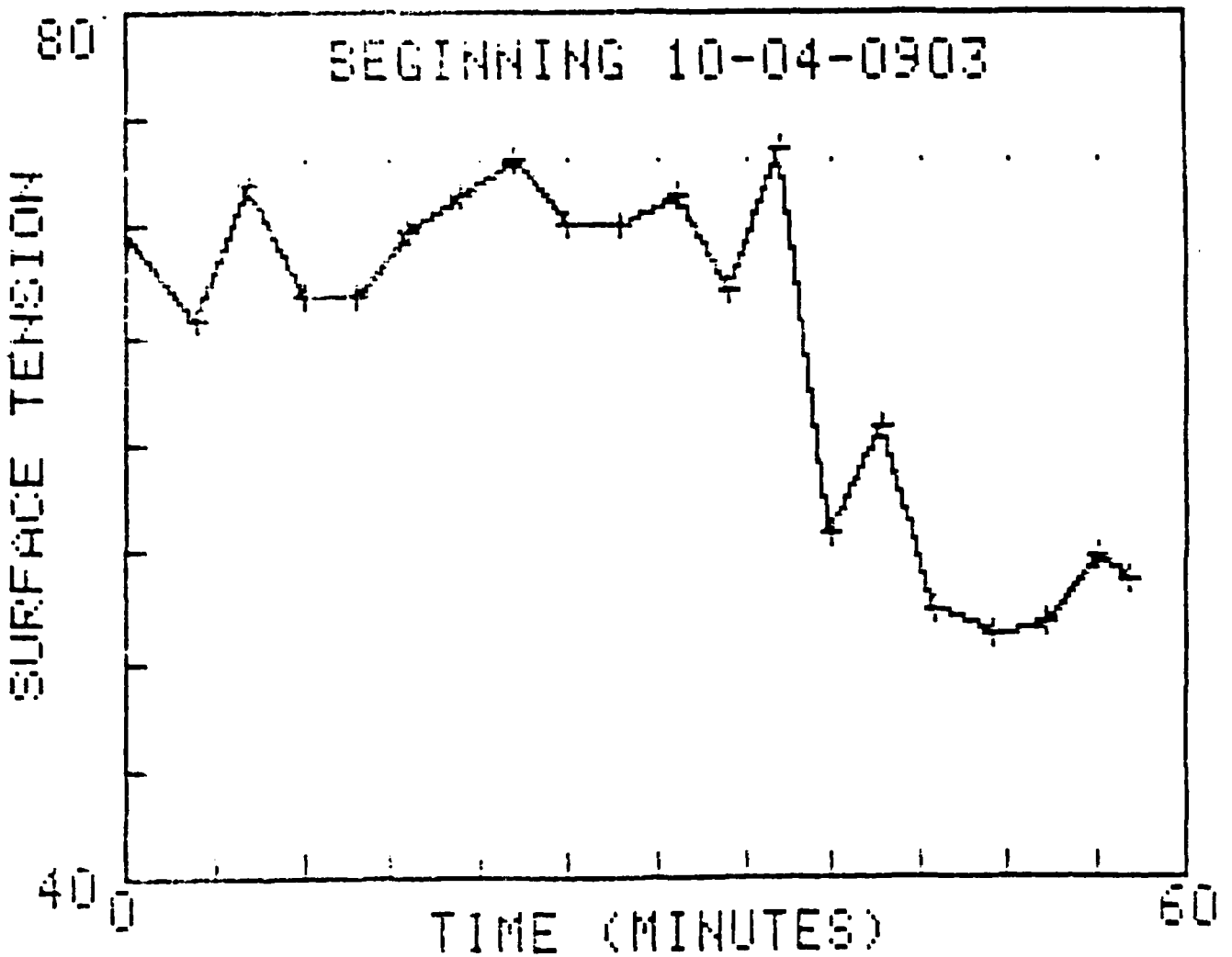

Figure 5. Calibration Monolayer, Glycerol Trioleate, Surface Tension Reduction - 17.

surface film was just large enough to pass the collection unit for one pumping cycle. There was a residual effect of the collected surface-active material for only one subsequent measurement cycle, after which the system appeared to have flushed completely, and the surface tension returned to a value near that of clean seawater. In the case of the glycerol trileate, a very large slick was produced, and the effect of the monolayer was measured over a number of measurement cycles. Two examples of documented natural surface events measured by SEMS are depicted in Figures 6 and 7, representing natural slicks from kelp and possibly from an internal wave convergence zone, respectively. In the case of the nonkelp slick (figure 7), calibrated spreading oil measurements yielded a surface tension reduction of 12mN per m at 10-08-1435, a value close to that measured by the SEMS. These results indicate that the SEMS accurately measures sea surface film tension if the surface-active layers are sufficiently large to cover the sampling unit during the pumping cycle, even though the system does not provide a direct in-situ measurement. Futhermore, it has been demonstrated that a one-molecule-thick film can be sample from the sea surface and its surface tension value accurately determined by the SEMS.

DATA QUALITY AND PLANNED INTERCOMPARISONS WITH OTHER TOWARD PRODUCTS

A catalog of surface tension data taken with the SEMS for both TOWARD experiemental periods, 20 September to 3 November 1984, and 8-26 April 1985, is attached as Appendix II. These data have been normalized on the basis of corresponding in-situ surface tension measurements made with calibrated spreading oils. The SEMS data will be additionally fine tuned to account for seawater surface temperature. Although we have temperature data for many days of operation, it will be necessary to obtain the missing values from other investigators. It should be noted that the SEMS acquired surface tension data at approximately three-minute intervals. Only periods with generally acceptable surface tension values are listed in the catalog. About 5% of these data are suspicious and require additional examination because of possible artifacts associated with the measurement system operation.

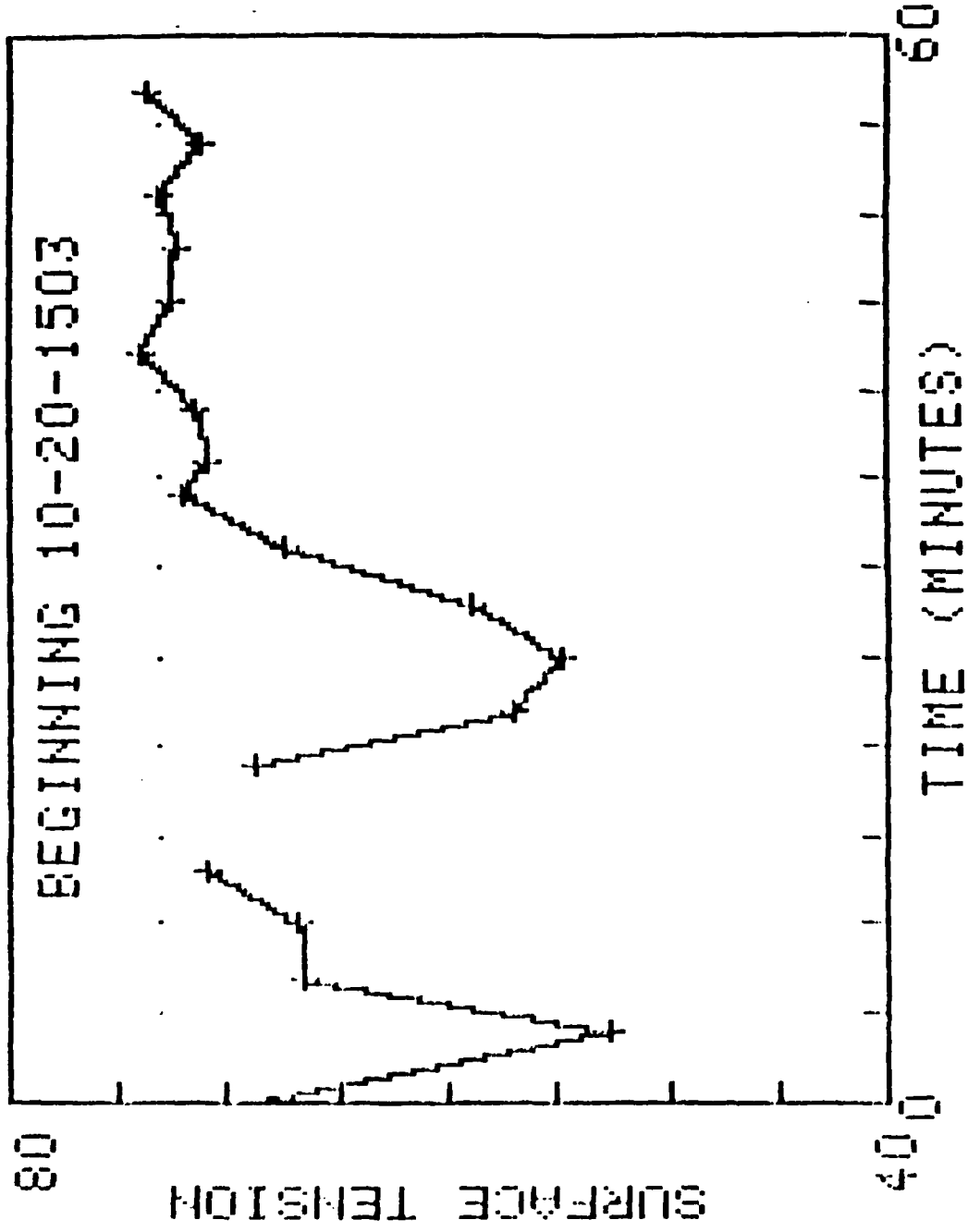

Figure 6. Kelp Slicks at Tower.

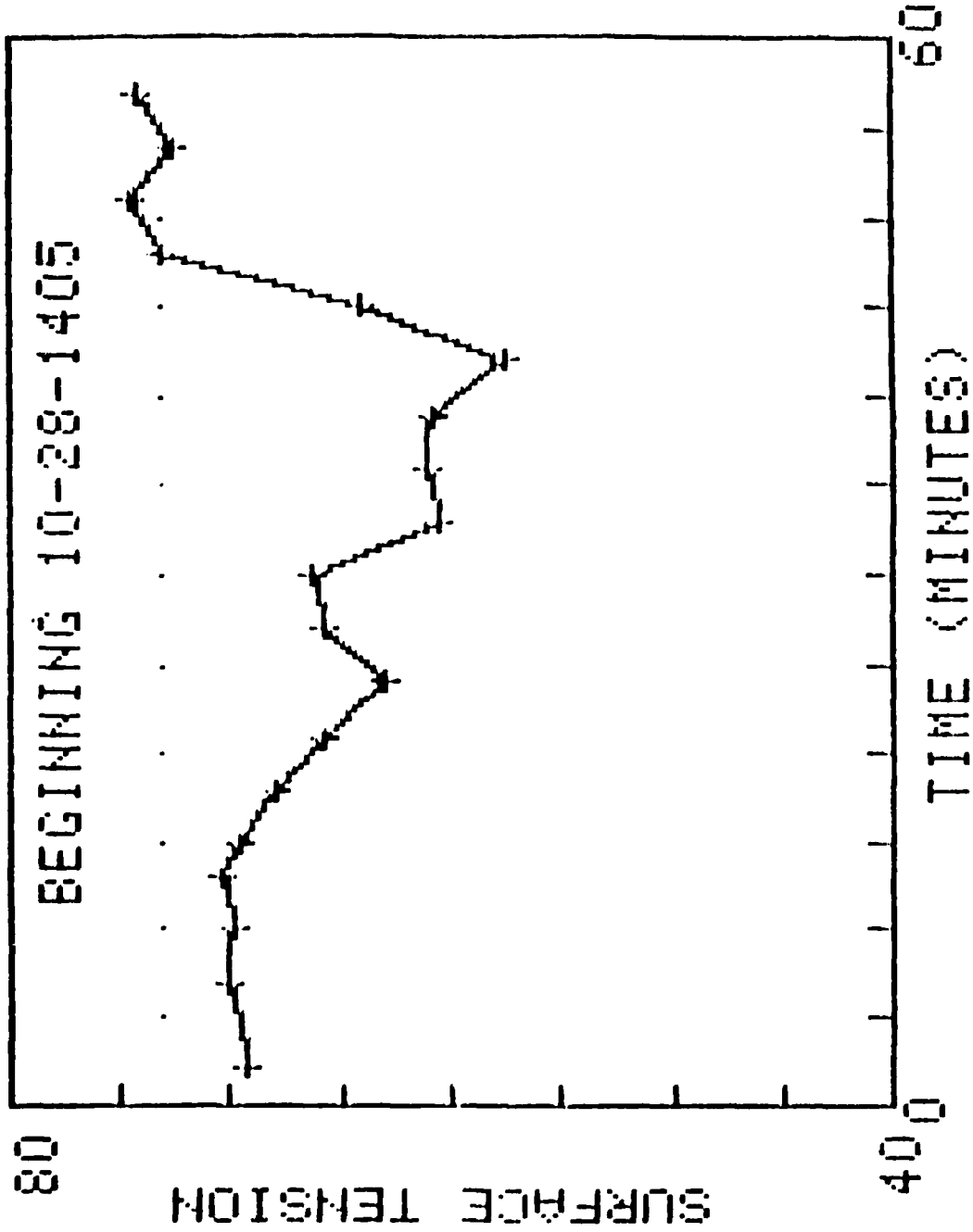

Figure 7. Natural Slicks, Surface Tension - 12.

After final processing, the surface tension data will be corelated with radar backscatter results and with internal wave events acquired simultaneously during the TOWARD Experiment. These data intercomparisons are of interest, because internal waves play a role in the formation of coherent banded organic surface films, while the organic films in turn attenuate and resist the formation of capillary waves and reduce microwave radar backscatter.

APPENDIX I

COMPUTER PROGRAM FLOWCHART

I. Surface Tension

The location of BASIC programs is changed to reserve memory for the graphics. Part II is called.

II. Surface Tension II

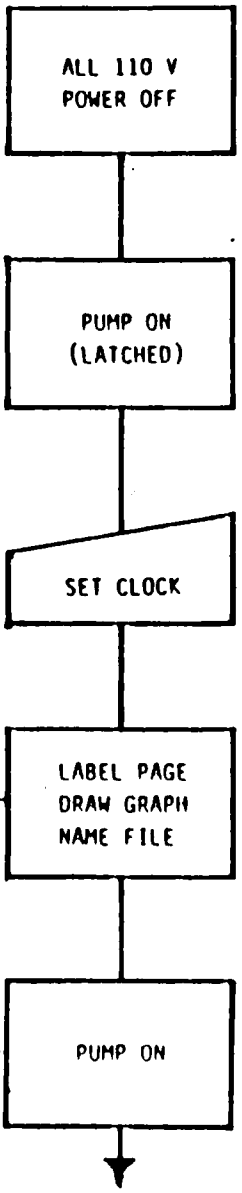

An initialization step.

Pump begins flushing system early during the first on cycle.

When the system is first turned on the date and time must be entered.

Printer labels paper. Graph axes are drawn on screen. Disk file is automatically named with date and time. (Repeated hourly).

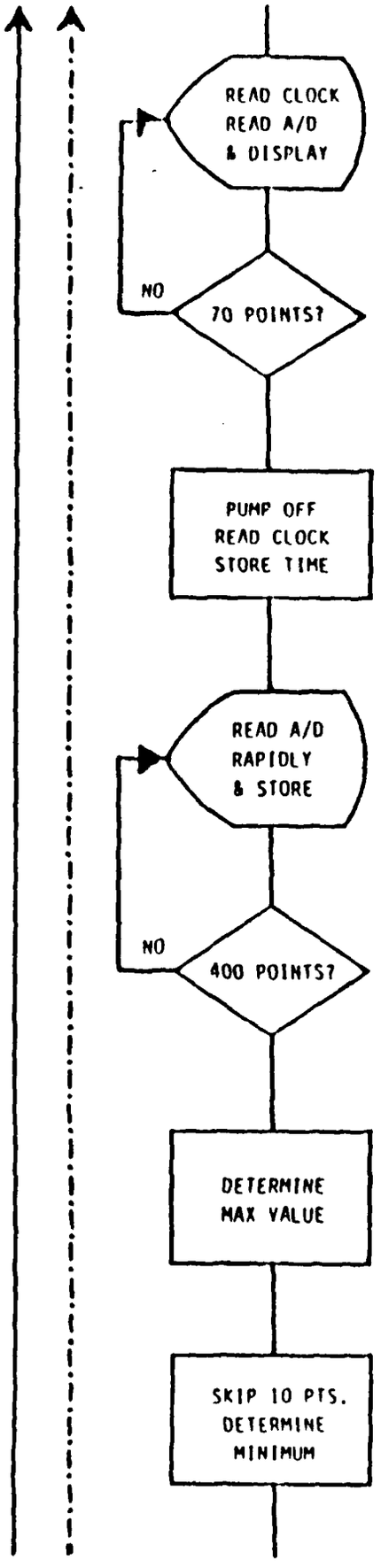

Time and sensor signal are shown on screen while water sample fills sample chamber and overflows.

The number of points determines how long water is pumped through the sample chamber.

The pump shut-off time is recorded as the sample time.

As water drains slowly from the chamber the signal is read rapidly 400 times. Values are stored.

The maximum value occurs when the glass plate detaches from the water surface.

Points prior to the maximum and 10 points after it are ignored. The remaining points of the 400 are averaged for the minimum.

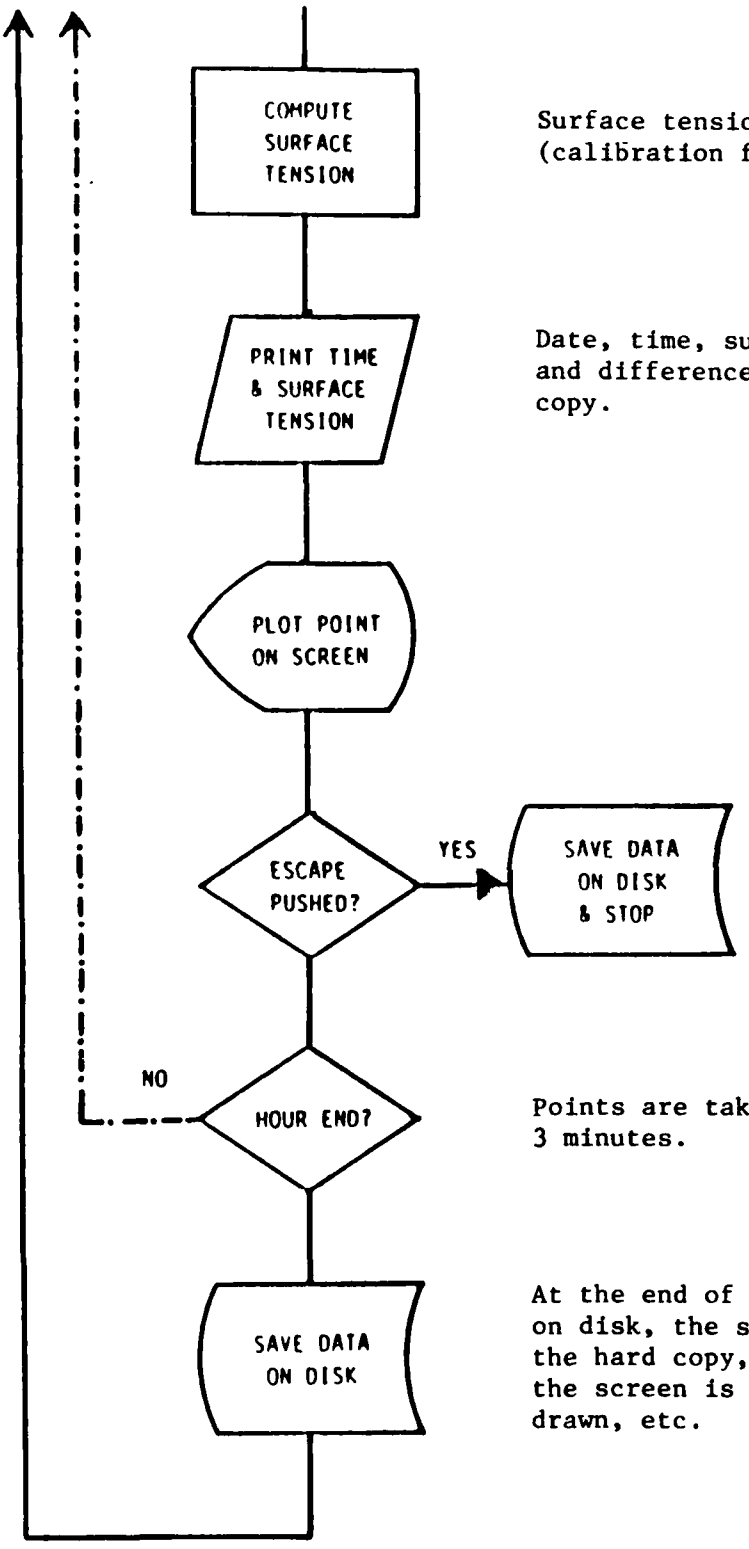

Surface tension = (max - min) X (calibration factor).

Date, time, surface tension, max, min, and difference are printed on the hard copy.

The cycle continues until stopped with the ESC key.

Points are taken approximately every 3 minutes.

At the end of an hour the data is saved on disk, the screen graph is drawn on the hard copy, a new file is created, the screen is erased and new axes are drawn, etc.

APPENDIX II

PROJECT TOWARD

NRL Surface Tension Measurement System

Catalog of Surface Tension Data

Date	Time
09-20-84	1620-1648
09-21-84	1624-1657
09-22-84	0836-0851
	0915-1013
09-24-84	0822-0958
	1013-1057
	1105-1232
	1240-1358
09-25-84	0814-0937
	1014-1058
	1109-1333
09-26-84	0853-0856
	0907-1459
09-27-84	0847-1459
09-28-84	0839-1210
	1223-1501
10-02-84	0924-1044
	1053-1558
10-03-84	0906-1520
10-04-84	0842-0957
10-06-84	1005-1150
	1129-1609
10-09-84	0556-0659
	0850-0918
	1341-1359
	1424-1450
10-11-84	1843-2008
	2030-2105
10-12-84	0841-1317
	1651-1814
10-15-84	1616-1703
10-16-84	0933-1146
	1157-1759
	1833-1842
10-17-84	0852-1414
10-18-84	0915-1238
	1315-1357
	1416-1440
10-20-84	0940-1144
	1315-1815
	1853-2223
10-23-84	0843-1006
	1152-1422
	1634-1722
10-24-84	0847-1128
	1208-1448
	1516-1654
10-25-84	0835-1256
	1454-1557
10-27-84	0847-1021
	1124-1654
10-28-84	1110 1250
	1315-1558
10-29-84	1109-1619
10-30-84	0823-1056
	1120-1519
10-31-84	0936-1256
	1415-1457

11-02-84	1017-1622
11-03-84	1319-1725
3-08-85	1015-1357
3-12-85	0915-1611
3-13-85	0853-1057 1130-1622
3-14-85	0822-1059
3-15-85	1110-1539
3-16-85	1013-1400
3-18-85	1032-1140
3-19-85	1001-1223 1513-1637
3-20-85	0826-1233 1505-1605
3-21-85	0943-1757
3-22-85	0828-1357 1553-1630
3-24-85	1208-1539
3-25-85	0823-1153 1346-1358 1543-1555 1611-1746 1819-1831
3-26-85	0929-1258 1520-1558

APPENDIX III

WAVE FOLLOWER MEASUREMENTS DURING TOWARD 84/85

Paul A. Hwang
Ocean Research and Engineering
La Canada, California 91011

FOREWORD

As a part of the TOWARD experiment, the wave follower measurements were to provide, among other things, ground truth of short waves for radar backscatter and SAR imaging groups. This report presents a short account on the scope of the measurements and the progress of the data analysis. The report is intended for internal use of the TOWARD investigators. The purpose is to specify the available data sets, define the analysis in progress and provide up-to-date results to potential TOWARD users.

CONTENTS

LIST OF ILLUSTRATIONS

LIST OF ILLUSTRATIONS (CONT)

LIST OF TABLES

1. INSTALLATION AND INSTRUMENTATION

The wave follower assembly was installed on the south extension structure of the NOSC Tower (see Figure 1). The assembly was placed 20 feet away from the tower structure and connected to it by a catwalk. The details of the wave follower and instrumentation are presented elsewhere (Shemdin, 1980; Shemdin and Hoff, 1986). The following gives a brief description of the system.

A set of instruments were installed at the bottom of the fixed structure (see Figure 2) to provide long wave directional measurements. For this purpose a pressure transducer (a) and a two-dimensional E-M current meter (b) were used.

On the moving frame (also referred to as C-frame), four instruments were mounted, as shown in Figure 3. Of these a capacitance gage was used as an elevation control sensor (c). This sensor provided the feedback signal to the servo-system to maintain the C-frame at a fixed elevation with respect to the instantaneous water level. A two-dimensional E-M current meter (d) was mounted on the lower arm of the C-frame to provide the two horizontal components of the current. The two-dimensional optical wave slope sensor (e) and the optical wave height sensor (Reticon camera, (f) were both used for measuring high frequency short waves. Both optical sensors used the 10 mW laser (g) that was mounted on the lower arm of the C-frame for a light source.

The wave slope sensor was calibrated in the laboratory before and after each experiment. Light refraction at the air-glass interface was used to simulate refraction of light at the air-water interface (see top insert of Figure 4). The magnitude of the refracted angle, was varied by moving the glass lens horizontally. By rotating the lens on the horizontal plane, changes in azimuthal angle, ψ were achieved (see bottom insert in Figure 4). A typical calibration result is shown in Figure 4. Averaged over the azimuthal angles, Figures 5a, b show the calibration curves for phases I and II of the experiment, respectively. The uncertainty is estimated to be the lesser of $\pm 0.5°$ or $\pm 13\%$ in the range 0 to 30° in water surface slope. This result is derived from phase II calibration tests where eight repetitions were performed. Only two repetitions were performed in phase I calibration tests.

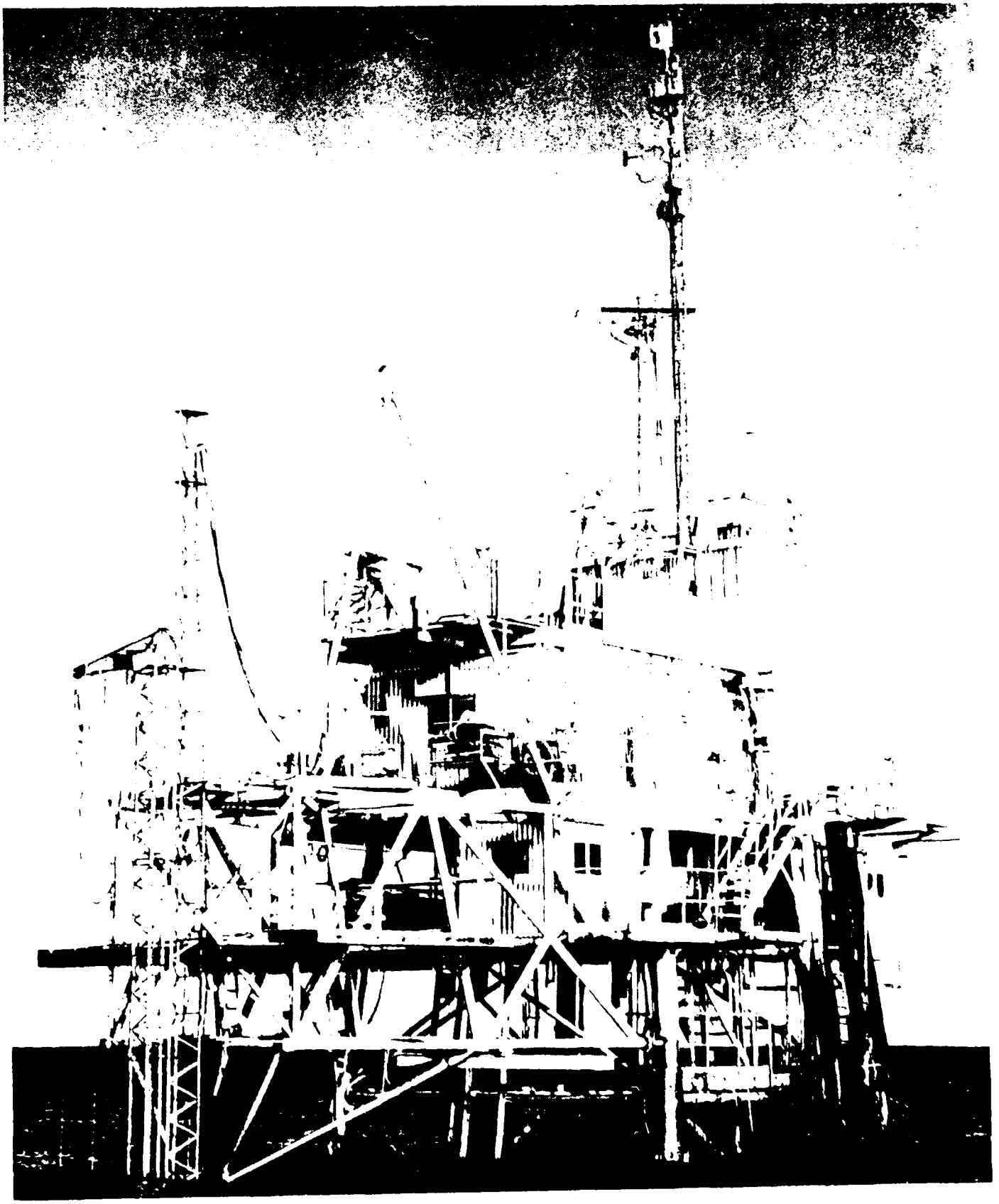

Figure 1. Photographic View of the Wave Follower Structure.

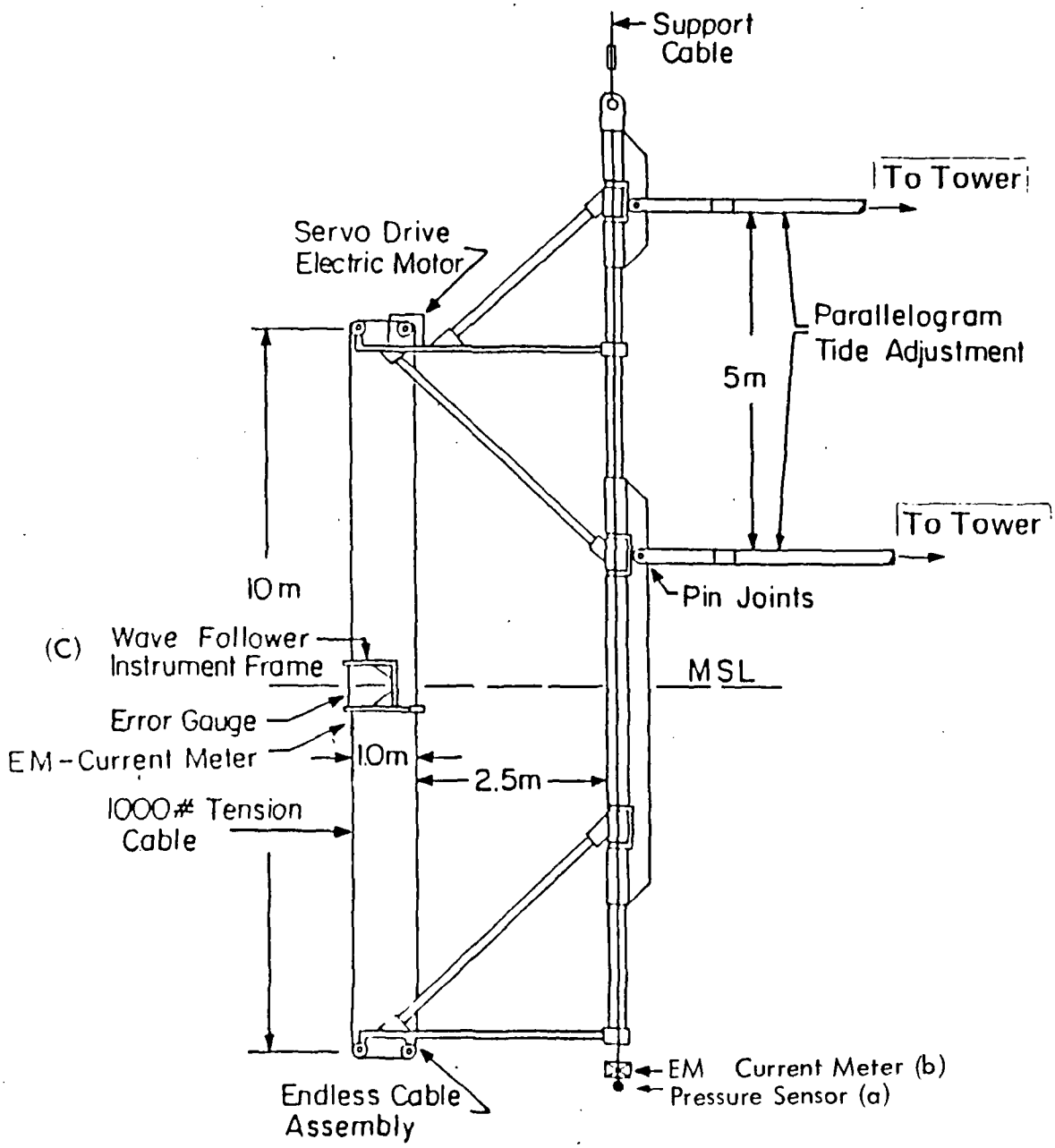

Figure 2. Wave Follower Structural Assembly.

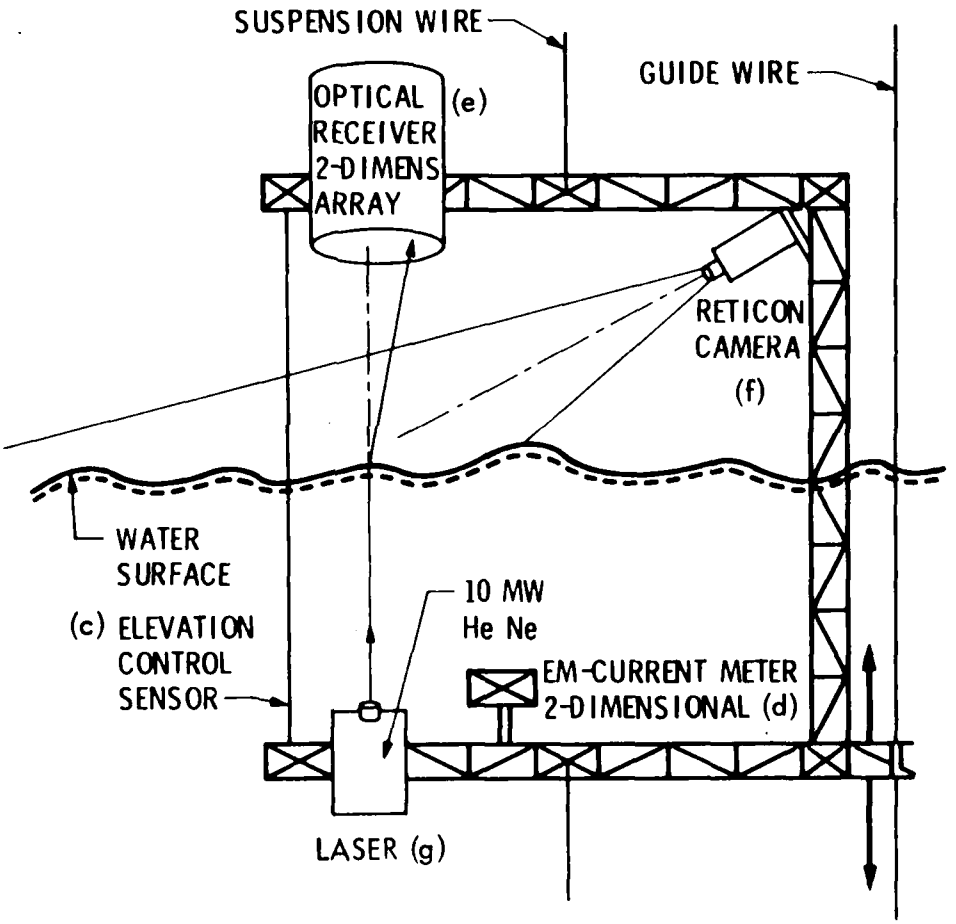

Figure 3. Wave Follower Instrument Frame. Capacitance Gage is used as Elevation Control Sensor (c); *Two-dimensional* current meter is used for measuring two horizontal currents components below water surface (d); Optical Receiver records two slope components of surface normal (e); Reticon camera records vertical displacement of water surface (f) and using He-Ne Laser (g).

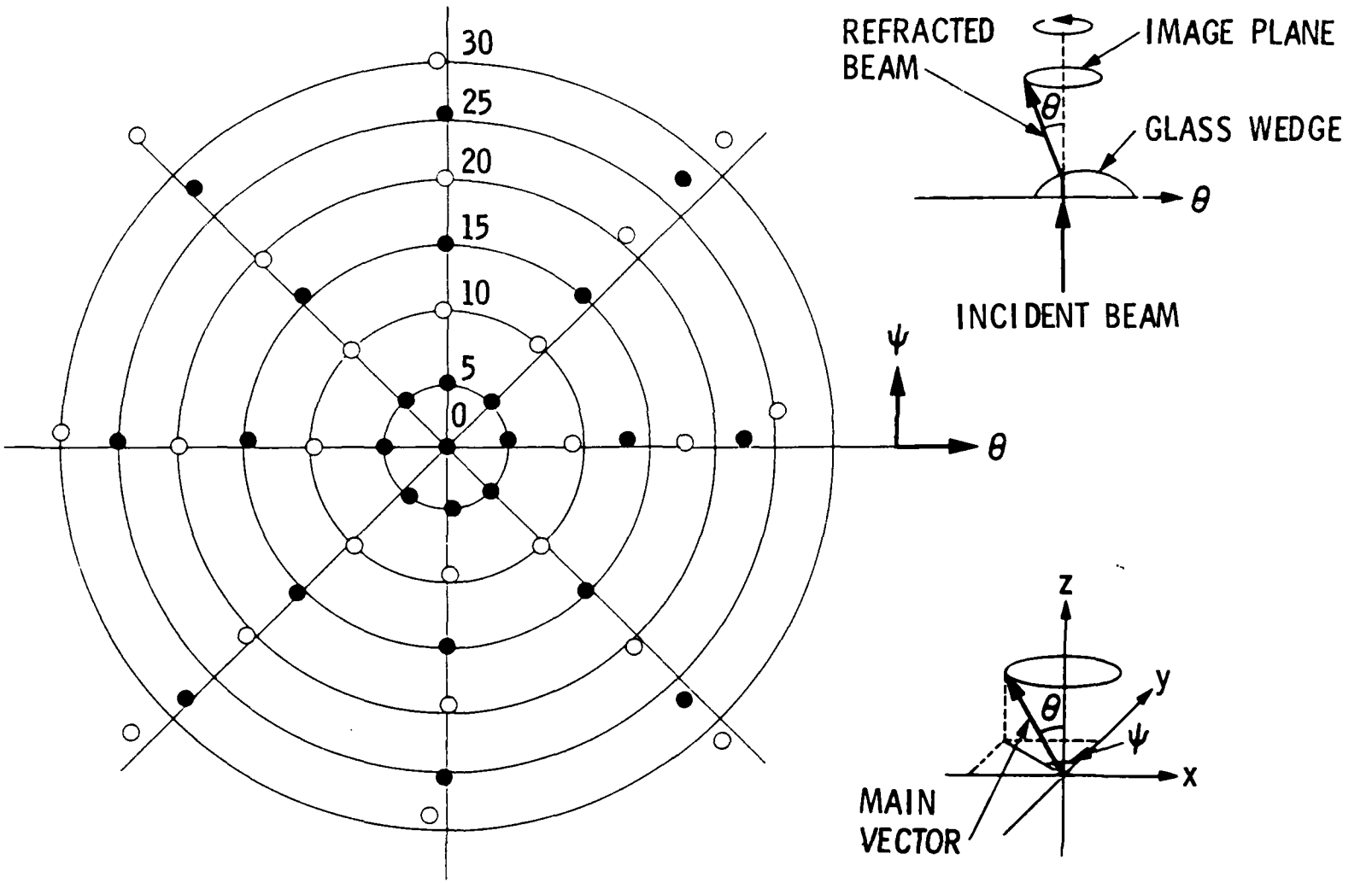

Figure 4. Laboratory Calibration of Wave Slope Instrument Used in TOWARD 84/85.

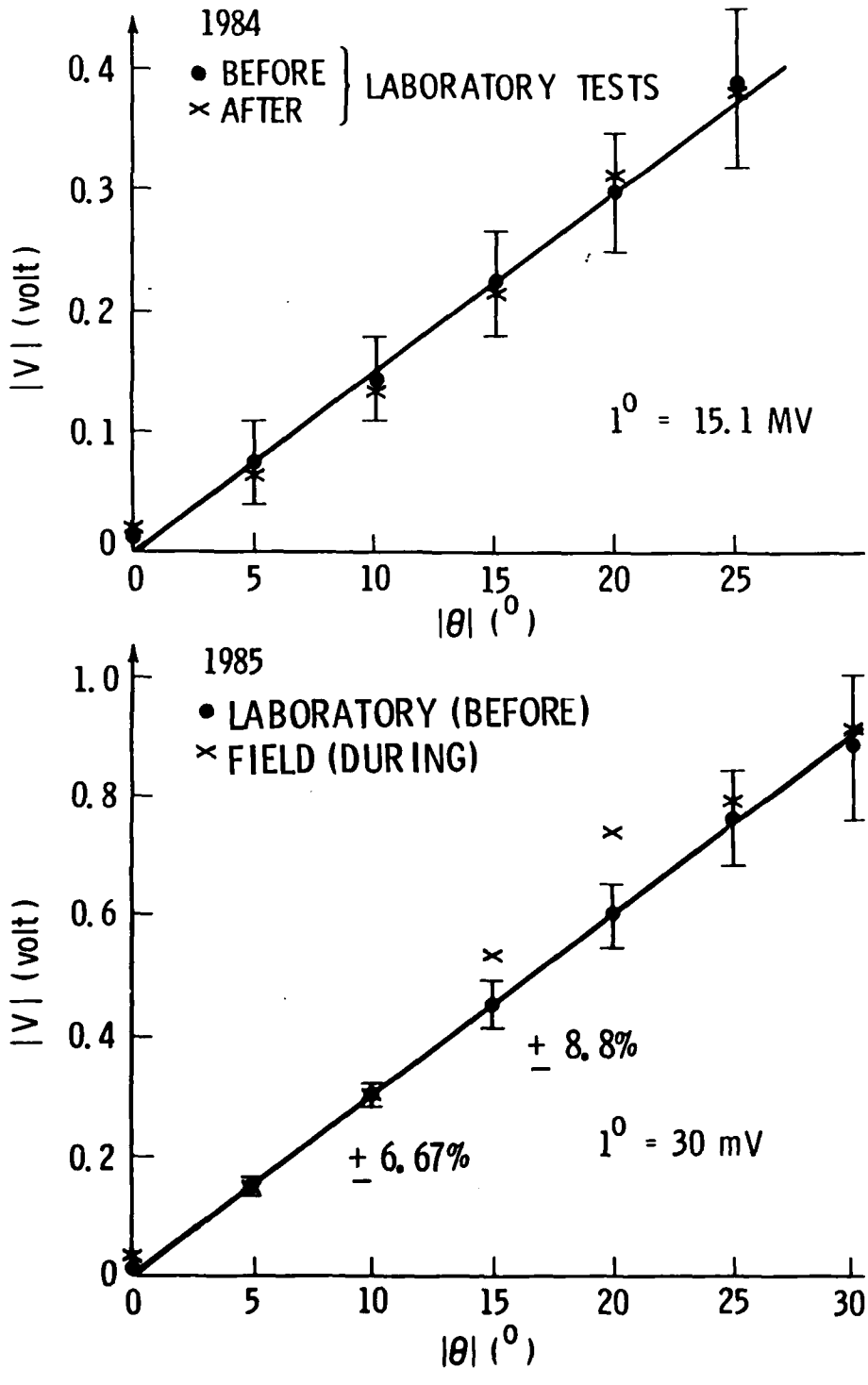

Figure 5. Calibration of Wave Slope Instrument.

2. DATA REDUCTION

During the two phases of the TOWARD experiment, more than 130 hours of data were recorded, from which 20 hours of data were selected for further studies. The criteria of selection were based on periods of aircraft flights, periods of stereo-photo sessions and range of wind and wave conditions. The environmental conditions varied from steady (for periods of at least 30 minutes) to transient (either in wind speed or wind direction). The waves ranged from large swell to strong local sea. Tables I and II list the conditions of the data segments that were digitized. At the time of this data compilation, the swell information had not been completed; it will be included in the final report. In Figure 6 the distribution of data segments versus wind speed is shown. In phase II, two storms swept through the tower region which generated wind speeds up to 25 knots (12.5 m/s). The latter events broadened significantly the range of wind speed measured.

Table I. Data Segments Recorded in Phase I.

Date	Pacific* Time	Wind Speed (m/s)	Wind Direction	Stereo Photo	Flights
10/17/84	1315 - 1345	7.5	285		CV990
10/20/84	1355 - 1455	6	265		
	2355 - 0025	4	120		
10/29/84	1435 - 1505	5	300		
	1520 - 1550	4.5	300		
10/30/84	1535 - 1605	3	290		
10/31/84	1030 - 1100	2.5	235		
	1300 - 1600	3-5	280-300	4 Series	CV990 F4
11/03/84	1820 - 2045	2.5	270		
	2330 - 2400	3	25		
11/04/84	0030 - 0130	3	10		
	0945 - 1230	2	220	1 Series	F4
	1530 - 1630	3	300	2 Series	
	1835 - 1930	1	175		
	2320 - 2350	2.5	0		
11/07/84	1625 - 1655	4	260	3 Series	CV990

*Pacific Time is 8 hours lag Greenwich Time.

Table II. Data Segments Recorded in Phase II.

Date	Time	Wind Speed (m/s)	Wind Direction (°)	Stereo Photo	Flights
3/19/85	1400 - 1530	6	260		CV990 F4, OV-ID
3/20/85	1000 - 1130	6	330		
3/21/85	1450 - 1500	3	310	1 Series	F4, OV-ID
	2030 - 2230	0			
3/22/85	0340 - 0410	1.5	90		
	1145 - 1215	3	290	2 Series	
3/24/85	1330 - 1400	3	270		
3/25/85	1120 - 1150	5	235		OV-ID
	1340 - 1700	7	240		
	1730 - 1800	6	230		
	1940 - 2010	2.5	180		
3/26/85	1011 - 1140	4	210	4 Series	F4, OV-ID
3/27/85	1020 - 1050	8	225	1 Series	
	1330 - 1530	9±	225		CV990
3/28/85	0930 - 1130	12±	225	2 Series	
4/1/85	2100 - 2230	0			

3. WAVE SLOPE DATA ANALYSIS

The SAR committee assigned "priority" to the L-band SAR flight of October 31, 1984, 1300 to 1500 hours local time. The wave follower effort was directed to study this particular data set. A sample of the capillary wave slope data are shown in Figure 7. Here, η_x, denotes slope in the upwind-downwind direction, and η_y denotes slope in the cross-wind direction. The surface displacement of long waves, η, is measured by a submerged pressure gage and is also shown in Figure 7. The starting time for this data series is 1300 local time. The wind speed at this time was 3.5 m/s and the wind direction was 280°. The swell period was 8 to 10 seconds, from direction 290°. The swell significant wave height was 1.2m. The variance of slopes in the two directions was found to be very similar ($\overline{\eta_x^2} = 3.72 \times 10^{-3}$ and $\overline{\eta_y^2} = 3.78 \times 10^{-3}$). In the following the results of analysis, up to date, are described.

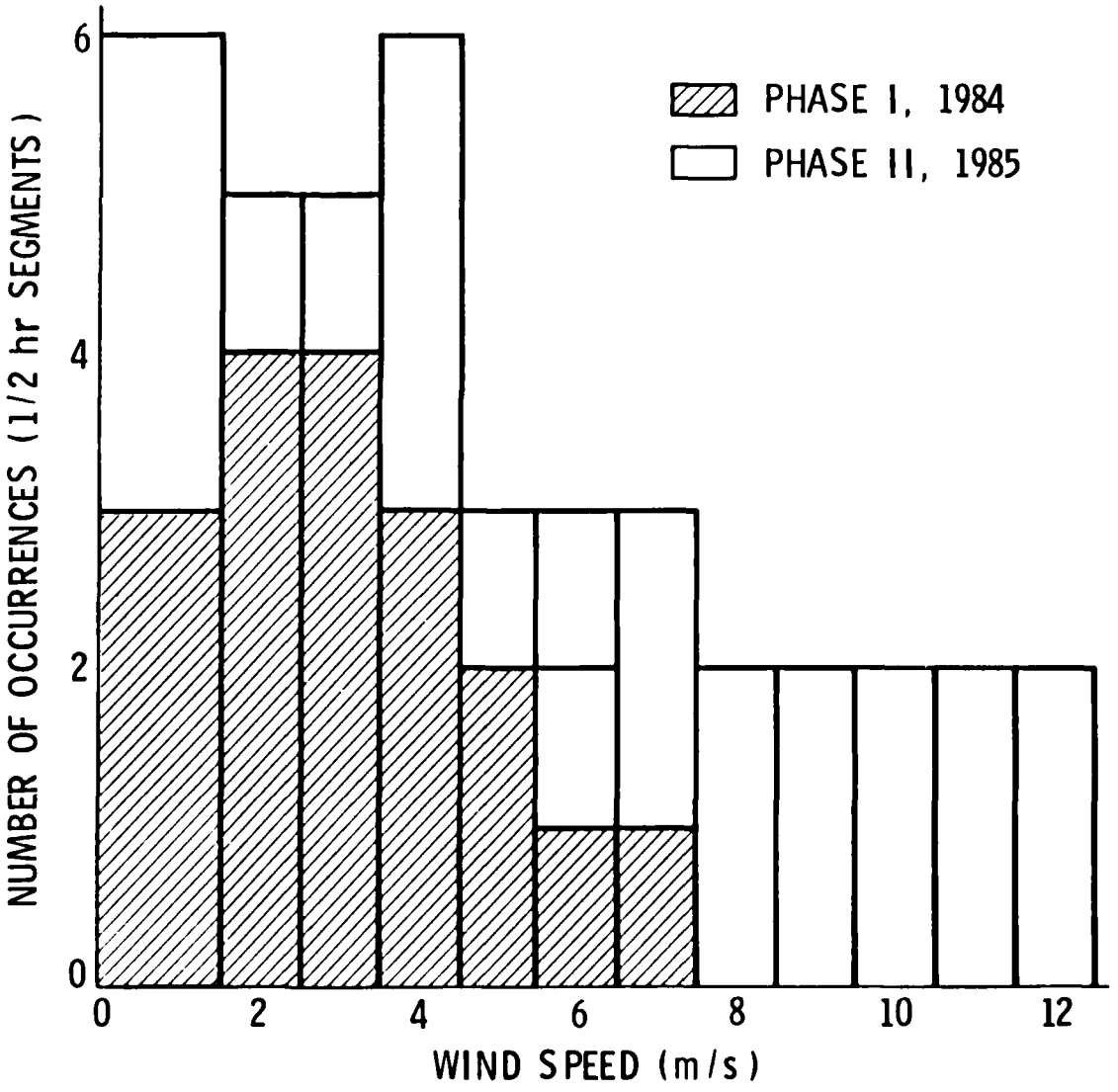

Figure 6. Experimental Conditions in TOWARD 84/85.

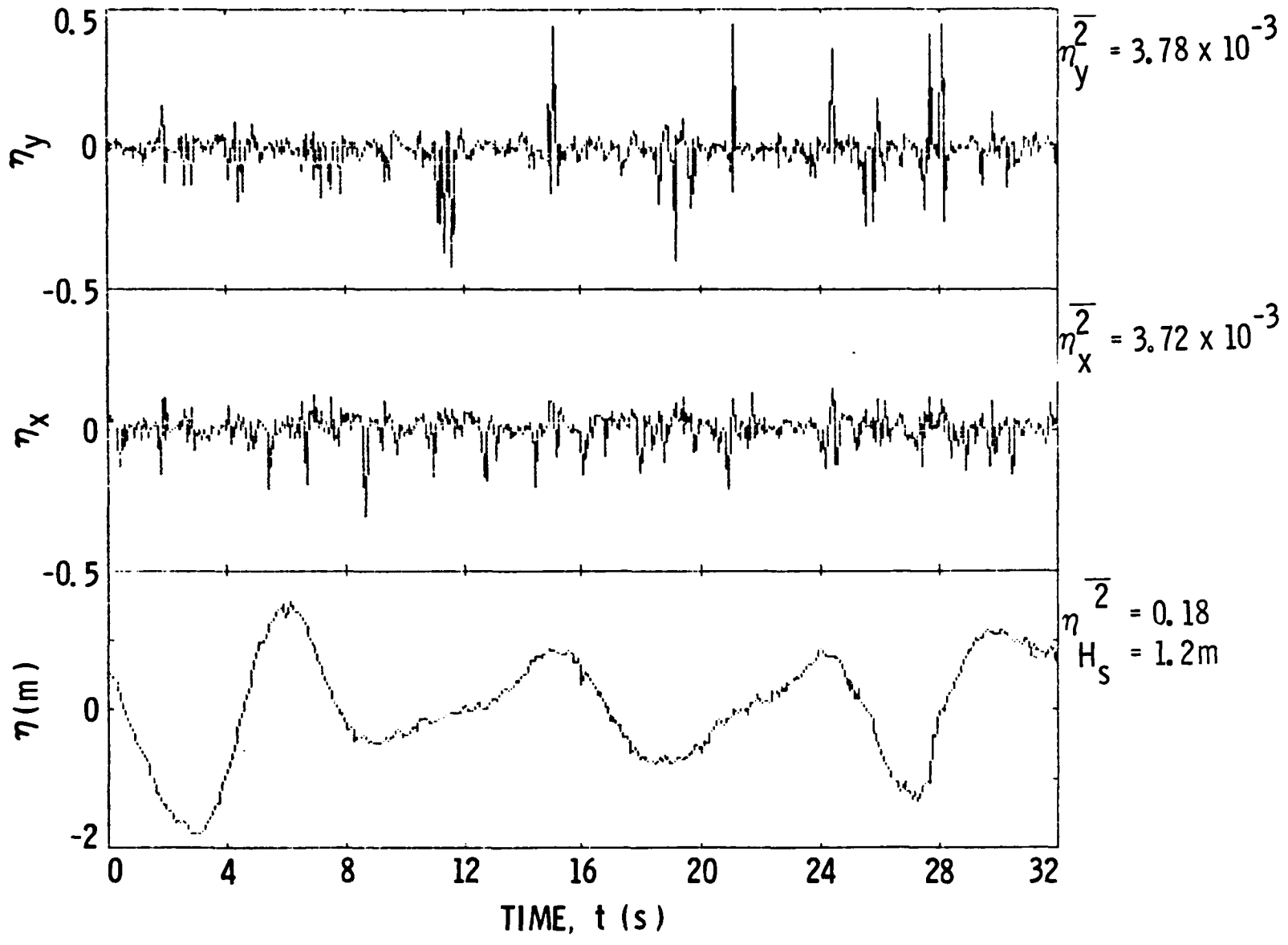

Figure 7. Records of Capillary Wave Slopes in the Upwind-Downwind and Cross-Wind Directions, and Water Surface Displacement Measured By a Submerged Pressure Gage.

3.1 The Probability Density Distribution of Wave Slopes

The probability density functions, PDF's, of the two slope signals are found to be somewhat different, as shown in Figure 8a. As observed in previous studies of sun glitter (Cox and Monk, 1954), the upwind-downwind component of slope is more skewed compared to the cross-wind components. For this wave record, the skewnesses, defined as

$$s_x = \left[\overline{\eta_x^3} \; / \left(\overline{\eta_x^2} \right)^{3/2} \right] , \tag{1}$$

and

$$s_y = \left[\overline{\eta_y^3} \; / \left(\overline{\eta_y^2} \right)^{3/2} \right] , \tag{2}$$

were found to be -2.04 and -0.60 for the x- and y-components, respectively. In Equations (1) and (2) the means of the signals are zero and the upper bar indicates time average. At low wind speeds, such as prevailed in this record, the PDF's are typically narrower than normal distribution. The peakness of distribution is defined as

$$k_x = \overline{\eta_y^4} \; / \left(\overline{\eta_x^2} \right)^2 , \tag{3}$$

and

$$k_y = \overline{\eta_y^4} \; / \left(\overline{\eta_y^2} \right)^2 . \tag{4}$$

They were calculated for these records to be 10.94 and 19.02, respectively. The normalization factors in Equations (1) through (4) are related to the variances of the two slope components, which as indicated before, are very close in value. The standard deviation is equal to the rms slope which becomes 0.061 (or approximately 3.5°) for slopes in both directions. From Figure 8, it is obvious that most waves have slopes less than or equal to 10°. There are, however, long tails on both end of the PDF curves. Here

slopes as high as 28° (excluding "dropouts" from the measurements - discussed later in the report) were registered. There is considerable interest in these high slope tails as they appear to correlate with the specular component of radar backscatter signals.

In the subsequent analysis, we apply frequency filters to the slope signals. Figures 8b, c, and d show the PDF's for the 2.5 Hz low-pass filter, 2.5 - 7.5 Hz band pass filter and 7.5 Hz high pass filter, respectively. For comparison, the rms slopes used for normalization of Figures 8b, c and d were those used for the unfiltered signals (Figure 8a). Comparison of these three plots indicates that the skewnesses of PDF's are mainly contributed by the low frequency range, or frequencies less than 2.5 Hz in the wave spectra. The steepnesses of these waves are generally small (less than 7°). Waves in the middle frequency range (2.5 - 7.5 Hz) show more symmetric slope distributions (see Figure 8c). Here the wave slopes are still low (less than 7°). The similarity of the upwind-downwind and cross-wind wave slopes in this middle frequency range indicates a more isotropic distribution of short waves. Finally, from Figure 8d, it is clearly shown that the steep components of wave slopes come entirely from the high frequency waves. The characteristics of long tails and narrow distributions in Figure 8d are similar to those of the unfiltered signals, Figure 8a.

The PDF's in the mid- and low-frequency ranges are very close to Gaussian when normalized by their respective rms slopes, as shown in Figures 9b and c. The distribution of the high frequency waves is very narrow (see Figure 9d). The unfiltered PDF is shown in Figure 9a for comparison. Table III shows the partitioning of variance in these three frequency ranges as well as the skewness and flatness (kurtosis) statistics. From this table the following observations are noted:

(a) The ratio of $\overline{\eta_x^2}/\overline{\eta_y^2}$ varies, 2.17 at low frequency, 1.29 at mid-range, and 0.65 at high frequency. This reflects the gradual change from two-dimensional (organized) long waves to a more random short wave distribution. The ratio 0.65, at the high frequency end is somewhat puzzling. The time series in Figure 7, (also, the drop-out statistics which will be discussed later) suggest that the cross-wind component of wave slope may contain more noise compared

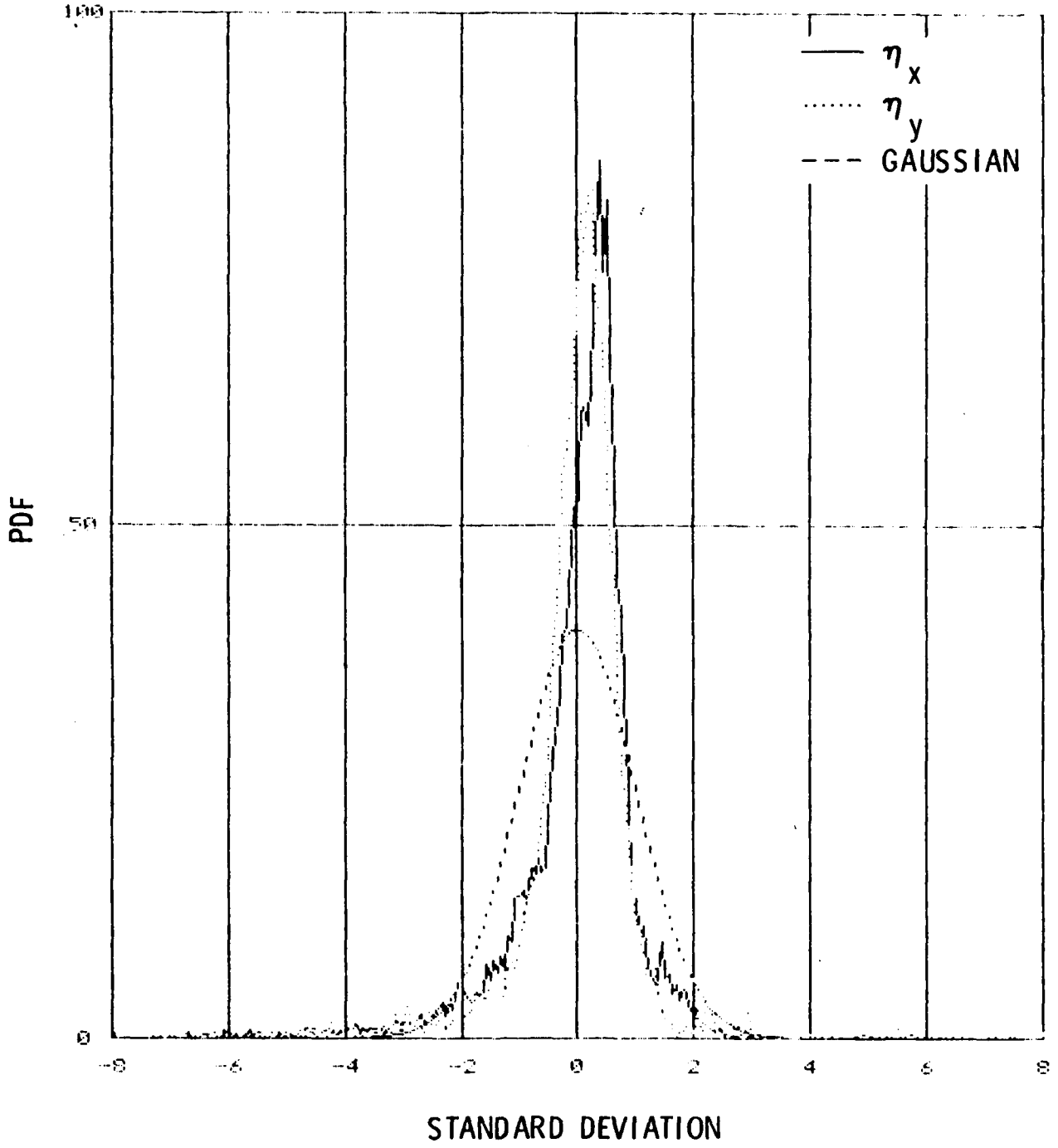

Figure 8a. PDF of Wave Slopes, Unfiltered. The RMS Variance of Unfiltered Signal Is Used for Normalization of Standard Deviation.

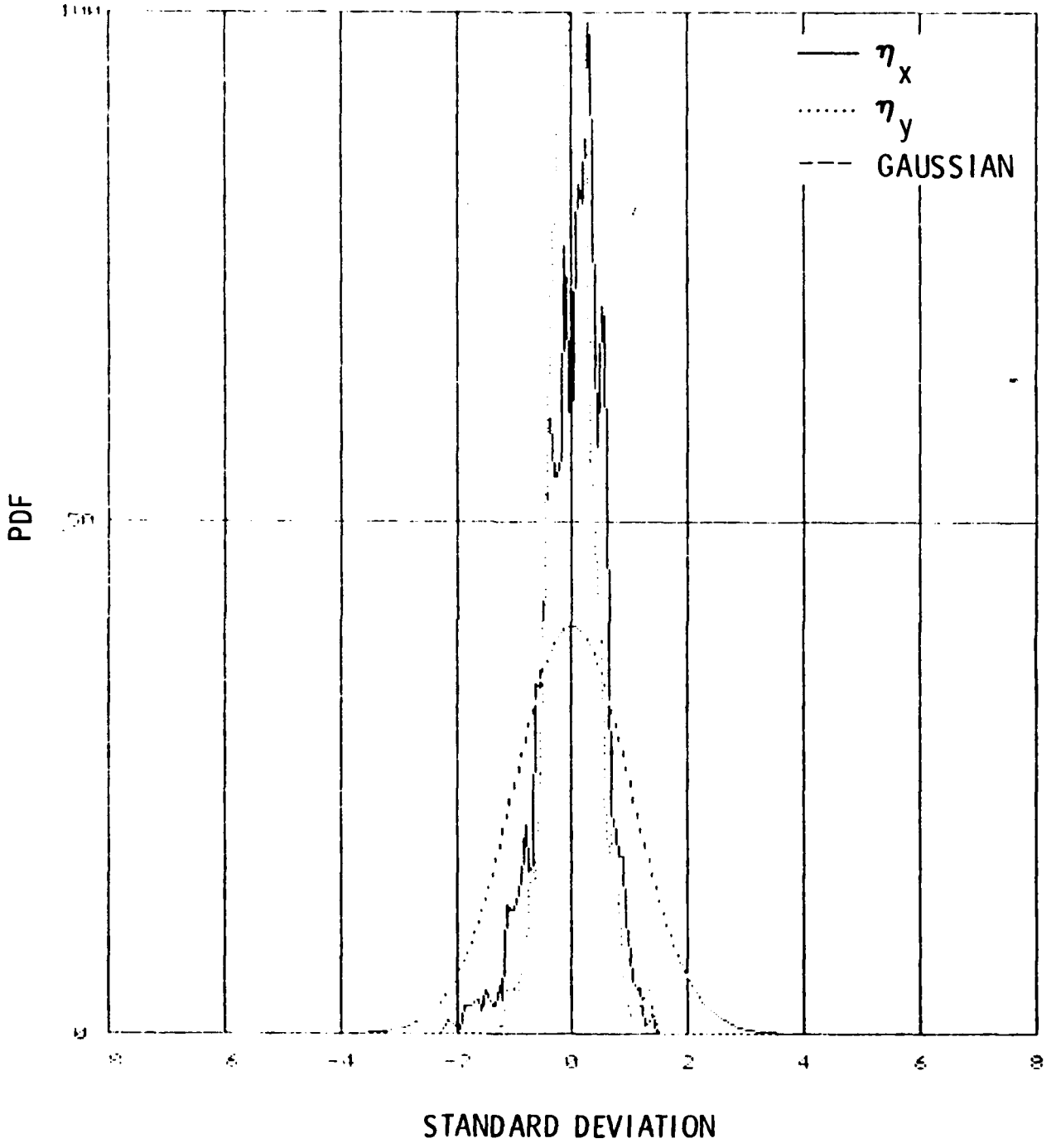

Figure 8b. PDF of Wave Slopes, 2.5 Hz Low Pass Filtered. The RMS Variance of Unfiltered Signal Is Used for Normalization of Standard Deviation.

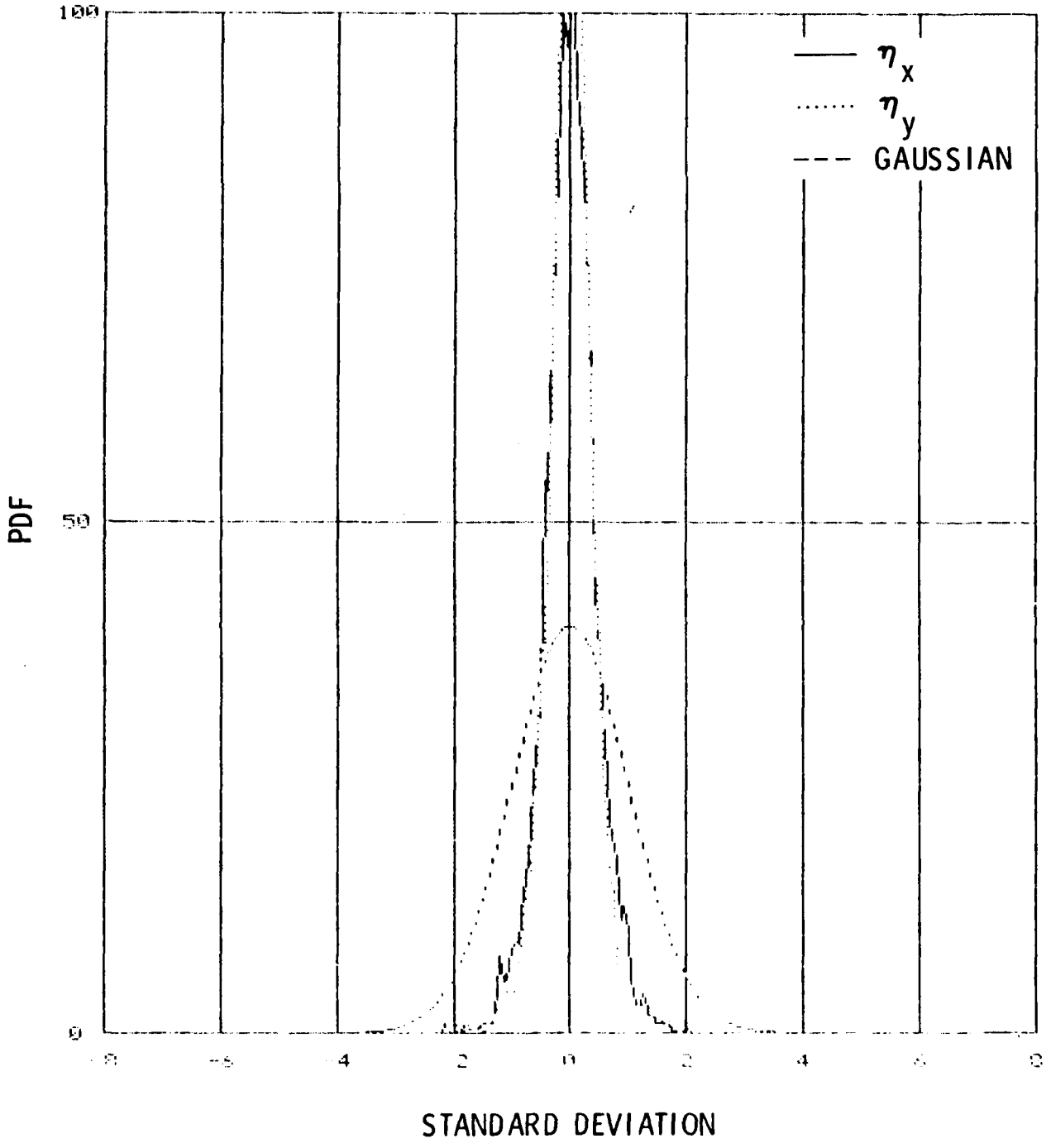

Figure 8c. PDF of Wave Slopes, 2.5 to 7.5 Hz Band Passed Filtered. The RMS Variance of Unfiltered Signal Is Used for Normalization of Standard Deviation.

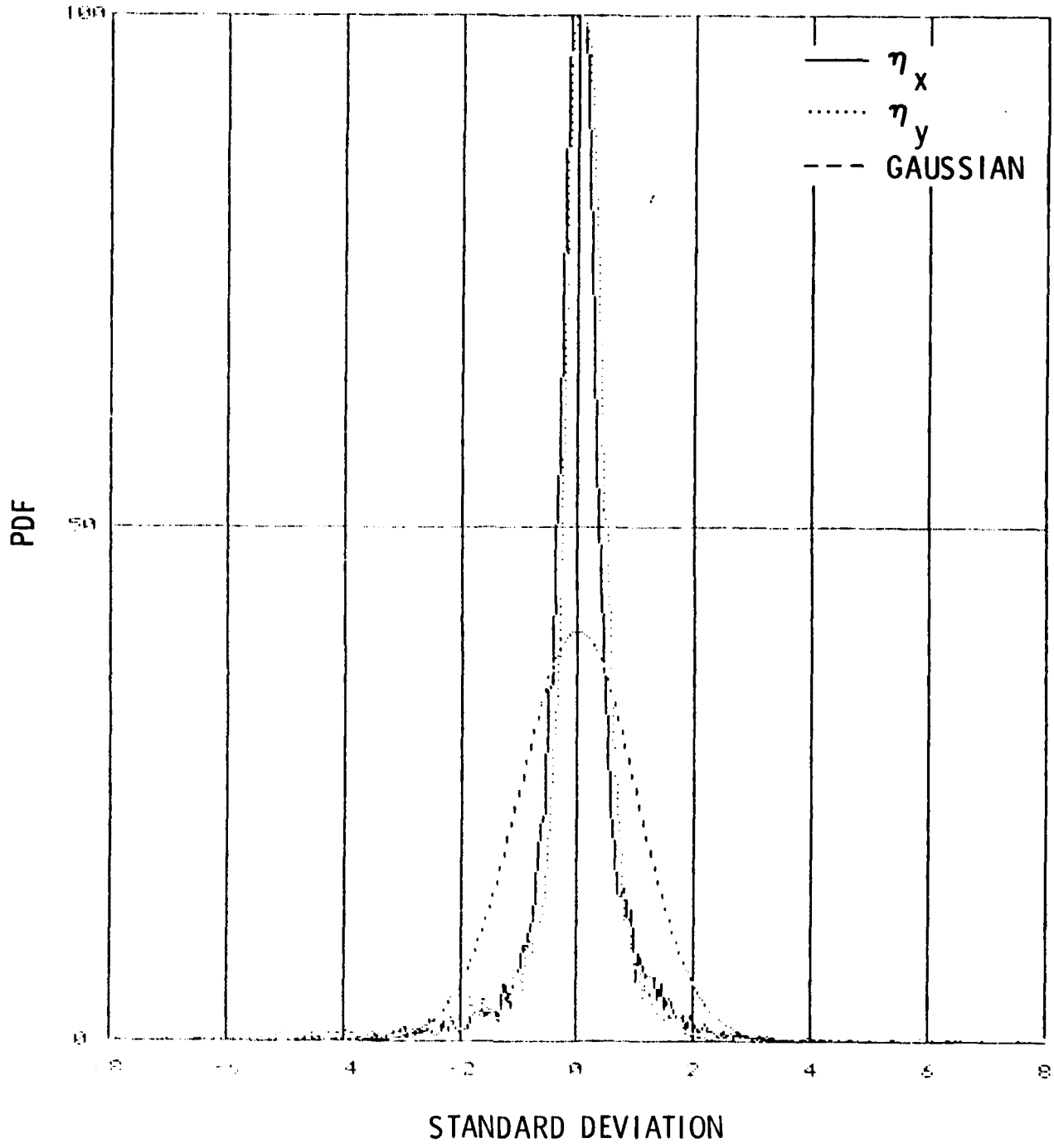

Figure 8d. PDF of Wave Slopes, 7.5 Hz High Pass Filtered Results. The RMS Variance of Unfiltered Signal Is Used for Normalization of Standard Deviation.

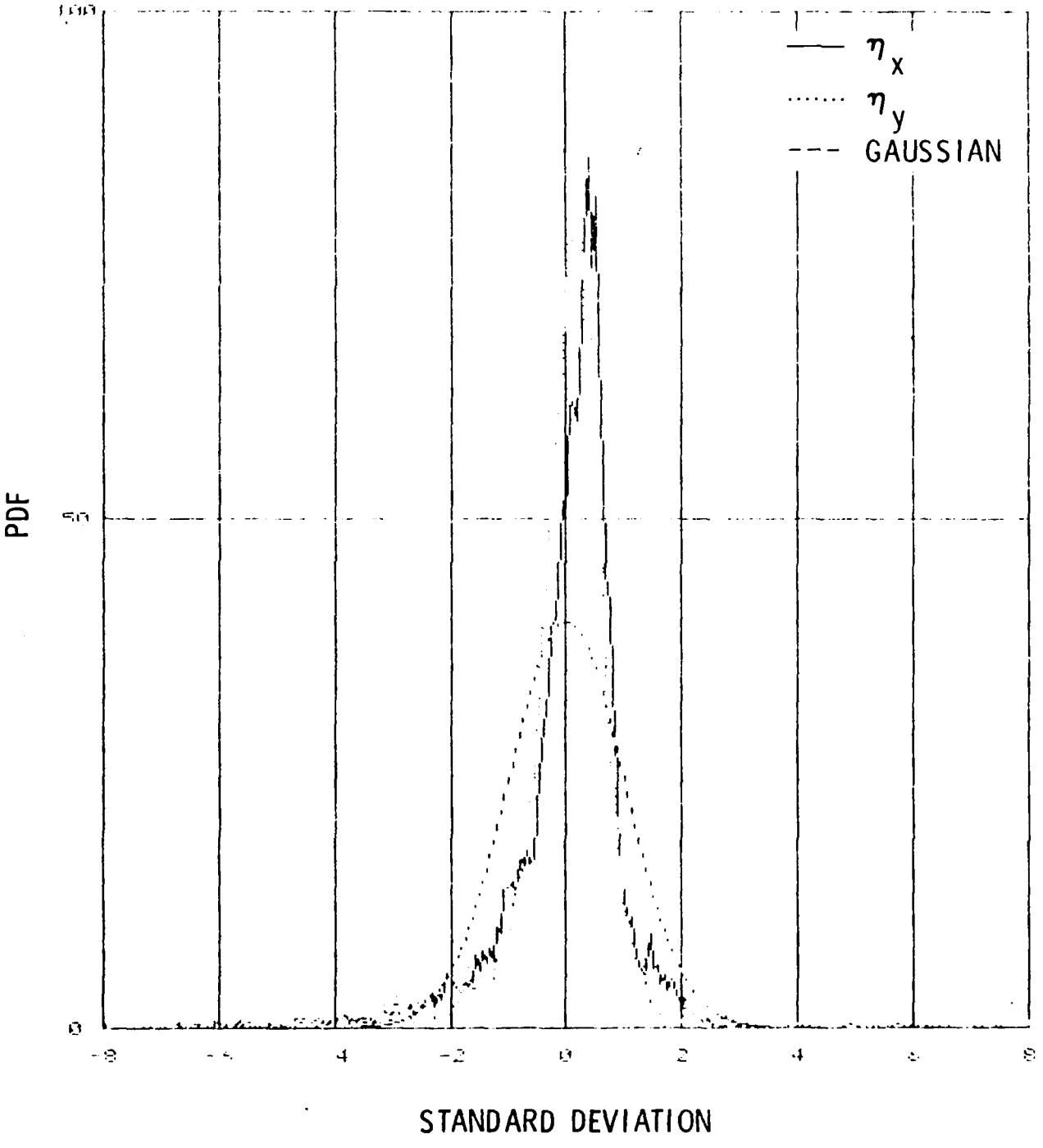

Figure 9a. PDF of Wave Slopes, Normalized by the Total Variance, Unfiltered.

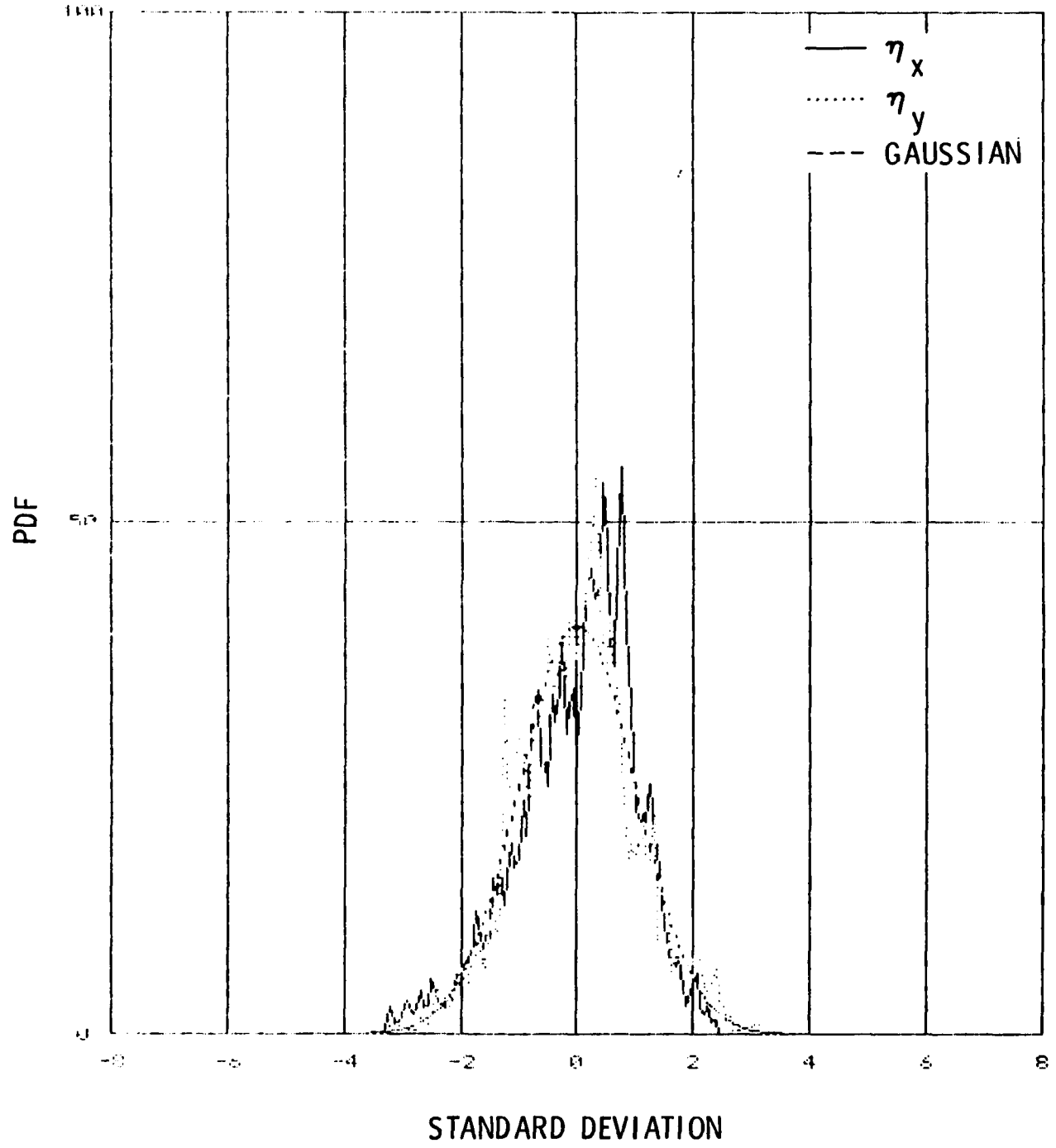

Figure 9b. PDF of Wave Slopes, Normalized by the Filtered Variance, 2.5 Hz Low Pass Filtered.

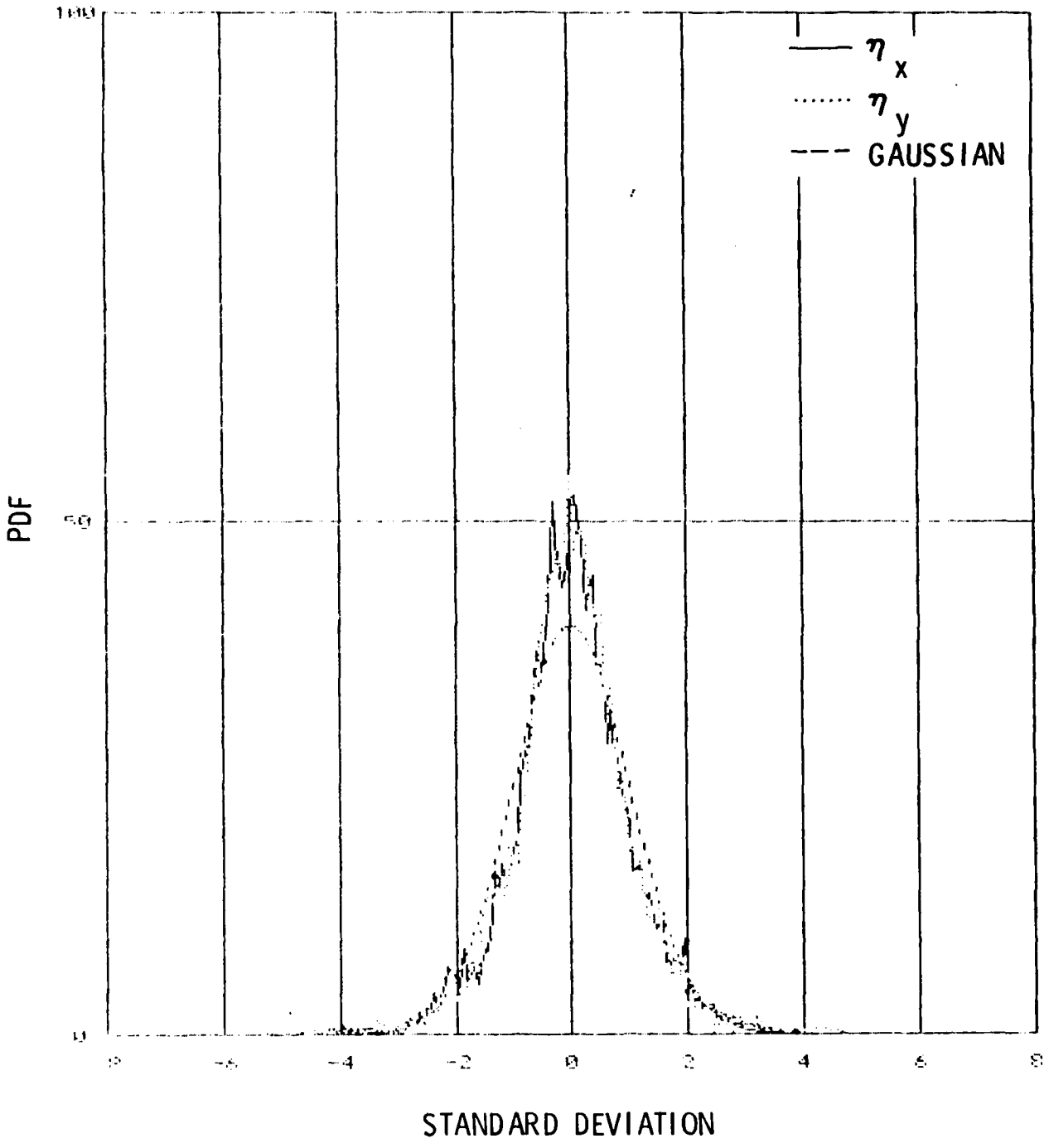

Figure 9c. PDF of Wave Slopes, Normalized by the Filtered Variance, 2.5 to 7.5 Hz Band Pass Filtered.

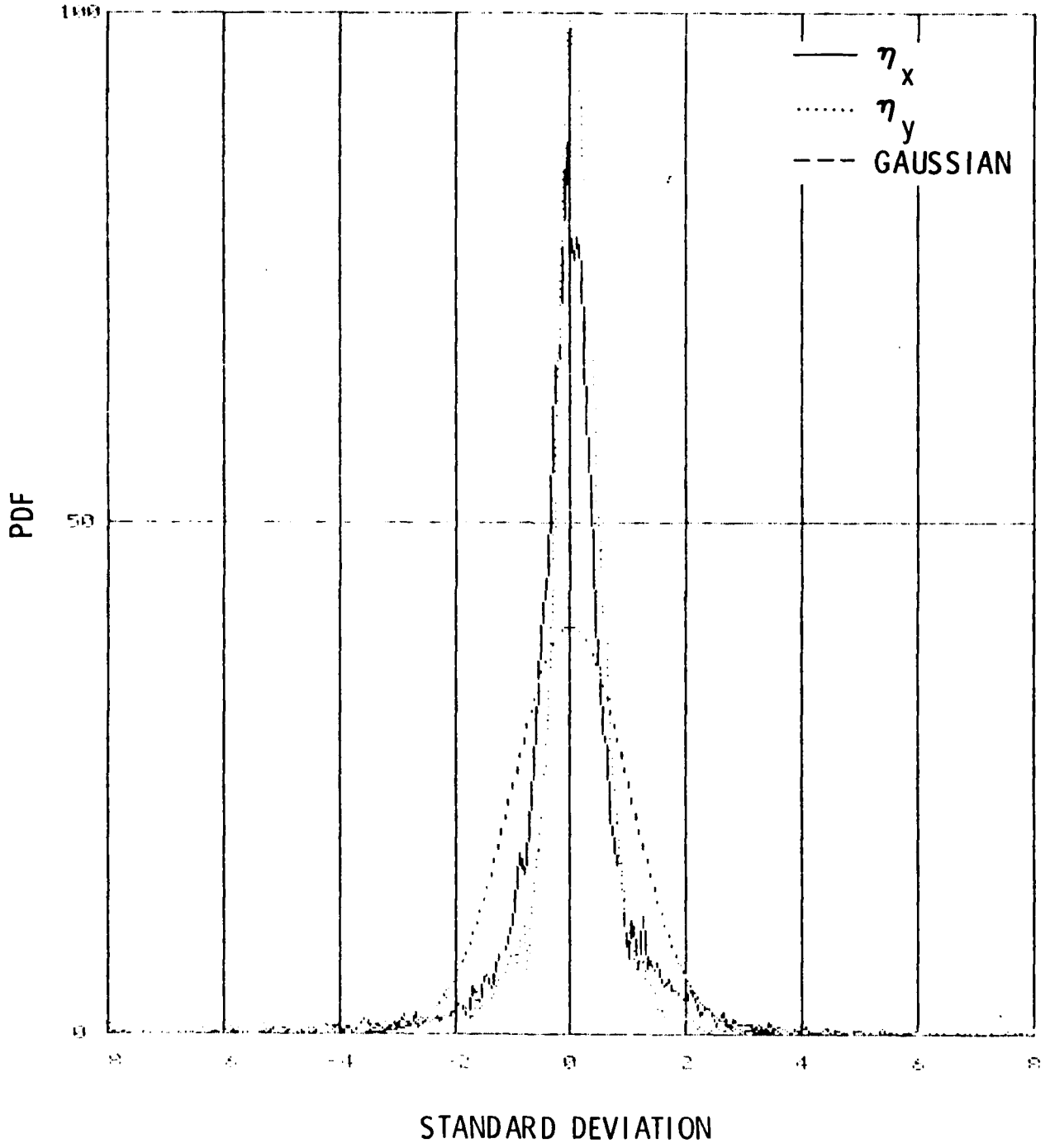

Figure 9d. PDF of Wave Slopes, Normalized by the Filtered Variance, 7.5 Hz High Pass Filtered Results.

Table III. Statistical Properties of the Frequency Band-Passed Wave Slopes

	i = x (up/downwind)				i = y (crosswind)			
	Unfiltered	Filtered			Unfiltered	Filtered		
		f<2.5Hz	2.5<f<7.5	f<7.5		f<2.5	2.5<f<7.5	f<7.55
$\overline{n_i^2}$	3.72×10^{-3}	1.15×10^{-3}	6.60×10^{-4}	1.66×10^{-3}	3.78×10^{-3}	5.31×10^{-4}	5.91×10^{-4}	2.57×10^{-3}
$\overline{n_i^3} / (\overline{n_i^2})^{3/2}$	-2.038	-0.541	-0.108	-0.550	-0.599	-0.069	-0.040	-1.130
$\overline{n_i^4} / (\overline{n_i^2})^2$	10.94	3.20	4.21	12.10	19.02	3.09	5.12	23.00

to the upwind-downwind channel. A more realistic ratio would be 1 for an isotropic short wave field. More analysis of data is needed to confirm this observation, and is planned.

(b) The skewness of the filtered signal is generally smaller than the unfiltered signal except for the high frequency component in the cross-wind direction. The small magnitudes of skewness in the low to intermediate frequency bands of the cross-wind slopes indicate possible two-dimensionality of these waves, i.e., long-crested waves.

(c) The flatness (kurtosis) estimates show an increasing trend toward the high frequency wave components. At the low frequency end, the magnitude is close to that of a Gaussian distribution (for which, the kurtosis is 3). An increase above this value indicates a tendency toward a narrower-band frequency distribution. The larger the magnitude of this statistical measure, the more the occurrences of very large and very small wave slopes, compared to a Gaussian distribution.

Cox and Munk (1954) found from their sun glitter measurements that the skewness in the cross-wind direction (their $C_{21} = 0.11 \pm 0.03$) is less than the upwind-downwind ($C_{03} = -0.42 \pm 0.12$) at high wind speed (14 m/s); and relatively small (nearly zero) at very low winds (velocity unspecified). The flatness (peakness in their terminology) estimates from their measurements shows higher cross-wind ($C_{40} = 0.4 \pm 0.2$) than upwind-downwind ($C_{04} = 0.2 \pm 0.4$) components. These results are consistent with our present measurements. Our frequency decomposition analysis, however, indicates that the distribution of wave slopes at different frequency bands are quite different from each other. More detailed studies on wind speed and swell dependence, and of longer time series, are forthcoming.

3.2 Longitudinal Variation of the Slope Variances

For the SAR and radar return studies, the longitudinal (or spatial) variation of short waves along the long wave profile is of considerable interest. The period of the swell on October 31, 1984 was in the range 8 to 10 seconds. In Figure 10 the mean square slope $\nabla\eta^2 = (\overline{\eta_x^2} + \overline{\eta_y^2})$, calculated

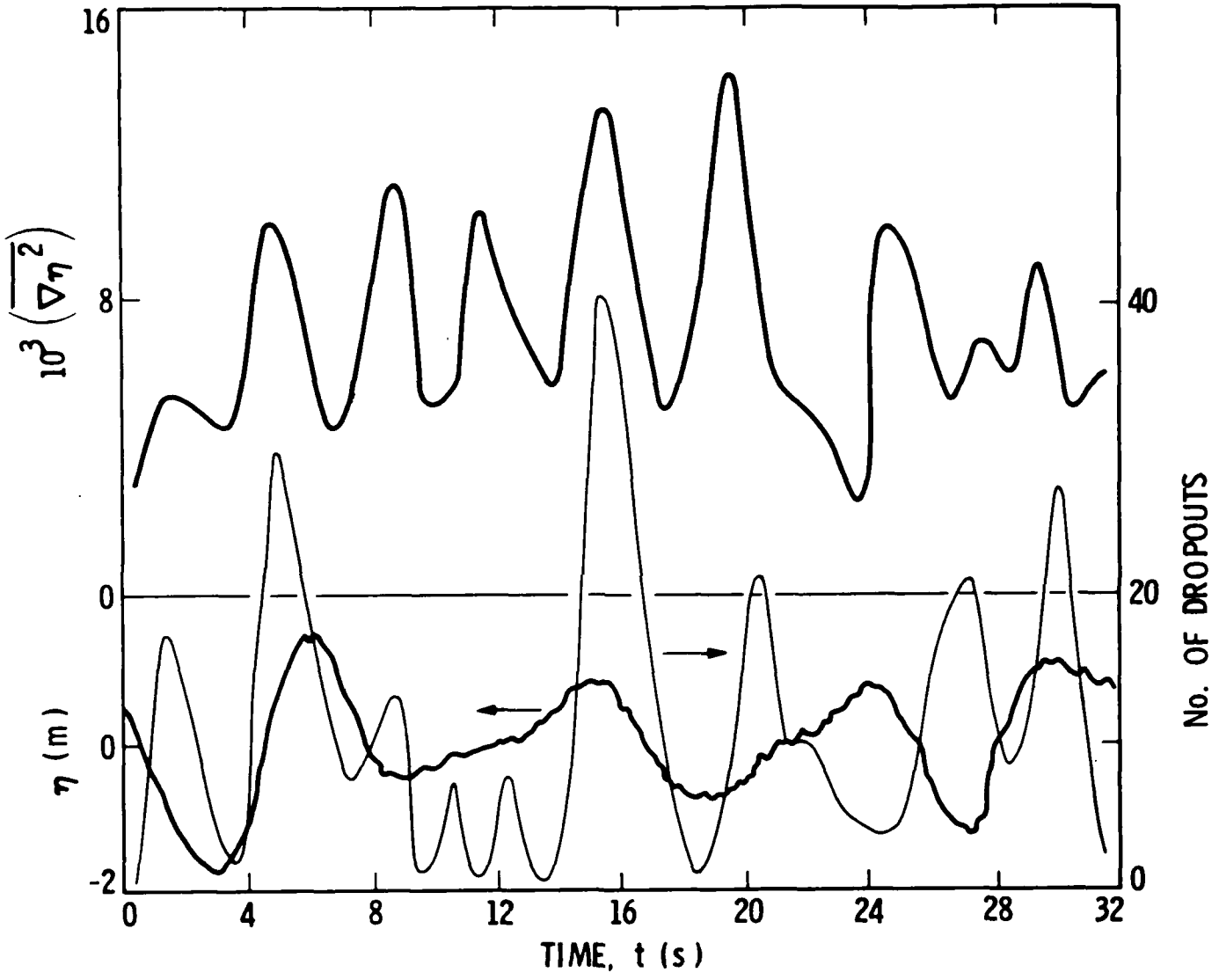

Figure 10. Longitudinal Variation of Mean Square Slope of Short Waves and Data Dropouts Along Profile of Long Waves.

from one second record length, is plotted in relation to the long wave profile. The large variation of the short waves at different phases of the long wave is clearly demonstrated. The maximum and minimum of the mean square slopes (one-second-averages) are found to be 1.42×10^{-2} and 2.23×10^{-3}, respectively. The mean value is 7.5×10^{-3}. The fluctuation is nearly 100% of the mean. When the small steepness of the long wave is considered (H_s = 1.23m, T_s = 9s, the "average" slope is approximately 0.01) the modulation of short waves is approximately 100 times that of long wave slope. Such a high degree of modulation is indeed significant. The local maxima of the slope variance generally occur near wave crests. It is noted that secondary maxima occur (not necessarily of smaller magnitudes) between the long wave crest. The peaks that appear above the wave troughs are located at 12 and 20 seconds along the time record. The strong local disturbances and secondary peaks suggest nonlinearity of short waves and possibly instability along the long waves. This observation of large modulation of short waves by the low-amplitude long waves is difficult to explain by a two-scale model such as that proposed by Longuet-Higgins and Stewart (1960) and Longuet-Higgins (1969).

In Figure 10 the number of data points that have a slope magnitude 0.5 or greater (this value is close to the theoretical wave breaking limit) are shown in relation to the long wave profile. These points are denoted as "dropouts." They bear a relationship to breaking waves. Note that at the time of this writing, the dropout count includes those points that have a negative slope less than -0.5. For correlation with breaking waves these points should be excluded. The mean square slope results shown here do not include the dropout points. The raw data had been edited by replacing the dropout values by the mean value of those points before and after the dropout group. The largest single group of dropouts occurs between 14 and 15 seconds. Here, a consecutive fourteen data points exceeded the threshold magnitude.

3.3 Wave Slope Spectra

3.3.1 Measured Frequency Spectra

The frequency spectra, shown in Figure 11, give the energy distribution of wave slopes at various frequencies. Both the upwind-downwind and

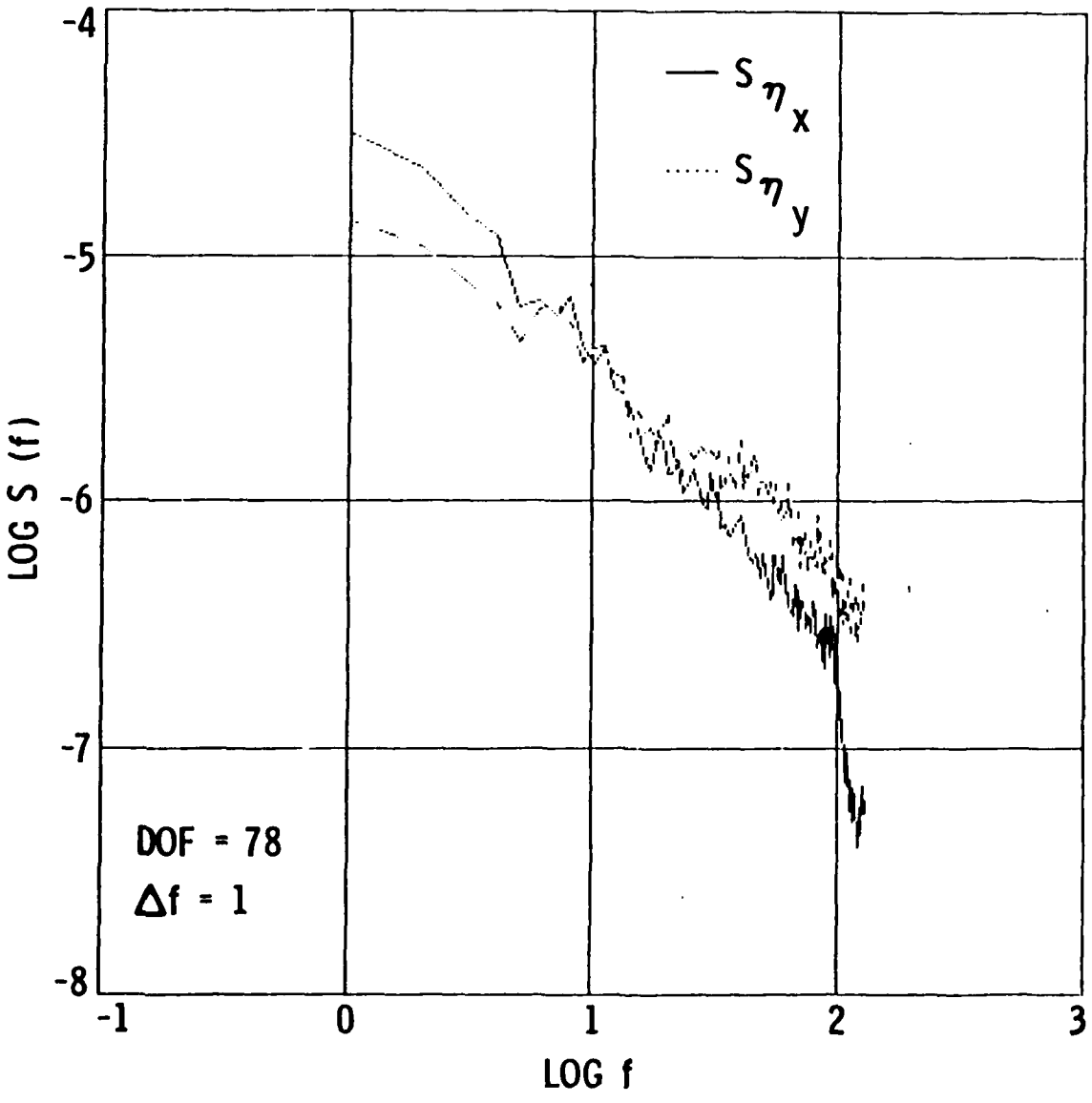

Figure 11. Wave Slope Frequency Spectra of Capillary Waves in Upwind-Downwind, and Cross-Wind Directions.

cross-wind slope spectra are included. The slopes of the spectra at the high frequency ends are both approximately -1.2. Similar to what was observed from the probability distribution of waves (Section 3.1) at low frequency, the spectral energy level in the upwind-downwind direction is much higher than in the cross-wind direction. The two curves gradually merge together at a frequency close to 10 Hz. There is a sudden step up of energy level in the cross-wind component at 23 Hz. A plateau is formed which extends to 43 Hz. Beyond this frequency the spectrums follows a -1.2 slope again. The region of the plateau and the elevated energy level in the cross-wind signal cannot be properly explained at the present time.

The frequency spectra computed from one-second data segments are shown in Figure 12 in relation to phase location along the long waves. Different shapes are observed at various phase locations along the long wave profile. Similar to the distribution of mean square slopes, such variation demonstrates the modulation of short waves by the long waves. Inspection of each individual spectrum indicates that near the trough regions, the upwind-downwind spectral slopes are generally smaller (flatter), with slopes ranging from -0.6 to -0.2, compared to other regions. The combination of the low mean square slope and a broad spectrum at the trough region implies strong interaction between wave-induced current and the short waves.

3.3.2 Conversion to Wave Number Spectra

For the SAR imaging and radar backscatter applications, wave number (versus wave frequency) spectra are more useful. Conversion of wave information either from time domain to space domain (Evans and Shemdin, 1980), or from frequency domain to wave number domain (Hughes, 1978; Atakturk, 1984) is not a simple task. After reviewing the various methods reported, the method employed by Hughes is adopted for this study. The method was discussed in detail in his paper of 1978. Briefly, the spectral energy at a particular frequency $G(\sigma)\, d\sigma$ has its contributions from all wave numbers and wave directions that satisfy the Doppler shifted dispersion relationship.

$$\sigma = \sigma_0 + \underline{u} \cdot \underline{k} \,, \tag{5}$$

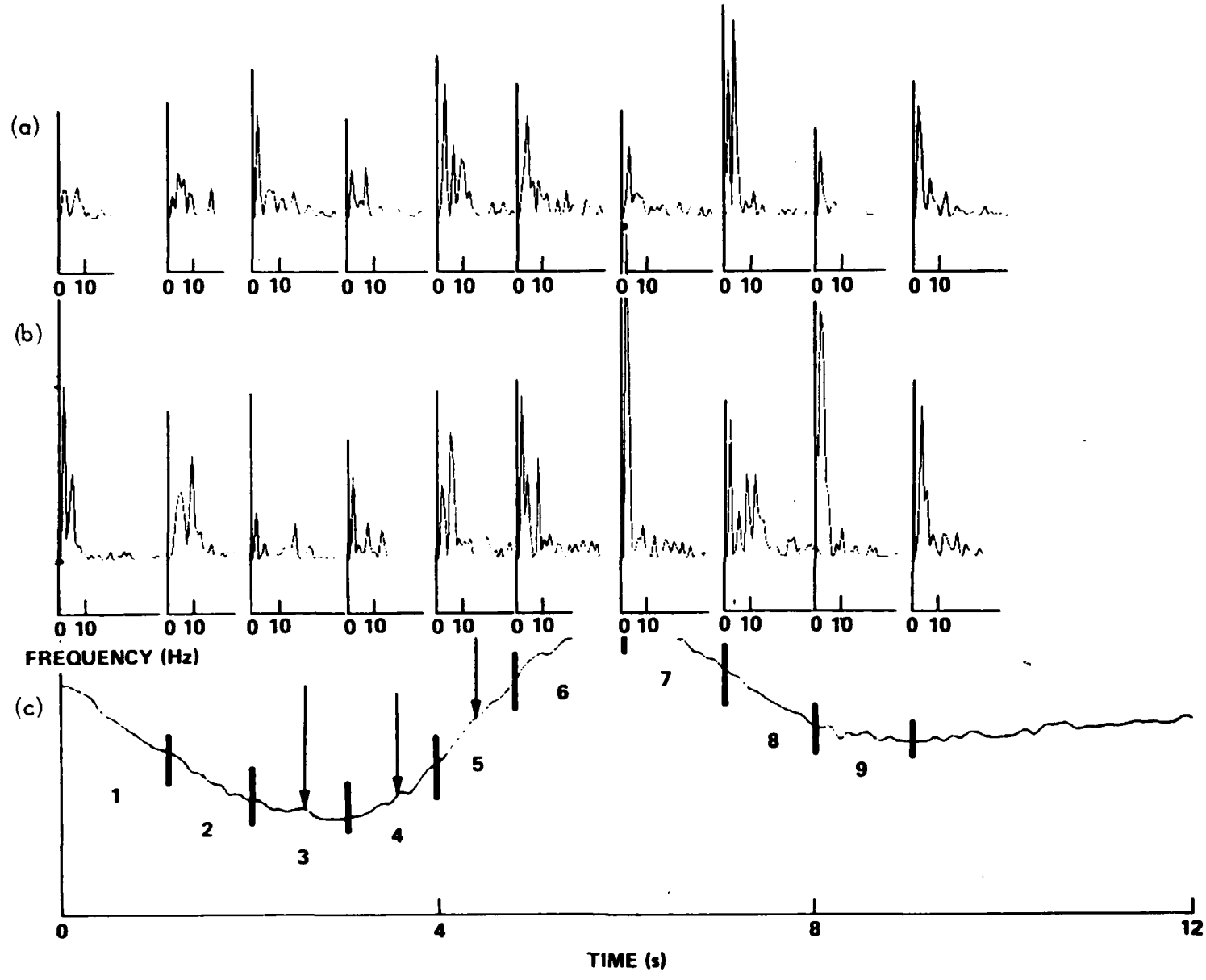

Figure12. Modulation of Frequency Spectra Along The Long Wave, (a) Slope Spectra of Cross-Wind Component, (b) Slope Spectra of Upwind-Downwind Component, (c) The Long Wave Profile.

and can be written as

$$G(\sigma)\, d\sigma = \iint_k F(k)D(\theta)\, B(k,\theta)\, \delta(\sigma, k, \underline{u}, \theta)\, d\theta dk \,, \tag{6}$$

where σ is the encounter frequency of the short waves, σ_0 is the intrinsic frequency, explicitly expressed as

$$\sigma^2 = gk + \tau k^3 \,, \tag{7}$$

$\underline{k}$ is the wave number vector with magnitude k and direction θ, $\underline{u}$ is the current vector with magnitude u and direction α, $F(k)D(\theta)$ is the wave number spectrum with k and θ dependence assumed separable, $B(k,\theta)$ the weighting function, its form depends on the type of signal analyzed. More explicitly

$$B(k,\theta) = \begin{cases} 1 & \text{for wave height spectrum } (S_\eta) \\ k^2\cos^2\theta & \text{for upwwind/downwind slope spectrum } (S_{\eta_x}) \\ k^2\sin^2\theta & \text{for cross-wind slope spectrum } (S_{\eta_y}) \\ k\cos\theta & \text{for height, upwind-downwind and cross-spectrum } (S_{\eta\eta_x}) \\ k\sin\theta & \text{for height and cross-wind cross-spectrum } (S_{\eta\eta_y}), \end{cases}$$

$\delta(\sigma, k, \underline{u}, \theta)$ is the delta function such that when k satisfies the dispersion relation (Equation 5), the value is 1, otherwise it is 0; g is the gravitational acceleration; and τ the surface tension of water.

Equation 6 can be written in matrix form

$$\underline{g} = \underline{\underline{A}}\, \underline{f} \,, \tag{8}$$

where $\underline{g}$ is the vector of which the elements are frequency spectral density $G(\sigma)$, $\underline{f}$ the corresponding wave number spectral density $F(k_j)$, matrix $\underline{\underline{A}}$ connects $\underline{g}$ and $\underline{f}$ and with elements a_{ij} expressed as

$$a_{ij} = \sum_{(k,\theta)_j} D(\theta_j)\, B(k_j,\theta_j)\, k_j\, \Delta\theta_j \left|\frac{\partial k}{\partial \sigma}\right|_{ij} \,, \tag{9}$$

where the $(k,\theta)_j$ pairs are those that satisfy dispersion relation for a particular frequency σ, and current $\underline{u}$. Note that in Equation 9, the absolute value of $\partial k/\partial\sigma$ was used since $d\sigma$ on the left-hand side of Equation 6 is the frequency "width" such that $G(\sigma)\, d\sigma$ is the spectral energy at frequency σ, and $kd\theta dk$ is the integration "area" such that the expression on the right-hand side of Equation 6 denotes partitioning of $G(\sigma)\, d\sigma$ in different wave numbers. Both the "width" and "area" need to be positive.

The algorithm developed was tested with a hypothetical spectrum and found to be satisfactory (details in the Appendix). In application to the measured data, the frequency spectra calculated from one-second records (Figure 12) were substituted for $\underline{g}$ vector in Equation 8, the matrix $\underline{\underline{A}}$ was readily constructed with a given directional distribution of the form

$$D(\theta) = \cos^{P}\theta \qquad \theta_1 < \theta < \theta_2 \,. \tag{10}$$

In the following presentation, $p = 2$, $\theta_1 = -\pi/2$, $\theta_2 = \pi/2$. The necessity of prescribing $D(\theta)$ is believed not to be a serious handicap since the measurements of η_x and η_y provides partial information of wave directional distribution. Possible forms of $D(\theta)$ were suggested by Hughes (1978) and Phillips (1985) among others. In the TOWARD Experiment, stereo-photo pairs were taken at different phase locations along the long wave. The stereo-photos are currently being analyzed. The results will clarify much of the uncertainties on the directional distribution of short waves. The inversion scheme developed is flexible and can accommodate any form of $D(\theta)$. For a preliminary computation Figure 13 presents the results of spectral conversion from frequency to wave number. The wave number spectra (of wave height) $F(k)$ showed more similarity in spectral shape along the long wave profile compared to its frequency counterpart. The 39 consecutive wave number spectra (only 21 presented in Figure 13) all can be fitted to form k^{-4}, with the exception of 1, 2, 10, 11, 19, and 20. The wave number spectra that deviate from k^{-4} occur exclusively in the trough regions of long waves and appear to have low mean square slopes. For some wave troughs (segments 10, 11 and 19, 20) the wave number spectra still have the k^{-4} shape at the short wave range, but the energy contents of the longer waves are considerably less. The fact that nearly all the wave number spectra are

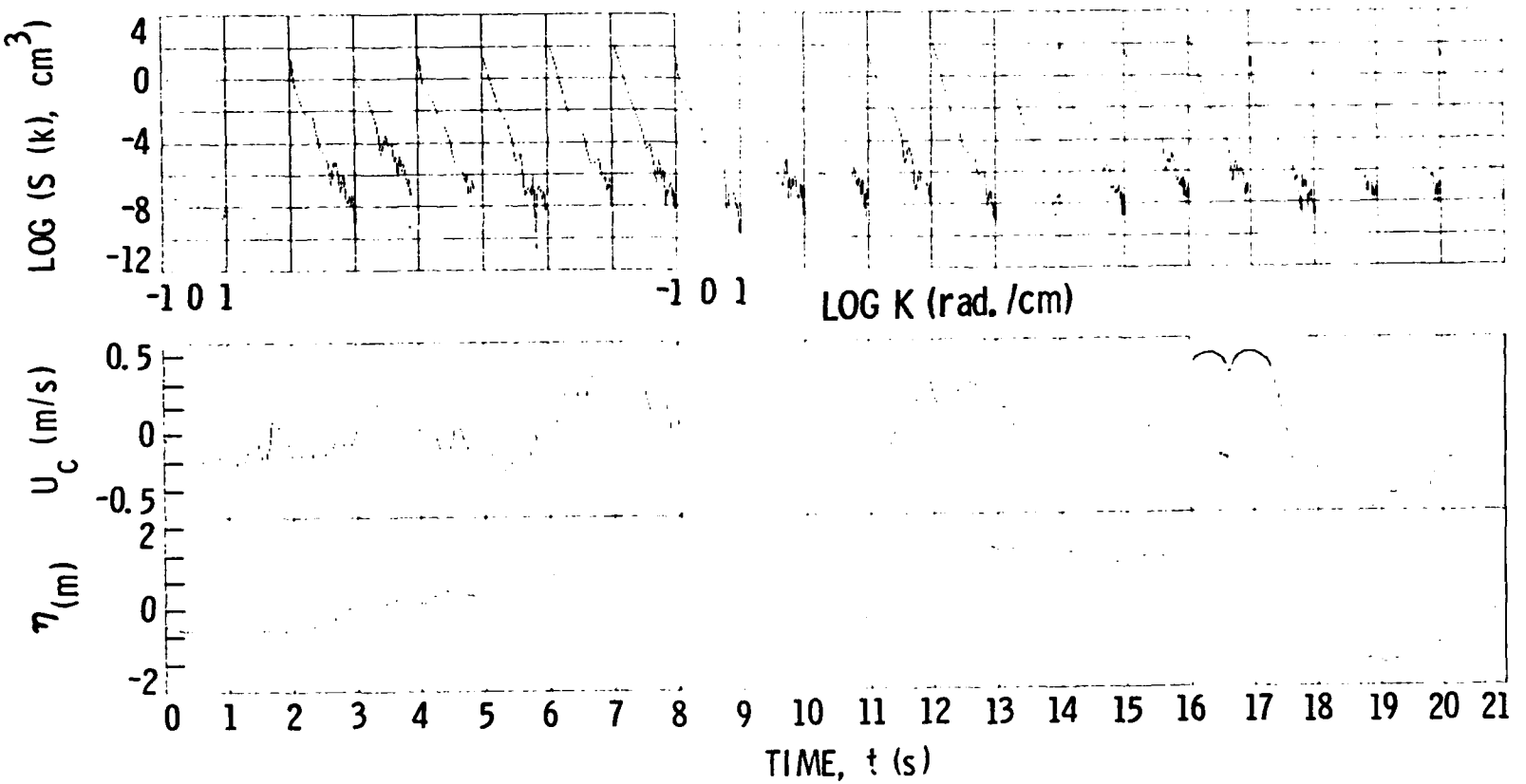

Figure 13. An Example of the Converted Wave Number Spectra Along the Profile of Long Waves.
Upper Curve - The Wave Number Spectra Are Calculated from One Second Wave Records,
Middle Line - The Measured Near Surface Current in the Long Wave Direction,
Lower Curve - The Measured Surface Displacement of Long Waves.

saturated or super-saturated seems to imply that short waves have small relaxation times. This is in agreement with the laboratory studies of Wu (1979) on decay and regeneration of ripples.

The wave number spectra converted from the cross-wind slope are less uniform, but still show consistent agreements with those obtained from the upwind-downwind slopes. The averaged wave number spectrum over the entire profile of long waves also shows the k^{-4} dependence, as shown in Figure 14.

4. DISCUSSION OF RESULTS AND CONCLUSIONS

In this report, we have presented the analysis of short wave modulation by long waves based on the two-dimensional wave slope measurements conducted in the TOWARD Experiment. At the time the present record was acquired (10-31-84, 1300 Pacific Time), the wind speed was 3.5 m/s, from direction 280°. The swell recorded had a period in the range 8 to 10 seconds and a significant wave height of 1.2 m. The swell direction was from direction 290°. During this period the wave follower performed exceptionally well. Based on this criterion of data dropout ($\tan\theta \geq 0.5$), the data quality in the upwind-downwind direction is considered excellent (with dropout rate of 0.47%. The cross-wind slope data quality is considered good (3.49% dropout rate). The accuracy of the slope measurements was ±0.5° at small slopes and ±13% of steepness near 30° (Figure 4).

The results from this analysis shows that:

(a) The probability distribution of the upwind-downwind slope is skewed. Tne most probable surface slope is approximately 0.7 degrees. Although the distribution is bell shaped, is is much narrower than Gaussian with a flatness factor of 10.94. The PDF of cross-wind slope is more symmetric and narrower (see Table III). When frequency filters are applied, it is obvious that the skewness comes from the low frequency components while peakness comes from the high frequency components. Furthermore, the large steepness is derived exclusively from waves with frequencies higher than 7.5 Hz. Slopes of waves below 7.5 Hz seldom exceed 7°. The ratio of $\overline{\eta_x^2} / \overline{\eta_y^2}$ for the unfiltered signals is close to 1, but differs considerably in the different frequency regions. The range is from 2.17 at low frequencies ($\leq$2.5 Hz), 1.29 at mid-range (2.5 - 7.5 Hz)

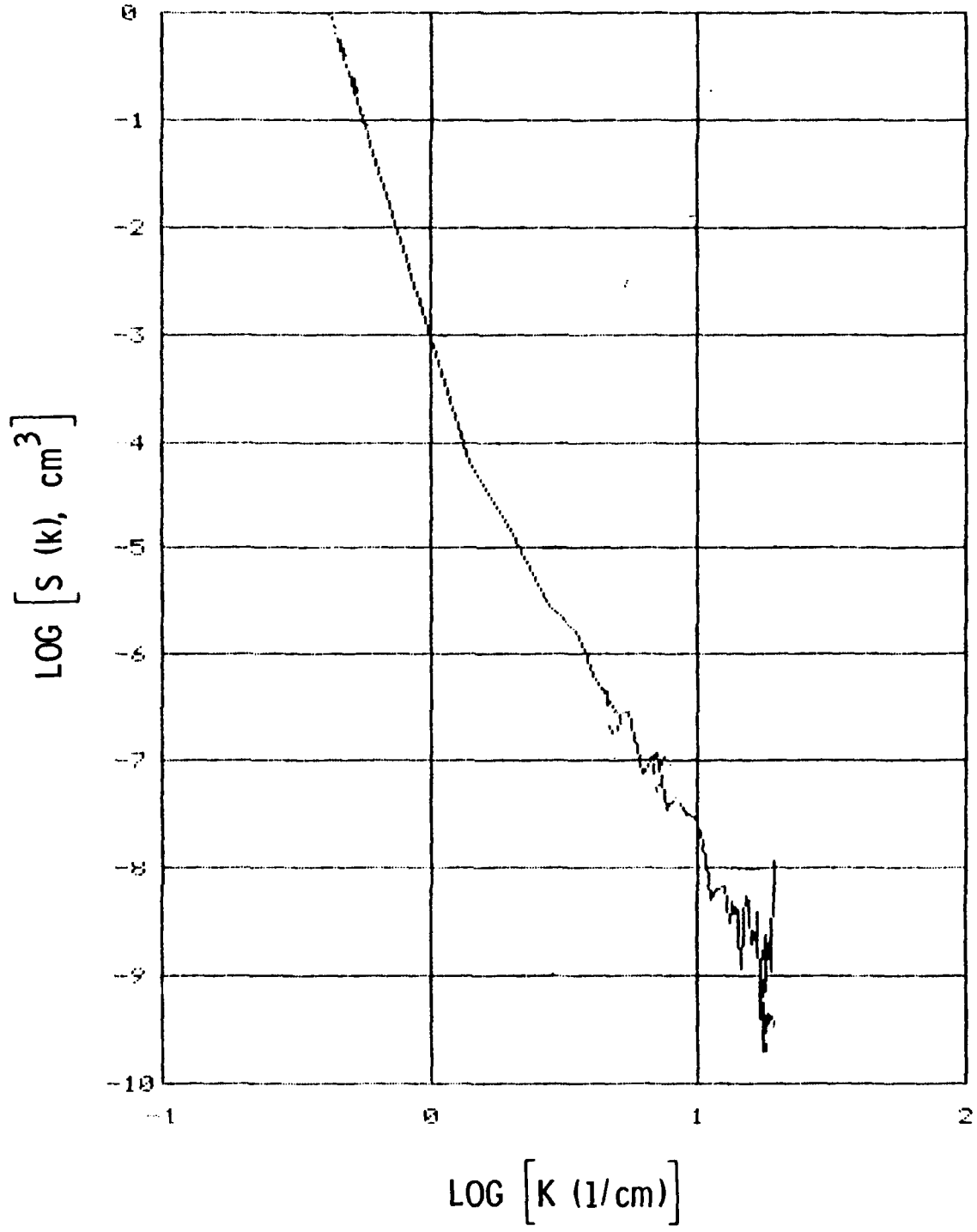

Figure 14. The Phase Averaged Wave Number Spectrum of 39 Segments (Each of One Second Data Length) for the Upwind-Downwind Component of Wave Slope Measurement.

and 0,65 at high frequency range (< 7.5 Hz). The PDF distribution is closest to Gaussian at low frequency, and most symmetric in mid range. The similarity of the normalized PDF of the two slope components at mid-range (wave lengths from X-band to L-band) is illuminating (Figure 8c).

(b) The frequency spectra averaged along the long wave profile display the form $f^{-1.2}$ in both upwind-downwind and cross-wind directions (Figure 10). This implies a close to saturation condition even at 3.5 m/s wind speed condition. Similarly, the averaged wave number spectra show the form k^{-4} (Figure 13).

(c) Strong modulation of short waves by long waves (Figure 9). The magnitude of modulation is nearly 100 times of the long wave slope.

(d) The frequency spectra are not only subject to the amplitude modulation similar to the mean square slopes, but also show significant variation in the spectral slopes or equivalently the spectral band width. The spectra are considerably broader over the trough regions where the wave induced orbital velocity is in the direction opposite to wind direction. The broadening of spectra in an adverse current region implies active interaction between the wave induced current and the short waves.

(e) The observation in (d) are also seen in the converted wave number spectra along the long wave profile. While at most phase locations along the long waves profile a k^{-4} relationship is observed, deviations from such a form is observed in the trough regions. The appearance of a saturated or supersaturated spectrum suggests that fast regeneration of modulated short waves is effected by wind.

The results discussed are based on a relatively short record (39 seconds). Subsequent computations on longer time series did not change the above observations, except in minor details. In the continuing data analysis, we expect to develop schemes for ensemble averaging for better statistical representation, and also to include various environmental conditions.

There is no doubt that more information can be extracted from the wave-follower data sets acquired in the TOWARD Experiment.

ACKNOWLEDGEMENT

We gratefully acknowledge the support from the Coastal Science Branch, the Office of Naval Research for this element of the TOWARD Experiment. Supports from the Instrumentation Group, Jet Propulsion Laboratory was critical to the success of the wave follower experiment. The efforts of Bob Martin, Don Hoff, Carl Thiel, John Stocker, and Doug Clark are much appreciated. Critical suggestions were given by members of the TOWARD Hydrodynamic Committee. Dr. Steven Borchardt, Professors M. S. Longuet-Higgins, B. A. Hughes, O. M. Phillips, and Jin Wu provided valuable guidelines for the analysis of these data sets.

REFERENCES

Atakturk, S.S., "Intrinsic Frequency Spectra of Small Scale Wave Amplitude Measured in a Lake," Master's Thesis, Dept. Atmosph. Sciences, Univ. of Washington, Seattle, Wash., 1984.

Cox, C. and W. Munk, "Statistics of Sea Surface Derived from Sun Glitter," J. Marine Research, 13, 198-227, 1954.

Evans, D.D. and O.H. Shemdin, "An Investigation of Modulation of Capillary and Short Gravity Waves in the Open Ocean," J. Geophys. Res., 85, 5019-5024, 1980.

Hughes, B.A., "The Effect of Internal Waves On Surface Wind Waves 2. Theoretical Analysis," J. Geophys. Res., 83, 455-465, 1978.

Longuet-Higgins, M.S., "A Nonlinear Mechanism for the Generation of Sea Waves," Proc. Roy. Soc., A. 311, 371-389, 1969.

Longuet-Higgins, M.S. and R.W. Stewart, "Changes in the Form of Short Gravity Waves on Long Waves and Tidal Currents," J. Fluid Mec., 8, 565-583, 1960.

Phillips, O.M., "The Dynamics of the Upper Ocean, 2nd ed., Cambridge Univ. Press, 1977.

-----, "The Dispersion of Short Wavelets in the Presence of a Dominant Long Wave," J. Fluid Mech., 107, 465-485, 1981.

-----, "Spectral and Statistical Properties of the Equilibrium Range in Wind-Generated Gravity Waves," J. Fluid Mech., 156, 505-531, 1985.

Shemdin, O.H., "Measurement of Wind and Surface Wave Slopes with a Wave Follower," Jet Propulsion Laboratory Report No. 715-123, 1980.

Shemdin. O.H. and Hoff, D., "A Wave Following Instrumentation System for Studying Processes Near the Air-Water Interface," Technical Report - In Preparation, 1986.

Wu, Jin, "Slope and Curvature Distributions of Wind-Generated Water Surface," J. Opt. Soc. Am., 61, 852-858, 1971.

-----, "Effects of Pulsating Wind on Velocity Profiles and Microstructure," J. Phys. Oceanogr., 5, 782-789, 1975.

-----, "Distribution and Steepness of Ripples on Carrier Waves," J. Phys. Oceanogr., 9, 1014-1021, 1979.

-----, "Temporal Rates of Growth and Decay of Microscopic and Macroscopic Surface Structures in a Wind-Wave Tank," J. Phys. Oceanogr., 9, 802-814, 1979.

APPENDIX - CONVERSION OF FREQUENCY TO WAVE NUMBER SPECTRA

The scheme for the spectral conversion from frequency to wave number domain described in the paper was tested using a hypothetical k^{-4} spectrum.

The frequency spectra for different current velocities were calculated directly from Equation 6 with $D(\theta) = \cos^2\theta$. Two ranges of θ, $\pm \pi/4$ and $\pm \pi/2$, were used, but no significant difference was found. The results presented in the following is for $-\pi/4 < \theta < \pi/4$.

The treatment of the dispersion relationship (Equations 5 and 7) is slightly different from that of Hughes (1979). In the original design, Hughes, based on the symmetricity of spectrum, chose to replace on the left hand side with $\pm \sigma$, and adopted both roots of the right hand expression in Equation 7 (here, surface tension is set to 0). This approach makes no difference if $u \geq 0$, since the two roots are symmetric with respect to the vertical axis. However, the RHS of Equation 5 does have two roots of k, the larger one turns out to be one of the three roots for the negative current case (Figure A-1). If mistakenly chosen, the results of conversion can be very different. We reasoned that since σ contains the information of the direction of wave propagation, in whatever coordinate system chosen, if σ is for the forward propagating waves, $-\sigma$ is for the backward propagating counterpart. For a reasonable wind condition, the major propagation direction of short waves should be obvious. Putting equal weights on $+\sigma$ and $-\sigma$ implies equal waves travel in either direction, which is against our concept of wind wave generation. The minus sign was therefore eliminated, and the directional information was left to θ.

One more complication for the reverse current case ($u < 0$) should be mentioned. As shown in Figure A-1, there are regions (in frequency) with multiple roots of wave numbers. Translated into the matrix equation, this means that for the region of monotonic k-σ relation, the submatrix is square, but for multiple roots region, the submatrix is not. Augmentation of this rectangular submatrix is necessary to enable matrix inversion. This can be done if more measurements are available. For example, η_x and η_y measurements provide three independent set of spectra: S_{η_x}, S_{η_y}, and $S_{\eta_x \eta_y}$ and

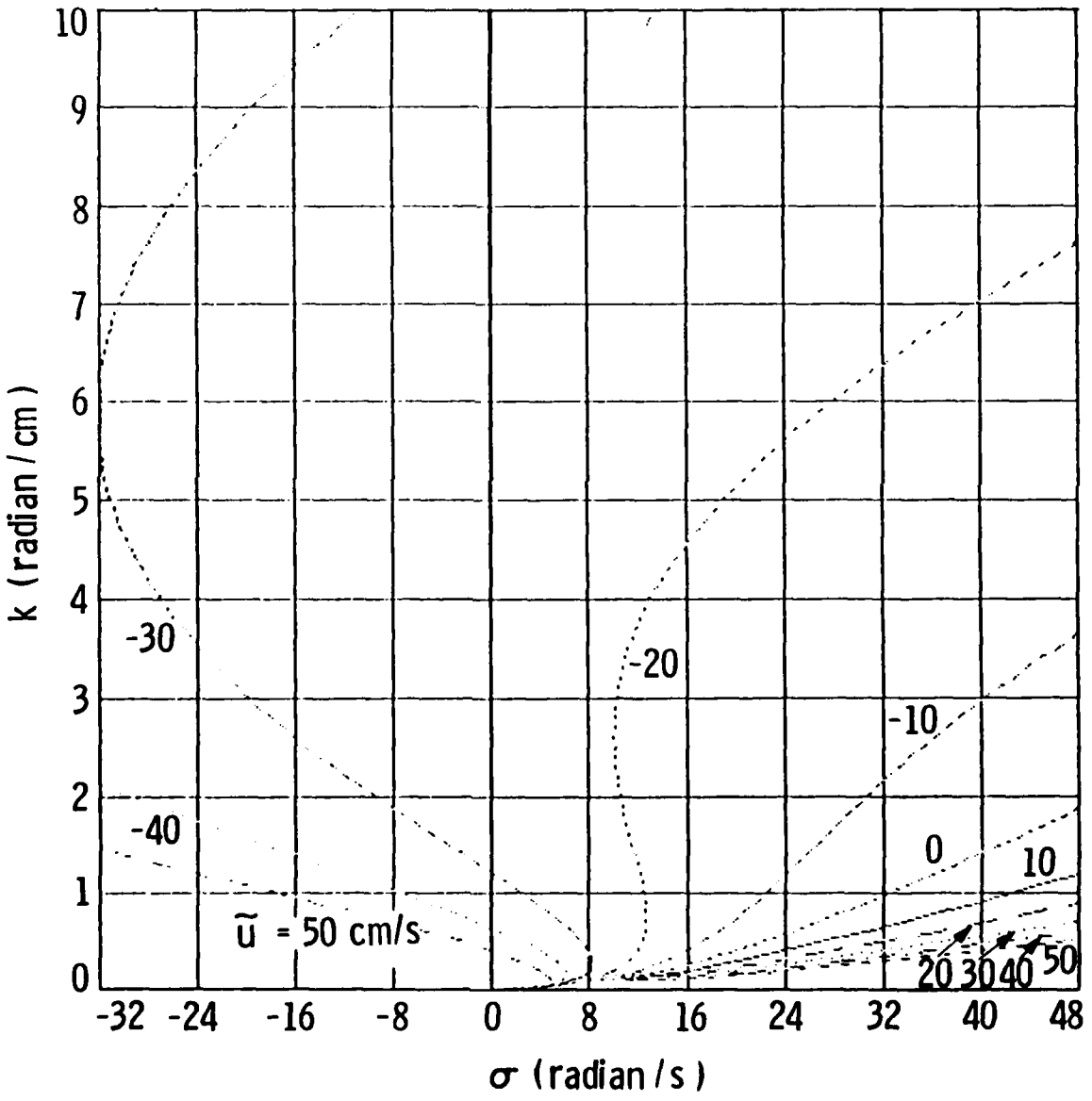

Figure A1. Dispersion Relationship with the Surface Tension Term Included; U is Current.

can supply enough equations for as many as three roots in the dispersion curves. If high frequency wave height measurement is also available, two more independent spectra, $S_{\eta\eta_x}$, $S_{\eta\eta_y}$ can be added. (S_η, S_{η_x}, and S_{η_y} are linearly dependent when wind and current are in the same direction, since then ($S_{\eta_x} + S_{\eta_y} = k^2 S_\eta$). An alternative to the matrix augmentation is to select a representative wave number for each multi-root frequency (this can be a weighted wave number since the weighting function B in Equation 9 gives the information of the relative contribution of each root to the total spectral energy) and still maintain a square matrix $\underline{\underline{A}}$. The alternative method is useful when not enough measurements were available or the data quality of various measurements are much different, and propagation of error into the high wave number region is not desired. The latter method was used in the field data conversion presented in the text. The following shows the conversion of the hypothetical spectrum using matrix augmentation.

Figures A-2 to A-5 show the pairs of spectra for u = 0, 40, -60 and -100 cm/s. In each figure, the left hand side (plot a) are the frequency spectra directly calculated, the right hand side (plot b) is the inverted wave number spectra. The recoverage of k^{-4} spectra is readily seen.

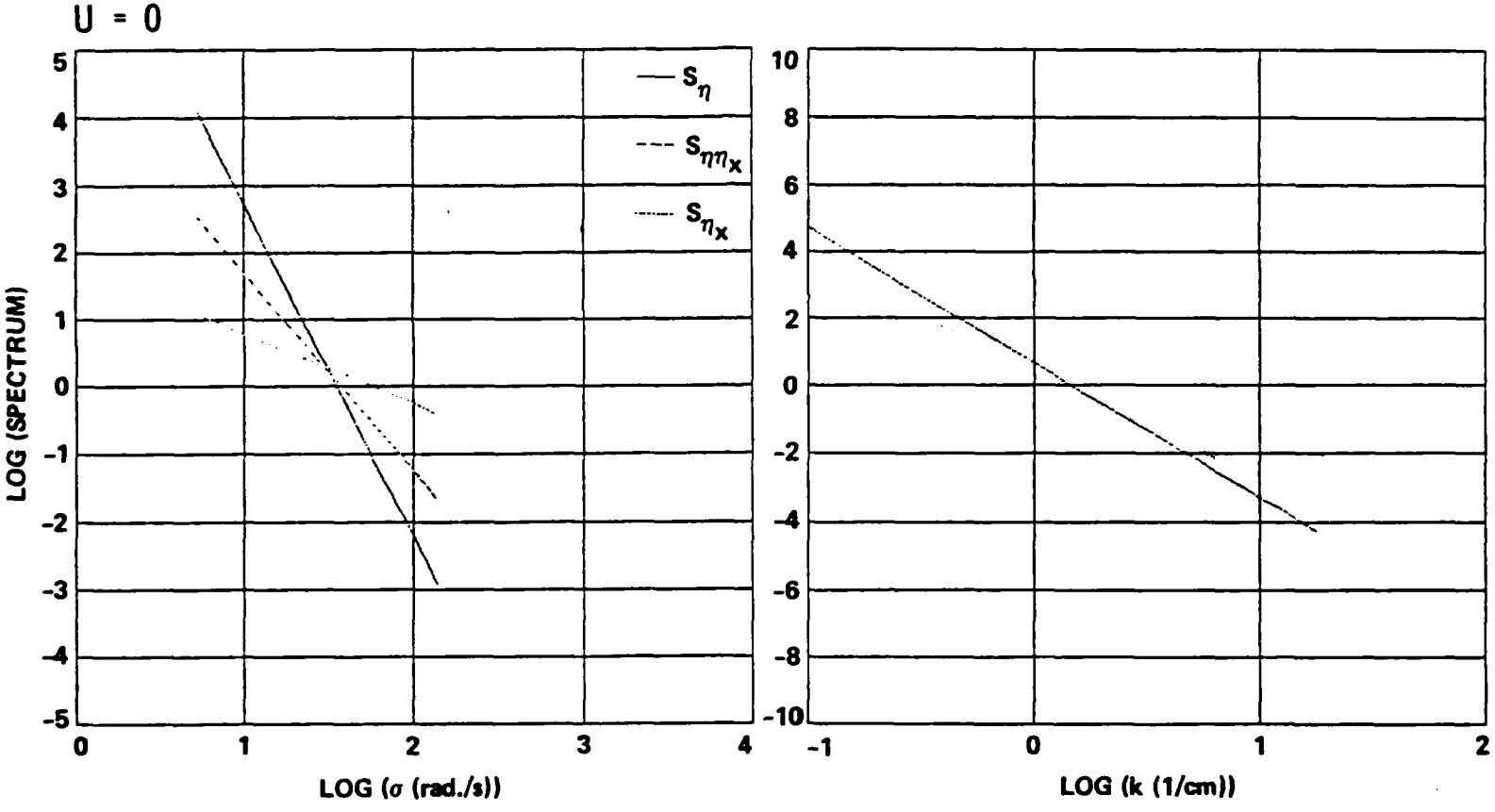

Figure A2. Conversion of Frequency Spectra (Left) to Wave Number Spectra (Right). U is Current Magnitude.

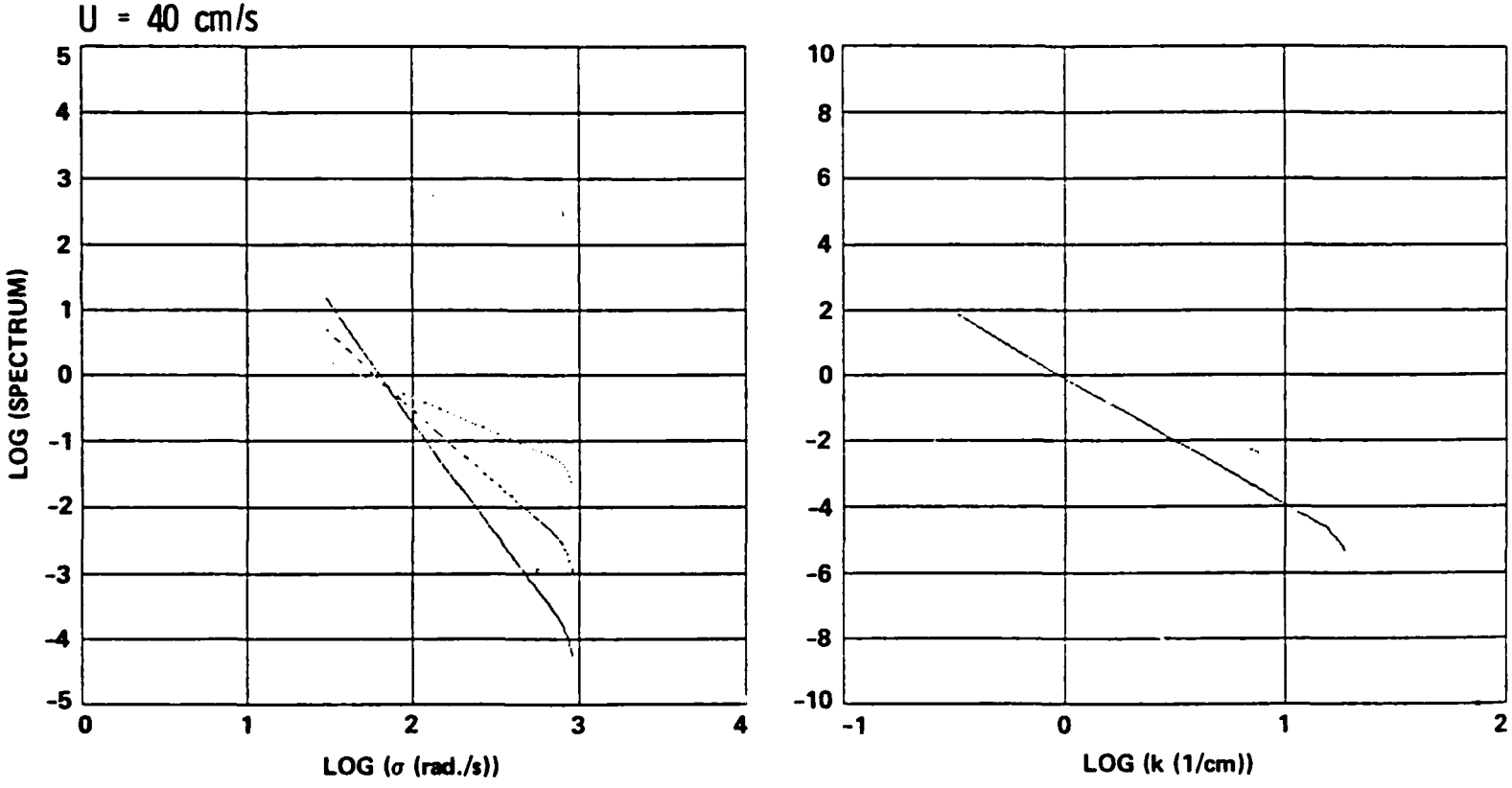

Figure A3. Converion of Wave Frequency Spectrum (Left) to Wave Number Spectra (Right). U is Current Magnitude.

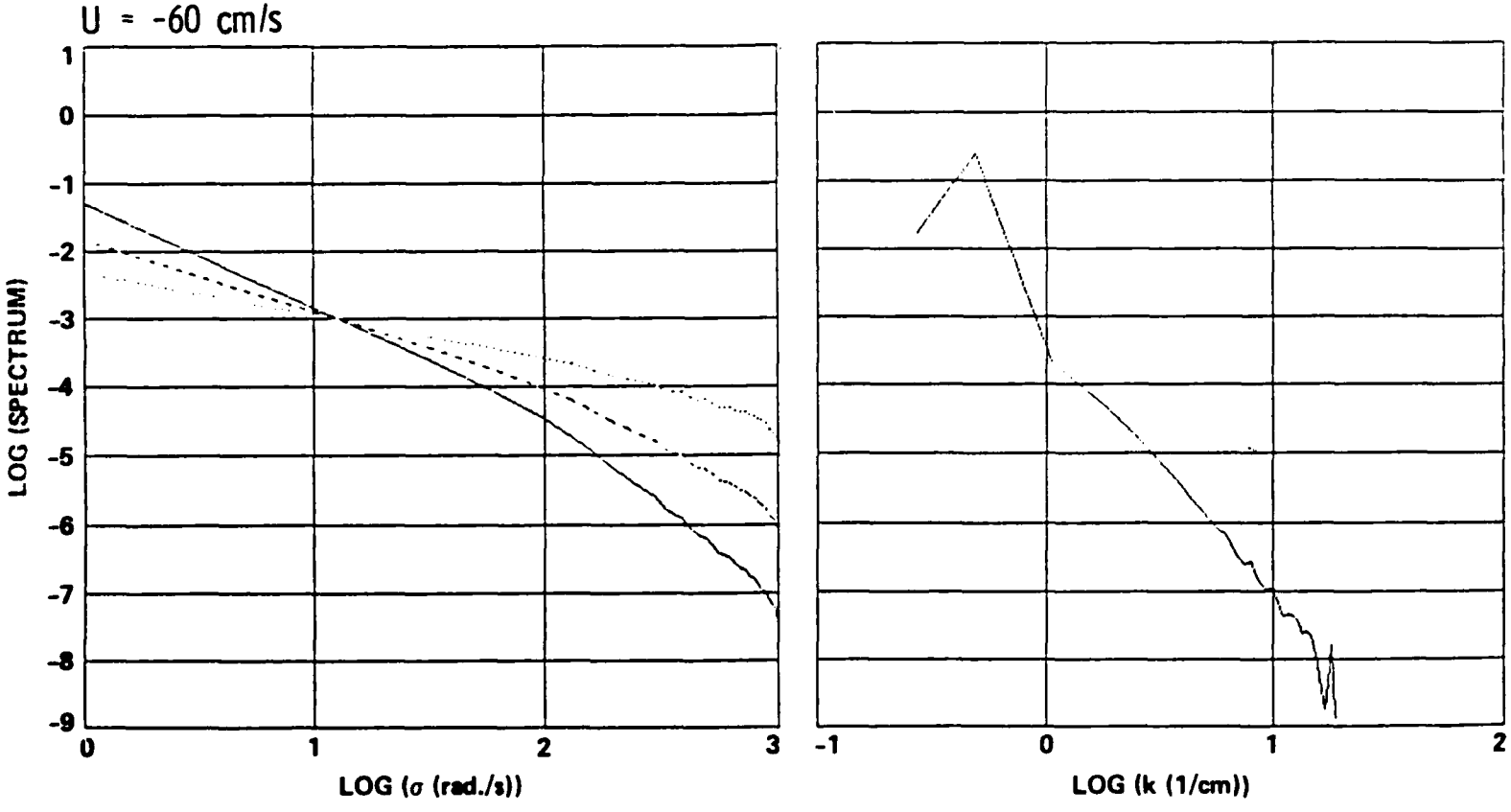

Figure A4. Conversion of wave Frequency Spectra (Left) to Wave Number Spectra (Right). U is Current Magnitude.

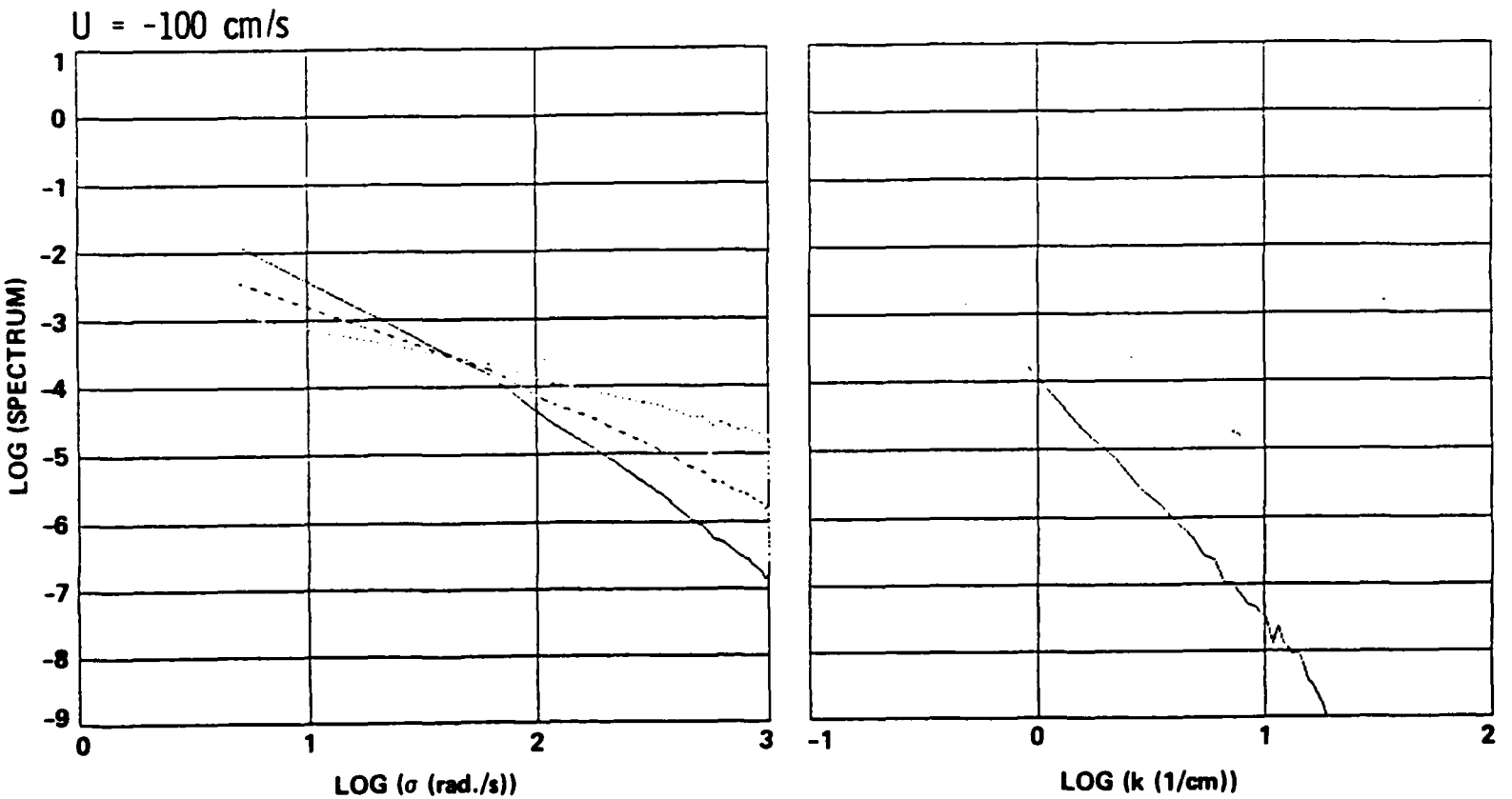

Figure A5. Conversion of Wave Frequency Spectra (Left) to Wave Number Spectra (Right). U is Current Magnitude.

APPENDIX IV

The propagation of short surface waves on longer gravity waves

Michael S. Longuet-Higgins, Department of Applied Mathmatics and Theoretical Physics, Silver Street, Cambridge, England and Institute of Oceanographic Sciences, Wormley, Surrey.

Abstract

This report summarizes some theoretical calculations carried out on behalf of the TOWARD program between October 1984 and September 1985. The purpose was to determine the theoretical variations in the wavelength and steepness of short gravity waves propagated over the surface of a train of longer gravity waves of finite amplitutde. Such variations may be calculated once the orbital accelerations and surface velocities in the longer waves have been accurately determined - a nontrivial computational task.

The results show that the linearised theory used previously for the longer waves is generally inadequate. The fully nonlinear theory used here indicates that for longer waves having a steepness parameter $\Lambda K = 0.4$, for example, the short wave steepness can be increased at the crests of the longer waves by a factor of order 8, compared with its value at the mean level. (linear theory gives a factor less than 2).

The calculations so far reported are for free, irrotational gravity waves travelling in the same or directly opposite sense to the longer waves. However, the method of calculation could be extended without essential difficulty so as to include effects of surface tension, energy dissipation due to short-wave breaking, surface wind-drift currents, and to arbitrary angles of wave propagation.

1. Introduction

An important component of radar backscatter from the sea surface arises from the Bragg scattering. This involves surface wavelengths of the order of a few centimetres for X-band radars, or tens of centimeters for L-band. In both cases the wavelengths are usually small compared to the dominant wavelengths of ocean surface waves (10 to 10^3 m). So it becomes an important question to study how the short wave energy is distributed with respect to the phase of the longer waves

In the present study we shall consider the classical model of a short train of gravity waves, of small but variable steepness ak, propagated over the surface of a longer train of gravity waves of finite steepness AK, as in Figure 1. Early workers (Longuet-Higgins and Stewart, 1960) assumed that $AK \ll 1$, and in that case it was found that the variation in the wavenumber k and amplitude a of the short waves was given by

$$\left.\begin{aligned} k/\bar{k} &= 1 + AK\cos\psi + C(AK)^2 \\ a/\bar{a} &= 1 + AK\cos\psi + O(AK)^2 \end{aligned}\right\} \quad (1.1)$$

where $\bar{k}$ and $\bar{a}$ are the (constant) values of k and a at the mean surface level and $\psi = K(x - Ct)$ is the phase of the long waves. This gives

$$ak/\bar{a}\bar{k} = 1 + 2AK\cos\psi + O(AK)^2, \quad (1.2)$$

AD-A171 038 'TOWARD 84/86' FIELD EXPERIMENT: INVESTIGATION OF PHYSICS OF SYNTHETIC AP (U) JET PROPULSION LAB PASADENA CA O H SHEMDIN MAY 86 2/3

UNCLASSIFIED F/G 17/9 NL

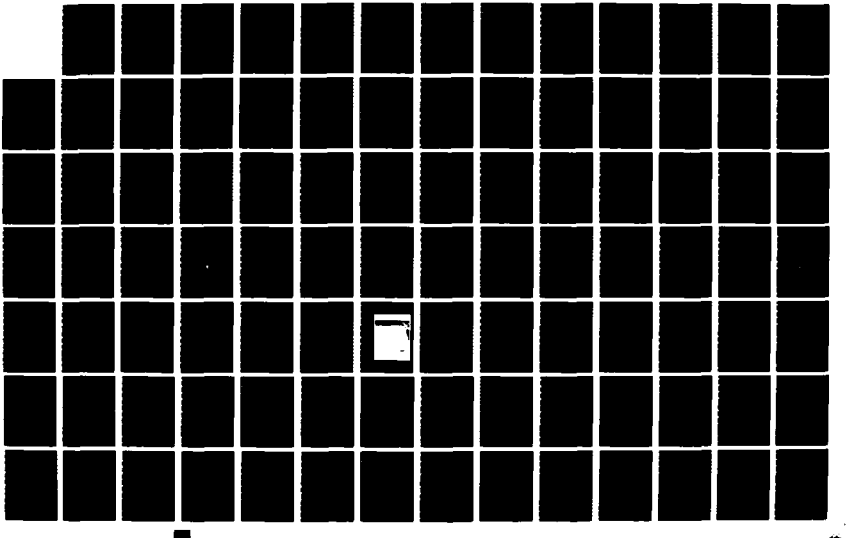

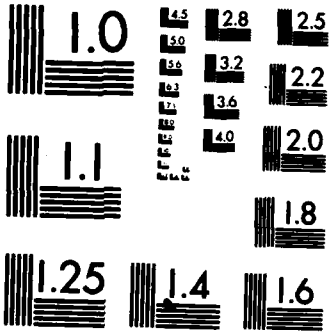

showing that the short waves are both shorter and steeper on the crests of the longer waves ($\psi = 2n\pi$). However, since $Ak \leq (Ak)_{max} = 0.443$ the maximum steepening predicted is less than 2.

Longuet-Higgins and Stewart (1960) interpreted this result by assuming (1) that the phase of the short waves was conserved, i.e. that

$$kq - \sigma = \text{constant} \tag{1.3}$$

where q is the particle speed in the long waves as seen by an observer travelling with the long-wave speed C, and σ is the intrinsic frequency of the short waves in a frame moving with speed q. Next, (2) that the intrinsic frequency σ and local wavenumber k of the short waves were related by

$$\sigma^2 = g' k \tag{1.4}$$

where g' was the effective value of gravity for the short waves i.e.

$$g' = g + \partial W/\partial t \tag{1.5}$$

W being the vertical component of orbital velocity in the long waves; and (3) that the short-wave energy density E was given by

$$E = \tfrac{1}{4} g a^2 + \tfrac{1}{4} a^2 \sigma^2 / k , \tag{1.6}$$

representing the potential and kinetic energies respectively. The changes in shortwave energy E over the long wave could then be attributed to (a) advection by the long-wave orbital velocities,

together with (b) work done by the straining of the long waves against the radiation stress of the short waves.

Garrett (1967) suggested that the same results (1.1) could be interpreted in terms of the conservation of wave action

$$A = E'/\sigma \tag{1.7}$$

where

$$E' = \tfrac{1}{2} g' a^2 \tag{1.8}$$

is an alternative form of the short-wave energy density, and he introduced the equation

$$\frac{\partial A}{\partial t} - \frac{\partial}{\partial x}\left[(q - c_g)A\right] = 0 \tag{1.9}$$

where c_g is the group-velocity of the short waves $\left(c_g = \tfrac{1}{2} c\right)$.

Finally, Bretherton and Garrett (1968) proved the validity of equation (1.9) for a general class of situations where a group of linearized short waves of wavenumber k is propagated through a slowly - varying medium with local velocity q, under the general assumption that

$$|\nabla q| \ll k q, \qquad \left|\frac{\partial q}{\partial t}\right| \ll \sigma q, \tag{1.10}$$

the energy density E' being defined as if the medium were locally uniform.

The great advantage of this formulation is its relative simplicity, and that there is no explicit restriction on the steepness A/λ of the long waves; it appears necessary to assume only that

$$ak \ll 1, \qquad k \gg K. \tag{1.11}$$

In the case of AK finite, one would take as the effective (vector) gravity

$$g' = g - \alpha \tag{1.12}$$

where α is the orbital acceleration in the long wave.

This principle has been partly applied (in principle) by Phillips (1981) to calculate the variation in amplitude of short capillary-gravity waves riding on longer gravity waves. The calculation could not be carried through in detail because the effective gravity g' was not at that time known with sufficiant accuracy. However, the accurate calculation of accelerations in steep gravity waves has recently been carried out by Longuet-Higgins (1985), and from this it is possible to infer g' by (1.12), hence both the shortening and steepening of the short waves. In this contribution we apply the results to short gravity waves, in the first place, with application particularly to backscattering in L-band. One significant result is that for finite values of AK the short-wave steepening can actually be much greater than that given by linear theory. Moreover, it will be seen that the basic calculation of g' opens the way to the solution of much more realistic cases, including the effects of capillarity,short-wave energy dissipation, etc.

The assumptions (1.11) make clear that the principle of action conservation is only approximate. To test the principle in a simple case we study, in section 6 of the present paper, a simple model analogue in which the equations of motion can be integrated precisely by numerical methods. The degree to which the principle is satisfied is reassuring.

2. Formulation of the problem

Relatively short gravity waves, of local height $2a$ and wavelength $2\pi/k$, ride on longer, progressive gravity waves of finite height $2A$ and wavelength $2\pi/K$ in deep water, where $k \gg K$ (see Figure 1). It is required to find k and ω as functions of the phase of the long wave.

The intrinsic frequency σ and the wavenumber k of the short waves are assumed to be related by equation (1.4), where g' is the magnitude of the effective acceleration g' given by (1.12). Clearly g' is always normal to the surface of the longer waves. The frequency σ and the phase-speed

$$c = \sigma/k \tag{2.1}$$

are taken as positive or negative according as the short waves travel in the same or opposite direction to the long waves. q denotes the particle speed at the surface of the longer waves, as seen in a frame of reference moving with the long-wave phase speed C. In this reference frame the long waves appear steady and the free surface is a streamline. At the mean level $y = \bar{y}$, we have $q = C$; (see Lamb 1932, C.9).

To determine the wavenumber k at points along the surface of the long waves we assume that the phase of the short waves is conserved, that is

$$k(q - c) = \text{constant} = 1/\gamma \tag{2.2}$$

say. Hence

$$c^2 = g'/k = \gamma g'(q - c) \tag{2.3}$$

or

$$c^2 + \gamma g' c - \gamma g' q = 0, \tag{2.4}$$

a quadratic equation for C with solutions

$$c = -\beta \pm (\beta^2 + 2\beta q)^{1/2}, \qquad \beta = \tfrac{1}{2}\gamma g'. \tag{2.5}$$

Having found c we may calculate k from (2.3) in the form $k = g'/c^2$.

To determine the local wave amplitude a, we assume that action is conserved, that is equation (1.9). In the steady flow relative to the moving frame of reference this implies that the flux of wave action is a constant, i.e.

$$(q - c_g) E'/\sigma = \text{constant} \tag{2.6}$$

where c_g the group-velocity of the short waves $(= \tfrac{1}{2}c)$ and E' is the intrinsic energy-density of the short waves, given by equation (1.8). Since $\sigma = g'/c$, equation (2.8) can also be written

$$(q - \tfrac{1}{2}c)\, c\, a^2 = \text{constant} \tag{2.7}$$

or

$$a \propto [(q - \tfrac{1}{2}c)c]^{-1/2} \tag{2.8}$$

(c.f, Longuet-Higgins and Stewart 1961).

Finally, the local wave steepening is defined as

$$\mathcal{R} = a k / (\bar{a} \bar{k}) \tag{2.9}$$

where a bar denotes the values at the mean level $y = \bar{y}$.

Clearly the above approach depends critically on the accurate evaluation of the velocity q and the orbital acceleration $\underset{\sim}{\alpha}$ in a (long) gravity wave of finite amplitude.

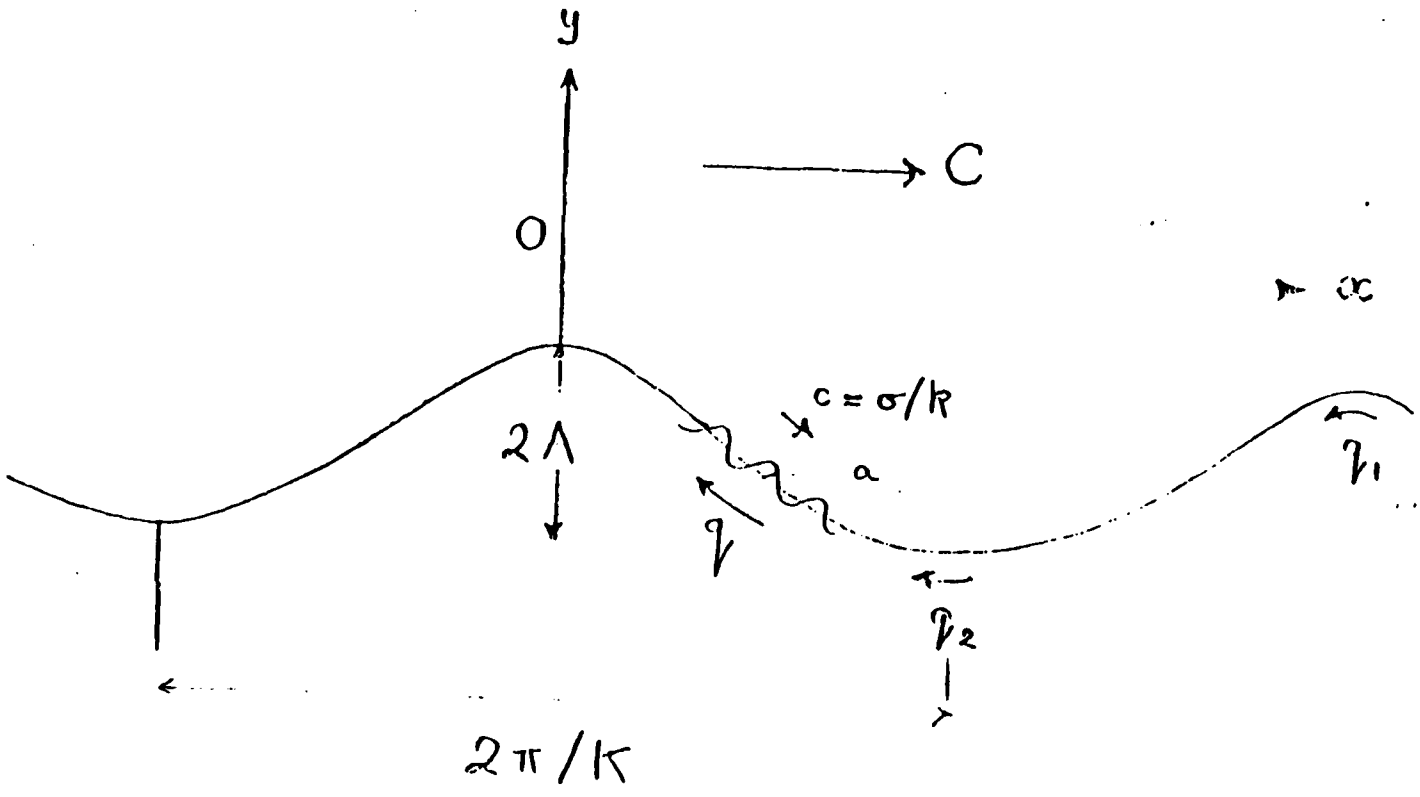

Figure 1. Definition sketch for short wave on long waves.

3. Method of Calculation

The real, or orbital acceleration in a surface wave must be carefully distinguished from the apparent accelerations as measured by a fixed vertical wave gauge (see Longuet-Higgins 1985c). The real accelerations, both vertical and horizontal, vary much more smoothly than the apparent accelerations, which can be very non-sinusoidal.

Numerical values of the real acceleration $\underset{\sim}{\alpha}$ were calculated by the method of Longuet-Higgins (1985a) which makes use of a set of quadratic relations between the Fourier coefficients a_n in Stokes's series for the cartesian coordinates (x,y) in terms of the velocity potential. Thus if $K=g=1$, the free surface is given by

$$\left.\begin{aligned} Ky &= a_0 + \sum_1^\infty a_n \cos(n\phi/c) \\ Kx &= \phi/c + \sum_1^\infty a_n \sin(n\phi/c) \end{aligned}\right\} \quad (3.1)$$

where ϕ is the velocity potential, then the coefficients $a_0, a_1, a_2, \ldots$ satisfy the relations

$$\left.\begin{aligned} a_0 b_0 + a_1 b_1 + a_2 b_2 + a_3 b_3 + \ldots &= -c^2 \\ a_1 b_0 + a_0 b_1 + a_1 b_2 + a_2 b_3 + \ldots &= 0 \\ a_2 b_0 + a_1 b_1 + a_0 b_2 + a_1 b_3 + \ldots &= 0 \\ \cdots\cdots & \end{aligned}\right\} \quad (3.2)$$

with $b_n = n a_n$, $n>0$ and $b_0 = 1$. These reations may be quickly and accurately solved for a given value of the phase-speed c (in general)

or of the wave amplitude

$$A = a_1 + a_3 + a_5 + \ldots . \tag{3.3}$$

The speed q at the free surface is then found from the Bernoulli relation

$$q^2 = 2y \tag{3.4}$$

and the vector acceleration $\underset{\sim}{\alpha}$ from the general relation

$$\underset{\sim}{\alpha} = \chi_z \chi_{zz}^* = -q^6 z_\chi^2 z_\chi^* \tag{3.5}$$

where $z = x + iy$ and $\chi = \phi + i\psi$, ψ the stream stream function. (A star denotes the complex conjugate). In real terms this is

$$\underset{\sim}{\alpha} = -q^6 (x_\phi + iy_\phi)^2 (x_{\phi\phi} - iy_{\phi\phi}). \tag{3.6}$$

The effective gravity g' is then found from (2.2).

Because of the slow initial rate of convergence of the series (3.1) at high values of Ak, care must be taken to include enough terms in these series. A recent study (Longuet-Higgins 1985b) has shown that after an initial rate of convergence like $n^{-5/3}$, a_n ultimately converges exponentially, the transition to exponential behaviour occurs when $n = n_c = O(\epsilon^{-3})$, where

$$\epsilon^2 = 2.0 \left| Ak - (Ak)_{max} \right| . \tag{3.7}$$

Since individual terms in the differentiated series for $x_{\phi\phi}$ and $y_{\phi\phi}$ at first increase like $n^{1/3}$, it is important, in order to ensure sufficient accuracy in the calculation, to include terms with a somewhat in excess of n_c .

Surface profiles corresponding to $Ak = 0.1,\ 0.2,\ 0.3,\ 0.4$ and the limiting value $Ak = 0.4432$ are shown in Figure 2.

The corresponding value of the effective gravity g' are shown in Figure 3. It will be seen that when $Ak = 0.4$ these range from $0.65g$ at the crest of the wave $(x=0)$ to about $1.31g$ in the wave trough.

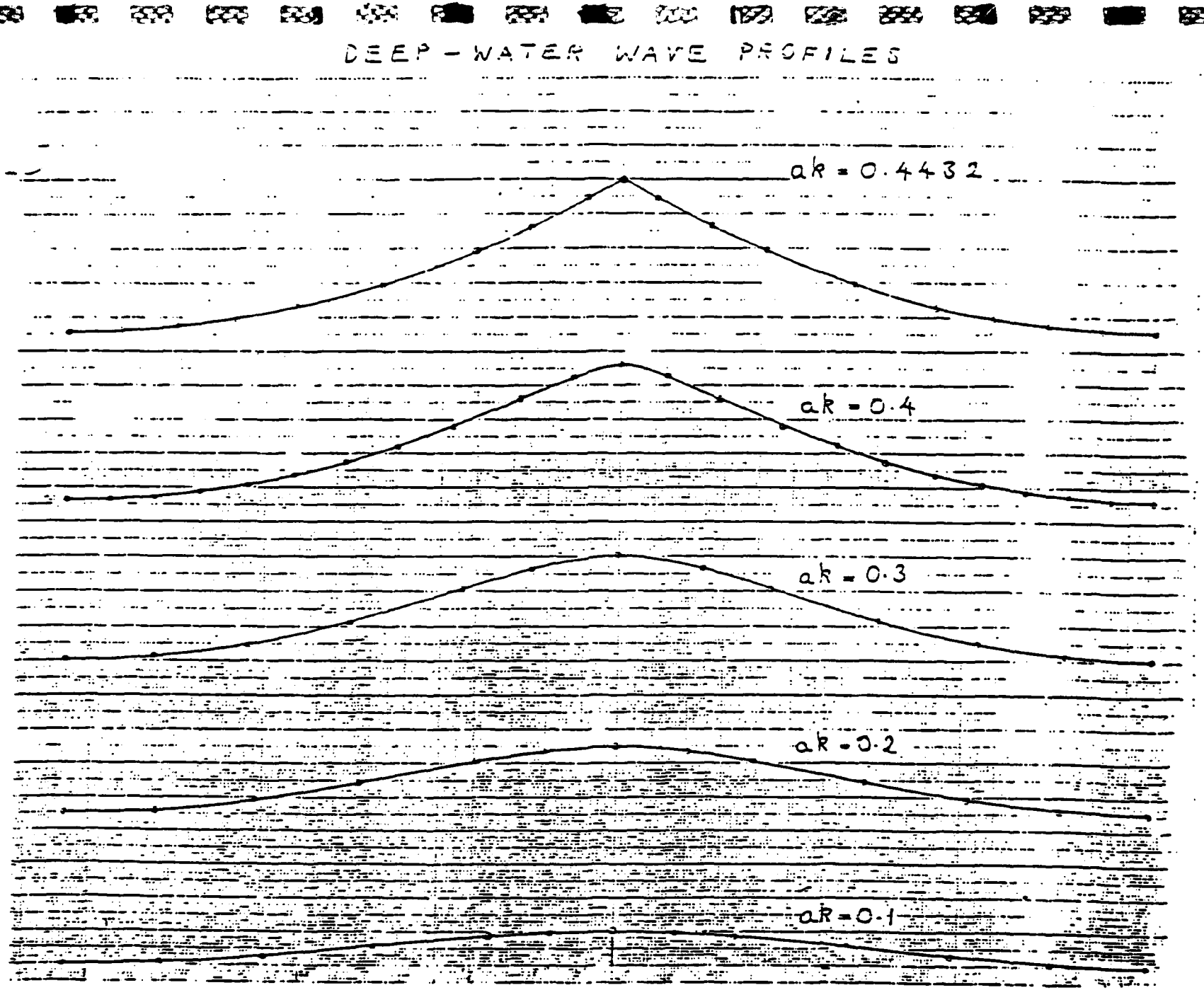

Figure 2. Surface profiles of gravity waves in deep water, for $AK = 0.1, 0.2, 0.3, 0.4$ and 0.4432.

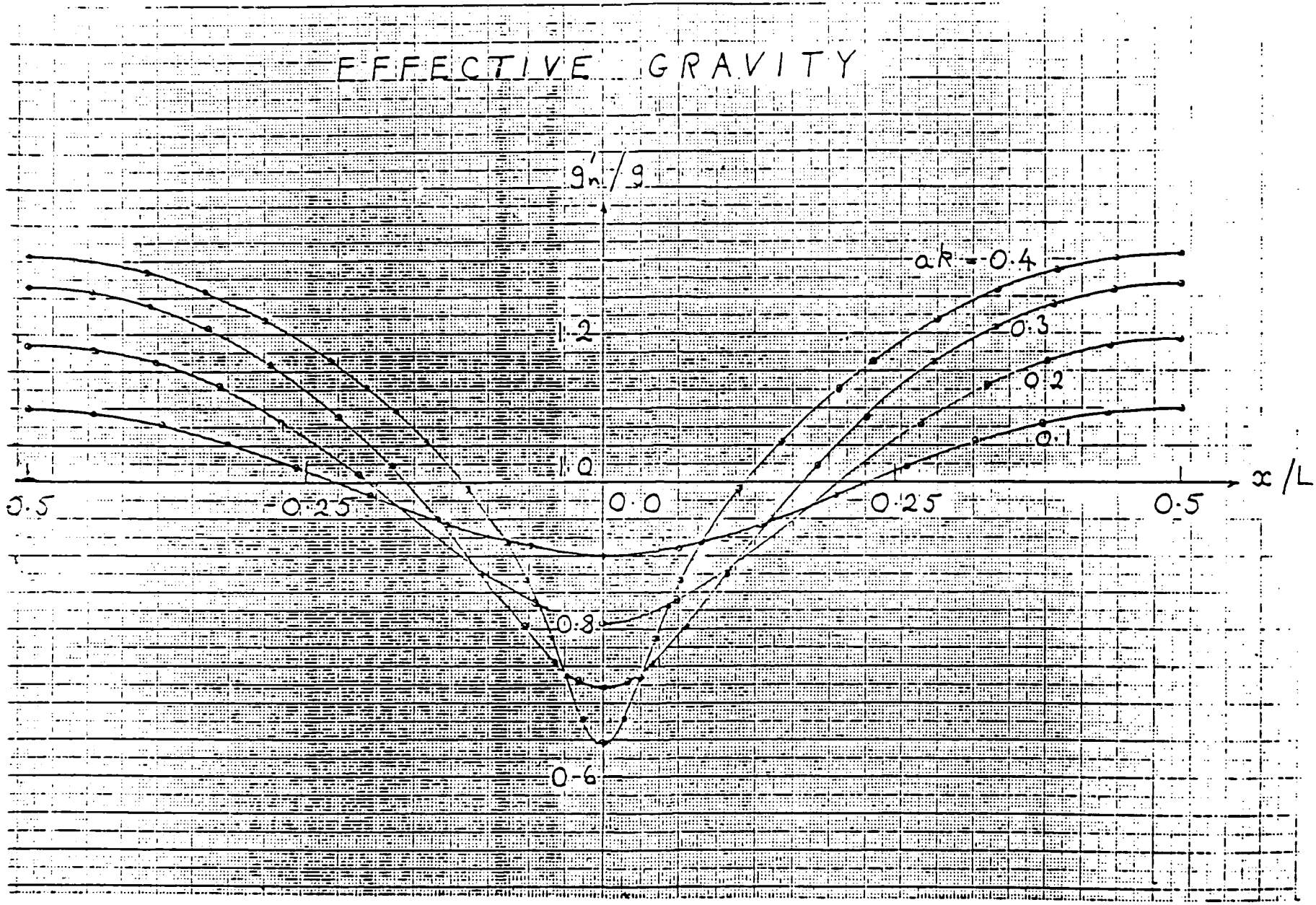

Figure 3. The effective value of gravity g' at the surface of steep waves, as a function of the horizontal coordinate x/L.

4. Results: variation in short-wave length.

Using suffices 1 and 2 to denote values at the long-wave crest and trough respectively, Figure 4 shows the relative shortening $k_1/\bar{k}$ at the crests of the long waves as compared to the mean surface level, in the three cases when $\bar{k} = 2$, 10 and 100. Similarly $k_2/\bar{k}$ shows the lengthening in the long-wave troughs. For values of AK up to 0.2 the three curves corresponding to $\bar{k} = 2$, 10 and 100 are almost indistinguishable, and even when $AK = 0.4$ there is little departure from the representative curve $\bar{k} = 10$, when $k_1/\bar{k} = 3.0$ and $k_2/\bar{k} = 0.82$. Thus, the short-wave length varies over a range of about 3½ to 1. This is for $c > 0$, when the short waves travel in the same sense as the longer waves. Figure 5 shows a similar plot when $c < 0$, and the short waves travel in the opposite sense. Here the variation in k is only slightly less. However, as $AK \to (AK)_{max}$ it can be shown that $k_1/\bar{k} \to \infty$ when $c > 0$, but remains finite when $c < 0$.

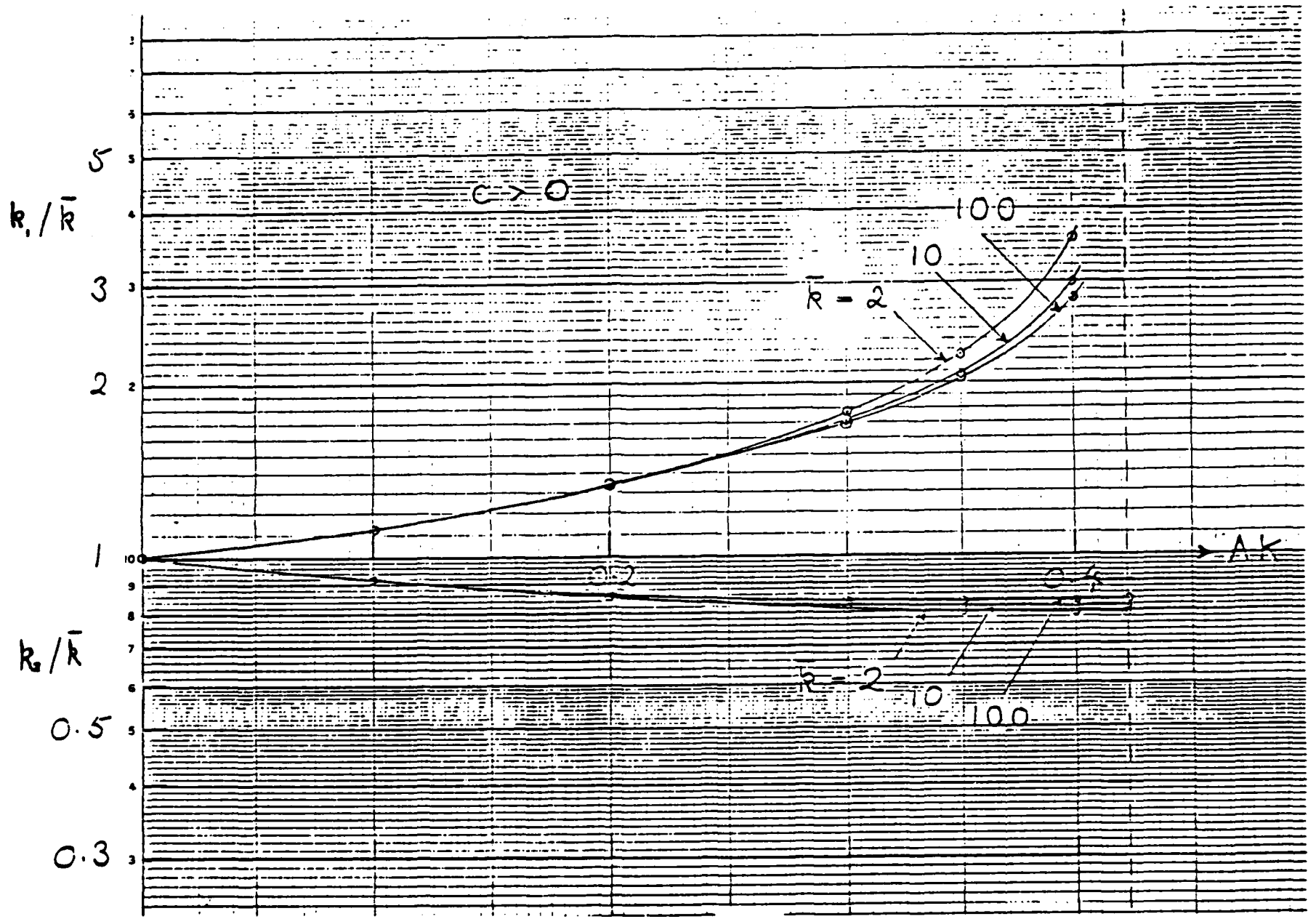

Figure 4. The relative shortening of short waves at the crests $(k_1/\bar{k})$ and in the troughs $(k_2/\bar{k})$ of long waves, as compared to the mean level; $c > 0$.

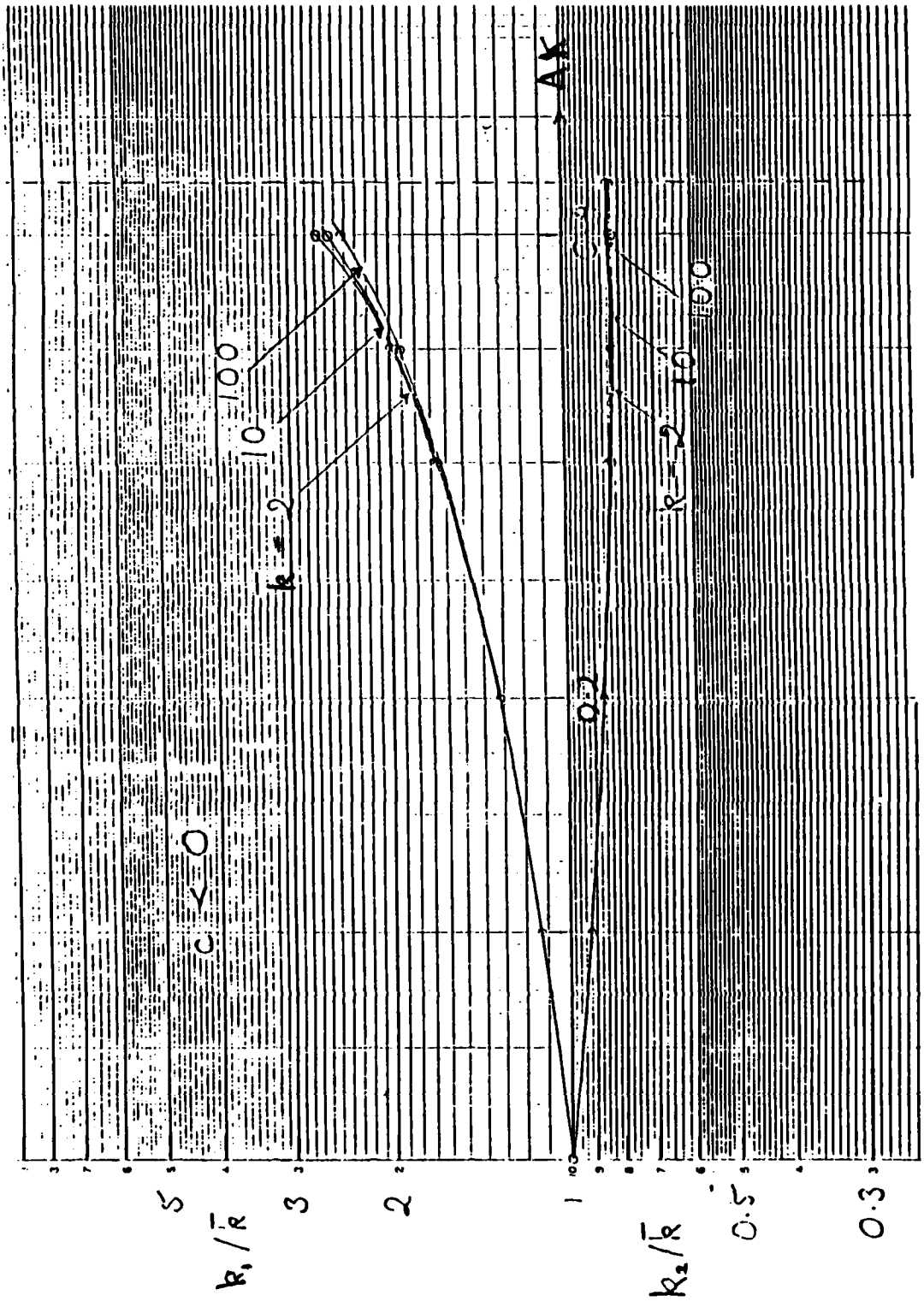

Figure 5. As Figure 5, but for $C < 0$.

5. Variation in the wave steepness

Figures 6 and 7 show the variation in steepening s_1 of the shorter waves, in a similar manner to Figures 4 and 5. Thus

$$s_1 = \frac{a_1 k_1}{\bar{a}\,\bar{k}}, \qquad s_2 = \frac{a_2 k_2}{\bar{a}\,\bar{k}}. \tag{5.1}$$

Again the three curves corresponding to $\bar{k} = 2, 10$ and 100 lie very close together, showing that not only the wavelength variation but also the steepness variation is practically independent of short-wave length.

When $AK = 0.4$, however, the short-wave steepness may vary by a factor of as much as 8 between the long-wave crests and the mean level. This compares with a factor less than 2 given by linear theory.

The variation of steepness s_1 over the profile of the long waves is shown in Figure 8 as a function of x/L, and for different values of AK, using the representative short wavenumber $\bar{k} = 8$. Comparing $AK = 0.4$ with $AK = 0.1$, one sees the distorting effect of nonlinearity in the long waves.

Finally, in Figure 9 the three curves of Figure 8 are plotted instead against $(y - \bar{y})/L$, that is the vertical height above the mean level $\bar{y}$. It now appears that all the curves collapse almost onto a single curve. This property may be useful in approximate analytical work. The appropriate nonlinear steepening is quite different from the linear theory, shown in Figure 9 by the broken curve.

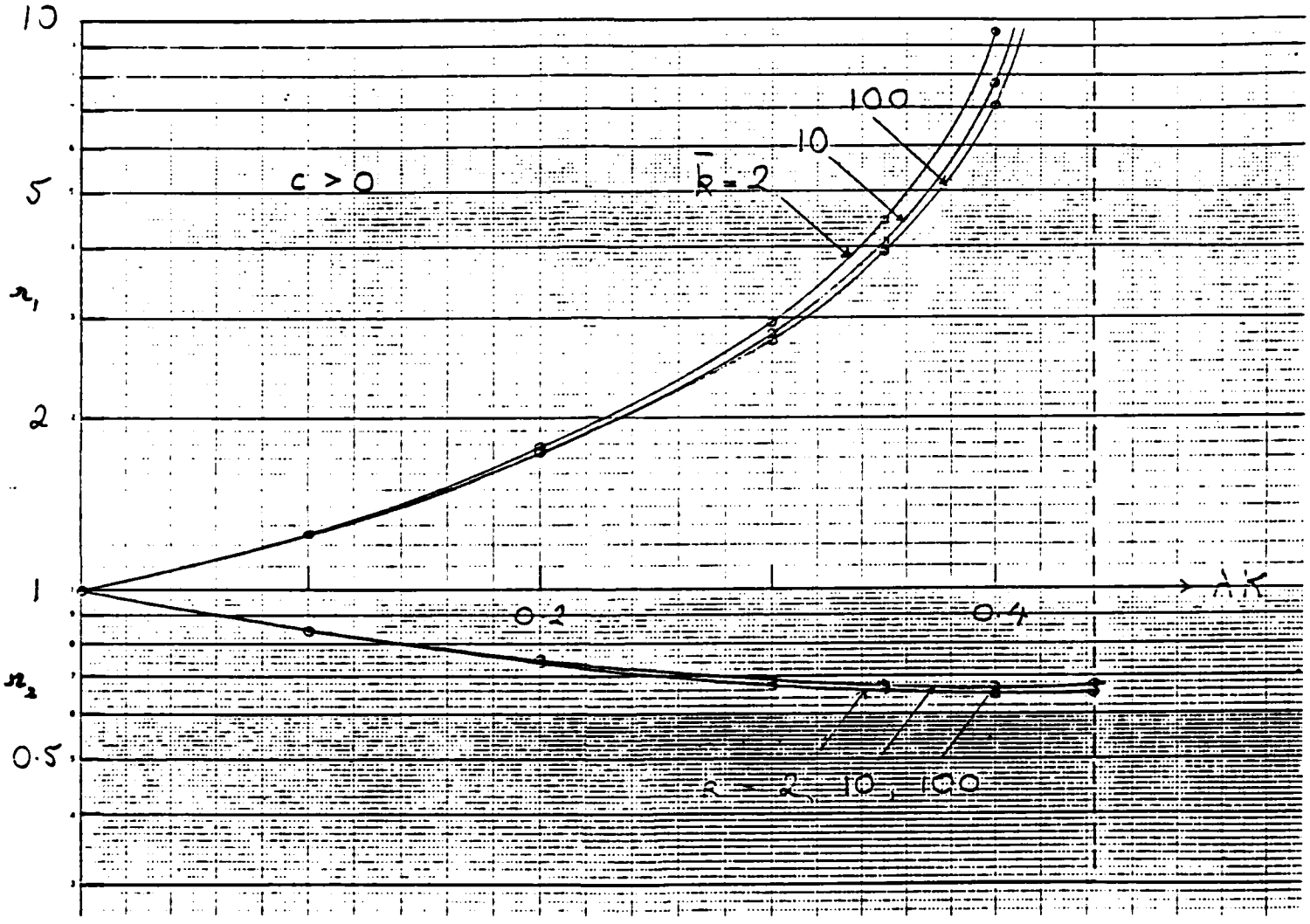

Figure 6. The relative steepening of short waves at the crests (η_1) and in the troughs (η_2) of long waves, as compared to the mean level: $c > 0$.

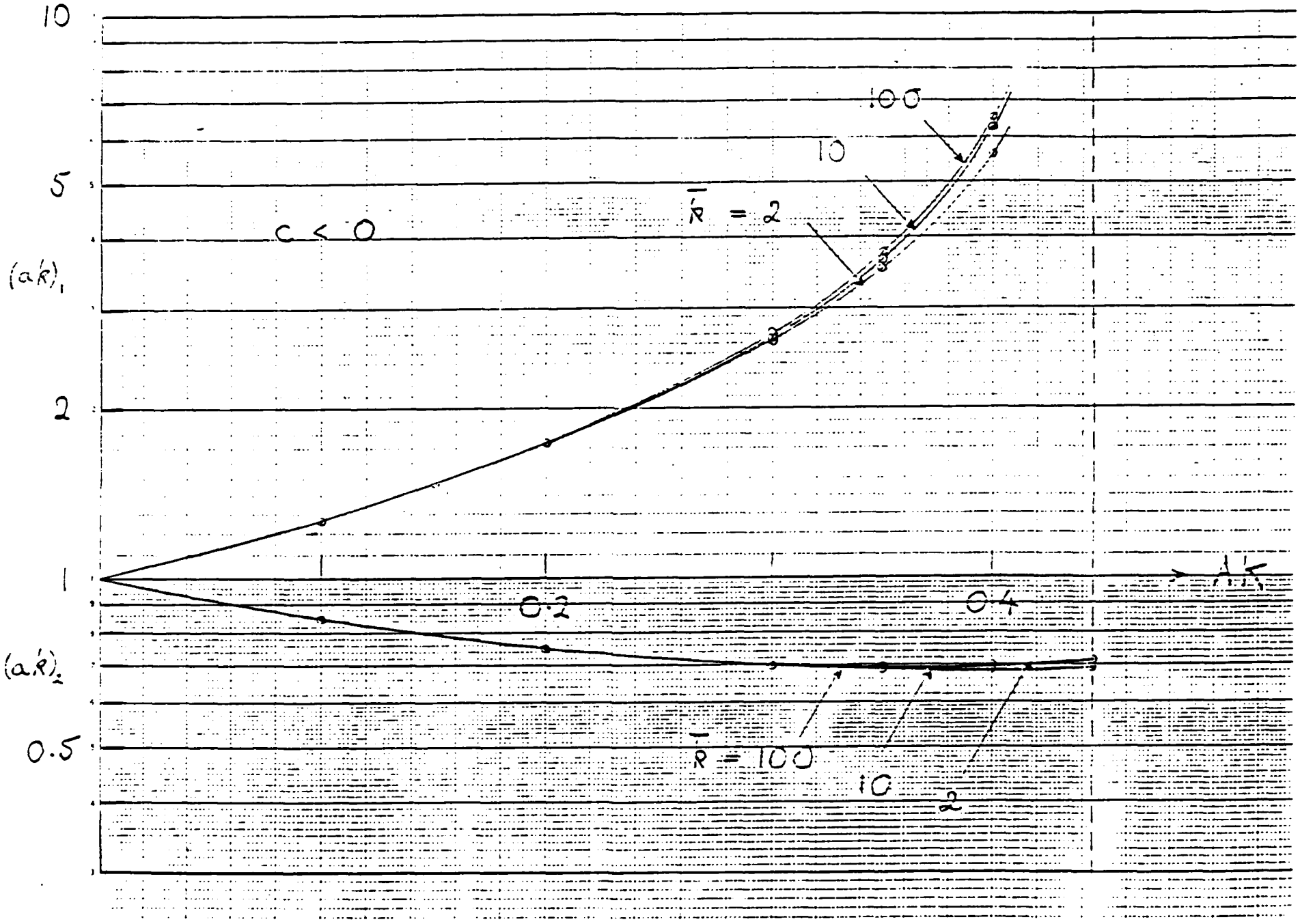

Figure 7. As Figure 6, but for $C < 0$.

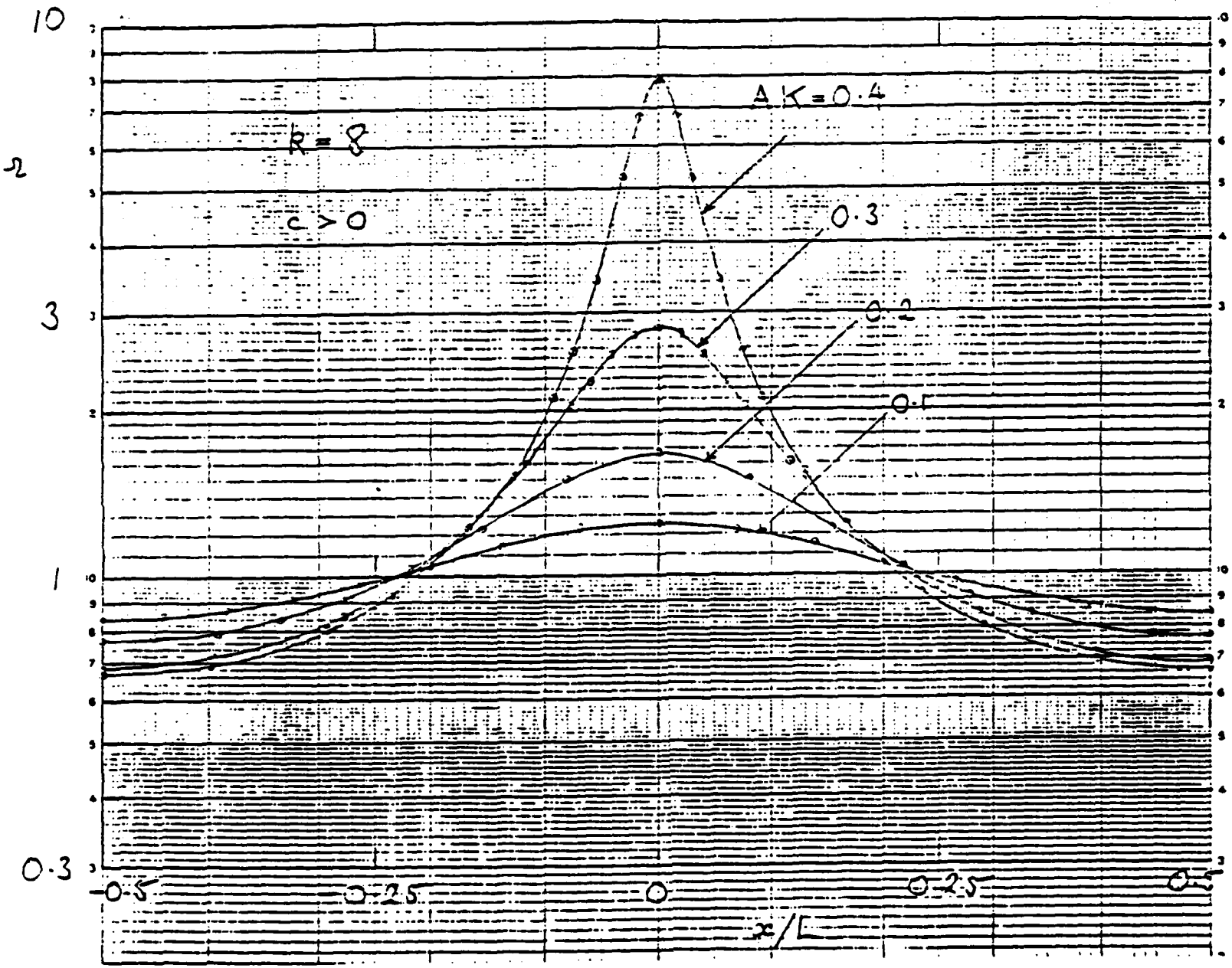

Figure 8. The relative steepening $\bar{\lambda}$ as a function of the horizontal coordinate x/L, when $\bar{k} = 8$, $c > 0$.

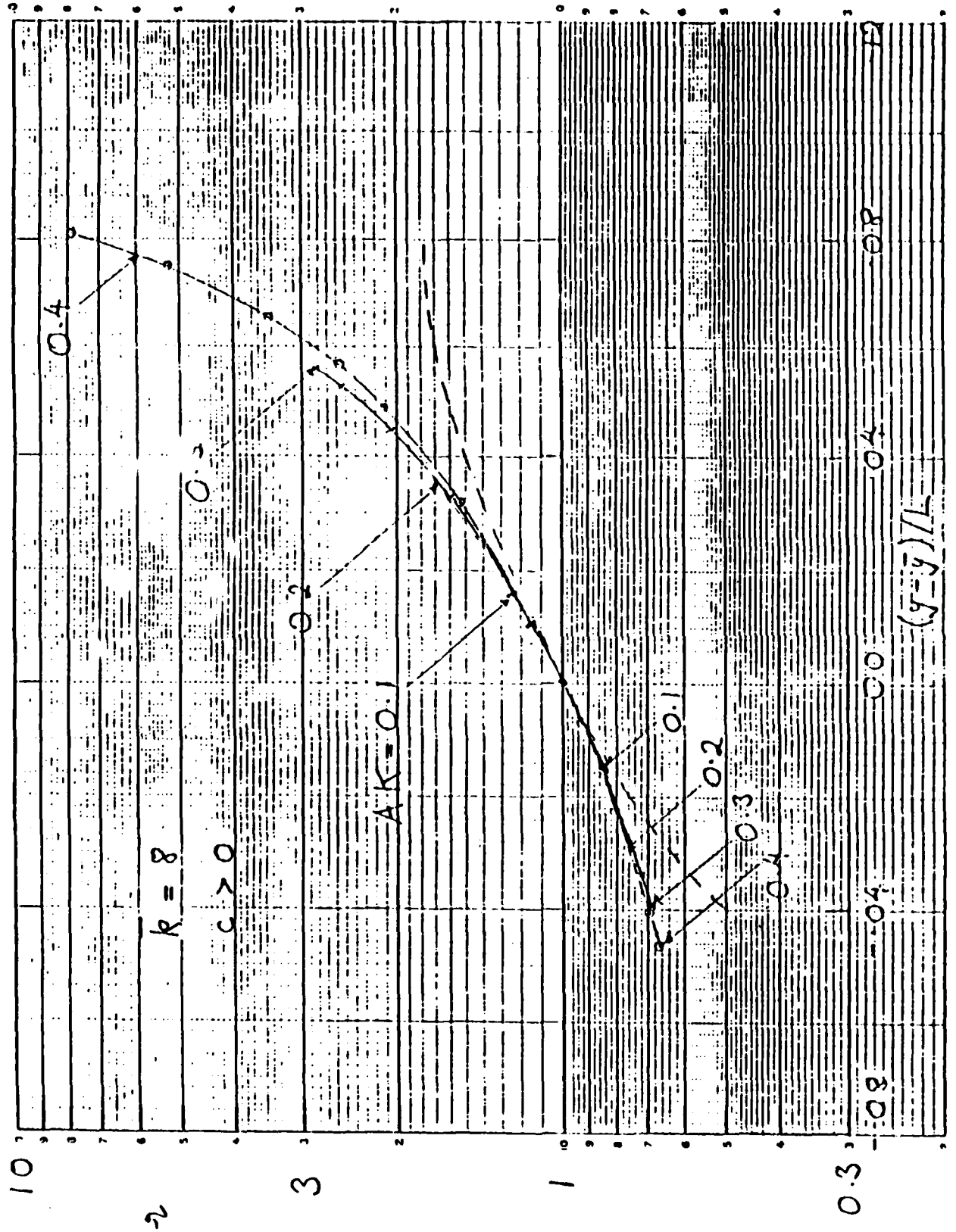

Figure 9. The relative steepening as a function of the vertical coordinate $(y-\bar{y})/L$ when $\bar{k} = 8$, $c < 0$.

6. A pendulum model

As a check on the principle of action conservation, which was used in the calculation of the wave steepness, a simple mathmatical model was constructed. The long wave was represented as a single "orbiting" pendulum of length L describing complete orbits in a vertical plane (Figure 10). To the bob of the longer pendulum, of mass M, is attached a smaller pendulum of length ℓ and mass m, where

$$\ell \ll L, \qquad m \ll M. \tag{6.1}$$

It is convenient to choose units so that

$$L = 1, \qquad M + m = 1, \qquad g = 1, \tag{6.2}$$

then the kinetic and potential energies of the system are respectively

$$\left.\begin{aligned} T &= \tfrac{1}{2}\dot{\theta}^2 + \ell m \dot{\theta}\dot{\phi}\cos(\theta - \phi) + \tfrac{1}{2}\ell^2 m \dot{\phi}^2 \\ V &= (\cos\theta + 1) + \ell m (\cos\phi + 1) \end{aligned}\right\} \tag{6.3}$$

where θ and ϕ denote the angles which the longer and shorter pendulums, respectively, make with the vertical. The Lagrange equations:

$$\left.\begin{aligned} \frac{d}{dt}\left(\frac{\partial T}{\partial \dot\theta}\right) - \frac{\partial T}{\partial \theta} &= -\frac{\partial V}{\partial \theta} \\ \frac{d}{dt}\left(\frac{\partial T}{\partial \dot\phi}\right) - \frac{\partial T}{\partial \phi} &= -\frac{\partial V}{\partial \phi} \end{aligned}\right\} \tag{6.4}$$

yield

$$\left.\begin{aligned} \ddot\theta + l m\left[\ddot\phi \cos(\theta-\phi) + \dot\phi^2 \sin(\theta-\phi)\right] &= \sin\theta \\ l\ddot\phi + \left[\ddot\theta \cos(\theta-\phi) - \dot\theta^2 \sin(\theta-\phi)\right] &= \sin\phi . \end{aligned}\right\} \tag{6.5}$$

These can be solved for $\ddot\theta$ and $\ddot\phi$ in terms of $\theta, \phi, \dot\theta$ and $\dot\phi$ and integrated numerically, for various initial conditions. As a check on the time-stepping we may monitor the total energy

$$T + V = H . \tag{6.6}$$

When either l or m vanishes, the system reduces to a simple (long) pendulum of length $L = l$ obeying the equation of motion

$$\ddot\theta = \sin\theta \tag{6.7}$$

and

$$\tfrac{1}{2}\dot\theta^2 + \cos\theta = \text{constant} = \tfrac{1}{2}Q^2 + 1 , \tag{6.8}$$

where Q is the value of $\dot\theta$ at the highest point $\theta = 0$. Writing $k = 1/Q$ we easily obtain

$$t = \int_0^{\theta} \frac{\kappa\, d\theta}{(1 + 4\kappa^2 \sin^2 \tfrac{1}{2}\theta)^{1/2}}, \qquad (6.9)$$

a known elliptic integral.

It will be seen that the effective gravity g' is always directed radially, and has magnitude

$$g' = \dot{\theta}^2 - g\cos\theta = Q^2 + 2 - 3\cos\theta. \qquad (6.10)$$

When $Q^2 > 1$, g' is always directed radially outwards.

We are interested in conditions when $Q \gg 1$ so that the long pendulum describes complete orbits rapidly, and gravity produces a relatively small perturbation. Then $\kappa \ll 1$, and expansion of (6.9) in powers of κ yields

$$Qt = (1 - \kappa^2)\theta + \kappa^2 \sin\theta + O(\kappa^4) \qquad (6.11)$$

and hence

$$\theta = \sigma t - a \sin \sigma t + O(\kappa^4) \qquad (6.12)$$

where

$$\left.\begin{aligned} \sigma &= \frac{Q}{1-\kappa^2} = \frac{\dot{\theta}_0}{1-\kappa^2} \\ a &= \kappa^2. \end{aligned}\right\} \qquad (6.13)$$

Equation (6.12) represents a uniform rotation together with a periodic perturbation, of radian frequency σ given by (6.13). In the next approximation we find

$$\sigma = \frac{\dot{\theta}_0}{1 - \kappa^2 + \frac{7}{4}\kappa^4}. \qquad (6.14)$$

In the general case when $\ell > 0$ and $m > 0$ we may define the energy of the small pendulum as

$$E' = \tfrac{1}{2}\ell^2 m\dot{\phi}^2 + g'\ell m\left[\cos(\phi - \theta + \pi) + 1\right] \tag{6.15}$$

where g' is the effective gravity. Then using equation (6.5) and neglecting terms in m^2 we find

$$\frac{dE'}{dt} = \ell m\left[3\dot{\theta}\sin\theta - 3\dot{\theta}\sin\theta\cos(\phi-\theta) - \dot{\theta}(\dot{\theta}^2 - \cos\theta)\sin(\phi-\theta)\right]. \tag{6.16}$$

It will be noticed that the terms in $\dot{\phi}$ are absent. After averaging over the fast phase ϕ we obtain, to lowest order

$$\left\langle \frac{dE'}{dt} \right\rangle = 3\ell m\dot{\theta}\sin\theta \tag{6.17}$$

as the approximate variation in the short-wave energy.

An alternative definition of the short-wave energy is to replace $\dot{\phi}^2$ on the right hand side of (6.15) by $(\dot{\phi} - \dot{\theta})^2$, so taking some account of the rotation of the longer pendulum. We denote the corresponding expression by E''. This leads to an equation similar to (6.17).

To test these two definitions of the energy we investigated the case

$$\ell = 10^{-1}, \qquad m = 10^{-4} \tag{6.18}$$

with initial conditions

$$\theta = \phi = 0, \qquad \dot{\theta} = 1, \qquad \dot{\phi} = 20 \tag{6.19}$$

at $t = 0$. Figure 11 shows the trajectory of the mass m, and Figure 12 indicates the angular velocity $\dot{\phi}$ as a function of $\dot{\theta}$; the point $\dot{\theta} = 1$ corresponds to $\theta = 0$, and $\dot{\theta} = 2.215$ to $\theta = \pi$ (lowest point of the larger mass M). Clearly the fluctuations in $\dot{\phi}$ are as great

as 18%. Figure 13 (upper curves) show the limits in the variation of E', which are about 7 percent of the mean. The lower curves, on the other hand, show the fluctuations in E'', which are clearly much less — about 0.5 percent. Thus E'' is a more satisfactory definition of the energy of the smaller pendulum than is E'. However the mean value of E'' still varies by about 20% over a complete cycle of $\dot{\theta}$.

Finally, to test the action priniciple we calculated the two ratios E'/σ' and E''/σ'' where σ' and σ'' are given by expressions analogous to (6.14), viz

$$\sigma' = \frac{Q'}{1 - \kappa'^2 + \frac{9}{4}\kappa'^4}, \qquad Q' = \dot{\phi}_{\theta - \phi = \pi}, \qquad \kappa' = 1/Q' \tag{6.20}$$

and

$$\sigma'' = \frac{Q''}{1 - \kappa''^2 + \frac{9}{4}\kappa''^4}, \qquad Q'' = (\dot{\phi} - \dot{\theta})_{\theta - \phi = \pi}, \qquad \kappa'' = 1/Q'' \tag{6.21}$$

The results are shown in Figure 14. The total variation in E''/σ'' is clearly less than that of E'/σ' and is of the order of 4% only. Some of this variation may be due to the approximate nature of the frequency formula (6.14).

This example was typical of those that were tested. On the whole, therefore, the principleof action conservation was well verified.

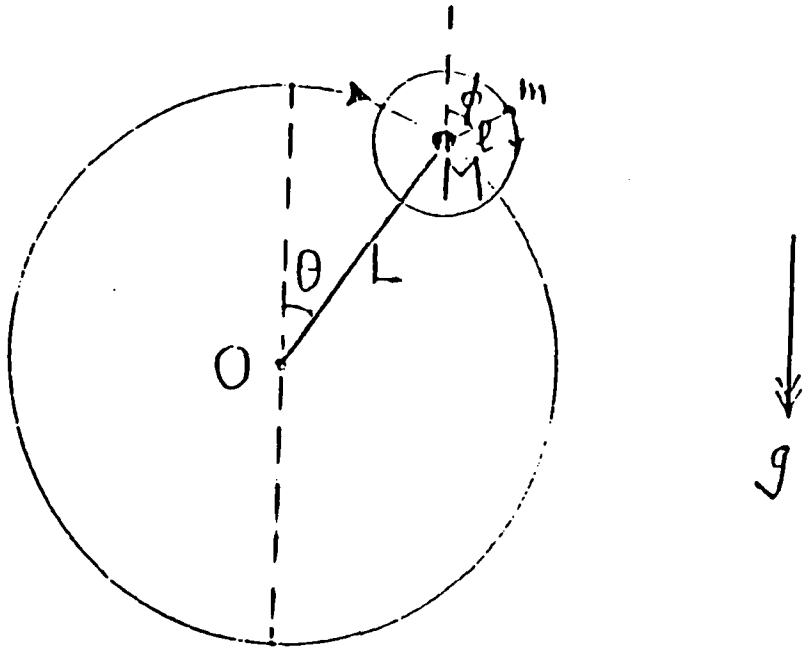

Figure 10. Definition sketch for the pendulum model.

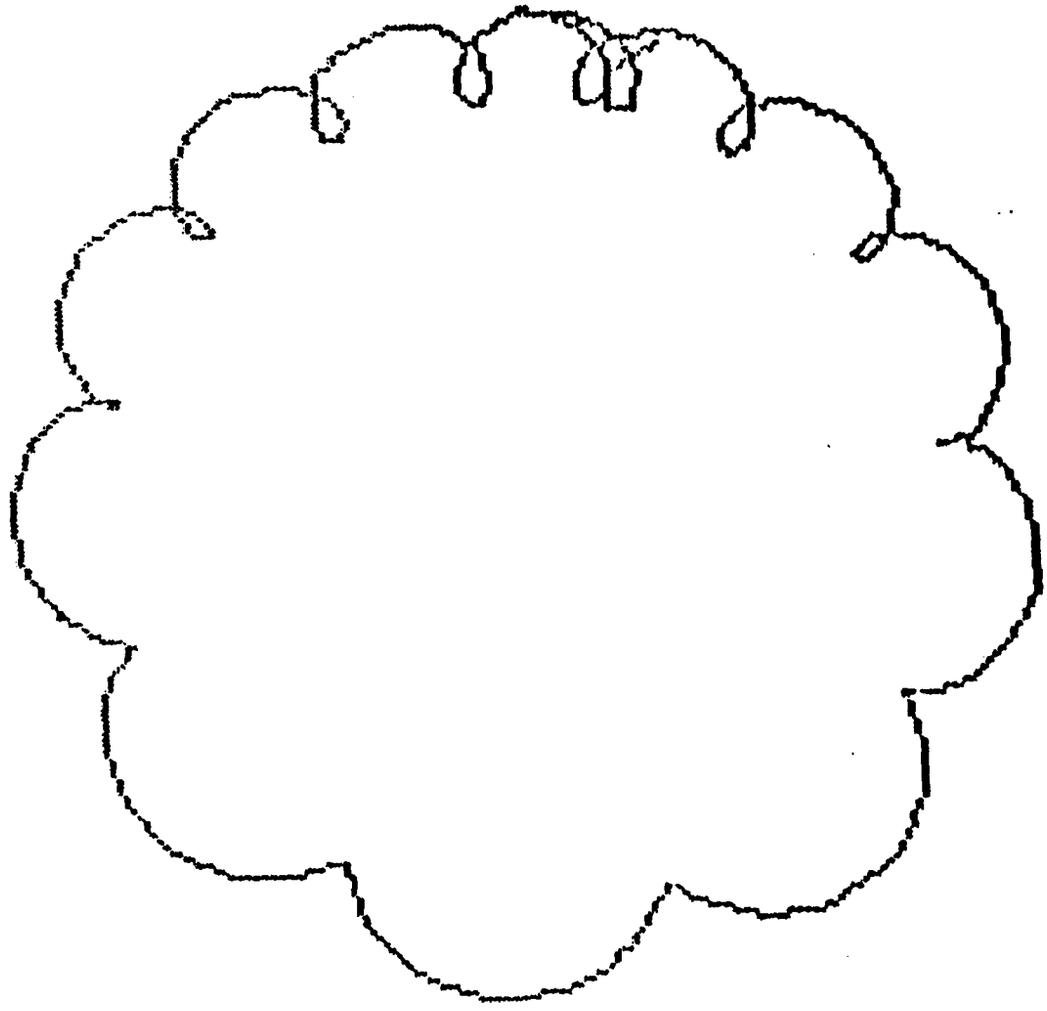

Figure 11. Trajectory of the mass m when $\ell = 10^{-1}$, $m = 10^{-4}$, and the initial conditions are that $\theta = \phi = 0$, $\dot{\theta} = 1$, $\dot{\phi} = 20$ when $t = 0$.

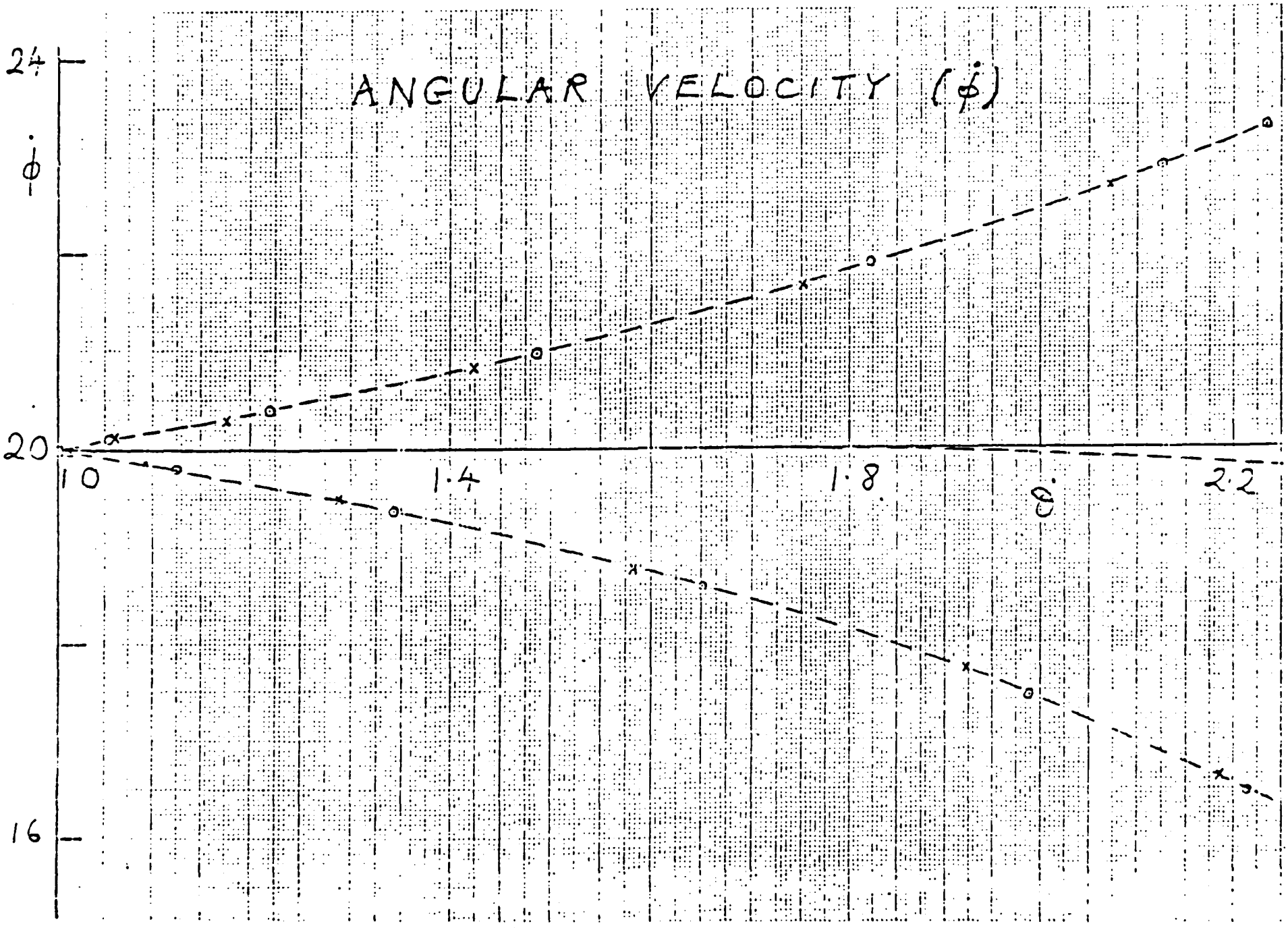

Figure 12. Maximum and minimum values of the angular velocity as a function of $\dot{\theta}$, corresponding to Figure 11.

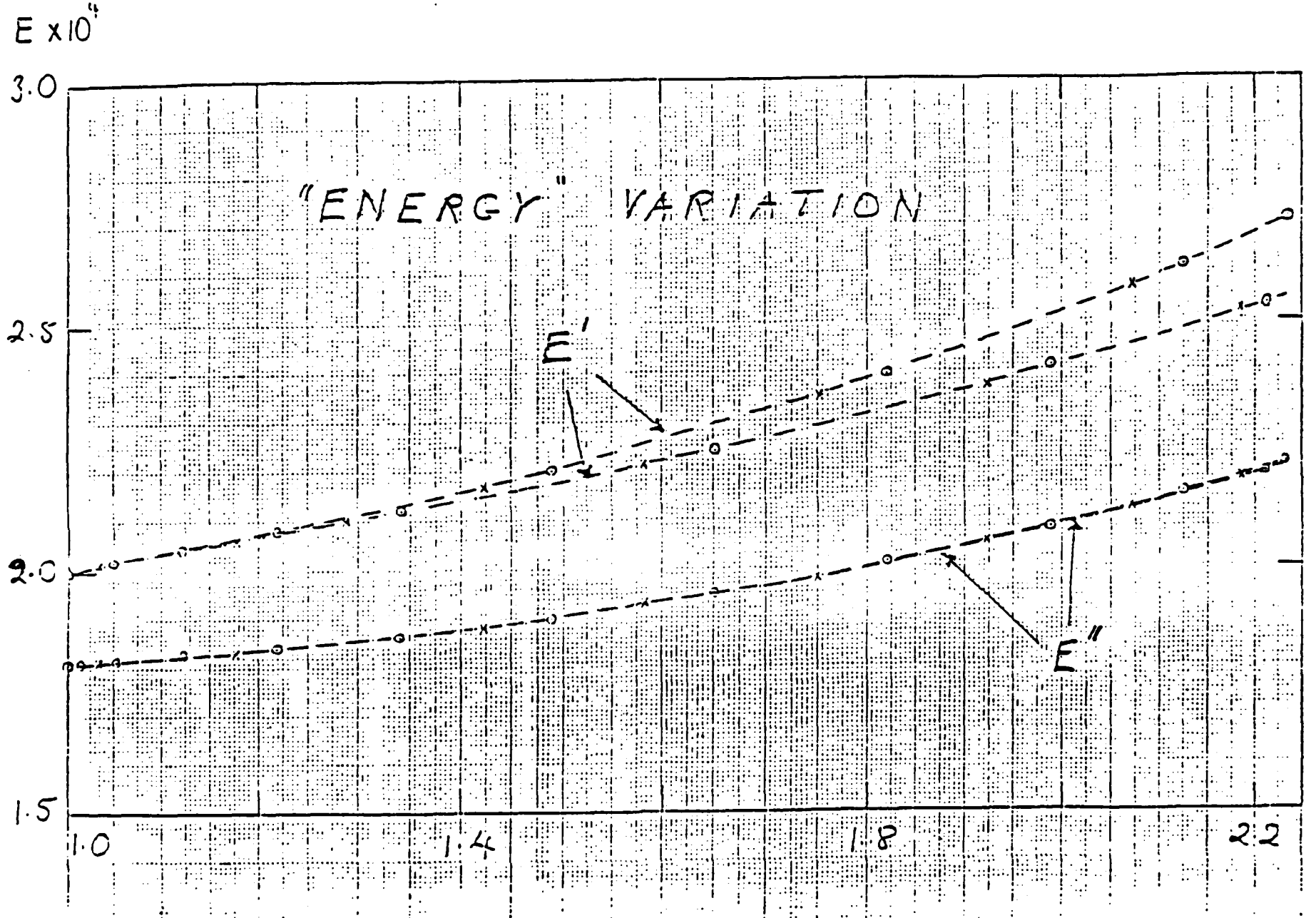

Figure 13. Maximum and minimum values of the "energy" E' (upper curves) and E'' (lower curves) as a function

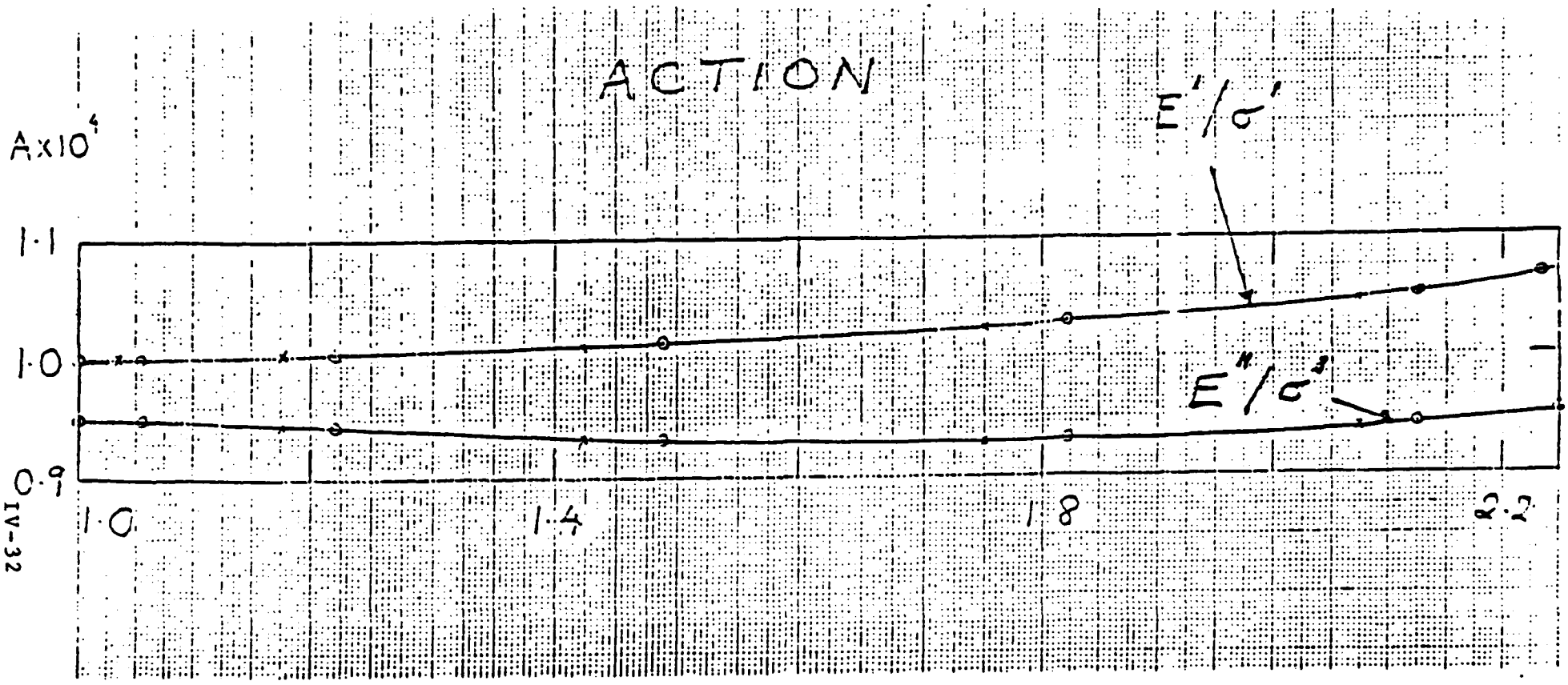

Figure 14. Variation in the "action" as defined by E'/σ' and E''/σ'' respectively. Conditions as in Figure 11.

References

Bretherton, F.P. and Garrett, C.J.R. 1968 Wavetrains in homogeneous moving media. Proc. R. Soc. Lond. A 302, 529-554.

Garrett, C.J.F. 1967 The adiabatic invariant for wave propagation in a nonuniform moving medium. Proc. R. Soc. Lond. A 299, 26-27.

Kenyon, K., Sheres, D. and Bernstein, R. 1983 Short waves on long waves. Preprint, Scripps Inst. of Oceanogr., April 1983.

Lamb, H. 1932 Hydrodynamics, 6th ed. Cambridge Univ. Press

Longuet-Higgins, M.S. and Stewart, R.W. 1960 Changes in the form of short gravity waves on long waves and tidal currents. J. Fluid Mech. 8, 565-583.

Longuet-Higgins, M.S. and Stewart, R.W. 1961 The changes in amplitude of short gravity waves on steady, non-uniform currents. J. Fluid Mech. 10, 529-549.

Longuet-Higgins, M.S. 1985a Bifurcation in gravity waves. J. Fluid Mech. 151, 457-475

Longuet-Higgins, M.S. 1985b Asymptotic behavior of the coefficients in Stokes's series for surface gravity waves. I.M.A. Journal of Appl. Math. 34, 267-277.

Longuet-Higgins, M.S. 1985c Accelerations in steep gravity waves. J. Phys. Oceanogr. (in press).

Phillips, O.M. 1981 The dispersion of short wavelets in the presence of a dominant long wave. J. Fluid Mech. 107, 465-485

Diagram legends

Figure 1. Definition sketch for short waves on long waves.

Figure 2. Surface profiles of gravity waves in deep water, for $Ak = 0.1,\ 0.2,\ 0.3,\ 0.4$ and 0.4432

Figure 3. The effective value of gravity g' at the surface of steep waves, as a function of the horizontal coordinate x/L.

Figure 4. The relative shortening of short waves at the crests $(k_1/\bar{k})$ and in the troughs $(k_2/\bar{k})$ of long waves, as compared to the mean level; $c > 0$.

Figure 5. As Figure 5, but for $c < 0$.

Figure 6. The relative steepening of short waves at the crests (λ_1) and in the troughs (λ_2) of long waves, as compared to the mean level: $c > 0$.

Figure 7. As Figure 6, but for $c < 0$.

Figure 8. The relative steepening λ as a function of the horizontal coordinate x/L, when $\bar{k} = 8$, $c > 0$

Figure 9. The relative steepening as a function of the vertical coordinate $(y - \bar{y})/L$ when $\bar{k} = 8$, $c < 0$.

Figure 10. Definition sketch for the pendulum model.

Figure 11. Trajectory of the mass m when $\lambda = 10^{-1}$,

$m = 10^{-4}$, and the initial conditions are that $\theta = \phi = 0$, $\dot{\theta} = 1$, $\dot{\phi} = 20$ when $t = 0$.

Figure 12. Maximum and minimum values of the angular velocity as a function of $\dot{\theta}$, corresponding to Figure 11.

Figure 13. Maximum and minimum values of the "energy" E' (upper curves) and E'' (lower curves) as a function of $\dot{\theta}$, for the same conditions as Figure 11.

Figure 14. Variation in the "action" as defined by E'/σ' and E''/σ'' respectively. Conditions as in Figure 11.

APPENDIX V

TOWARD METEOROLOCY MEASUREMENTS

by

G.L. Geernaert
Naval Research Lab.
Code 7784, Washington, D.C. 20375

Meteorology investigators:

G.L. Geernaert	NRL, Code 7784 Washington, D.C. 20375
K.L. Davidson	NPS, Code 63 Monterey, CA 93943
J. Byars	NPS, Code 63 Monterey, CA 93943
Soren Larsen	Meteorology Dept., Riso National Lab. DK-4000 Roskilde, Denmark
Torben Mikkelsen	Meteorology Dept., Riso National Lab. DK-4000 Roskilde, Denmark

Outline

1. Introduction
2. Basic theory
3. Preliminary scientific results
4. Illustration: 31 Oct. 1984
5. Meteorology During SAR flights
6. Research plans

1. Introduction

Meteorological measurements at the NOSC tower were collected in order to obtain accurate estimates of the wind stress at the air-sea interface. Two independent systems were used to measure the stress: sonic anemometer, which directly measures the momentum flux, and hot film system, which indirectly evaluates the momentum flux based on a turbulent energy balance. Because the flux data presented in this report are based on the hot film system, the theory required to obtain the wind stress from this method will briefly be described. Data from the sonic anemometer are not yet ready for distribution.

The basic meteorology quantities measured were wind speed and direction, air temperature and dew point temperature. The water temperature, meausured by NOSC, was incorporated into the meteorology data set. In addition to the momentum flux, high frequency measurements at temperature and water vapor were collected in order to evaluate the fluxes of latent and sensible heat. During TOWARD 85, the meteorology data set was supplemented by twice daily radiosonde profile data, launched from the tower. Net solar and infra-red radiation measurements were additionally collected during spring 1985. The measurements are summarized in Table 1.

Estimates of the momentum flux by the dissipation method (hot film) were continuous during normal tower operations. Sonic anemometer measurements were restricted to conditions such as moderate to high westerly winds and/or times of overflights.

The evaluation of data quality required consideration of mast flow distortion, fog/rain conditions, and convection off the tower body during light winds. Because the mast on which all the meteorlogy sensors were mounted (except radiation) was located on the north end of the NOSC tower, the greatest flow distortion occurred during southerly flow. The most favorable direction for measurements were northerly winds from the west through the northeast.

Fog and rain interfered considerably with both the sonic and hot film systems. Because the sonic is based on the relative time for a sound pulse to travel over a short distance, a thin film of water on either the source or detector gave an erroneous measure of the wind velocity. The hot film, on the other hand, when in contact with a water droplet, produced a voltage spike with the latent heat release during evaporation.

Finally, light winds adversely affected the quality of the flux estimates due to both enhanced flow distortion and convection off the body of the tower.

Tabel 1

Arrangement of sensors on the NOSC Tower
(variables defined in Section 2)

Sensor	Variable Measured	Height above MSL
Sonic anemometer	u,v,w,T	22 m
Lyman-α	q,q'	19 m
Cold wire	T'	22 m
Hot film	ε	22 m
T_{air}, T_{dp}	T_{air}, RH	18 m
Cup anemometer	u (slow response)	18 m
Wind vane	θ (0° = North)	17 m
Water temperature	T_o	-3 m
Solar/Infrared Rad.		
Radiosondes		

2. Basic Theory

2.1. The direct method

Generally, the wind stress (or momentum flux), τ, may be written in nearly exact terms as:

$$\tau = -\overline{\rho u w} \qquad (1)$$

where ρ is air density, and u and w are the instantaneous horizontal and vertical wind velocities. If an averaging time is chosen

to be long enough so that w = 0, then equation (1) reduces to

$$\tau = -\overline{\rho u' w'} \tag{2}$$

The sonic anemometer uses this method for obtaining τ. The friction velocity is simply a scaling parameter for wind stress (with units of velocity) and is defined as:

$$u_* = (\tau/\rho)^{1/2} \tag{3}$$

Because geophysical modellers of air-sea interaction processes needed spatial field estimates of the wind stress, the bulk aerodynamic formula was derived. This formula requires knowledge of the mean meteorological quantities (winds and temperatures) and is written as:

$$\tau = \rho C_D \bar{u}^2 \tag{4}$$

where C_D is the drag coefficient. The drag coefficient is known to vary considerably with atmospheric stratification and height. If the measurement height is chosen to be 10 m above the surface and the stratification is neutral, $C_D \sim .001$, i.e., roughly a constant up to a windspeed of 10 m/sec. Above 10 m/sec, C_D becomes a slowly increasing function of windspeed. As the atmospheric surface layer becomes more unstable, C_D increases; and conversely, as the surface layer becomes more stable, C_D decreases.

Wind stress data are often reported in terms of the drag coefficient and its neutral-stratification counterpart, C_{DN}. For given meteoroligical conditions, C_{DN} may be evaluated from C_D and knowledge of the surface layer stability, assuming that the observed windspeed is common to the surface layer equations. The only reason C_{DN} is calculated from TOWARD data is to compare to past investigations of the drag coefficient over the sea. Even further, since stability is a known parameter that affects the magnitude of the drag coefficient, performing statistics on the neutral drag coefficient hopefully will yield information on a secondary parameter that affects C_D, i.e., sea state. Such an analysis is more simplified by stating:

$$C_D(\Psi, WS) = C_{DN}(WS) \tag{5}$$

where Ψ is a stability function, which in known, and WS is wave state, which is unknown. Any trends in C_{DN} with wave conditions will provide clues to this function; preliminary results are presented herein. Both the sonic and hot film systems are capable of providing estimates of $U*$, C_D, and C_{DN}.

2.2. The indirect dissipation method

The hot film system utilized the dissipation technique for estimating the wind stress. This method requires estimates for the balance of turbulent kinetic energy (TKE), where the TKE equation is written as:

$$\frac{\partial e}{\partial t} = u_*^2 \frac{\partial u}{\partial z} - \frac{g}{T}\overline{w'T_v'} - \frac{\partial}{\partial z}\left(\overline{w'e} + \frac{1}{\rho}\overline{w'p'}\right) - \varepsilon \qquad (6)$$

where e is TKE, g is gravity, ε is the TKE dissipation rate, and p is pressure. If the flow is not excessively stable or unstable, the third term on the r.h.s. in (6) is relatively small and can be ignored. Similarly, for steady state conditions, and (6) reduces to:

$$u_*^2 \frac{\partial u}{\partial z} - \frac{g}{T}\overline{w'T_v'} - \varepsilon = 0 \qquad (7)$$

If one assumes that the vertical profile of horizontal windspeed, $\partial u/\partial t$, may be defined as:

$$\frac{\partial u}{\partial z} = \frac{u^*}{KZ}\phi_M(z/L), \qquad (8)$$

where ϕ_M is a known stability function dependent on z/L, i.e.

$$\frac{z}{L} = \frac{gkz\ \overline{w'T_v'}}{Tu_*^3} \qquad (9)$$

then the friction velocity is evaluated, after rearranging (7), to be:

$$u_*^3 = \frac{\varepsilon kz}{\phi_M(\frac{z}{L}) - \frac{z}{L}} \qquad (10)$$

L is the Monin-Obukhov length, k is the von Karman constant.

The dissipation rate, ε, is evaluated by spectrally decomposing the horizontal wind field according to turbulent eddy frequency. The inertial subrange, i.e., the turbulence with frequencies of motion above around 1 Hz, is well described by the Kolmogoroff spectrum; i.e.,

$$S(k_\lambda) = \alpha \varepsilon^{2/3} k_\lambda^{-5/3} \qquad (11)$$

where $k\lambda$ is wavenumber, $S(k\lambda)$ is energy density, and α is a constant equal to 0.52. Equation (11) is transformed simply into frequency space by applying Taylor's hypothesis, which assumes the concept of frozen turbulence advection, i.e.

$$k_\lambda = \frac{2\pi f}{u} \qquad (12)$$

Equations (11) and (12) combine to become:

$$S(f) = \alpha\left(\frac{2\pi}{u}\right)^{-5/3} \varepsilon^{2/3} f^{-5/3} \qquad (13)$$

Although the spectral decomposition of the horizontal windspeed will yield s(f) and f, and consequently ε, the method used in TOWARD was to integrate (11) and then apply (12). This yielded:

$$\sigma_u^2 = \frac{3\alpha}{2}\left(\frac{\varepsilon u}{2\pi}\right)^{2/3}\left(f_1^{-2/3} - f_2^{-2/3}\right) \qquad (14)$$

where the data aquisition system employed filter frequency bounds, f_1 = 5 Hz and f_2 = 50 Hz. σ_u^2 is a quantity evaluated due to the filtering process.

With (14), ε was evaluated, and consequently with (10), estimates of u* were provided. These estimates are provided on both 5 and 30 minute intervals during the TOWARD experiment. For those occasions when the data were of bad quality, u* estimates were made by assuming a neutral drag coefficient, C_{DN}, of 1.4×10^{-3} (according to Large & Pond, 1981). The drag coefficient, C_D, applied to (4) in this case used the relation

$$C_D = \left(C_{DN}^{-1/2} + \Psi/k\right)^{-2} \qquad (15)$$

where Ψ is a stability function. For unstable conditions $C_D > C_{DN}$ and for stable conditions $C_D < C_{DN}$. For neutral stabilities, $C_D = C_{DN}$.

3. Preliminary Scientific Results

Plotted in Figure 1 are the dissipation-derived neutral drag coefficients from both phases of the TOWARD experiment. The conditions of these data include westerly and northwesterly directions; these directions were dominant in the data set and were estimated to induce minimal flow distortion.

Figure 1 was statistically analyzed at 1 m/sec intervals; these results are listed in Table 2. Tabulated alongside the results of Figure 1 are parallel results from C_{DN} measurements for short fetch (less than 4 km).

The results of Table 1 may be summarized as follows: 1) C_{DN} is constant over the windspeed range of 4 to 9 m/sec; 2) The scatter in the data decreases with increasing windspeeds; 3) C_{DN} increases substantially as a function of windspeeds for winds above 9 m/sec; and 4) C_{DN} is generally larger for conditions of short fetch than for long fetch.

The data analysis indicated systematic trends within the range of windspeeds where C_{DN} was found to be constant, i.e., $4<U_{10}<9$ m/sec. C_{DN} was observed to decrease with time during the course of a sea breeze (see illustration - Figure 2), and to increase markedly prior to a frontal passage (see illustration - Fiugure 3). Both of these cases are assumed to be due to the surface wave

Table 2

C_{DN} vs. U_{10}: statistics

Windspeed	Long Fetch		Short Fetch	
(m/sec) Interval	10^3 C_{DN}	$\sigma(C_{DN})$	10^3 C_{DN}	$\sigma(C_{DN})$
1-2	2.12	-	5.03	-
2-3	1.49	0.83	2.02	0.85
3-4	1.43	0.85	1.66	0.41
4-5	0.96	0.44		
5-6	0.98	0.44		
6-7	0.90	0.38		
7-8	0.86	0.46		
8-9	0.94	0.25		
9-10	1.41	0.10		
10-11	1.48	-		

From (4-9) m/sec; 10^3 C_{DN} = 0.93±.40

field undergoing rapidly changing conditions. In the sea breeze case, the wave field is rapidly growing at all wave frequencies and is making an asymptotic adjustment towards equilibrium conditions. In the second case, the convergence of wave trains in

the pre-frontal region (from both ahead and behind a cold front) acts to increase the steepness of waves of all frequencies, thereby increasing the surface roughness. Both these findings from TOWARD will significantly improve our understanding of scatterometer backscatter algorithms and their relations to the overlying winds.

4. Illustration: 31 October 1984

In Figure 4 and 5, one may find plots of meteorology data during the SAR flight on 31 October 1985. Because the flight was conducted after 1300, the sea breeze was westerly with windspeeds strong enough to exhibit confidence in the data quality.

5. Meteorology during SAR flights

Tabulated in Table 3 are meteorological data quality assessments and general conditions during each SAR flight.

Table 3

Meteorology during over Flights
(* = CV 990)

Flight	Wind Conditions	Stratification	Dissipation Data Quality
2 Oct	S 3-4	N	G
6 Oct	NW 8-5	S	G
7 Oct	NW 5-7	N	G
17 Oct*	NW 7-8	U	G
31 Oct*	W 3-6	N	G
4 Nov*	NW 2-4	U	G
7 Nov*	W 4-5	S	G
13 Mar	W 4-5	N	G
18 Mar	NW 3-10	N	G
19 Mar*	W 5-6	N	G
20 Mar	NW 5-7	N	G
24 Mar	W 3-4	S	G
25 Mar	SW 6-7	S	G
26 Mar	SW 4-5	S	G
27 Mar*	SW 5-8	S	I

Legend:			
	South West	Stable	Good
	North West	Neutral	Intermittent
	South	Unstable	
	West		
	Windspeed (m/sec)		

6. Research Plans

6.1. Short Term

a. Technical report of bulk data and u_* estimates from the dissipation method. Jan. 1986

b. Presentation of these TOWARD findings described herein at the Air-sea Interaction Conference, Miami, Florida. Jan. 1986.

c. Submit to JGR results of (b). Spring 1986.

d. Cooperation with NPS, NRL, UK, JPL, Riso and NOSC. Ongoing.

6.2. Long Term

a. Sonic data analysis of u_*. Spring 1986.

b. Spectra of U, θ, T, g, u_*^2, w'T', w'g'. Spring 1986.

Figure 1.

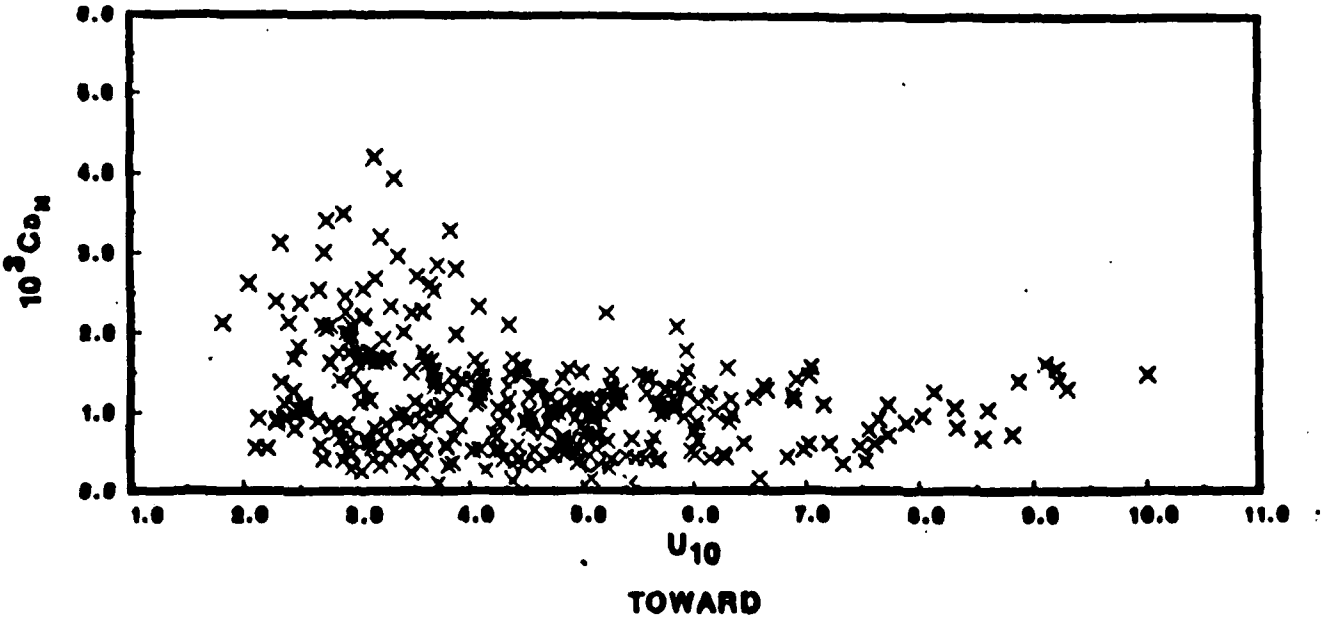
$10^3 C_{DN}$
0.0
1.0
2.0
3.0
4.0
5.0
6.0
1.0
2.0
3.0
4.0
5.0
6.0
7.0
8.0
9.0
10.0
11.0
U_{10}
TOWARD
WIND DIRECTION 260-330

Figure 2a.

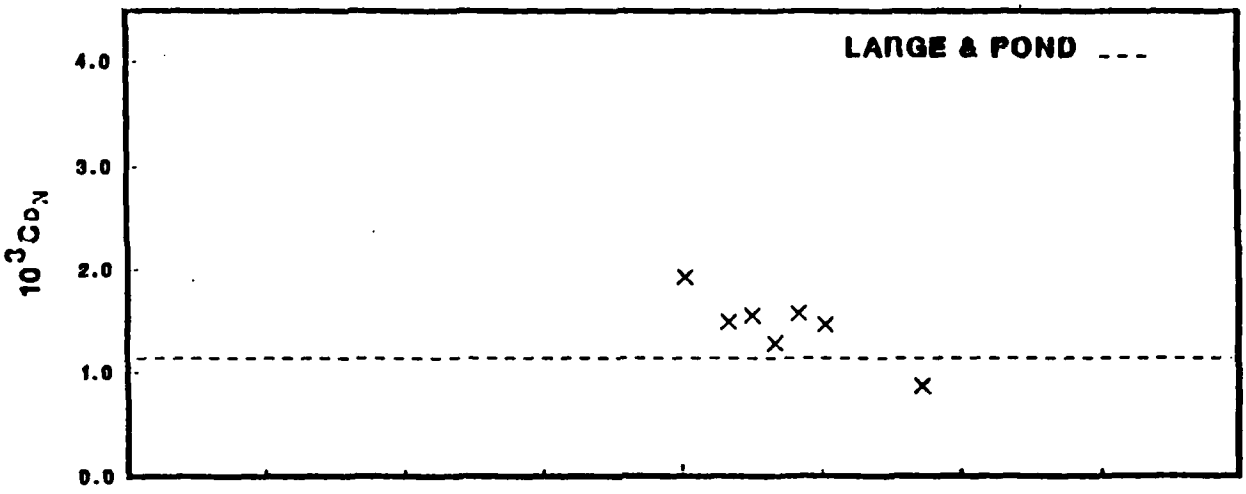

Figure 2b.

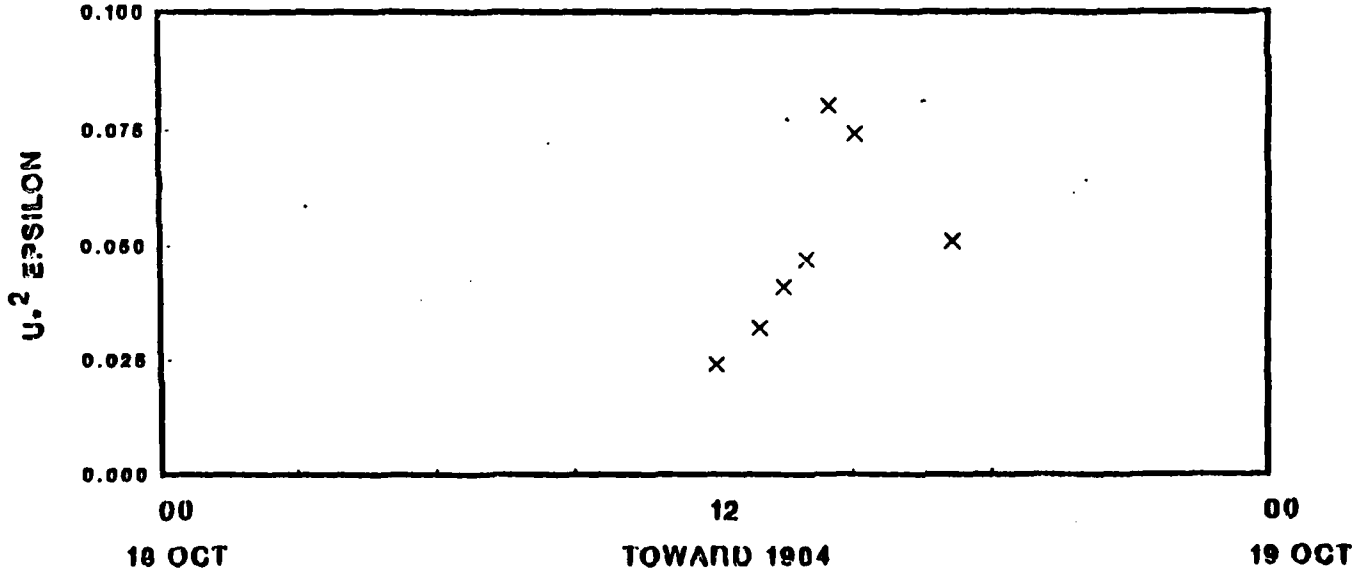

Figure 3a.

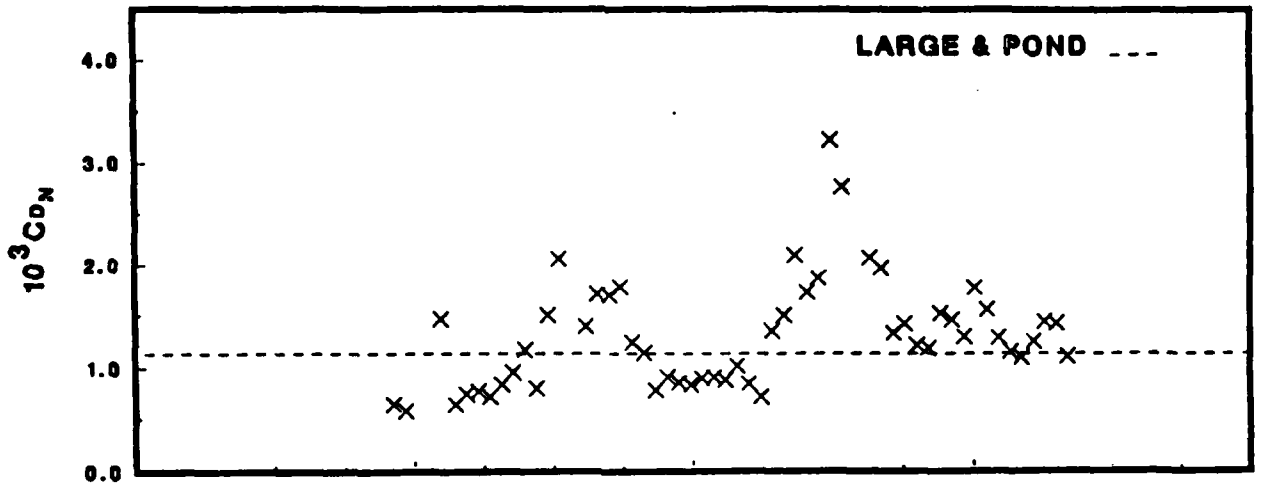

Figure 3b.

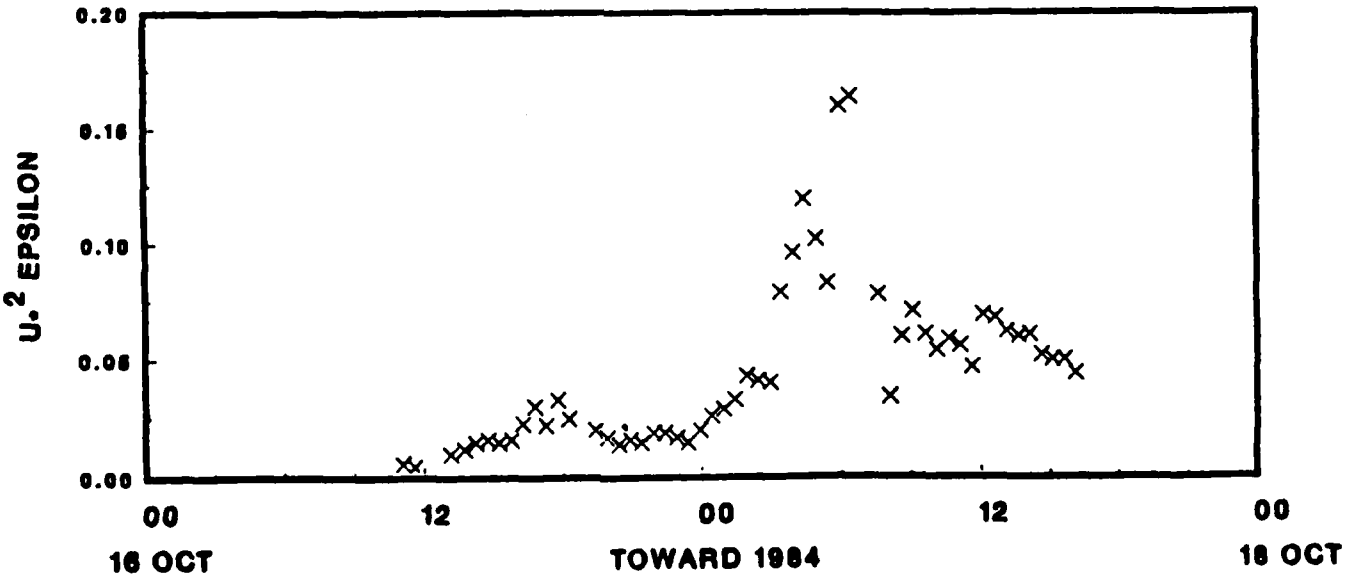

Figure 4a.

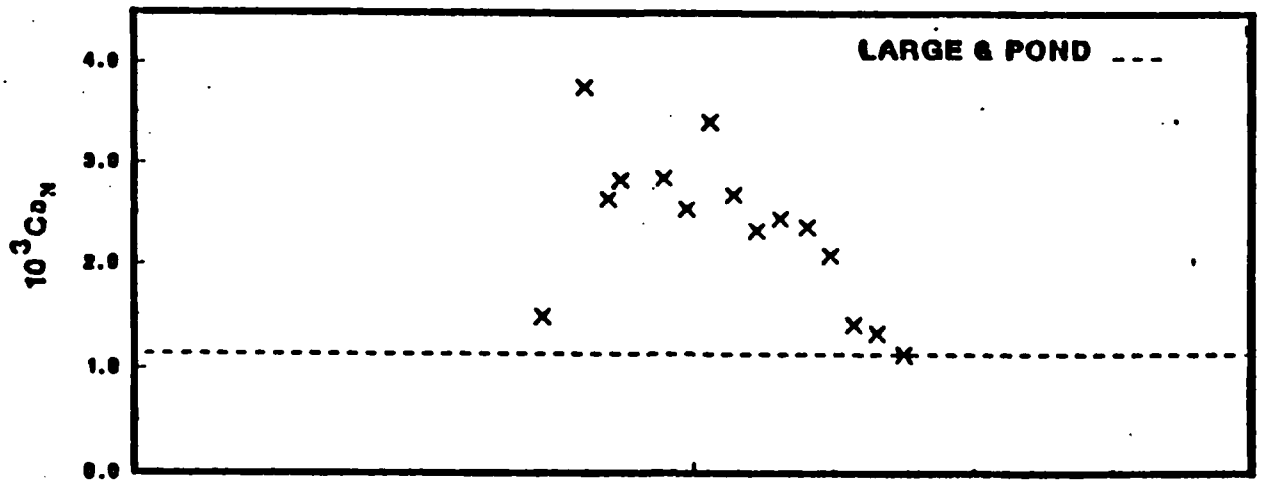

Figure 4b.

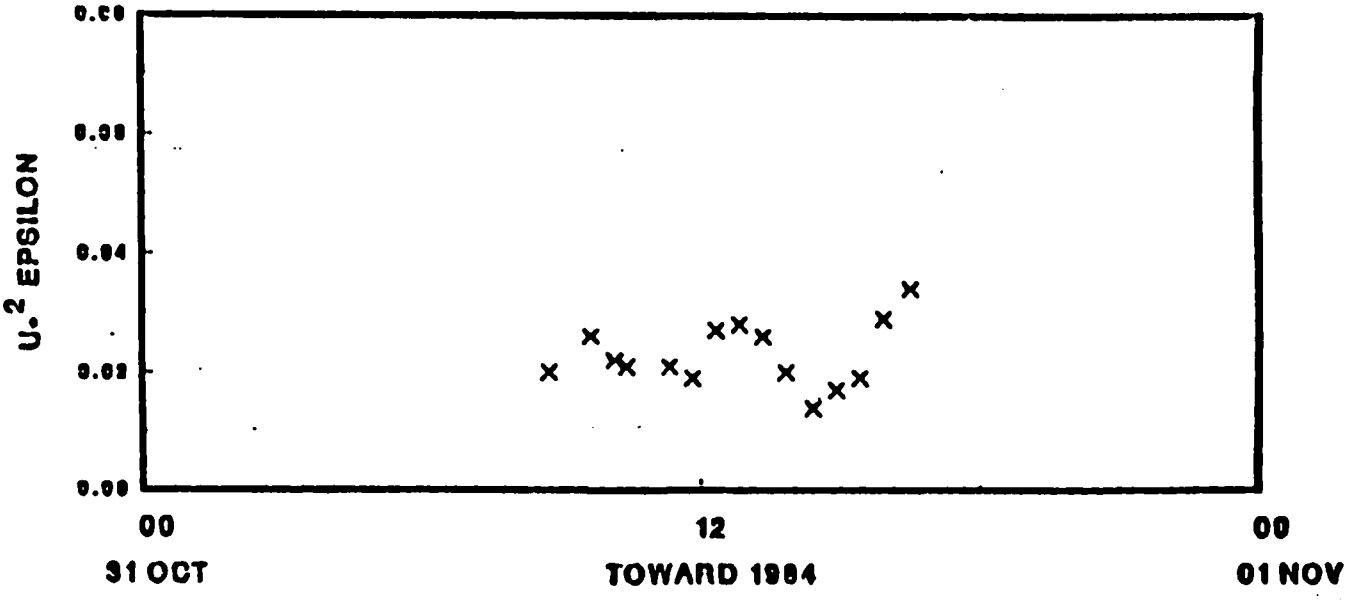

Figure 4c.

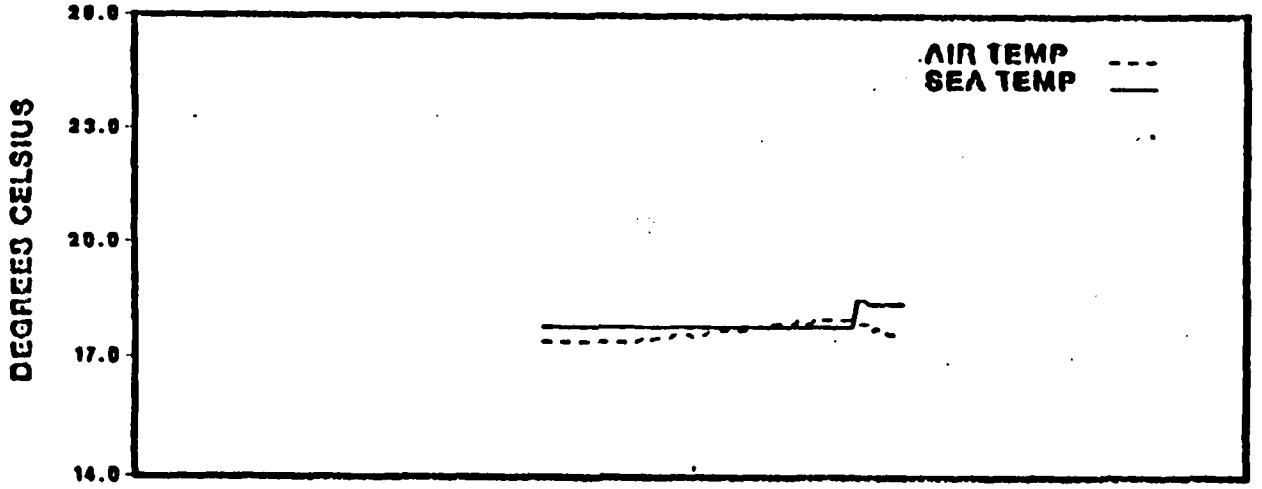

Figure 4d.

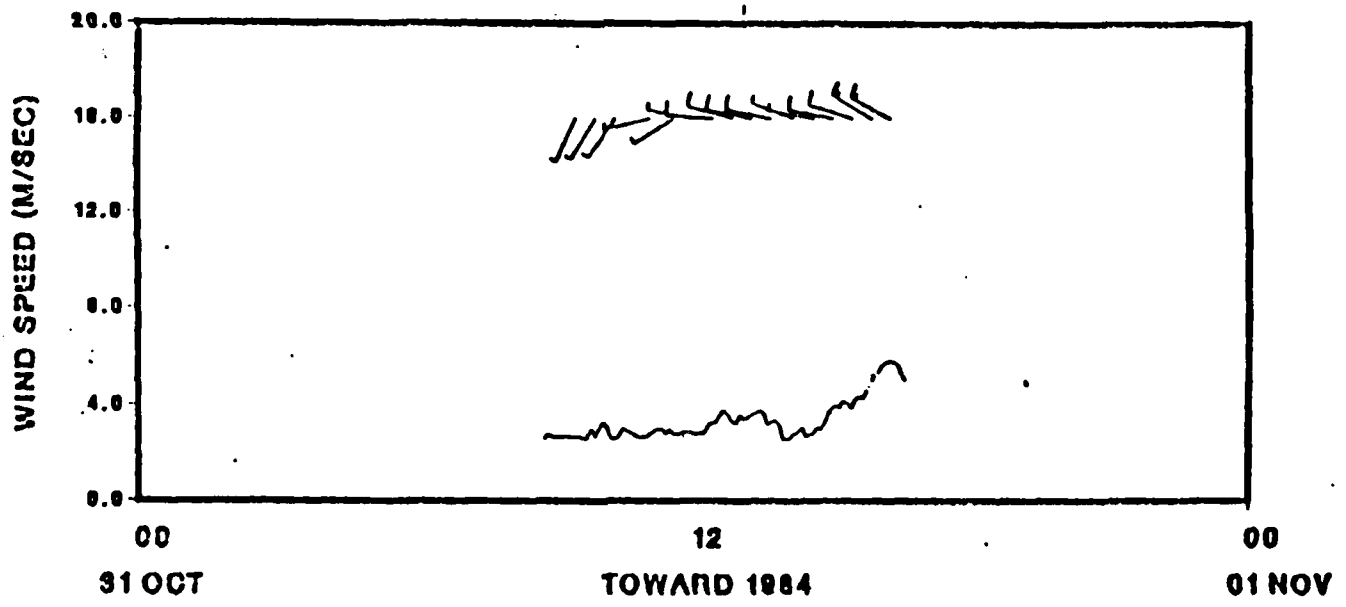

APPENDIX VI

PROCESSING OF JPL SAR FRAME:

AZIMUTHAL WAVES ON 31 OCTOBER 1984

by

Edmond K. Tajirian
Ocean Research and Engineering
La Canada, CA 91011

TABLE OF CONTENTS

LIST OF FIGURES

LIST OF TABLES

1. Background

In this section a brief overview of the SAR experiments and theories for imaging ocean waves is presented. The experimental results and the limitations imposed on them are reviewed. Predictions of the various SAR imaging theories are discussed. An overview of SAR flight data for the TOWARD experiment is also presented.

1.1. Introduction:

Images of ocean waves produced from the MARINELAND and MARSEN experiments have shown improved contrast or Peak-to - Baseline Ratios, PBR, by adjusting the focus parameters in the SAR optical processor. Only optical recording and optical processing were used in these experiments. These have limited dynamic range, and are less precise in determining ocean wave parameters and focus settings compared to digital processing.

It was considered essential in TOWARD 84/85 that digital processing provide the basis for careful assestment of the conflicting SAR imaging theories. Hence, SAR measurements were recorded in both optical and digital modes. Also, the images were processed in both optical and digital modes.

1.2. SAR FLIGHTS in the TOWARD EXPERIMENT

The CV-990 SAR flight pattern over the NOSC tower are shown in Figure 1 which shows the approximate bearings for the legs. The flight dates and duration over the tower in phase-1 are given in Table 1. The environmental conditions during these flights are shown in Table 2. A typical CV-990 flight pattern in phase-1 is outlined in Figure 2 and the JPL-SAR characteristics

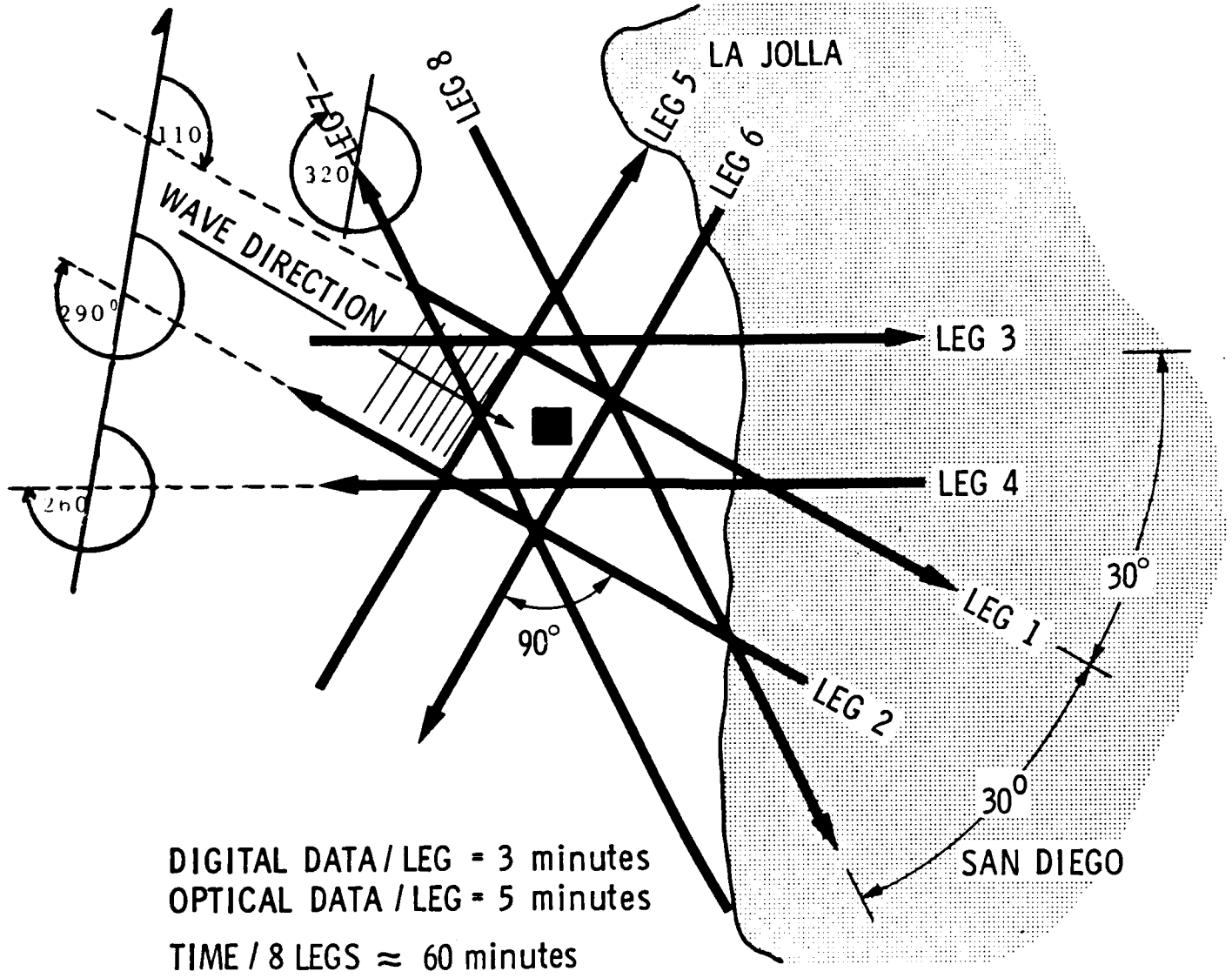

Figure 1. CV-990 SAR Flight Paths Over Tower.

Table 1. Aircraft Flights During Phase-I of TOWARD 84/85
The Flight Intervals are Noted for Each

	CV-990	F-4
2 October 1984		1046 - 1156
6 October 1984		1505 - 1600
7 October 1984		904 - 958
17 October 1984	1253 - 1536	
31 October 1984	1257 - 1542	1500 - 1614
4 November 1984	1512 - 1700	1131 - 1231
7 November 1984	1356 - 1640	

Table 2. Environmental Conditions During Flights in October-November, 1984: Phase-I.

Date, 1984	17 Oct	31 Oct	4 Nov	7 Nov
Time Analyzed	1250-1413	1300-1600	1512-1625	1412-1625
Wind Speed (knots)	15	6-8	5-7	10
Wind Direction (deg)	~275	~280	~300	~250
Mean Current (cm/sec) (5 cm Below Surface)	<5	<5	<5	~10
Significant Wave Height (cm)	126	124	158	110
Air T (°C)	17.2	17.5	18.5	17.5

DATE: 31 October 1984

PLATFORM: CV-990, Postflight

RADAR FREQUENCY: L-Band

WAVE DIRECTION: 300°

INCIDENCE ANGLE: 35°

WIND DIRECTION: 290°

PLATFORM ELEVATION: As Tabulated

PLATFORM SPEED: 450 knots

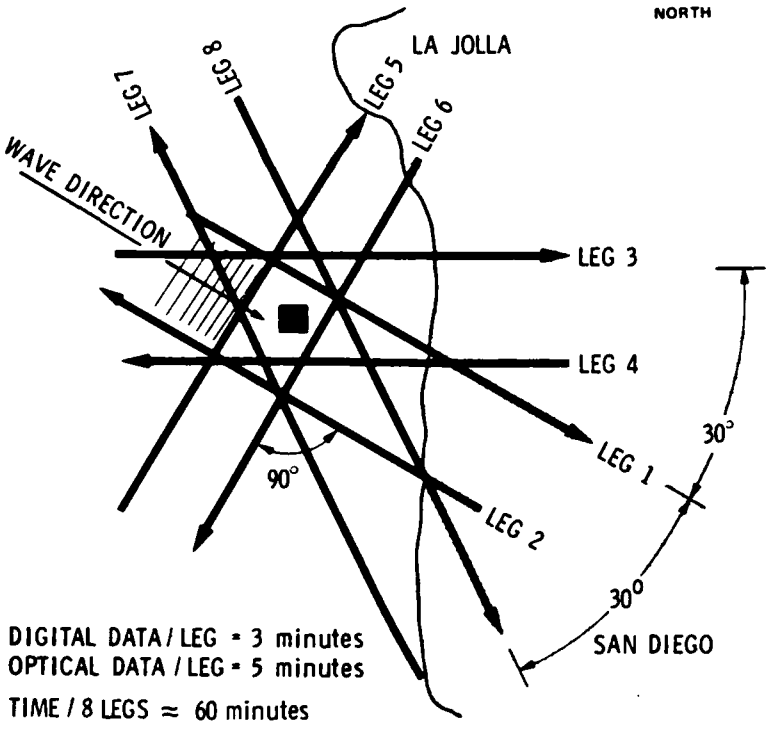

Flight Sequence

Altitude	Run	Leg	Time	A/C Heading	Radar Look Direct.
7,000	1	7	1257	320	R - 050
7,000	2	1	1307	110	R - 200
7,000	3	4	1316	260	R - 350
7,000	4	2	1319	290	R - 020
20,000	5	7	1343	320	R - 050
20,000	6	1	1351	110	R - 200
20,000	7	4	1358	260	R - 350
20,000	8	2	1450	290	R - 020
20,000	9	6	1429	200	R - 290
38,000	10	7	1455	320	R - 050
38,000	11	1	1503	110	R - 200
38,000	12	4	1512	260	R - 350
38,000	13	2	1528	290	R - 020
38,000	14	6	1539	200	R - 290

Figure 2. Typical CV-990 Flight Pattern Executed in Phase-I.

are given in Table 3.

Ten SAR frames have been selected by the SAR Data Analysis Committee for focusing studies. These are shown in Table 4. The frame that has been analized is for leg 1 at 38,000 feet altitude, collected on October 31, 1984. The processing for the other frames is now completed, and detailed analysis is presently in progress.

1.3 Theoretical and Experimental Background on Focusing Effects

The available theoretical and experimental investigations on focusing is reviewed here to provide the perspective for the focusing analysis discussed in this study. Defocusing has been related to motion of the ocean surface. Two such motions are dominant: 1) the phase velocity of dominant ocean surface waves, and 2) their orbital velocity. According to Jain (1978, 1981): the optimum image is obtained when the matched-filter of radar processor is adjusted in proportion to the azimuth component of the wave phase velocity. Also, Harger (1985 a,b) refers to the surface-wave phase velocity as the source for defocusing of the SAR images, and hence for the modeling and analysis of surface waves.

Alpers and Rufenach (1979) state that: the wave like patterns in the SAR image is caused by orbital motions and will occur even for uniform radar scattering cross sections. The motion causes degradation in azimuthal resolution and is dominant for azimuthally traveling waves. Also, they state that velocity bunching can cause an enhancement of ocean wave patterns, or the occurrence of two and possibly three intensity peaks per true wave length, depending on ocean and SAR parameters. Their work indicates that images can not be improved by refocusing the optical processor of the radar. Plant and Keller (1983) use a two-scale Radar Wave Probe simulation of the SAR to infer that

Table 3. Nominal SAR Data Processing Characteristics for JPL L-Band SAR.

4 OPTICAL Channels = HH - VV - HV - VH
4 DIGITAL SUBFRAMES = HH - VV - HV - VH
Angle of Incidence at Center of Image = 35°
Optical/Digital Slant Range Coverage = 7 km (Quad Pol Mode)
Optical/Digital Slant Range Coverage = 12 km (Dual Pol Mode)
Optical Along Track Coverage = 60 km
Digital Along Track Coverage (Raw) = 30 km
Digital Along Track Coverage (Image) = 11 km
Digital Image Size = 927 pixels range x 1024 pixels azimuth
Optical Image Size = 50 mm cross track, 1:250,000 along track
RFP = 3 x (CV-990 Ground Speed in m/s)
= 600 @ 200 m/s, 750 @ 250 m/s
Digital Image Pixel Spacings = 7.5 m Slant Range x 11.0 azimuth

Table 4. SAR Frames Especially Processed for Focusing Studies.

Days ——————→	17 Oct	31 Oct	4 Nov	7 Nov
Alt (feet)				
7,000		Legs 4, 7		
20,000	Leg 2	Leg 1	Leg 2	Leg 2
38,000/38,000		Legs 1, 2 4, 7		

SAR images are not faithful reproductions of cross-section variations over the surface. Distortions in the image are due to the velocity bunching mechanism. Application of focusing correction does not remove the distortions from the simulated image.

Based on experimental results, Shuchman and Shemdin (1983) indicate that, based on analyis of modulation depths as a function of focus setting in the SAR processor, the maximum in modulation depth occurs when the motion correction corresponds to a velocity that is of the order of the wave phase velocity of the dominant surface waves. This occurs for both azimuth- and range-traveling waves. Therefore, the detectability of these waves can be improved by focusing. Jain and Shemdin (1983) investigate this point in the MARSEN data using both radar and in-situ measurements. They show that the focus dependance for optimum imaging is that for a surface moving with the wave phase velocity. Also, azimuthally traveling waves are as visible as range traveling waves when the optimum focus setting is made.

2. Data Processing

In this section analysis of the digitally processed image, for leg 1, 38,000 feet altitude on 31 October 1984, provided by JPL is discussed. Examination of the visual images at different focus settings is described. The procedure for locating the data blocks on the visual images and then on the computer compatible (cc) magnetic tapes is presented. Definitions of the terms and parameters used, and the significance of the information collected are discussed. Processing methods that are not optimal (in the SNR sense) are compared to that which is optimal.

2.1. Examination Photographic Representations of Digitally Processed Images

A sample of digitally-processed image provided by JPL is shown in Figure 3 for one focus setting. JPL provided 15 such images at focus setting ranging from -1.75c to +1.75c, where c is the wave phase velocity of dominant surface wave. The image in Figure 3 is therefore referred to as the Black and White (B&W) image, for later comparison with computer-enhanced results.

2.2 Locating Data Blocks

Two blocks of data are shown in Figure 4, each block is 256 pixels (10.98m per pixel) by 256 pixels (10.98m per pixel). One block (No. 2) is in an area where the water depth is approximately 30 fathoms (60m). The second block (No. 3) is in an area where the water depth is approximately 13 fathoms (26m). The second block includes the NOSC tower where the wave measurements were carried out. All blocks have the same inner and outer ranges. The location of the data blocks are chosen such that they will contain the most visible waves, as shown is Figure 3. The NOSC tower location is shown in Figure 5.

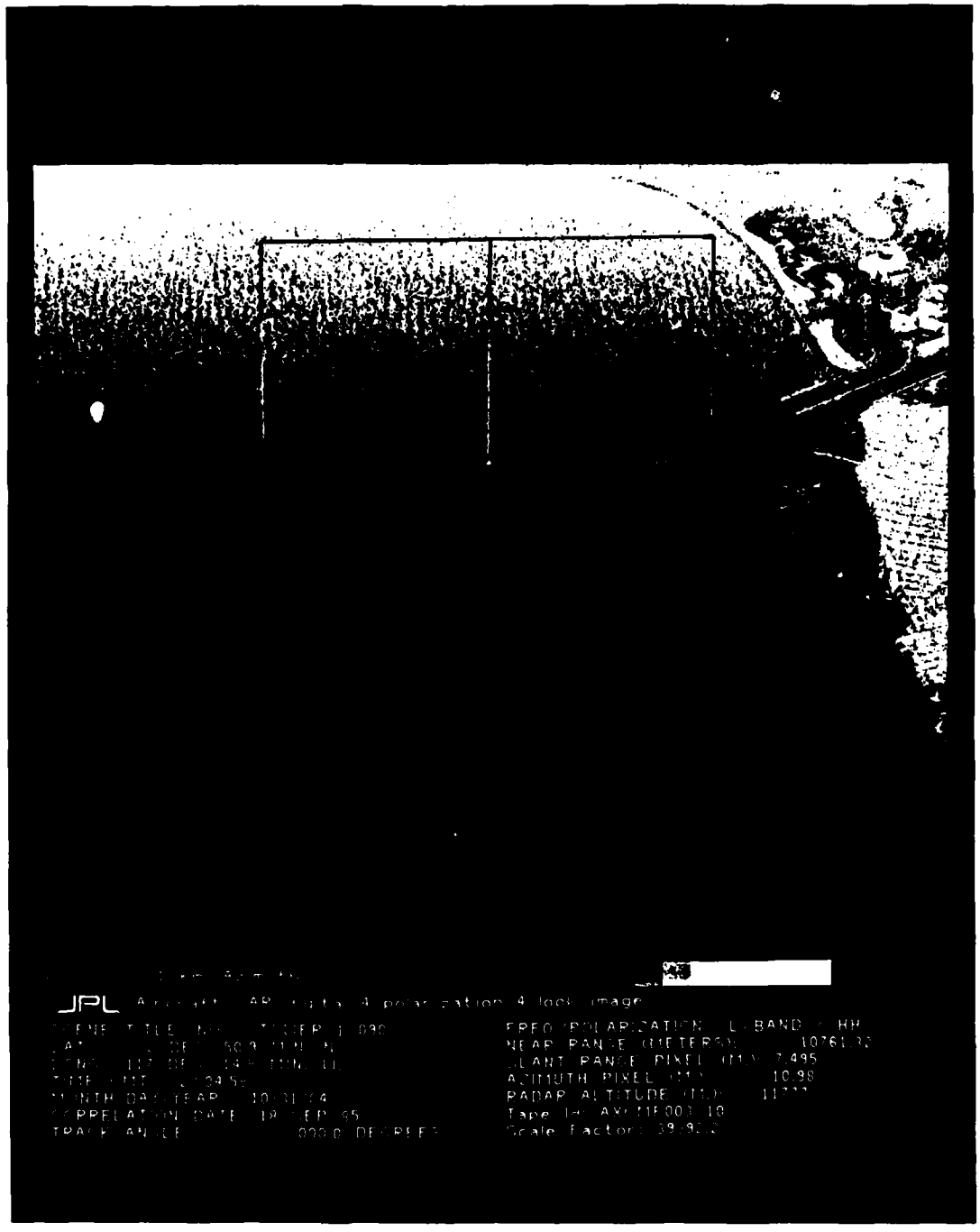

Figure 3. Sample of Digitally Processed Image Used in Present Analysis.

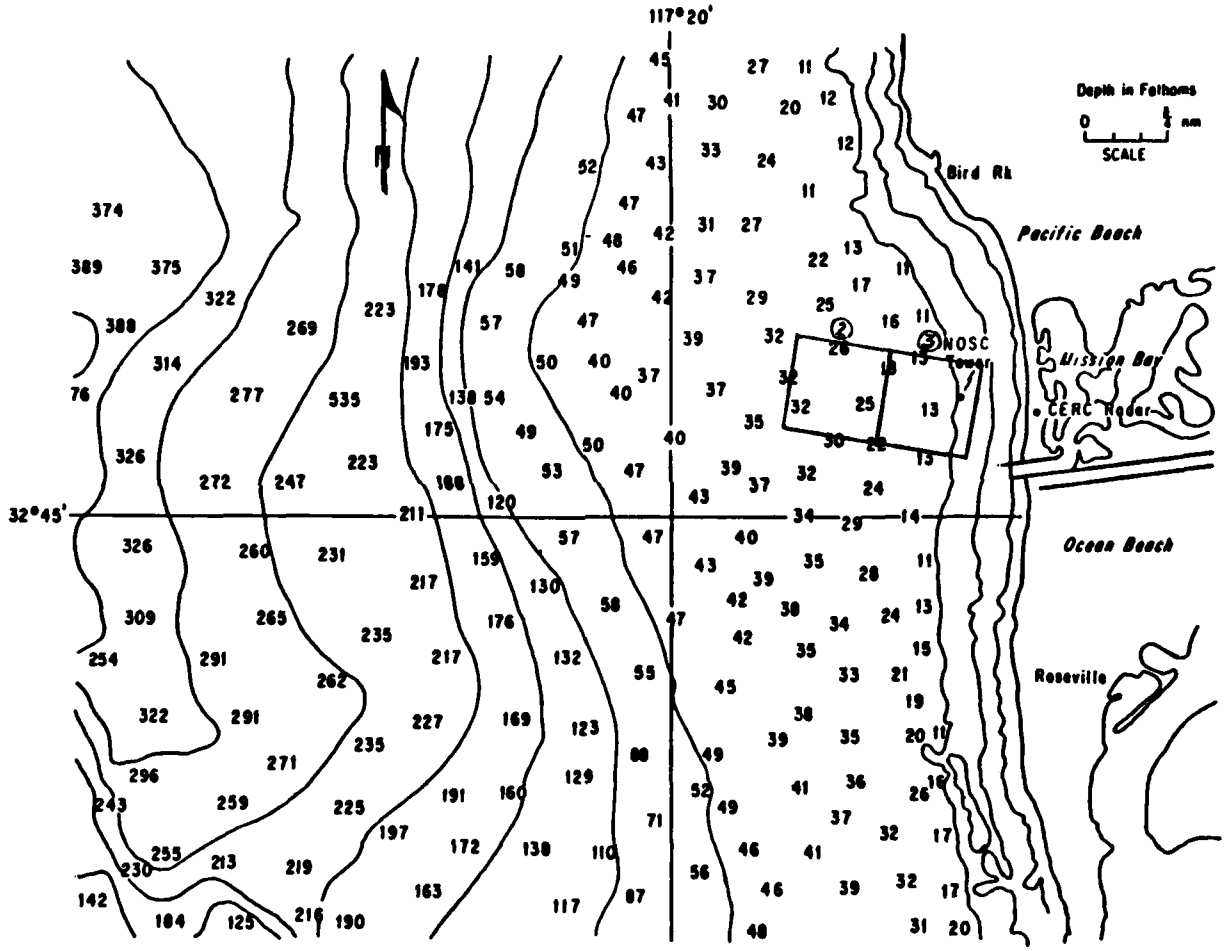

Figure 4. DATA BLOCKS Aproximate Location on Area Map (The depth contours are in fathoms).

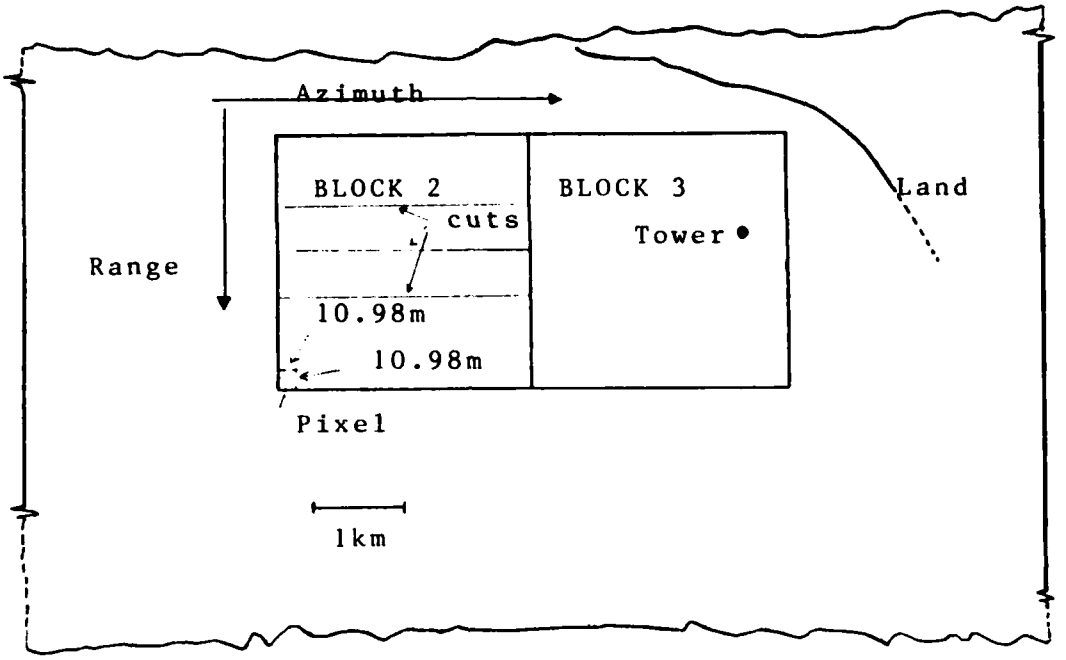

Figure 5. Recorded Data Blocks and Their Location on the Image.

2.3. Locating Data Blocks In Data Files

The tape format is such that each focus file has 1,280 blocks and each block contains 1,024 bytes. The 1,024 bytes compose one line along the azimuth (i.e. constant range) direction. There are 1,280 lines parallel to the azimuth direction, each is at a unique range. The lines are divided into 4 equal segments each in one block. Therefore, each line has 256 bytes in a block. Also, each block has 256 lines. The distance from the edge of the image is measured to the edge of the data block. This is converted to number of pixels using the scale 1 pixel = 10.98m. The number of pixels obtained is the number of lines (or blocks) to be skipped before reading the tape. For recording the data for block 2, the first 256 points of each line within the range limits of the block are skipped and the second 256 points (bytes) are recorded. In recording the third block data, the first 512 points of each range line is skipped and the following 256 points are recorded. This is done for 256 lines. Same procedure is used on all the focus files.

2.4. Averaging Methods

To investigate the spectra of dominant wave numbers, different smoothing and averaging methods are used. Space averaging refers to averaging values of a few pixels in the range direction at a given range value. This is done such that an equal number of pixels are taken on each side of the given range number , which is taken to be the range value of the cut. All cuts in the processing are taken to be parallel to the azimuth direction.

Wave number smoothing refers to averaging neighboring energy densities of the transform of an azimuthal cut. The average is over energy densities at equal number of points on each side of the given wave number.

Another wave-number domain averaging is averaging of spectra of different cuts. In this method, the corresponding

energy densities of the different transforms are averaged. This is called Wave number averaging.

2.5. Energy Considerations

The Total Energy of the Signal is defined as $\sum_n |f(n)|^2$, where f(n) are the space domain sampled signal. The Total Energy of the Spectrum is taken to be $\sum_{k^1} |F(k)|^2$ where F(k) is the discrete fourier transform of f(n) and k^1 includes all spectral points except k=0. From Parseval's relation for discrete transforms:

$$\sum_n |f(n)|^2 = N \sum_k |F(k)|^2 = N\left(\sum_{k^1} |F(k)|^2 + |F(0)|^2\right).$$

The total signal energy remains the same for all the focuses for a given range. This is true for all the range cuts examined.

2.6. Opimality of Processing In Terms of Signal To Noise Ratio

Different data processing methods were carried out to reach a method that generates a spectrum with a high signal to noise ratio-SNR. The different processing methods tested are briefly discussed below.

In processing trials with 3 range cuts, the cuts are taken at ranges = 64, 128, 192 (corresponding to incidence angles = 32.5^0, 34.9^0, 37.1^0, respectively). The discrete Fourier Transforms, DFT, of each cut is taken. The spectral energy is calculated and smoothed over 5 wave numbers. The smoothed spectra are then nomalized and averaged. The averaged spectrum is plotted.

For processing trials with 5 range cuts, the cuts are taken at ranges = 64, 96, 128, 160, 192 (corresponding to incidence angle = 32.5^0, 33.7^0, 34.9^0, 36.0^0, 37.1^0, respectively). The procedure mentioned above for 3 cuts is then repeated for the 5 cuts.

For processing trials with 5 range cuts and no area normalization, five cuts are taken at ranges = 64, 96, 128, 160, 192. The DFT's of each cut are calculated. The energy spectrum is obtained and smoothed over 5 wave numbers. The smoothed spectra of the 5 cuts are then averaged.

In processing with lateral pixel averages (referred to as IΔ), where IΔ = 40 at range 128 implies a range cut at 128 that is averaged over 81 pixels (128 $\pm$ 40 pixels). The DFT is taken for this space averaged signal and the energy spectrum then calculated. Similarly, for IΔ = 19, the procedure implies that the averaging is done over 39 pixels (128 $\pm$ 19). For IΔ = 15, the same procedure implies averaging over 31 pixels (128 $\pm$ 15).

The above processing methods are compared in terms of SNR values, where the SNR is defined as the ratio of the energy density at the dominant wave number to the background energy density. A sample energy spectrum with the background level shown is given in Figure 6. The SNR values for different processing trials are given in Table 5. From Table 5 it is seen that IΔ = 15 processing trial produces the largest SNR values for all focus settings. Hence, this averaging trial is adopted as the optimum processing technique for all the SAR data.

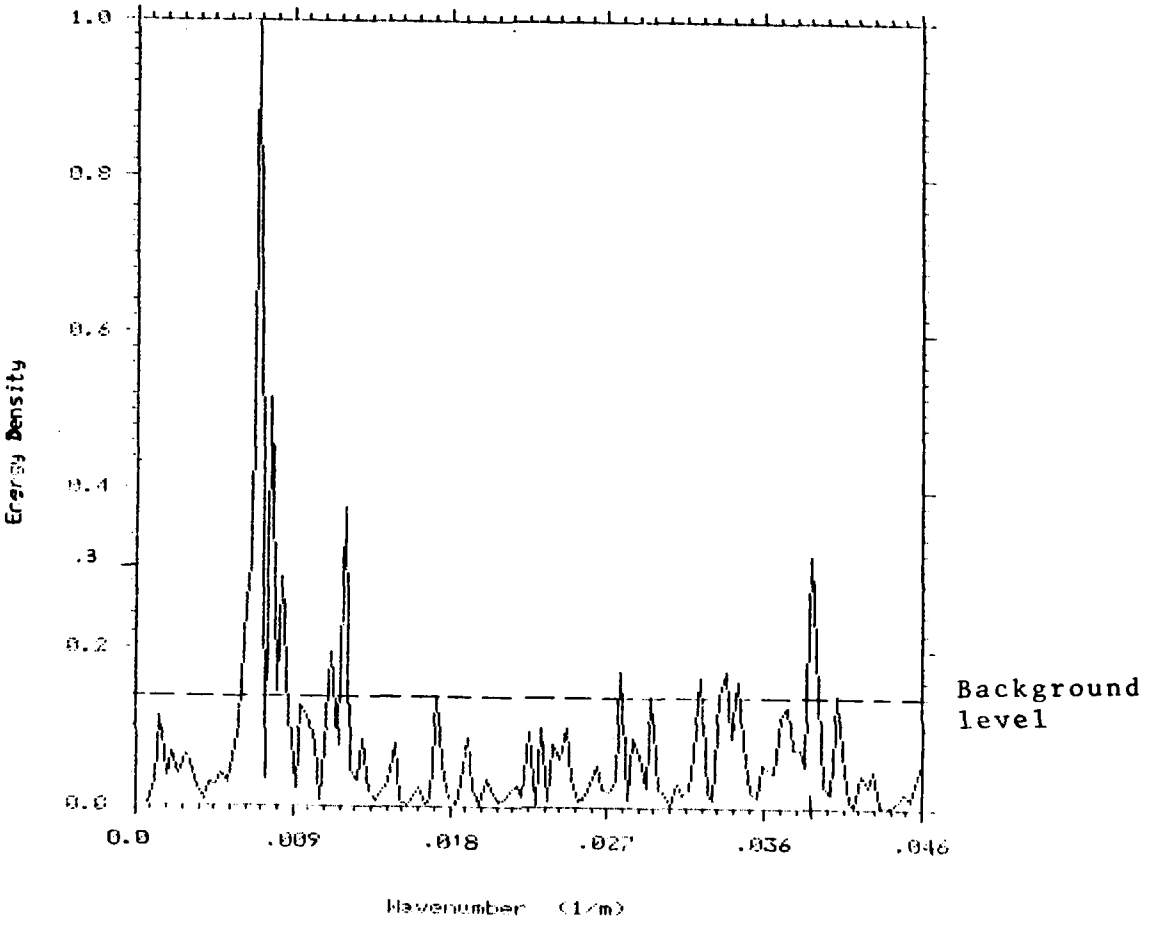

Figure 6. A Spectrum With Noise (background) Level Indicated Approximately (SNR≅7.1).

Table 5. SNR as a Function of Focus
For the Different Processing Methods.

Processing Method	Focus														
	-7	-6	-5	-4	-3	-2	-1	0	1	2	3	4	5	6	7
5 Range Cuts Normalized	2.	2.2	2.	2.	2.	2.5	3.3	3.3	2.6	2.3	2.2	2.5	2.3	2.5	2.0
5 Range Cuts No Normilization	2.0	2.0	2.1	2.	2.	2.5	2.8	2.6	2.5	2.2	2.2	2.2	2.5	2.5	2.4
3 Range Cuts	1.	1.	1.	1.	1.	1.	1.	1.	1.	1.	1.	1.	1.	1.	1.
IΔ = 40	-	-	-	-	-	-	4.8	4.8	5.6	7.1	7.1	8.3	8.3	8.3	8.3
IΔ = 19	4.6	3.8	3.3	3.3	6.3	6.3	6.3	6.3	7.1	6.3	6.3	9.1	9.1	7.14	7.14
IΔ = 15	5.	4.2	3.9	3.3	3.8	7.1	7.1	8.3	8.3	8.3	10.	10.	10.	10.	10.

3. Results

In this section the results from the adopted processing method are discussed. The dependence of the signal energy on incidence angle (range) and on focusing is presented. The dependence of the dominant wave energy density on focus is shown. The dependence of the energy in the non-zero part of the wave number spectrum is calculated vs. range and focus setting.

3.1. Dependence of Energy Density at Dominant Wave On Focusing

The plot of the energy density as a function of focus setting is given in Figure 7. Here, the dominant wave number is at a wave that is 140m long. Figure 7 shows energy density levels with no wave number smoothing (N =0), and with wave number smoothing over 3 contiguous wave numbers (N = 3). The values at optimum focus corresponding to N = 0 and N = 3 are 19.5 and 10.2, respectively. When defocused, the spectral density values are 6.2 and 4.8, respectively corresponding to N = 0 and N = 3. The location of the peak values are in the expected region according to the theories presented by Jain (1979) and possibly Harger (1985). Symmetric extension of the curves gives a central peak between foces +3 and +4 for both N = 0 and N = 3 curves, shown in Figure 7. These results indicate that the optimum focus setting is between .75c (focus +3) and C (focus +4), where C is the phase speed of the dominant ocean wave.

The Peak-to-Base-Ratio (PBR) Curves are given for N = 0 and N = 3 in Figure 8. The PBR is defined as the ratio of the energy density at the dominant wave number to the energy density of the dominant wave number for the defocused spectrum. The corresponding PBR's are 3.21 and 2.14 for N = 0 and N = 3, respectively. The optimum focus is approximately 0.8 the phase velocity. For comparison, the PBR values by Jain and Shemdin (1983) are shown in Figure 8.

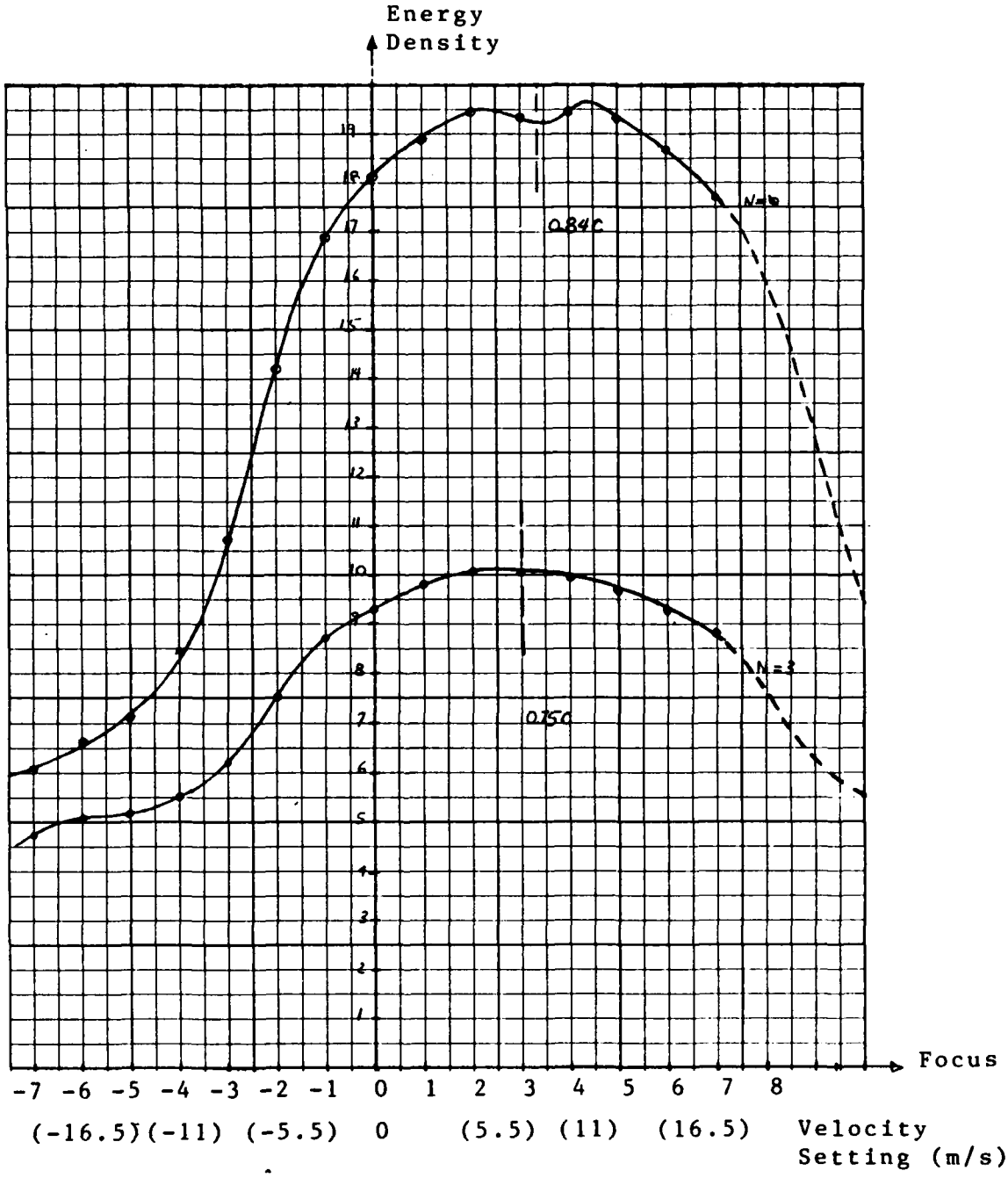

Figure 7. Energy Density at λ=140m vs. focus; $\theta_i = 34.9^0$.

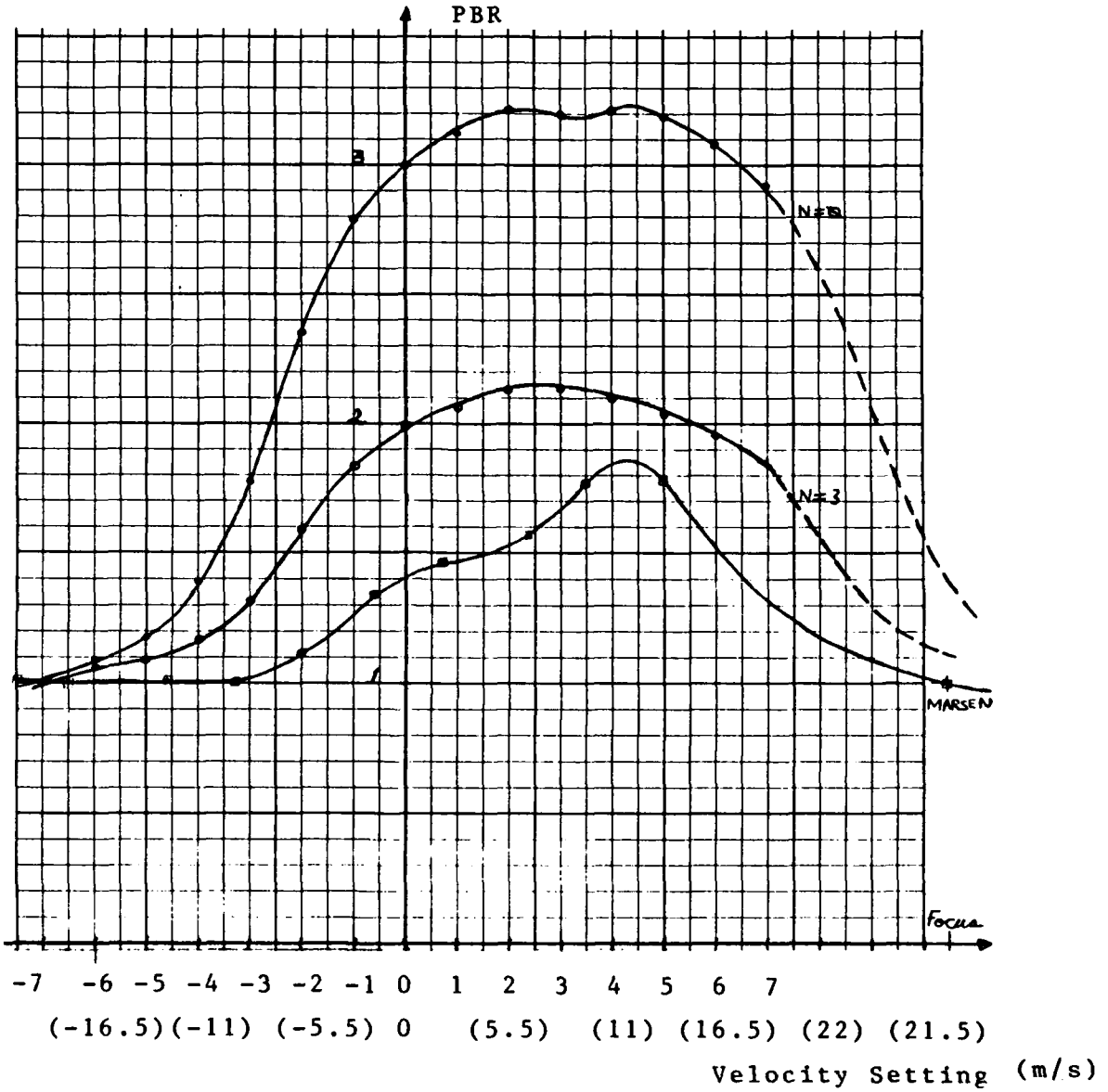

Figure 8. PBR at λ = 140m and MARSEN PBR vs. Focus. (IΔ=15, Range=128).

3.2. Total Energy Dependence on Incidence Angle and Focus Setting

The total energy decreases monotonically with increasing range (increasing incidence angle-θ_i), as shown in Table 6. This total energy is insensitive to focusing. If the D.C. is removed the remaining energy at each focus setting exhibits a local maximum at range = 128 ($\theta_i = 34.9^0$), as shown in Figure 9. This peak is sharpest for the optimum focus setting (+4).

Without D.C., the remaining energy also shows a dependence on focus setting. This dependence is plotted for the cut at range = 128 ($\theta_i = 34.9$) in Figure 10. This Figure shows the total energy to vary smoothly as a function of focus setting, and to reach a peak at focus setting (+3). The equivalent PBR graph is shown in Figure 11, where the maximum PBR value is 1.96. Here, PBR is defined as the ratio of the total energy of the spectrum without D.C. to the total energy of the defocused spectrum (without D.C.).

Table 6. Dependence of Total Energy (Including D.C.) on Incidence Angle.

Focus	Total Energy		
	30.0^0	33.9^0	37.1^0
-7	11.89×10^6	6.810×10^6	3.572×10^6
-6	11.89×10^6	6.822×10^6	3.580×10^6
-5	11.77×10^6	6.750×10^6	3.531×10^6
-4	11.70×10^6	6.683×10^6	3.509×10^6
-3	11.70×10^6	6.671×10^6	3.524×10^6
-2	11.69×10^6	6.680×10^6	3.529×10^6
-1	11.58×10^6	6.633×10^6	3.509×10^6
0	11.45×10^6	6.567×10^6	3.493×10^6
1	11.42×10^6	6.550×10^6	3.502×10^6
2	11.43×10^6	6.573×10^6	3.523×10^6
3	11.40×10^6	6.569×10^6	3.523×10^6
4	11.39×10^6	6.564×10^6	3.519×10^6
5	11.43×10^6	6.579×10^6	3.525×10^6
6	11.49×10^6	6.609×10^6	3.533×10^6
7	11.54×10^6	6.643×10^6	3.541×10^6

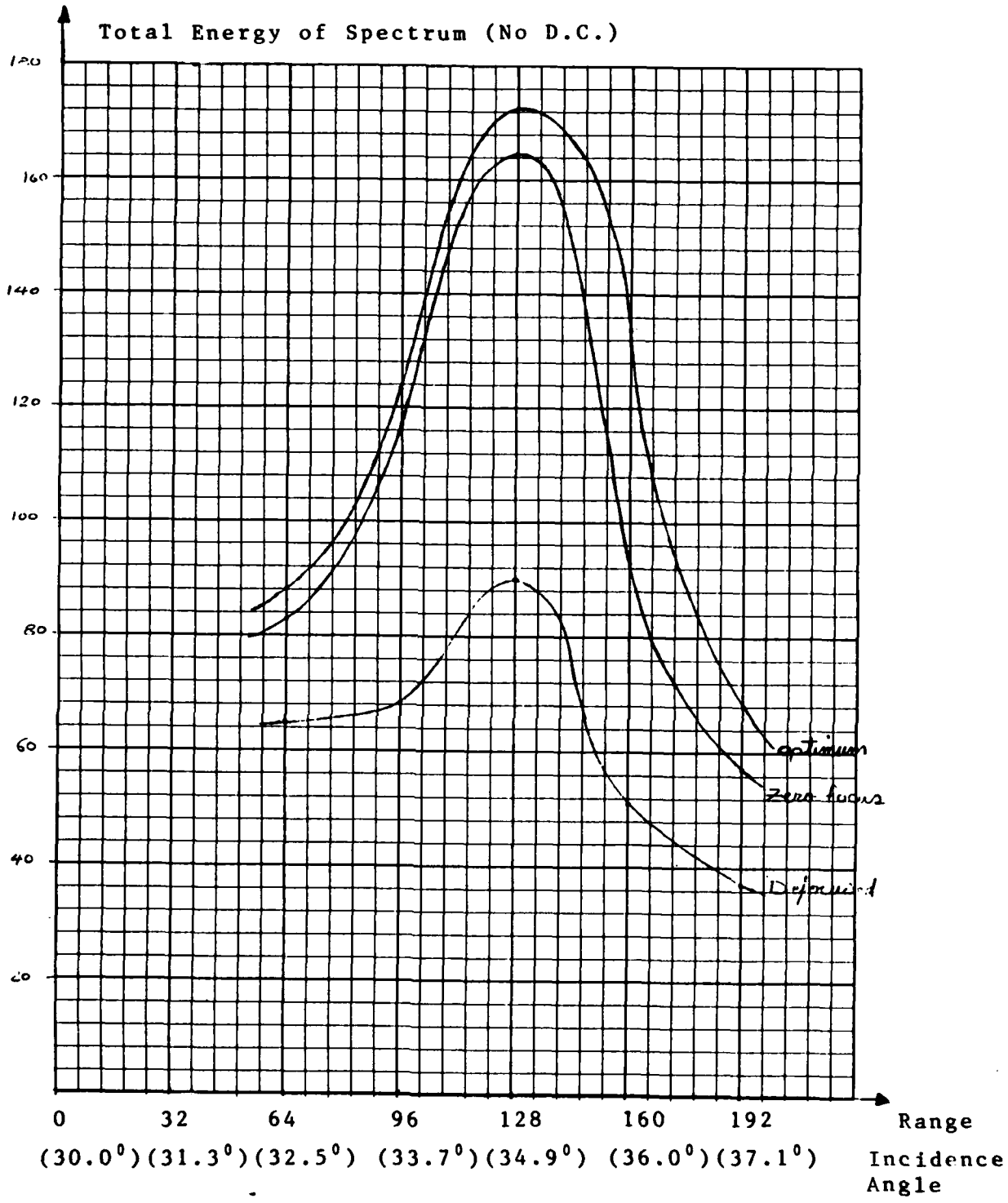

Figure 9. Total Spectrum Energy vs. Range (IΔ=15).

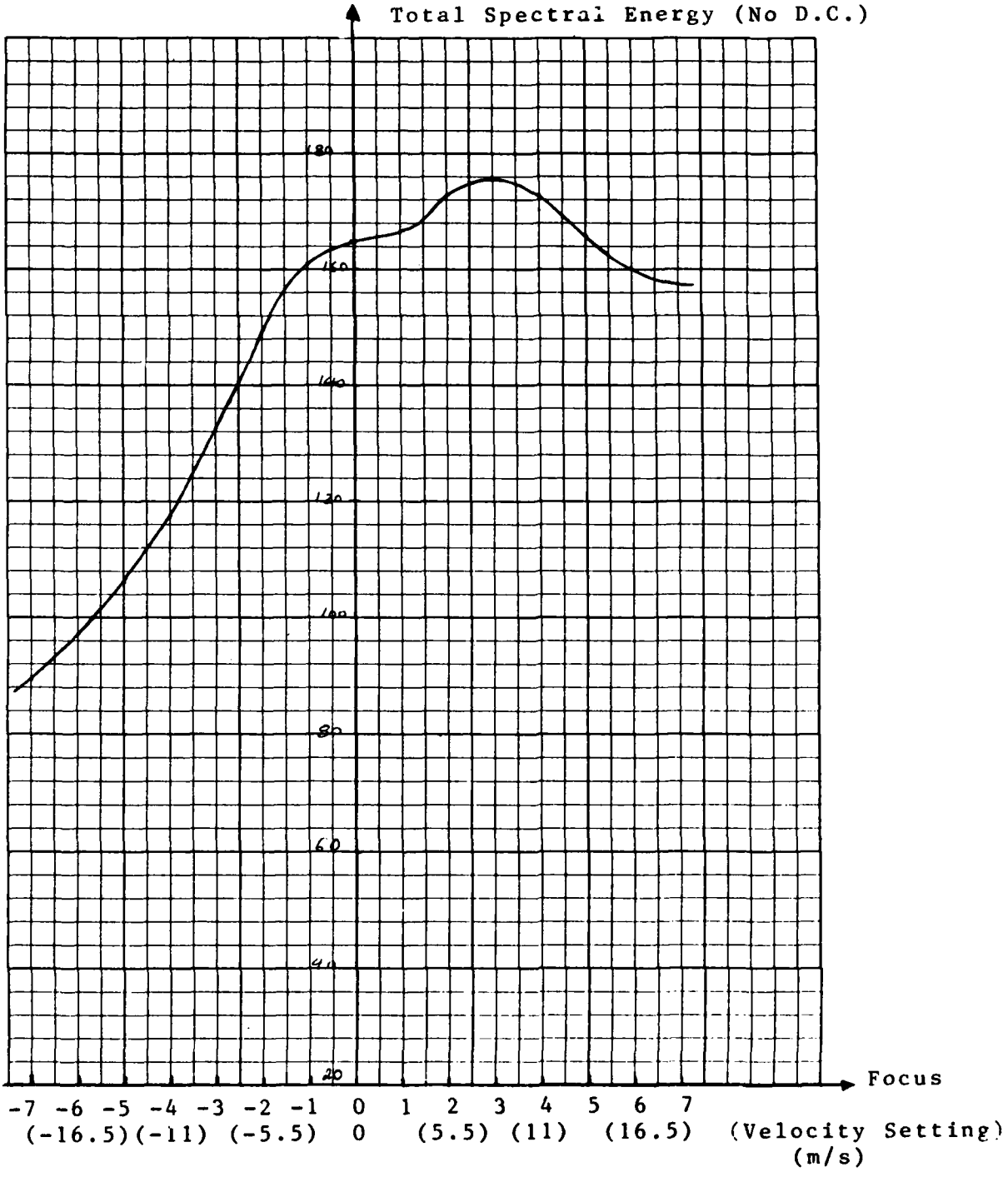

Figure 10. Total Spectral Energy vs. Focus (Range=128, IΔ=15).

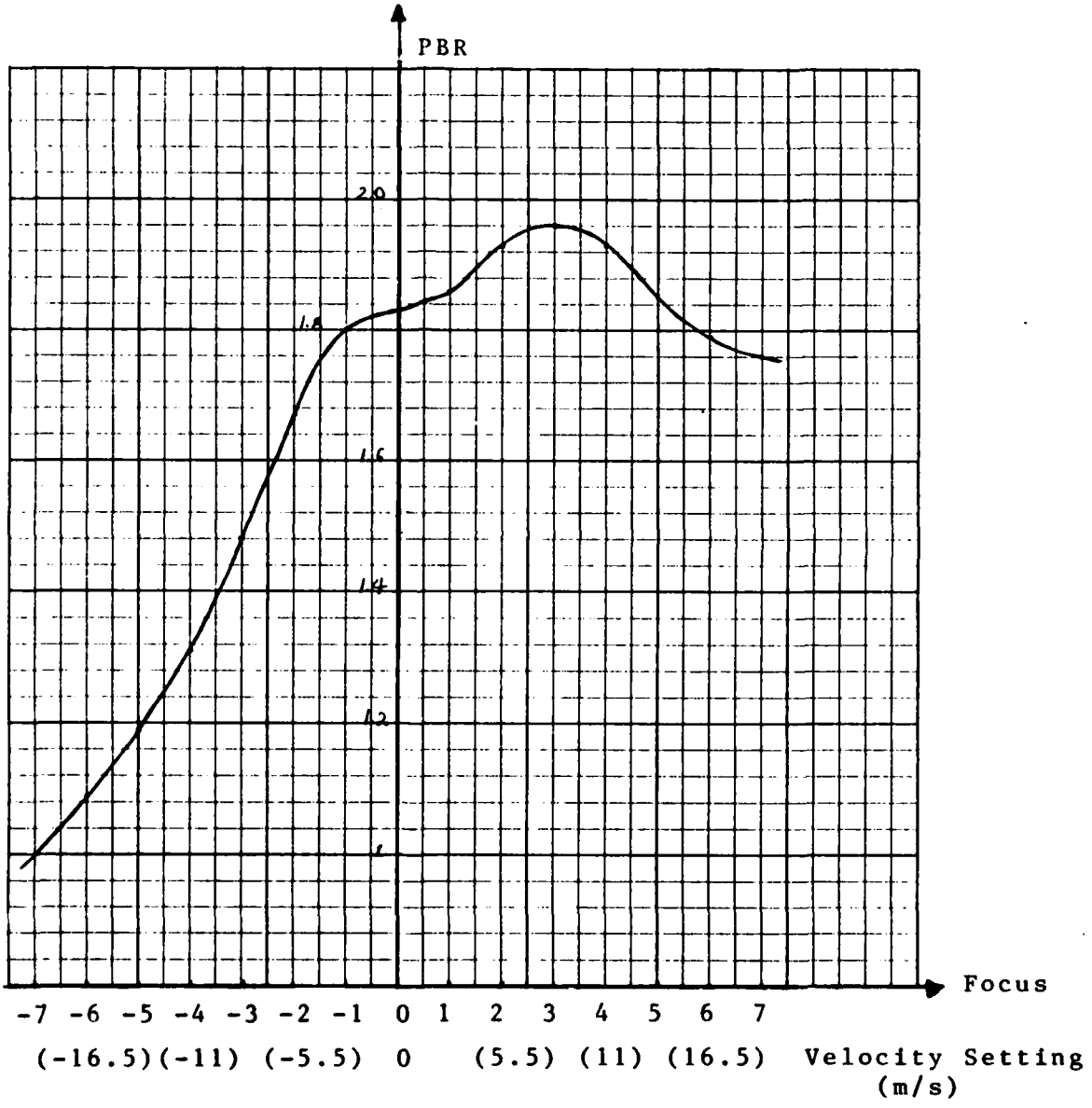

Figure 11. PBR vs. Focus (PBR=$E/E_{defocused}$, Range=128, 1Λ=15).

4. Summary and Conclusions

Different processing methods have been tested on one image data. Processing with IΔ = 15 (See section 2.6.) produced the largest signal to noise ratio. The dominant wave length is found to be 140 meters. The plot of the energy density at the dominant wave number as a function of focus setting indicates a peak energy density value at a speed that is of order of wave phase speed. Also, the non-D.C. signal energy variation with focus peaks at focus setting of the order of wave phase speed.

5. References

Alpers, W. and Bruening, C. (1985) "On the Non-Linearity of the Synthetic Aperture Radar Response to Moving Ocean Surface Waves," Private Communication.

Alpers, W. and Rufenach, C. (1979) "The Effect of Orbital Motions on Synthetic Aperture Radar Imagery of Ocean Waves," IEEE Trans. Ant. and Prop., Vol. AP-27, No. 5.

Harger, R. (1985) "The SAR Image of Short Gravity Waves on a Long Gravity Wave: An Explication," Submitted to IEEE J. Ocean. Eng.

Harger, R. (1985) "Some Preliminary Comparisons of the Predictions of a Fundamental SAR Imagin Model and Data From the TOWARD Experiment," Private Communication.

Ippen, A. Editor (1966) "Estuary and Coastline Hydrodynamic" McGraw Hill, N.Y.

Jain, A. (1978) "Focusing Effects in the Synthetic Aperture Radar Imaging of Ocean Waves," Appl. Phys.,15, 323-333.

Jain, A. (1981) "SAR Imaging of Ocean Waves: Theory," IEEE J. Ocean. Eng., Vol. OE-6, No. 4.

Jain, A. and Shemdin, O. (1983) "L-Band SAR Ocean Wave Observations During Marsen," J.G.R., 88, 9792-9808.

Oppenheim, A. and Shafer, R. (1975) "Digital Signal Processing," *Prentice-Hall, Englewood Cliffs.*

Plant, W. and Keller, W. (1983) "The Two-Scale Radar Wave Probe and SAR Imagery of the Ocean," J.G.R., Vol. 88, No. C14, PP. 9776-9784.

Shuchman, R. and Shemdin, O. "Synthetic Aperture Radar Imaging of Ocean Waves During the MARINELAND Experiment," IEEE J. Ocean. Eng., Vol. OE-8, No. 2.

Skolnik, M. (1970) "Radar Handbook" McGraw-Hill, N.Y.

APPENDIX VII

SAR IMAGERY SIMULATED FROM TWO-SCALE RADAR WAVE PROBE RETUREN

William J. Plant

Naval Research Laboratory
Washington, D.C. 20375

The coherent ouput from NRL's L-Band, pulsed radar which was mounted on the NOSC tower during the TOWARD experiment was used to simulate SAR Imagery of the ocean. This analog output of the radar was beat down to a 60 Hz offset frequency and recorded on analog FM magnetic tape during the experiment. In the laboratory it was digitized at a rate of 1024/T Hz where T is the maximum SAR integration time for which simulation is desired. Digitized data were stored on nine track magnetic tape and subsequently read into the simulation program. There the simulation proceeded as detailed in Plant and Keller (JGR, 88, p. 9976, 1983). Basically, the raw data were both averaged after squaring and Fourier transformed over an integration time which could be T, T/2, or T/4. The transform was performed after clipping the data and multiplying by a chirped, offset cosine signal whose chirp frequency was related to the focus adjustment. The power spectrum derived from this transformed signal was then convolved with the squared and averaged signal which had been normalized to yield cross section. This process gave a simulated value for the spectrum every T/4 seconds according to the relation

$$I(x_0) = \int_{-L/2}^{L/2} \sigma_0(x)\, \psi(x_0 - x)\, dx$$

where X_o was determined from the time by multiplying by the phase speed of the dominant ocean wave and $\Psi(X_o - x)$ was obtained from the above-mentioned power spectrum $\Psi(f)$ using the relation

$$f = \frac{R_o V (X_o - x)}{\pi R_o} .$$

Note that only simulations of az muthal cuts through a SAR image are produced by the above procedure. Subsequent processing involved obtaining power spectra of the simulated SAR intensity images and averaging several of these spectra together to form the final clutter-averaged SAR image. Examples of the results of these simulations are shown in the following figures along with power spectra of the cross sections obtained during the process. All simulations shown correspond to the 38,000 ft flights of the SAR on October 31, 1984.

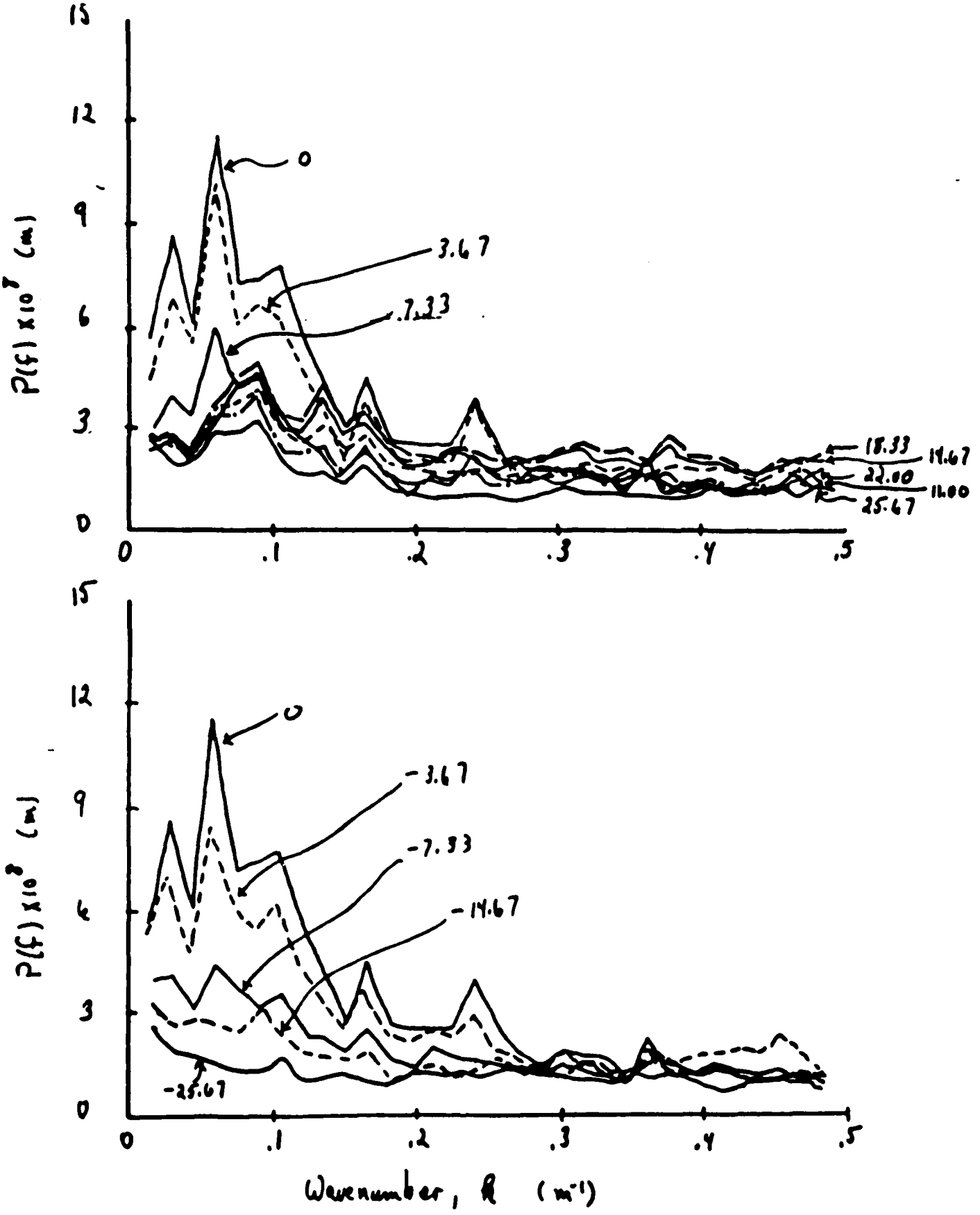

Figure 1. Effect of Focus on Simulated Image Spectrum - $\vec{V} \cdot \vec{k} = \cos(11°)$, Leg No. 1, 10/31/84, Single-Look, N = 27, V/R = 0.019 Hz, T = 2.2 sec.

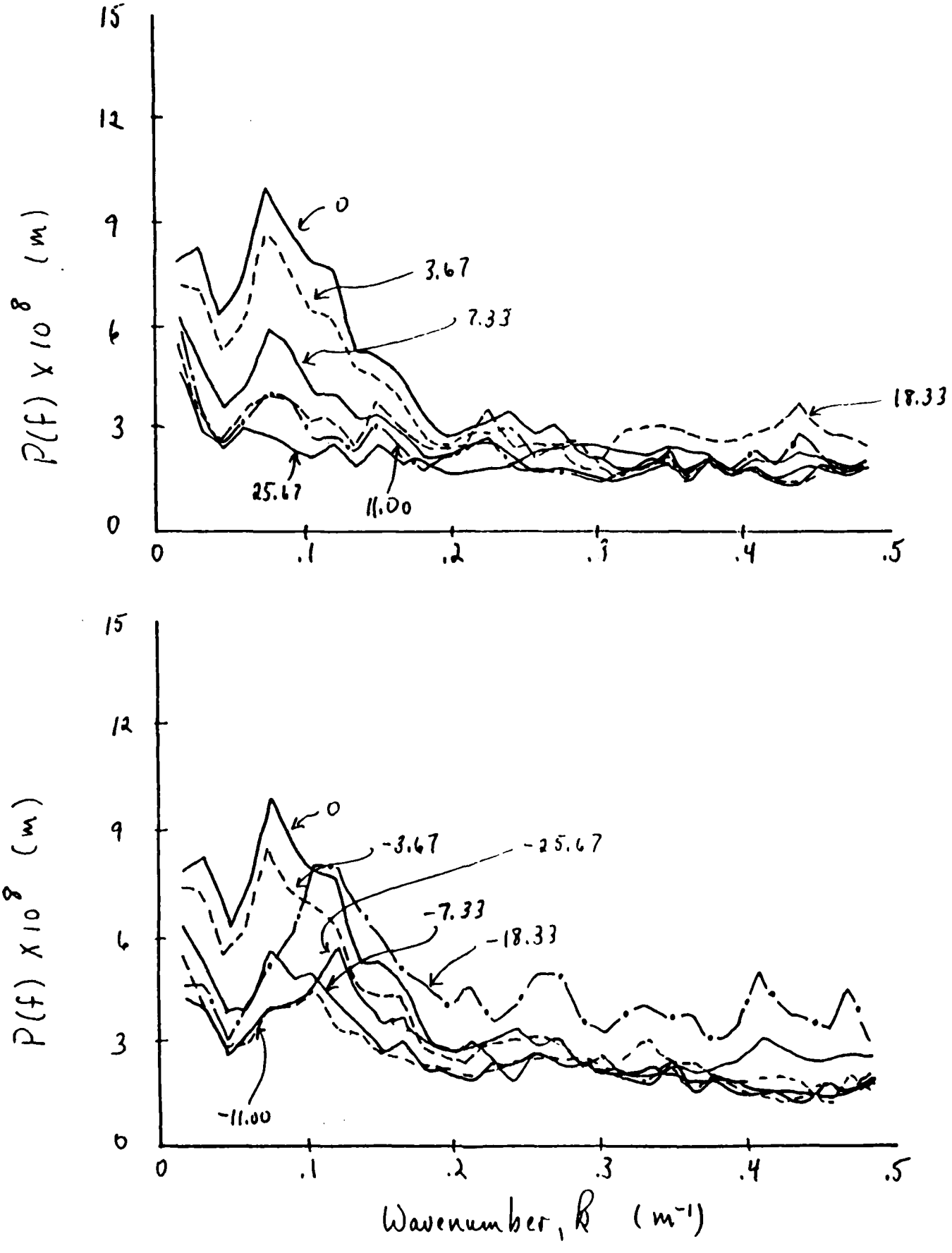

Figure 2. Effect of Focus on Simulated Image - $\vec{V} \cdot \vec{k} = \cos(-176°)$, Leg No. 2, 10/31/84, Single-Look, N = 46, V/R = 0.015 Hz, T = 2.6 sec.

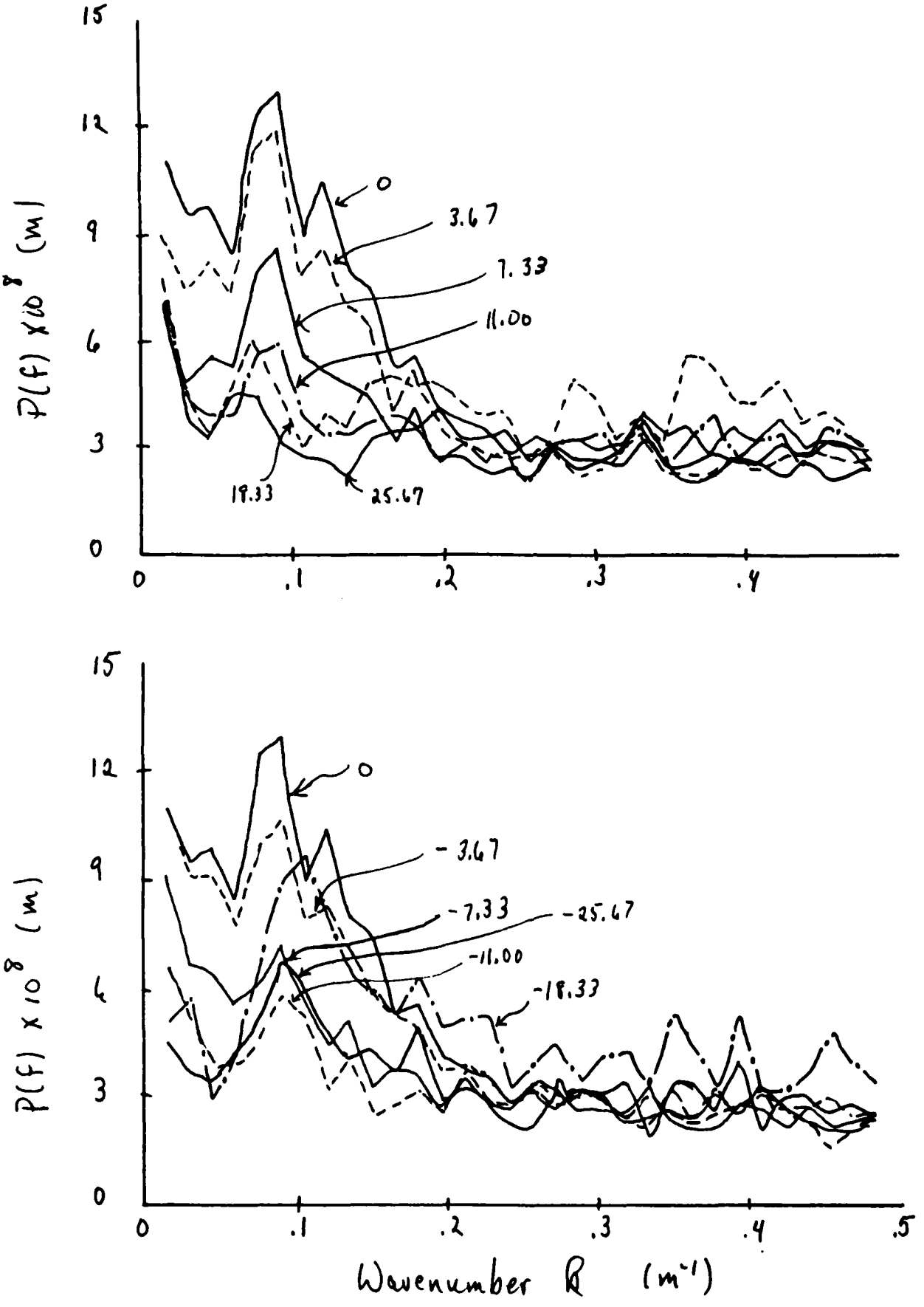

Figure 3. Effect of Focus on Simulated Image- $\vec{V} \cdot \vec{k} = \cos(158°)$, Leg No. 4, 10/31/84, Single-Look, N = 29, V/R = 0.015 Hz, T = 2.6 sec.

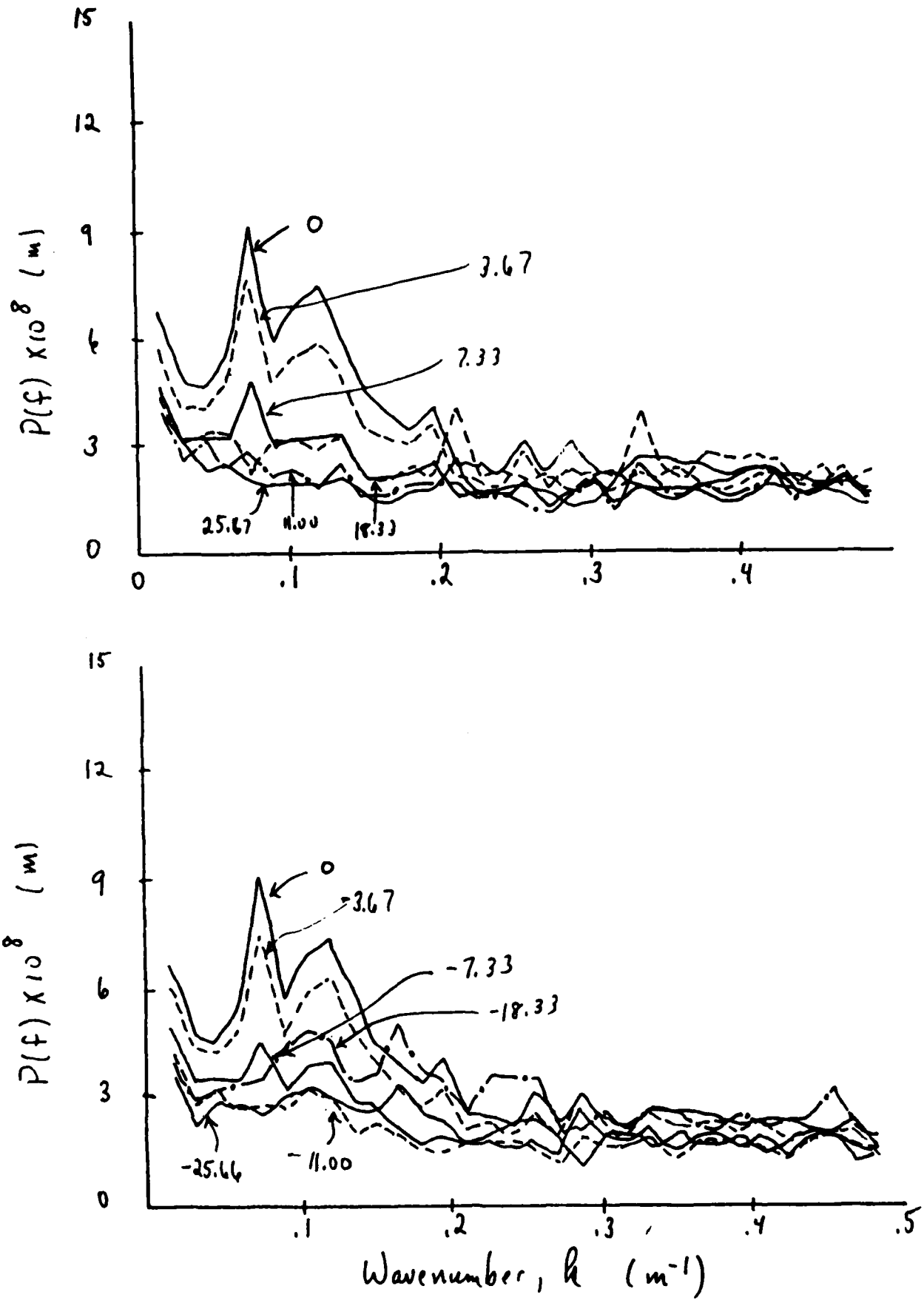

Figure 4. Effect of Focus on Simulated Image - $\vec{V} \cdot \vec{k} = \cos(-142°)$, Leg No. 7, 10/31/84, Single-Look, N = 36, V/R = 0.015 Hz, T = 2.6 sec.

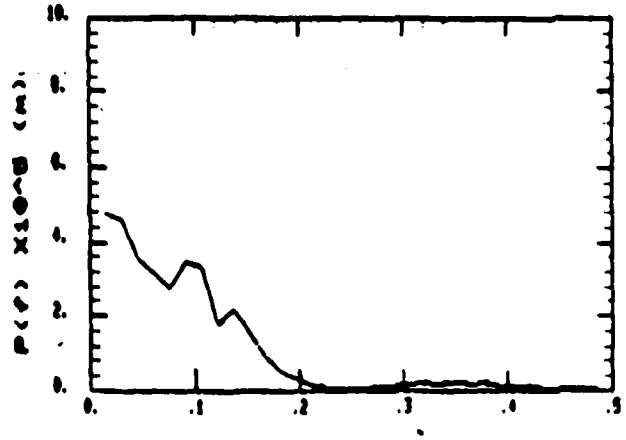

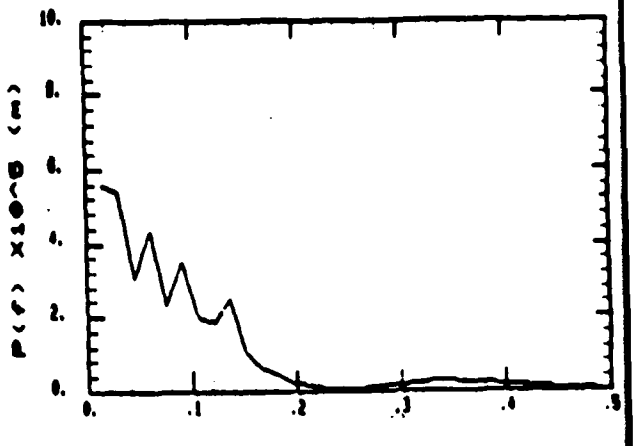

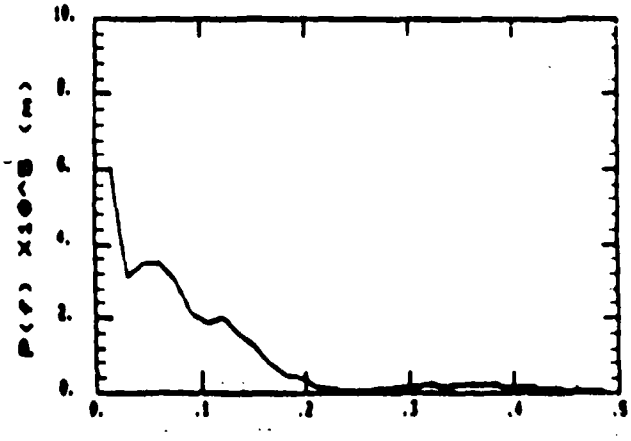

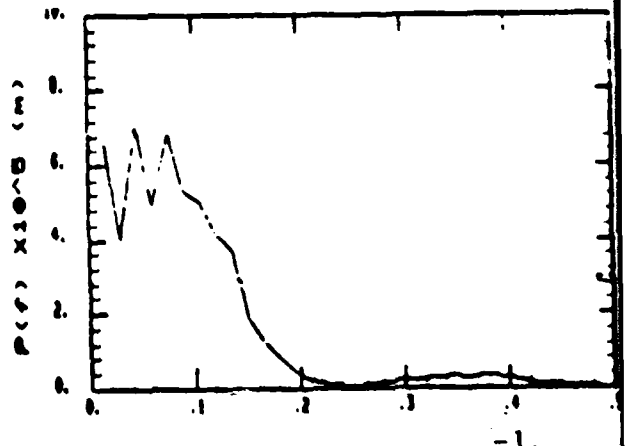

Figure 5. Spectra of Cross-Section at Zero Focus with Conditions Corresponding to: (a) Figure 1, (b) Figure 2, (c) Figure 3 and (d) Figure 4.

APPENDIX VIII

SAMPLE PREDICTIONS AND SIMULATIONS OF SAR OCEAN IMAGERY

Robert O. Harger
Electrical Engineering Department
University of Maryland
College Park, Maryland

SUMMARY

In [1] and [2] models for the SAR image of a sea surface composed of a random ensemble of small gravity waves propagating on, and modified by, a sinusoidal long wave were developed from fundamental models of hydrodynamics, electromagnetic scattering, and SAR theory. Generally speaking, the hydrodynamic and electromagnetic models assume "two-scales" and are therefore especially applicable to L-Band systems and appropriate seas- as, e.g., encountered during the TOWARD experiment.

The detailed analysis of [2] yielded a fairly complete understanding of the nature of these models. The behavior exhibits a diversity: a recapitulation will not be attempted here. However, briefly, it was shown that a major influence on the SAR image nature was the "wavenumber band limiting" effected by the SAR system on the phase modulation factor due to the round-trip ray patch to the large-scale surface. In electrical engineering parlance, there will be an "output" when this phase's derivative- a "local wavenumber"- lies in the wavenumber band passed by the SAR. When the rate of change is sufficiently large, the "output"- if otherwise unperturbed- would approximate the SAR impulse response. The "perturbations" can be described analytically and lead to predictions on the image nature and details such as the "focusing problem".

A principal prediction of [2] was that, under appropriate conditions on SAR and long wave parameters, "well-focussed" extrema can occur in the image intensity at locations corresponding to the crests of the long wave, while "dispersed and defocussed" contributions occur around locations corresponding to the troughs of the long wave. In particular, the average (over the small scale ensemble) can have this feature.

The following is an excerpt form information circulated informally within the TOWARD group in summer, 1985, and contains predictions of certain properties of the SAR images. The discussion assumes that the long wave can be approximated, at least locally, by an appropriately chosen sinusoid.

CHOICE OF RUNS FOR INITIAL ANALYSIS

The runs (2,6,11) of October 31, 1984, were chosen for an initial "quick look" because (i) there is evident "wave-like" imagery of good quality, especially at the 38,000 ft. altitude, and (ii) the long wave is azimuth-directed: this has been the more "controversial" situation in SAR theory and practice and is (therefore)the most completely elaborated case of my theory.

Parameter choices for analysis and simulations - The following choice of a parameter set was made for this preliminary study.

aircraft parameters: height: 38,000 ft. = 14,140 m
20,000 ft. = 7,442 m
7,000 ft. = 2,605 m
velocity: 231.66 m/sec
"crab angle": 0

longwave parameters: wavelength: 94 m
amplitude: 0.435 m
dispersion relation: gravity wave, 18 m depth
direction: "along leg 1"
shape: sinusoidal

small scale wave parameters: (Bragg wavelength = 28.83 m^{-1})
nominal phase velocity: 0.5831 m/sec
(wind direction: "along leg 1")
"white" spectral density over influential wavenumbers
"single family" with "-σ" gravity dispersion relation
no current effects

SAR: resolution ("4-look"): 10 m
spectral weighting: Gaussian shaped, truncated at "3σ" = 3/10 wavenumber bandwidth
incidence angle: 35
beam direction: normal to flight path

By way of further comment, the longwave wavelength was chosen on the basis of the nominal data supplied, the approximate spectrum supplied, and checked against a comparison of SAR imagery and bathymetry. The longwave amplitude was chosen so that its sinusoidal form would have the same rm's height as the (average) observed long wave: the "significant wave height" (nominal) was supplied by Scripps. The assumption of the lack of significant current was based on current information supplied by Scripps.

NOMINAL PREDICTIONS OF THEORY

As discussed earlier -- see, e.g., my MEMORANDUM to the TOWARD Data Analysis Committee, dated June 5, 1985 -- when the longwave amplitude (A) is sufficiently large, a stationary phase approximation usefully describes the SAR image contributions of each wavelet. (The required condition is $\sqrt{A\beta} \geq 1$; here $\sqrt{A\beta} = 4.232$; on the basis of experience with the simulation program -- which does not use this approximation -- the condition is adequately met).

Such a wavelet's image contribution, recall, is described by a doublet (pair) of SAR azimuth impulse responses, periodically repeated at the longwave interval, and translated in azimuth by

$$\Delta = - \left[\frac{1}{\hat{K}} \left(\frac{v_{p20}}{v}\right) + \frac{\delta}{A\beta K_{20}^2}\right] k_{mn_x} + \frac{\sigma_v(K_{mn})}{\hat{K}} \qquad (1)$$

and degraded by the quadratic phase "error"

$$- \left[\frac{1}{\hat{K}} \left(\frac{v_{p20}}{v}\right) + \frac{\delta}{2A\beta K_{20}^2}\right] k^2 \; ; \qquad (2)$$

$\delta = + 1$ for one member of the doublet and $\delta = - 1$ for the other.

Here, with little error,

$$\frac{\sigma_v(K_{mn})}{\hat{K}} \approx \frac{\sigma_v(2k_0 \sin\delta_0)}{\hat{K}} \approx \begin{cases} 3.760 \text{ m}, & R_0 = 2{,}605 \text{ m}, \\ 10.743 \text{ m}, & R_0 = 7{,}442 \text{ m}, \\ 20.412 \text{ m}, & R_0 = 14{,}140 \text{ m}, \end{cases} \qquad (3)$$

The influential wavenumbers of the small-scale are so that

$$|k_{mn_x}| \leq \frac{\Omega}{2} + (1 + A\beta) K_{20} \approx 1.314 \text{ m}^{-1} .$$

Then, in (1), for the three altitudes in order as in (3),

$$[\text{ " }] \approx \begin{cases} \begin{cases} 15.2 \text{ m} \\ 19.7 \text{ m} \\ 26.2 \text{ m} \end{cases}, & \delta = + 1, \\ \begin{matrix} - \\ - \\ + \end{matrix} \begin{cases} 9.98 \text{ m} \\ 5.29 \text{ m} \\ 1.20 \text{ m} \end{cases}, & \delta = - 1 \end{cases}$$

Therefore, we have the bound

$$|[\bullet]k_{mn_x}| \leq \begin{cases} \begin{Bmatrix} 19.97\ \text{m} \\ 25.88\ \text{m} \\ 34.43\ \text{m} \end{Bmatrix}, & \delta = +1, \\ \begin{Bmatrix} 13.11\ \text{m} \\ 6.95\ \text{m} \\ 1.58\ \text{m} \end{Bmatrix}, & \delta = -1. \end{cases} \tag{4}$$

Because k_{mn} may be of either sign, the "spread" of the (degraded) SAR impulse locations os twice this number. AS the longwave wavelength is 94 m and the SAR resolution 10 m, we see that:

1 - When $\delta = -1$, the locations are fairly well clustered, especially so at the highest altitude and less well at the lowest altitude;

2 - When $\delta = +1$, the locations are rather widely spread out, especially so at the highest altitude.

We now turn to an analysis of the effect of the quadratic phase "error". This can be seen by calculating the resultant rms "resolution" of the SAR impulse: assuming an un-truncated Gaussian shape for the azimuth transfer function, we get the approximation

$$\rho_v = \sqrt{\rho^2 + \left\{ \frac{2}{\rho} \left[\frac{1}{K} \left(\frac{v\rho_{20}}{v} \right) + \frac{\delta}{2A\beta K_{20}^2} \right] \right\}^2} \tag{5}$$

Here, then,

$$\rho_v = \begin{cases} \begin{Bmatrix} 10.27\text{m} \\ 10.90\text{m} \\ 12.28\text{m} \end{Bmatrix}, & \delta = +1, \\ \begin{Bmatrix} 10.00\text{m} \\ 10.17\text{m} \\ 11.02\text{m} \end{Bmatrix}, & \delta = -1 \end{cases} \tag{6}$$

We see that both members of the doublet are degraded rather little at all the altitudes, for this particular data set.

We can now make some predictions of the image nature based on the above simple analysis.

1 - The image nature is primarily affected by the translations (wavenumber-dependent) of the individual image contributions of each wavelet; it is affected rather little by the degradations of the doublets.

2 - The image will have local maxima, spaced at the longwave wavelength. Accounting for the relatively small translations of these impulse responses, their "resolution", or rms spread, will be estimated as about

$$\begin{cases} 36 \text{ m}, R_0 = 7{,}000 \text{ ft.} = 2{,}605 \text{ m}, \\ 24 \text{ m}, R_0 = 20{,}000 \text{ ft.} = 7{,}442 \text{ m}, \\ 13 \text{ m}, R_0 = 35{,}000 \text{ ft.} = 14{,}140 \text{ m}, \end{cases}$$

3 - The "background" against which these local maxima appear will be of increasing spread -- hence (to a limit) of reduced level, as the height increases.

- Therefore, the "contrast ratio" should increase with increasing height.

Thus, we expect to see, at all three heights, local maxima, spaced at the longwave wavelength, with "contrast ratio" best at the largest height, worst at the lowest height.

The optimum value of the focus correction parameter C -- see the above-cited MEMORANDUM -- is, here,

$$C_{opt} = -10.4 * 10^{-2} + \begin{cases} 24.1 * 10^{-2}, R_0 = 2{,}605 \text{ m}, \\ 8.44 * 10^{-2}, R_0 = 7{,}442 \text{ m}, \\ 4.44 * 10^{-2}, R_0 = 14{,}140 \text{ m}, \end{cases}$$

In the TOWARD experiment the observed long wave spectral density was apparently not especially narrow in its support, giving impetus to extending the theory of [2] in this regard: this has now been done under appropriate approximations. A basic difficulty is that an adequate theory for the modification of short waves on a suitably general long wave is even now under development. (See Longuet-Higgins, Appendix IV herein).

If the bandwidth of the long wave ensemble is not unduly broad, its sample functions will have a quasi-sinusoidal nature and we expect that, locally, the main features of the above analysis carry over: this is borne out by the simulations.

Some examples of simulation results will be discussed below for a set of parameters that include an assumed 5m resolution. The JPL SAR employed- at least some of the time- a very widebeamed antenna having an intrinsic resolution about ten times finer, while the imagery distributed to the investigators was degraded to various coarser resolutions- e.g., 11 m. The effects of motion in such data can be approximately equivalent to those of a SAR with such a resolution- e.g., 11m. A more precise simulation would likely require the program to be transported to a computer of significantly greater capacity. (A VAX 785 is currently being used).

The pricipal parameters assumed in the simulations cited below are listed here.

SAR resolution: 5 m

SAR slant range: 14,000 m

SAR RF wavelength: 0.25 m (L-band)

SAR incidence angle: 35 deg

Long wave: (a) sinusoidal, wavelength 100 m, amplitude 0.5 m

(b) random with wavenumber spectral density of Scripps for Oct. 31, 1984

water depth: 18 m

Small scale ensemble: random with "white" spectral density, one "sigma family"

Simulation sample distance: 1 m

Number of object samples: 1024

Number of image samples: 338

In Figure 1a is shown the simulated image for the sinusoidal long wave and a small-scale wavelet consisting of a single sinusoid at the "Bragg-matched" wavenumber. Its nature is fully explained by the analysis of [2]- recall the image extrema correspond to the crests of the long wave. The corresponding spectrum (Fourier transform) is shown in Figure 1b: of course it has strong "lines" as a result of the apparent periodicities in the image. (Note that the harmonic relation to the long wave becomes more pronounced at the higher wavenumbers. Also recall that a long wave traveling with the SAR has wavelength its increased- here a few percent).

Figure 1a.

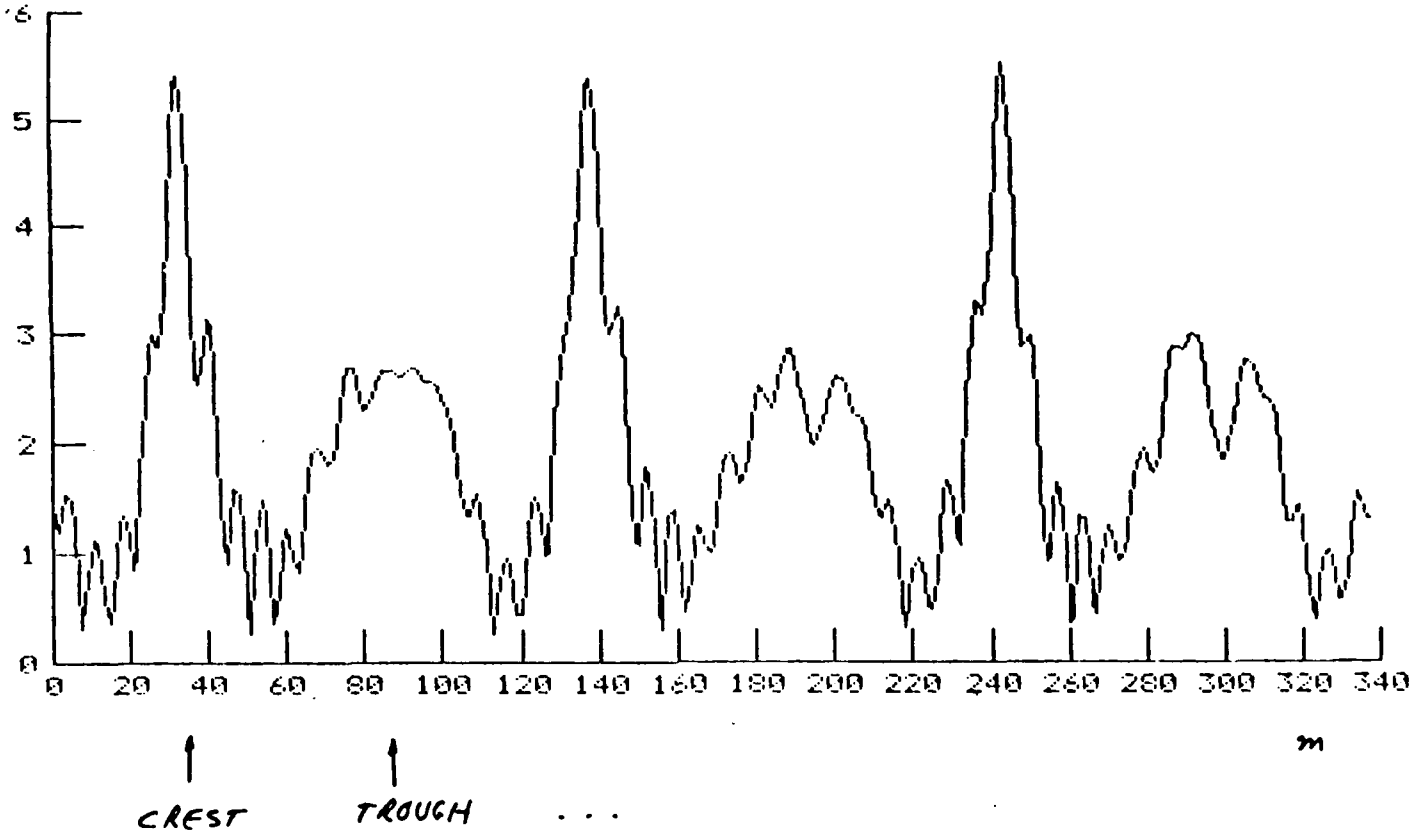

Figure 1b.

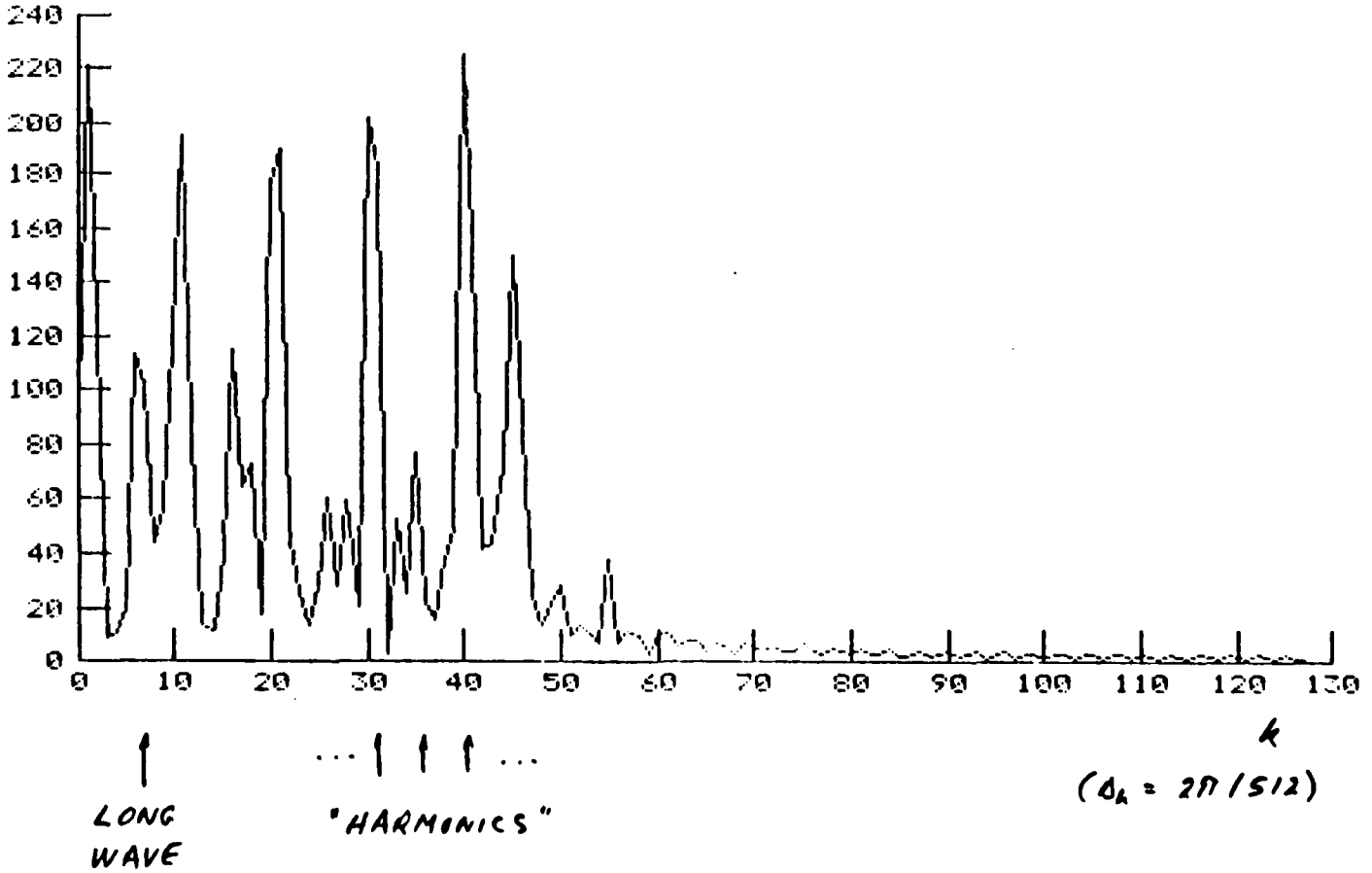

In Figure 2a is shown the sample average of about two dozen images for the same sinusoidal long wave but with a full spectrum of small-scale wavelets. Again, the analytic predictions of [2] are supported by the numerical simulation. The corresponding spectrum is shown in Figure 2b: the "lines" due to the image periodicities are still clear, though not as abundant.

In Figure 3a is shown a segement of a sample function, at the mean observation instant, of the long wave random ensemble. This (Scripps) spectrum has considerable support and, correspondingly, the sample functions fluctuate more rapidly than a single sinusoid at the dominant wavenumber. Based on the analysis of [2], we expect image maxima, generally, corresponding to the crests of the long wave sample function.

In Figure 3b this expectation is borne out. The theory of [2] predicts an image translation of, here, about 21 m due to the mean effect of the small-scale wave motion: if 3b is so translated, its extrema lie rather as predicted.

The corresponding spectrum is shown in Figure 3c: the "lines" appearing are, at the higher wavenumbers, generally, harmonically related to a wavelength about 100 m- approximately the dominant wavenumber. However, at the lower wavenumbers there is strong spectral content attributable to the longwave and image fluctuation which is a fraction of the long wave period.

A (limited as yet) number of similar simulations indicate that, rather as would be expected, the image nature will strongly depend on the particular long wave sample function "drawn by nature" from the ensemble charaterized by the spectral density measured by Scripps. Such a situation calls for a suitable averaging process over the long wave ensemble.

AD-A171 038 'TOWARD 84/86' FIELD EXPERIMENT: INVESTIGATION OF PHYSICS OF SYNTHETIC AP (U) JET PROPULSION LAB PASADENA CA O H SHEMDIN MAY 86 3/3

UNCLASSIFIED F/G 17/9 NL

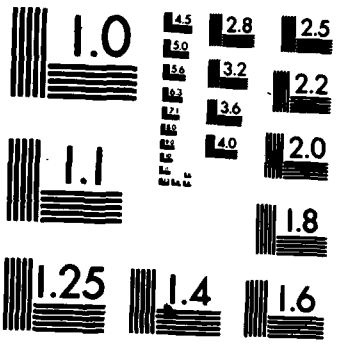

Figure 2a.

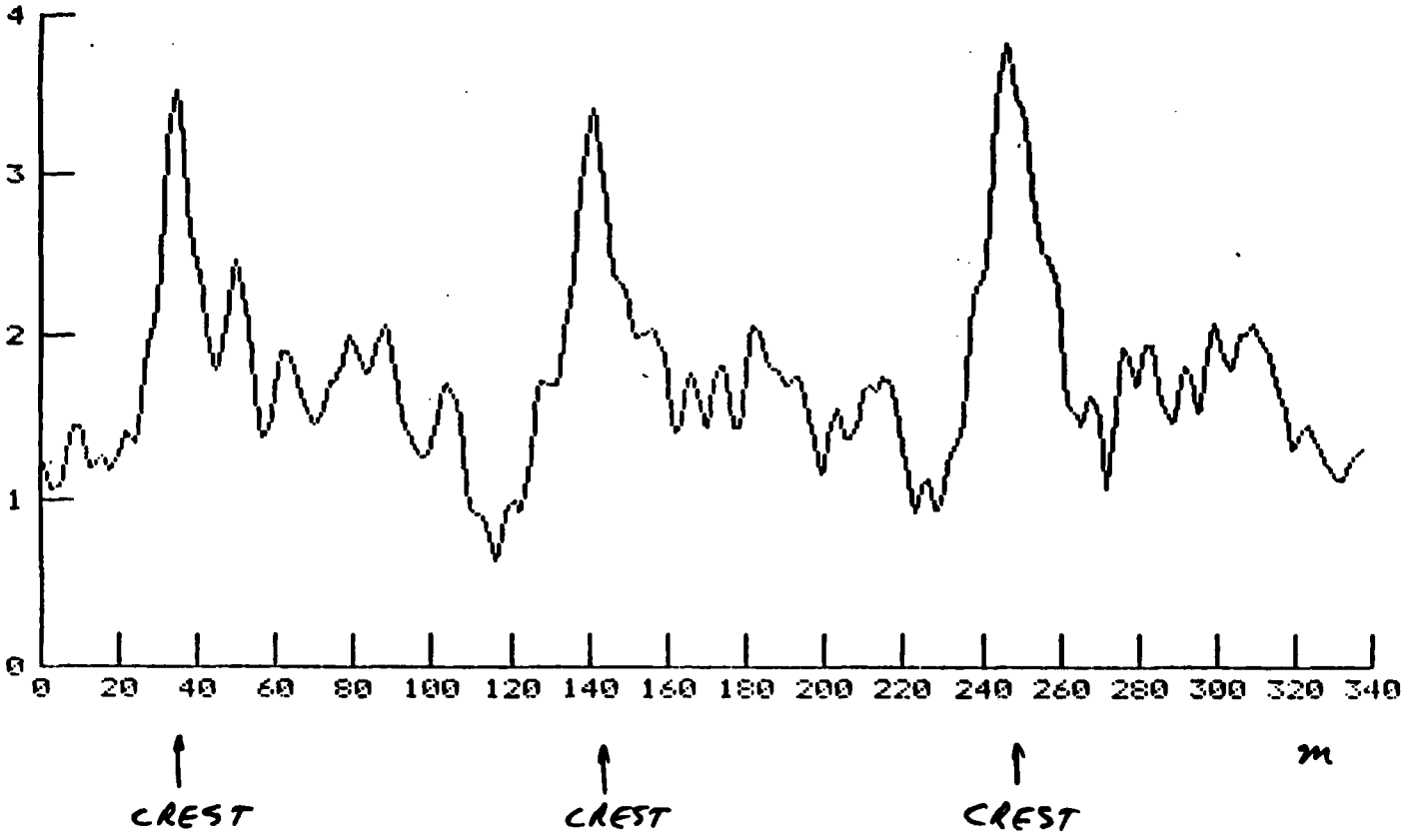

Figure 2b.

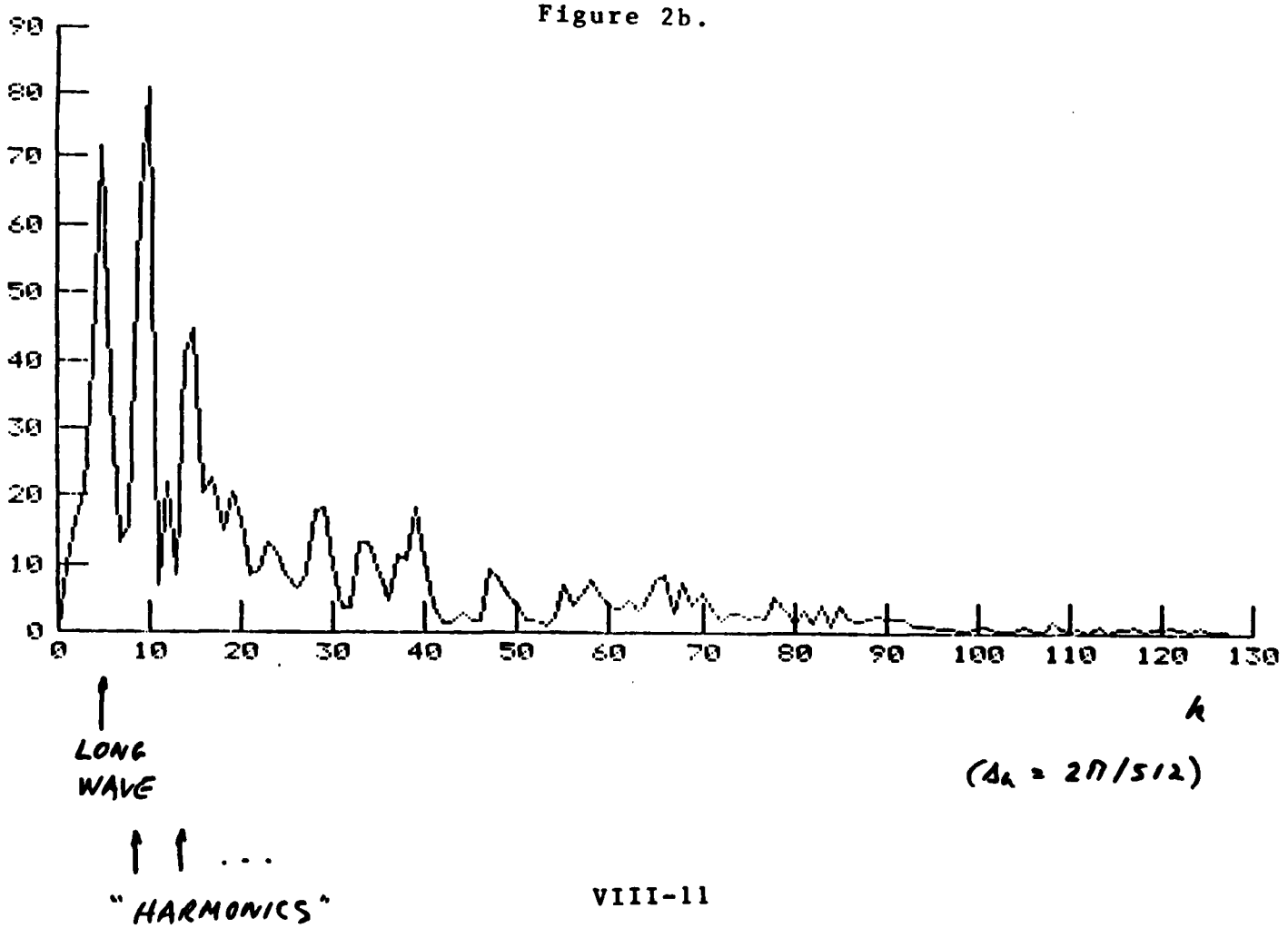

Figure 3a.

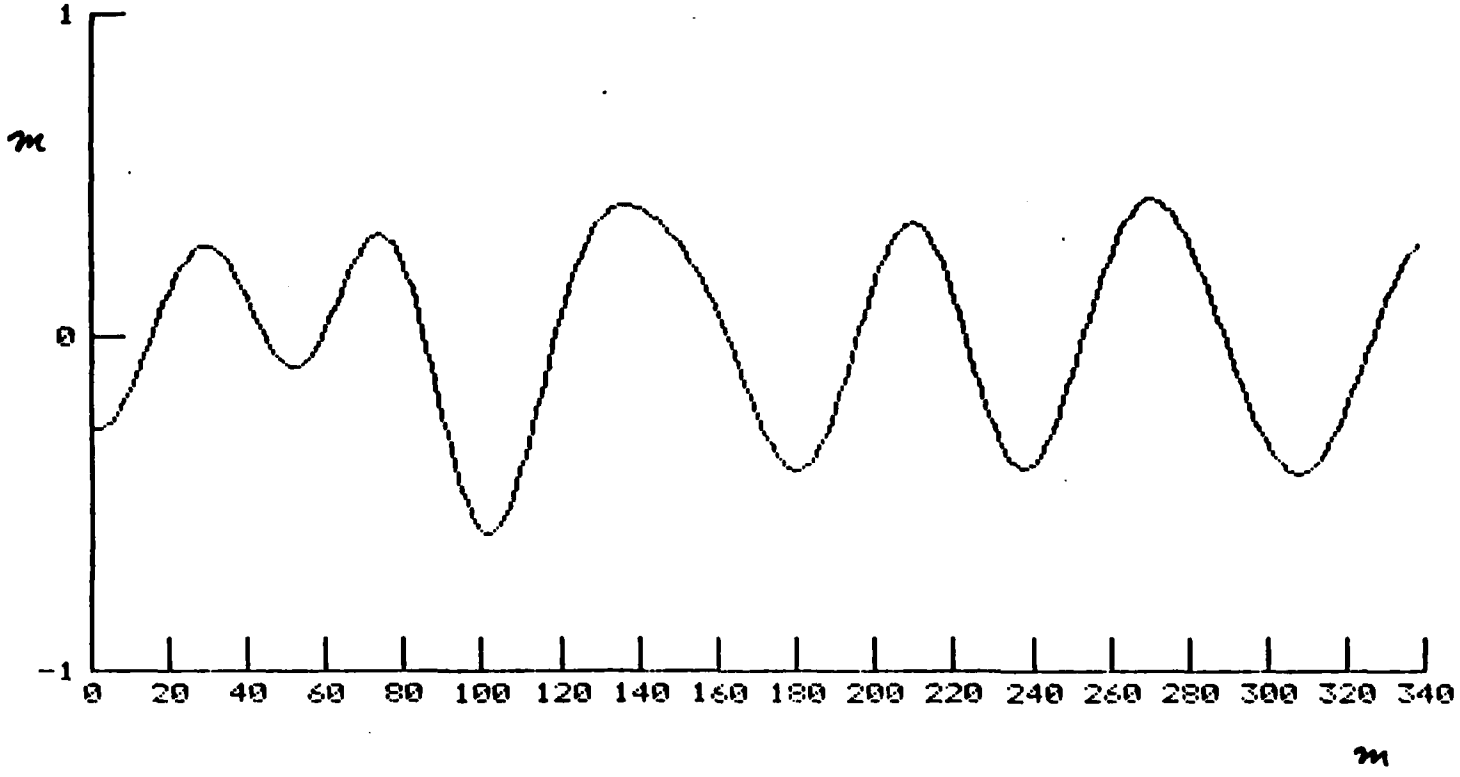

Figure 3b.

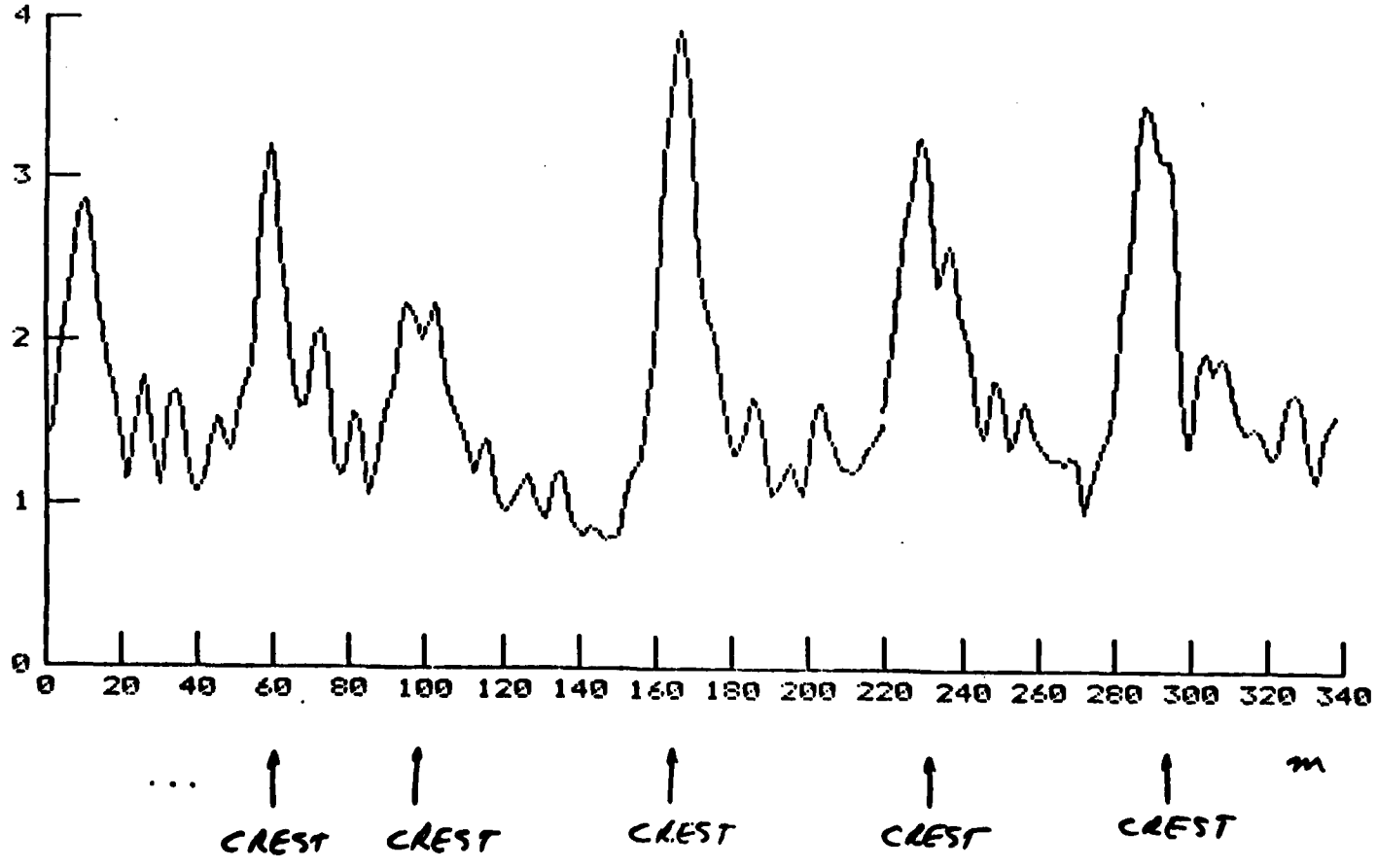

In Figure 4 is shown a "standard" ([3], p. 556) spectral density estimate using 24 complex, simulated SAR images. on each run both the long wave and the small scale were drawn randomly.

We may compare this spectral density estimate based on the simulation with the actual SAR image data. Presently at hand is a spectral density estimate obtained by the same "standard" method- but using 100 adjacent range cuts: therefore, because of the nearly azimuth-directed nature of the long wave, the long wave samples are rather correlated. Such a spectral density estimate is shown in Figure 5.

Comparing Figures 4 and 5 we see that the SAR image spectrum is "full" to wavenumbers cutoff by the bandwidth of the SAR system. Also, comparing to the long wave spectral density measured by Scripps, appearing elsewhere in this report, we see that it does not resemble at all either the "actual" or "simulated" SAR spectral densities. While subject to refinement, we expect the above conclusion to hold and is a very important observation since many have mistakenly believed that they are similar.

As a final simulation example, a SAR image of 344 m (azimuth) by 210 m (range) is shown in Figure 6. (The aspect ratio is incorrect, being taken "as is" from the printer). The (randomly occurring) maxima attributable to the long wave are evident.

This simulation capability could be a powerful assist in understanding SAR imagery of ocean phenomenon in various situations and applications.

Figure 3c.

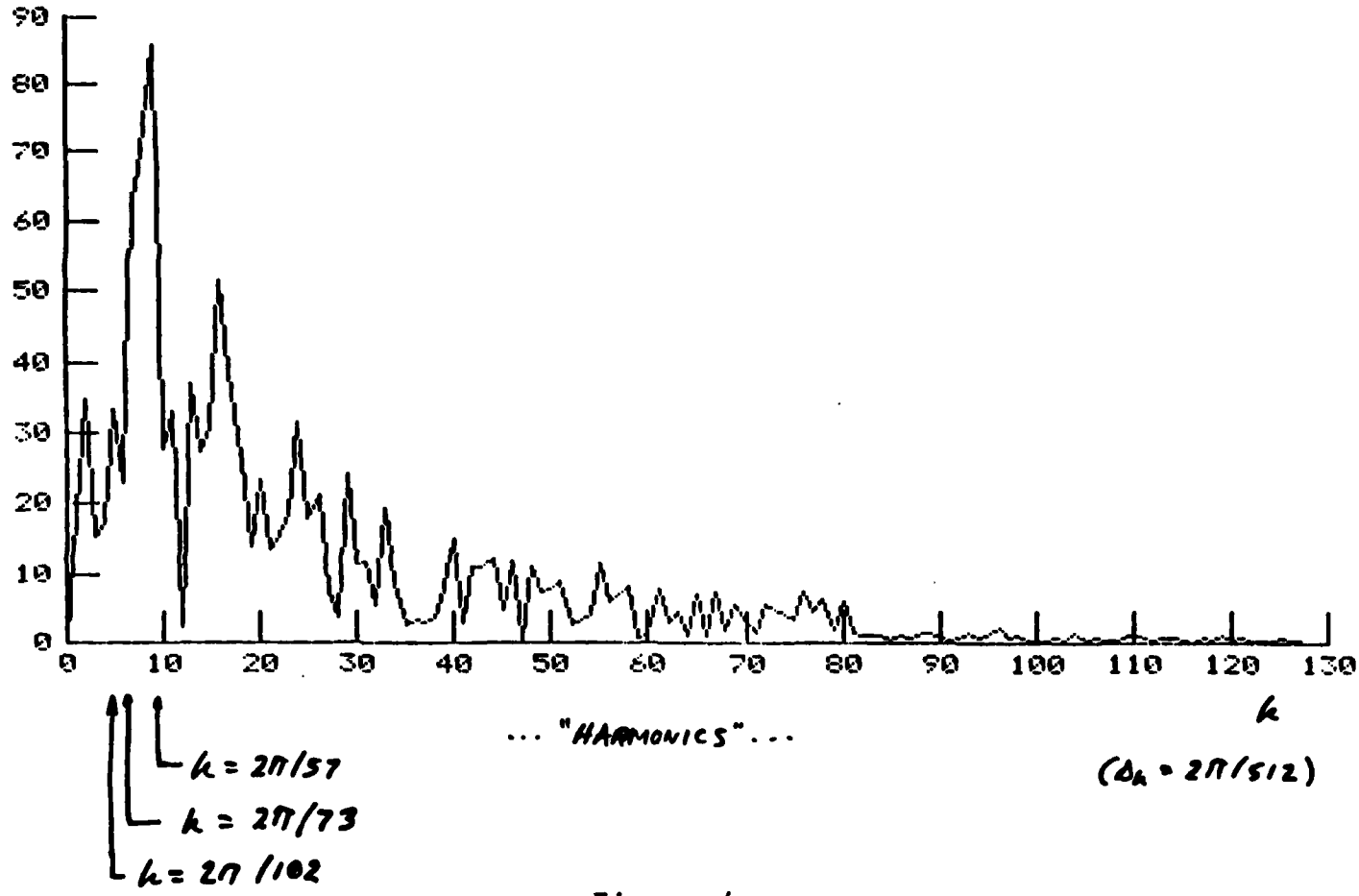

Figure 4.

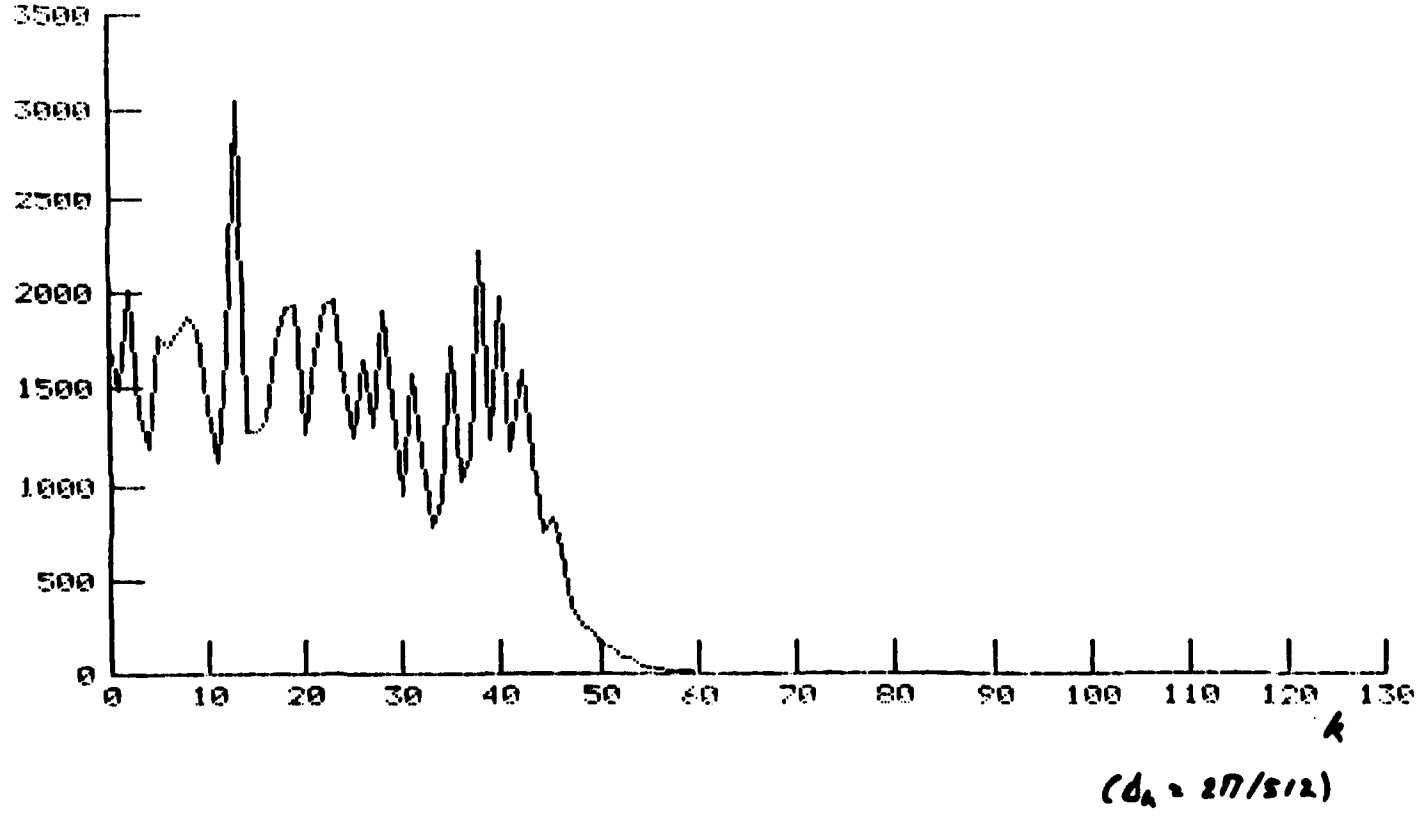

Figure 5.

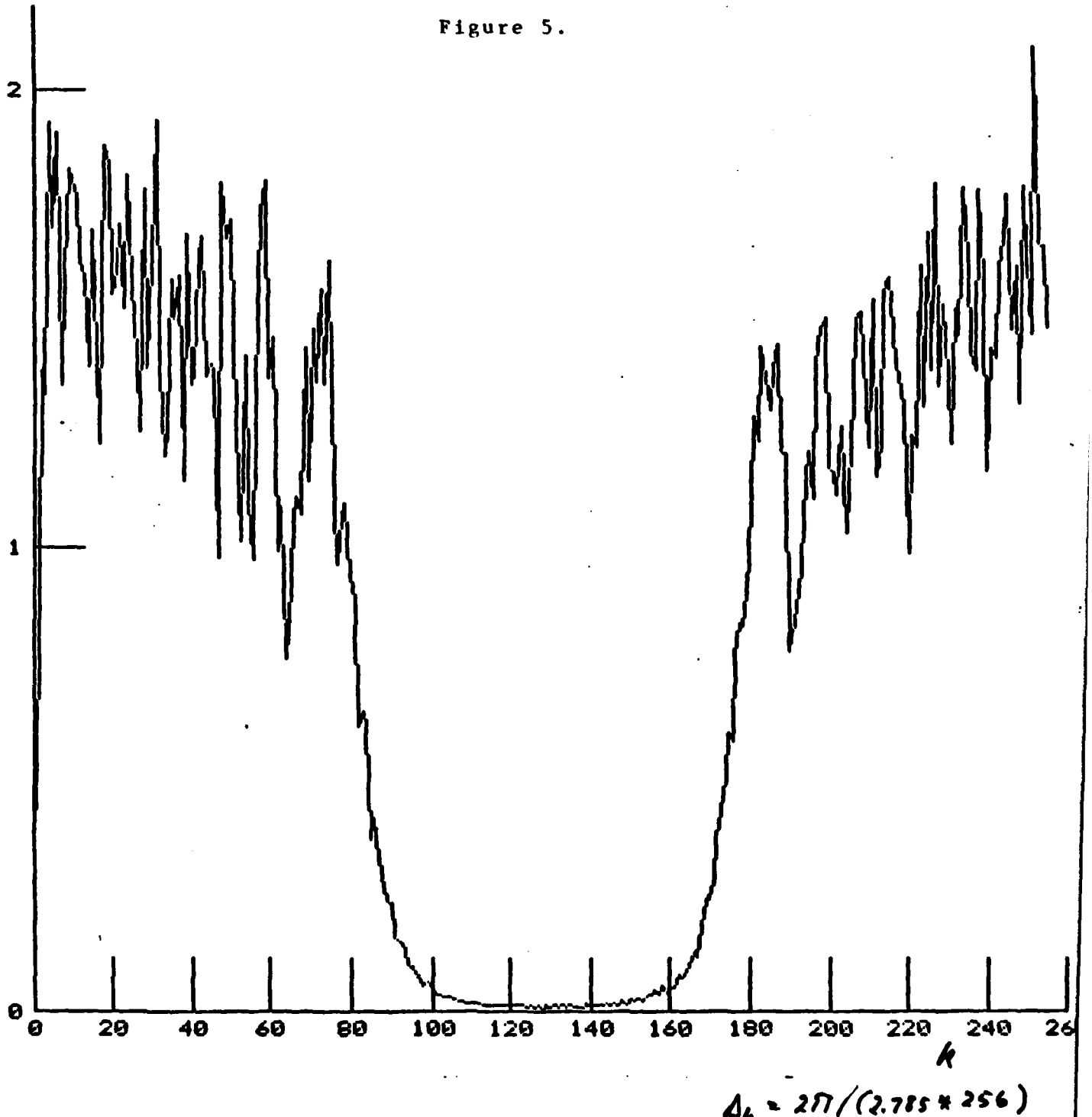

Figure 6.

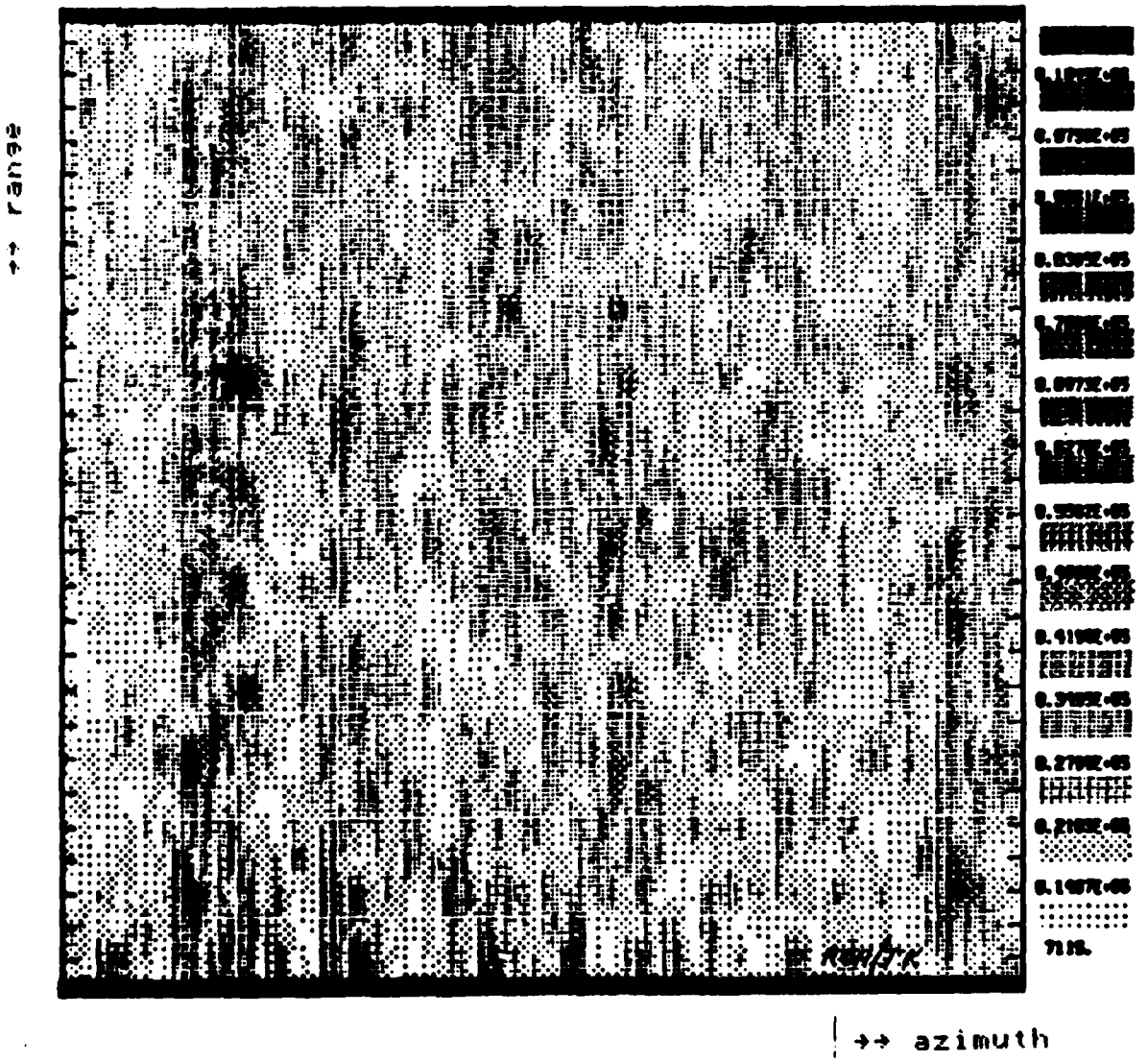

REFERENCES

1. R.O Harger, "The SAR image of short gravity waves on a long gravity wave", IUCRM Symposium on Wave Dynamics and Radio Probing of the Ocean Surface, Miami, Fla. 1981. To appear as Chapter 25 of proceedings, O. Phillips and K. Hasselmann, Eds.: 1986, Pergamon Press.

2. R.O. Harger, "The SAR image of short gravity waves on long gravity wave: an explication", to appear in IEEE Journal of Ocean Engineering.

3. A. Oppenheim and R. Schafer, Digital Signal Processing. Prentice Hall, 1975.

END

DTIC

9-86